Spectroscopic Investigations of Renewable Fuel-Forming Reactions Catalyzed by Electrified Interfaces

Jingyi Li

A dissertation
submitted to the Faculty of
the Department of Chemistry
in partial fulfillment
of the requirements for the degree of
Doctor of Philosophy

Boston College
Morrissey College of Arts and Sciences
Graduate School
Advisor: Professor Matthias M. Waegele

August 2021

Spectroscopic Investigations of Renewable Fuel-Forming Reactions Catalyzed by Electrified Interfaces

Jingyi Li

Advisors: Matthias M. Waegele, Assistant Professor of Chemistry

Electrocatalysis can promote reactions that are critical for the sustainable production of fuels and high-value commodity chemicals. For example, the electrochemical reduction of CO_2 on various metal electrodes and their alloys has been demonstrated to provide access to a diverse range of industrially relevant products, including carbon monoxide, formate, ethylene, acetate, and ethanol. To enable these and other reduction reactions on a large scale, an abundant supply of electrons and protons is required. The water oxidation reaction has the potential to acts as such a source. The electrochemical reduction of CO_2 is generally associated with poor product selectivity and high overpotentials, which are necessary to drive the reaction. Driving the water oxidation reaction requires high overpotentials, too. To address these challenges, it is essential to reveal the interfacial properties that determine the catalytic activity and selectivity of the electrode/electrolyte contact and to probe the reaction mechanisms and their dependence on experimental conditions. In this dissertation, we utilize spectroscopic and electroanalytical techniques to reveal the intricate relationships between interfacial properties and catalytic activity and selectivity, and reaction mechanisms and experimental conditions.

In the first part of this dissertation, we focus on how electrolyte and electrode characteristics influence the reduction of CO_2 on copper electrodes. In Chapter 3 of this dissertation, using a series of quaternary alkyl ammonium cations ($methyl_4N^+$, $ethyl_4N^+$, $propyl_4N^+$, and $butyl_4N^+$), we systematically tuned the properties of the liquid reaction environment to probe how it affects the electrocatalytic reduction selectivity of CO to hydrocarbons on Cu electrodes. Employing differential electrochemical mass spectrometry (DEMS), we

observed that ethylene is produced in the presence of methyl$_4$N$^+$ and ethyl$_4$N$^+$ cations, while this product is absent in propyl$_4$N$^+$- and butyl$_4$N$^+$-containing electrolytes. With surface-enhanced infrared absorption spectroscopy (SEIRAS), we show that the cations do not block CO adsorption sites and that the cation-dependent interfacial electric field is too small to account for the observed changes in selectivity. Strikingly, SEIRAS reveals that the hydrophobicity of the two larger cations disrupts the intermolecular interaction between surface-adsorbed CO and interfacial water. This observation suggests that this interaction promotes the hydrogenation of surface-bound CO to ethylene.

In Chapter 4 of this dissertation, using two types of rough Cu thin-film electrodes, we sought to understand how their distinct atomic-level surface morphologies determine the catalytic activities of the two types of electrodes. DEMS shows that copper films that are electrochemically deposited on Si-supported Au films (CuAu-Si) exhibit an onset potential for ethylene that is $\approx 200 \pm 65$ mV more cathodic than the one of copper films (Cu-Si) that are electrolessly deposited onto Si crystals. Cyclic voltammetry (CV) reveals that the (111) surface facet prevails on CuAu-Si, while the (100) facet is predominant on Cu-Si. SEIRAS reveals the existence of disparate surface morphologies, which manifest themselves in the from of different potential-dependent behaviors of the line shape of the C$\equiv$O stretching band of atop-bound CO. We rationalize the observation with a Boltzmann model that takes into account the difference in CO adsorption energy on terrace and defect sites. This study establishes SEIRAS of surface-adsorbed CO as an important tool for the *in situ* investigation of the atomic-level surface morphology of rough metal electrodes.

In the second part of this dissertation, we explore the potential-dependence of the mechanism of the water oxidation reaction on cobalt-oxide based electrocatalysts. To a significant extent, the mechanisms of the water oxidation reaction on heterogeneous catalysts remain obscure. A key elementary step of the water oxidation reaction is the formation of the O-O bond. The intramolecular oxygen coupling mechanism (IMOC) and the

water nucleophilic attack mechanism (WNA) have been proposed as possible pathways of O-O bond formation. However, it is still unclear to what extent the accessibility of each pathway is controlled by the applied potential.

In Chapter 5 of this dissertation, employing water-in-salt electrolytes, we systematically altered the water activity, which enabled us to quantify the impact of the water activity on the rate of the reaction. We discovered that the water oxidation mechanism is sensitive to the applied electrode potential: At relatively low driving force, the reaction proceeds through the IMOC pathway, whereas the WNA mechanism prevails at high driving force. Density functional theory (DFT) calculations provide an explanation for our experimental observations: Prior to water nucleophilic attack, the WNA pathway requires one additional oxidation, which is associated with a high thermodynamic overpotential. Further, using SEIRAS, we detected a superoxo species, a key reaction intermediate on heterogeneous cobalt-oxide based catalyst. This work demonstrates that the IMOC and WNA mechanisms prevail in different potential regimes, an important consideration when determining electrolyzer operation conditions.

In summary, the work presented in this dissertation provides fundamental insights into the operating principles of electrocatalytic interfaces. These insights are of practical significance and are expected to benefit the design of electrolyzers with high efficiency.

Contents

List of Figures

List of Tables

Acknowledgement

First, I wish to express my most sincere gratitude to my advisor Prof. Matthias M. Waegele, for his guidance and support throughout my PhD study. As an excellent and careful scientist, Prof. Waegele himself acts as a role model for me. He uses his deep knowledge and rich experience in chemistry to teach me how to perform research from a broader view, how to critically analyze data, how to efficiently address scientific challenges, and how to be a true scientist. I am extremely fortune to be the first students in the Waegele team so that I received tremendous instructions and guidance directly from him. I cannot thank him more for how much I have grown in lab in the past years.

I am grateful to my committee members: Prof. Dunwei Wang, Prof. Udayan Mohanty, and Prof. Lucas Bao. Prof. Wang co-advises me for the water oxidation project. His deep knowledge in material science, solid-state chemistry, and electrochemistry has helped me greatly in envisioning a broader scientific picture. I also wish to thank Prof. Mohanty for sharing his strong theoretical knowledge in those helpful discussions about the projects I worked on. I am also grateful to Prof. Bao for your insight in this thesis. I also wish to express my gratitude and memory to Prof. Frank Chia-Kuang Tsung. He was my committee member for my oral qualification exam, during which he helped me to understand my research more comprehensively. I am also thankful to my collaborators in water oxidation project: Dr. Ke R. Yang, Prof. Victor S. Batista, and Prof. Gary W. Brudvig at Yale University. They provided valuable theoretical support and helpful discussion to the project.

Next, I wish to acknowledge my dear labmates: Dr. Charuni Gunathunge, Xiang Li, Vincent J. Ovalle, R. Paul Hicks, Jingchen Yang, Julie Hong, Yu-Shen Hsu, Dr. Hongna Zhang, Connor Gallacher, Tingjun Ye, Sammi Wu. We spent so much good time together in the lab and out of the lab. We share success, happiness, frustration about research and life. We support and help each other out whenever we could. I really enjoyed working

in such a friendly environment, especially with Charuni and Xiang, together with whom I started my PhD study in the same year.

I also like to thank the collaborative water oxidation team between the Waegele lab and the Wang lab: Dr. Hongna Zhang, Dr. Yuanxing Wang, Chaochao Lang, Dr. James Thorne, Dr. Benjamin Williams, Tianying Liu. I learned a lot from them through in-depth discussion.

Same gratitude goes to my other colleagues and friends, Dr. Jingru Luo, Dr. Qi Dong, Dr. Xiahui Yao, Dr. Da He, Dr. Yumin He, Dr. Wei Li, Dr. Yanyan Zhao, Dr. Qingmei Cheng, Dr. Haoyi Li, Dr. Rong Chen, Haochuan Zhang, Tongtong Luo, Wei-Shang Lo, Dr. Zhehui Li, Yang Li, and Ailun Wang. I am very grateful to the great relationships among the physical chemistry groups.

I wish to acknowledge all the administrative and technical staffs in the Chemistry Department, the Physics Department, and the Integrated Sciences Cleanroom and Nanofabrication Facility of Boston College.

I will save the last and the most important space to thank my family. To my parents, Ms. Qisi Liang and Mr. Xiangtao Li, my grandparents and other family members. It is your continuous love and care that keep me fighting tirelessly. Especially, I want to thank my husband, Qi Dong. No words ever exist in this world that I can borrow to express my love to you. You support me unconditionally in whichever way you can think of. With you, I learned what family truly means to me. I am looking forward to the journey in front of us. I also wish to thank my daughter, Isabella Dong, for bringing in so much happiness and laughter to my life. You help me to grow, to mature, to be a responsible parent. I wish for your life to be filled with everything that makes you happy. I also wish for you to understand that no matter what life may bring, we will always be your constant.

Dedication

To my parents Qisi Liang, Xiangtao Li, my husband Qi Dong, and my daughter Isabella Dong.

Chapter 1

Introduction

1.1 Novel Approaches for Solving the Energy Crisis

1.1.1 Electrochemical Carbon Dioxide Reduction

Ever since the industrial revolution, the need for fossil fuels has soared rapidly [1]. From large-scale industrial processes, such as electricity generation, to our day-to-day life (*e.g.*, transportation), we heavily rely on fossil fuels. However, the availability of fossil fuels is limited in both domestic and international reverses. It was predicted that, with respect to the year of 2005, the fossil fuel depletion time will be 35, 107, and 37 years for oil, coal, and gas, respectively [2]. The surging dependence on feedstock can be mitigated by the advancement of modern technologies such as hydraulic fracking and the utilization of natural gas. Additionally, the combustion of fossil fuels has caused a rapid rise of CO_2 level to 400 ppm in the earth's atmosphere [3]. The outcome of such increase of CO_2 concentration is global climate change, which is projected to give rise to sea level rise and more frequent extreme weather conditions [3, 4]. We have already experienced some of these effects, all of which point to the importance transitioning to a carbon-neutral economy.

One strategy is decarbonization: For example, solar panels, wind turbines, and hydroelectricity provide energy that does not rely on fossil fuels. Great success has been

achieved with this approach of lowering CO_2 emission [5]. However, because of the desirable properties of liquid hydrocarbons (high energy density, relatively safe to transport, etc.) a continued need for carbon-based fuels is likely in the near future.

Another strategy, CO_2 recycling, aims to convert CO_2 into value-added hydrocarbons. This process closes the carbon cycle, effectively eliminating net emission CO_2 into the atmosphere. CO_2 can be recycled by reducing it by adding protons and electrons [6]. The CO_2 reduction reaction (CO_2RR) is typically coupled to the water oxidation reaction. The overall general chemical equation is:

$$x\mathrm{CO_2} + y\mathrm{H_2O} \rightarrow \mathrm{products} + z\mathrm{O_2} \tag{1.1}$$

Heterogeneous catalysts for the promotion of the CO_2RR has attracted much attention because of its potential for renewable liquid fuel production. Moreover, when coupled with renewable electricity sources, *e.g.*, wind and solar, it also enables sustainable energy storage in the forms of chemicals.

The principle of this technology is shown in Figure 1.1, in which the recycling of CO_2 is performed in an electrochemical cell. With CO_2 dissolved in the aqueous electrolyte, the solution serves as the proton donor required for the hydrogenation.

Depending on the number of electrons and protons transferred during the CO_2RR, this process can generate up to 16 different hydrocarbon or oxygenate products in the gas or liquid phases [7]. The simplest products involving two electrons are carbon monoxide (CO) (generated on Au, Ag, Zn, Pd, and Ga electrodes) and formate ($HCOO^-$) (produced on Pb, Hg, In, Sn, Cd, and Tl cathode) [8]. Other multi-electron products include C_1-C_3 hydrocarbons and oxygenates are produced on copper [7]. The hydrogen evolution reaction (HER) is the major competing reaction during the CO_2RR in aqueous electrolytes.

Copper is the only pure metal that is able to reduce CO_2 to C_{2+} hydrocarbons and oxy-

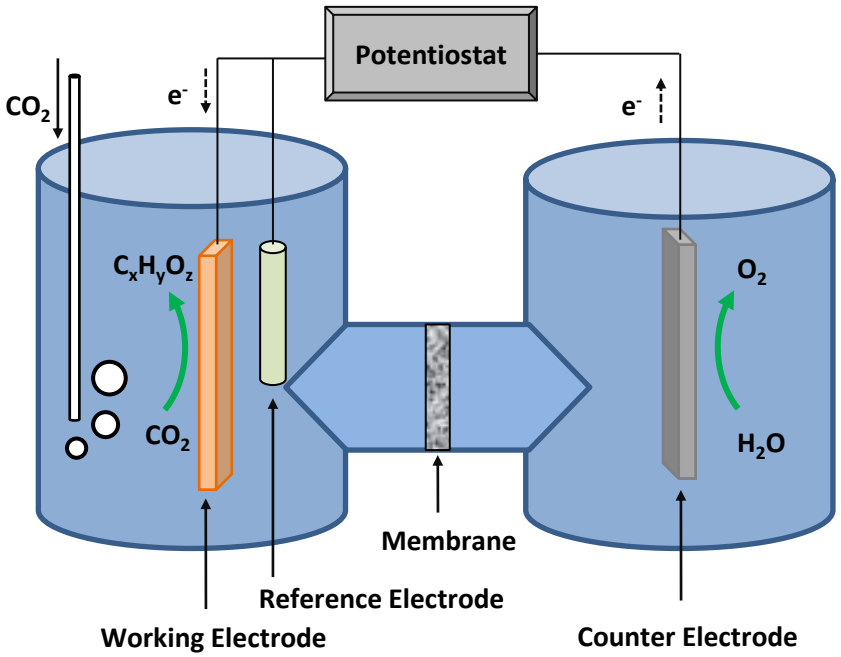

Figure 1.1: Schemetic of CO_2RR setup.

genates at significant rates. The underlying reason for Cu to be such unique in CO_2RR is the moderate binding energy for CO, a key reaction intermediate [9]. This special property of Cu as a CO_2RR catalyst has propelled major research efforts in tailoring Cu electrodes in terms of morphology and composition to increase the catalytic activity and tune the catalytic selectivity: For example, oxide-derived copper (OD Cu) has been reported to be highly selective toward C_{2+} products during CO_2RR [10, 11]. The formation of grain boundaries on the surface on this catalyst is considered the main contributing factor promoting the high selectivity [12–14]. It is also well known that the crystallographic facets play an important role in catalytic activity and selectivity. Cu(100) is a better catalyst in ethylene evolution compared to Cu(111) [8]. Alloying Cu is another strategy to tune product selectivity. By doping the Cu electrode with other metals such as Au, Ag, Ni, and Zn, and Sn, the tandem catalysts synergistically boost the formation of desired products [15–22]. These examples illustrate that the careful design of the electrode composition and morphology is essential for steering the CO_2RR.

The CO_2RR takes place at the electrode/electrolyte interface. The nature of the electrolyte can profoundly affect the reaction activity and selectivity by changing the local reaction environment [23–33]. For example, cation identity and concentration have shown great impact on catalytic processes [32]. For instance, the CO_2RR shows an up to six times better selectivity toward hydrocarbon formation with respect to the HER in the presence of Cs^+-containing electrolyte compared with that in Li^+-containing electrolyte [27]. Spectroscopic investigation showed that Cs^+ can maintain the interfacial pH better than Li^+ due to the higher buffering ability of hydrated Cs^+ [28]. Also, Cs^+ near the vicinity of the electrode can introduce a stronger local electric field compared with that in Li^+-containing electrolyte [30]. Large electric fields can play an important role in the promotion of reactions involving intermediates and/or transition states with large dipole moments and/or polarizability. These examples demonstrate that electrolyte design is of great importance for achieving high activity and selectivity.

1.1.2 Electrochemical Water Oxidation

The $4e^-$, $4H^+$ water oxidation reaction, often termed oxygen evolution reaction (OER), turns water into molecular oxygen. Simultaneously with the liberation of dioxygen molecules, this reaction also generates four protons and four electrons:

$$2H_2O \rightarrow O_2 + 4H^+ + 4e^- \tag{1.2}$$

As described in equation 1.1, these electrons and protons are required for all reductive catalytic processes, such as CO_2RR, HER, and nitrogen fixation [34–36]. The OER is also involved in rechargable metal-air batteries and regenerative fuel cells technology [37, 38]. Therefore, the central significance of OER is evident. However, the water oxidation reaction is notoriously energy inefficient [39]. To address this issue, more efficient water

oxidation catalysts (WOC) need to be developed.

In Nature, the generation of oxygen is carried out by photosynthesis with Photosystem II (PSII), which is a Mn and Ca based protein complex employing solar light as the energy input to turn water into oxygen [40]. Inspired by the biological model, a series of molecular catalysts for water oxidation were discovered [41–44]. The active catalytic center includes Mn, Fe, Co to Ru and Ir. The best homogeneous water oxidation complex is a Ru-based synthetic analogue of PSII, which is capable of oxidizing water to oxygen at a comparable rate to the biology system [45]. Due to the oxidative reaction condition, these molecular catalysts are susceptible to deactivation, *e.g.*, the ligand oxidation or degradation, resulting in the formation of metal oxide nanoparticles in the most extreme cases [46].

From an industrial application perspective, heterogeneous water oxidation catalysts are preferred because of their great potential in stability, scalability, as well as lower cost in comparison to homogeneous ones [47]. Transition metal oxides (TMO, *e.g.*, Ru, Ir, or other Groups 7, 8, and 9 members) have been proven to offer good water oxidation catalytic activity [47–49]. It is worth mentioning that Ir oxide catalysts offer the best combination of activity and stability among all the TMOs [50, 51]. Other earth abundant transition metal (*e.g.*, Co, Ni, Fe) based materials have also propelled great research effort due to their affordability, and the good performance under alkaline condition [52]. The robustness of heterogeneous water oxidation catalysts has inspired research with the aim to understand reaction mechanisms and develop more efficient and cost-effective derivatives [53–55].

1.2 Existing Challenges

1.2.1 Electrochemical Carbon Dioxide Reduction

The CO_2RR can be coupled with a renewable energy source, thereby offering a strategy to achieve a sustainable energy economy. While the blueprint is promising and great progress has been made in the past decades, the large-scale employment still faces major hurdles, which we discuss in this section.

First, while significant progress has been made, much remains to be learned about the mechanism of the CO_2RR, especially on the aspect of how to steer the reaction selectivity toward the desired product. Further progress is needed in regards to understanding how the reaction is influenced by catalyst surface morphology, chemical composition, and oxidation states under operational conditions. The fundamental understanding of these aspects will greatly benefit the design of more durable and selective electrocatalysts.

Second, the design of an industrially viable CO_2RR device poses significant engineering challenges. The production rate, *i.e.*, operation current density, should meet the threshold of 250-350 mA cm^{-2} [56]. The reaction selectivity toward a specific product is described by Faradaic efficiency (FE). A high FE is essential to avoid energy-intensive post-electrolysis product separation [57]. Most of the research on CO_2RR to date has only demonstrated an operation time up to 100 hours, whereas the commercial water splitting devices show prolonged operation over 80000 hours [58]. The stability of the electrolyzer is of paramount importance and requires more research effort.

A practical CO_2RR electrolyzer must take all the above-mentioned factors into account to be industrially viable and profitable. The understanding of the reaction mechanisms, the factors that control the product selectivity, and the pathways for catalyst deactivation are important fundamental questions of practical significance. Further, the design of elec-

trolyzers that are capable of operating a high current density with optimal efficiencies at a large scale for a prolonged time presents a significant engineering challenge. Only when these issues are properly addressed can the CO_2RR technology be widely applied on an industrial scale.

1.2.2 Electrochemical Water Oxidation

For CO_2RR devices, one important factor is the overall energy efficiency. In most cases, the anodic half-reaction is the OER. The large overpotential for the OER contributes to an overall low device efficiency. A catalyst to overcome this obstacle must be active, stable, scalable, and affordable. Generally, heterogeneous WOCs outperform the homogeneous branch in the context of stability and scalability. To date, the most active OER catalysts are RuO_2 and IrO_2. However, both metals are scarce and expensive. The limitation of these two catalysts urges the development of earth abundant catalyst substitutes with high performance. Affordable catalysts based on Co, Ni, and Fe, often require high overpotentials (*e.g.*, up to 400 mV) to operate at a current density of 10 mA cm^{-2} [50]. This high overpotential contributes to a large overall cell potential, lowering the energy of the electrolyzer. The target cell voltage for a profitable water splitting device is 1.5 V vs. RHE at a current density of 2 A cm^{-2} [59], while the current state-of-art performance only offers 0.12 A cm^{-2} at 1.55 V for a stable system [60]. Additionally, the elevated electrolyzer temperature and pressure (*i.e.*, 50-80 ^{o}C and up to 30 bars) in industrial processes [60] highlights the importance of robust catalysts that can operate over long periods of time.

Developing an understanding of the principal bottlenecks of the reaction pathway of water oxidation on prototypical, earth-abundant catalysts is therefore essential the design of more efficient water oxidation catalysts. The elucidation of reaction mechanisms can also benefit a deeper understanding of the catalyst failure mechanism. All of these aspects can be greatly benefited by the employment of operando techniques to reveal the interfacial

characteristics and surface adsorbed intermediates.

Chapter 2

Theory

2.1 Infrared Spectroscopy

By probing the vibrations of molecules, infrared (IR) spectroscopy reveals information on the molecules' chemical structures. It measures the frequency of absorption when a sample is irradiated with infrared electromagnetic radiation. The vibration of a certain chemical bond varies with its strength and chemical environment. Consequently, IR spectroscopy is a powerful tool in identifying molecular-level chemical information.

2.1.1 Gross Selection Rule of IR Spectroscopy

For a certain vibrational mode to be IR active, it must fulfill the gross selection rule of IR spectroscopy. For a molecule to absorb (or emit) light at a frequency ν, it must have a (transient) dipole moment. Quantum-mechanically, a transition dipole moment μ_{fi} involving two states described by the wavefunctions ψ_{i} and ψ_{f} can be expressed as [61]:

$$\mu_{\mathrm{fi}} = \int \psi_{\mathrm{f}}^{*} \hat{\mu} \psi_{\mathrm{i}} d\tau \tag{2.1}$$

where $\hat{\mu}$ is the dipole moment operator, and the integral is over all space. For the vibration of a diatomic molecule, the transition dipole moment integral can be expressed as a function of bond length r between the vibrating atoms:

$$\mu_{\mathrm{fi,vib}} = \int \psi^{*}_{\mathrm{f,vib}} \mu(r) \psi_{\mathrm{i,vib}} dr \tag{2.2}$$

The change of the dipole from the equilibrium position (r_{e}) can be expressed in terms of a Taylor expansion of the equilibrium dipole moment:

$$\mu = \mu_{\mathrm{e}} + \left.\frac{d\mu}{dr}\right|_{r_{\mathrm{e}}} (r - r_{\mathrm{e}}) + \frac{1}{2} \left.\frac{d^2\mu}{dr^2}\right|_{r_{\mathrm{e}}} (r - r_{\mathrm{e}})^2 + \ldots \tag{2.3}$$

Combining Eq. 2.2 and 2.3 yields:

$$\mu_{\mathrm{fi,vib}} = \mu_{\mathrm{e}} \int \psi^{*}_{\mathrm{f,vib}} \psi_{\mathrm{i,vib}} dr + \left.\frac{d\mu}{dr}\right|_{r_{\mathrm{e}}} \int \psi^{*}_{\mathrm{f,vib}} (r - r_{\mathrm{e}}) \psi_{\mathrm{i,vib}} dr + \ldots \tag{2.4}$$

The first term in Eq. 2.4 equals zero, because vibrational wavefunctions of the same electronic state are orthogonal to each other. Consequently, the intensity (I) of the vibrational transition can be expressed as:

$$I \propto |\mu_{\mathrm{fi}}|^2 \propto \left|\frac{d\mu}{dr}\right|^2_{r_{\mathrm{e}}} \tag{2.5}$$

Eq. 2.5 states that for a vibrational mode to be IR active, there must be a change in the dipole moment associated with that vibration.

2.1.2 Surface-Enhanced Infrared Absorption Spectroscopy

Infrared absorption spectroscopy (IRAS) is a powerful technique to identify and characterize surface-adsorbates on the basis of their signature vibrational properties. However, due to the low vibration absorption cross-sections in mid-infared range, a large surface-coverage of analytes is typically required for detection. One way to overcome this limitation to boost detection limits by employing surface enhancement effects. In surface-enhanced infrared absorption spectroscopy (SEIRAS), molecules adsorbed on metal films

consisting of islands or particles display infrared absorption signals with up to 1000 times magnification compared to conventional IRAS: Enhancement effect has been demonstrated in different IR modes including transmission [62], attenuated total reflection (ATR) [63, 64], external reflection [65], and diffuse reflection [66].

Surface enhancement is generally attributed to electromagnetic and chemical effects [67]. In principle, the infrared absorption intensity (I) of a surface adsorbed molecule can be expressed as [68]:

$$I = \mid \partial\mu/\partial r \cdot E_{\mathrm{loc}} \mid^2 = \mid \partial\mu/\partial r \mid^2 \mid E_{\mathrm{loc}} \mid^2 \cos^2\theta \tag{2.6}$$

where $\partial\mu/\partial r$ is the derivative of the vibrational dipole moment with respect to a normal coordinate *r* (see previous section), E_{loc} is the local electric field that excites the molecule, and θ is the angle between the two aforementioned terms.

The electromagnetic effect gives rise to an enhanced local electric field E_{loc} as a result of the coupling between incident photon and the nanostructured metal surfaces via the excitation of a collective electron resonance [69]. This localized surface plasmon resonance engenders a strong local electromagnetic near-field on the nanometer scale, resulting in the enhancement of absorption of surfaced adsorbed molecules.

Based on the localized plasmon model [70, 71], metal islands that resemble ellipsoids are polarized by the incident radiation through localized plasmon excitation. A dipole moment *p* will be produced at the center of the ellipsoid. This dipole moment generated by the incident electric field (*E*) can be expressed as:

$$p = \alpha V E \tag{2.7}$$

where α is the polarizability and *V* is the volume of the metal ellipsoid. This dipole induces an local electric field E_{loc} around the metal ellipsoid where the adsorbed molecules can be

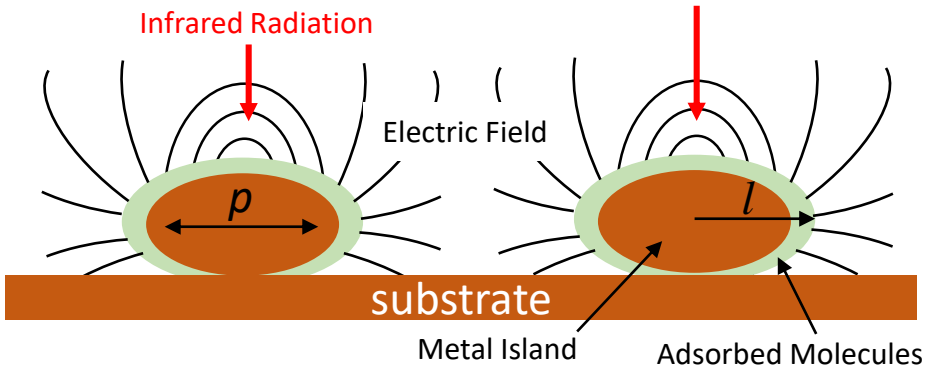

Figure 2.1: Polarization of metal islands by the incident IR radiation and the electric field around the metal island.*p* denotes the dipole moment induced by the infrared radiation, *l* denotes the distance between the surface adsorbates to the center of the metal island. Adapted with permission from Ref[68]. Copyright 2004 Optical Society of America.

excited (Figure 2.1). The amplitude of the local electric field that the adsorbed molecules experience can be written as

$$\mid E_{\mathrm{loc}} \mid^2 = \frac{4p^2}{l^6} \tag{2.8}$$

where l is the distance between the adsorbed molecule and the metal center.

The enhancement effect is greatly dependent on the surface morphology of the metal surface. Both physical vapor deposition [72, 73] and chemical deposition [74–76] methods have been demonstrated to generate metal island films that exhibit good signal enhancement. The largest enhancement is observed when the surface is populated with metal islands that are smaller than the incident light wavelength but not touching each other [77].

Chemisorbed molecules tend to show larger enhancement effect than the physisorbed molecules, which proves the theory of the chemical effect. The chemical effect assumes an enlargement of $\mid \partial\mu/\partial r \mid^2$ resulting from the charge oscillations between the metal surface and molecular orbitals of the adsorbed species, which enlarge the absorption coefficient of the molecule [69, 78]. Another origin of the chemical effect lies in the orientation of the adsorbed molecules [62]. Chemisorption induces molecular alignment. For molecules

that possess a dipole change normal to the surface, this alignment enhances the signal by bringing the transition dipole moment in alignment with the local electric field (Eq. 2.6). For the molecules that possess dipole change parallel to the surface, an opposite effect is observed.

By lowering the detection threshold, SEIRAS has become an indispensable technique for probing adsorbates on metal surfaces. Particularly, the past decades have witnessed a surge of SEIRAS application in *in situ* electrochemistry investigations by monitoring electrode/electrolyte interface under operation conditions [79–82]. By employing molecular probes in spectro-electrochemistry, the interfacial properties, such as electrode morphology and electric double layer structure, can be revealed [82–84]. SEIRAS has been demonstrated on various metal thin films, *e.g.*, Ag, Au, Cu, Ni, Pt, Pd, Rh, Ru, and Fe [62, 74–76, 85, 86].

2.1.3 Attenuated Total Reflection

Attenuated total reflection (ATR) employs the total internal reflection (TIR) property which results in an evanescent wave that penetrates from the surface of an internal reflection element (IRE) into the sample by a few microns depending on the incidence wavelength. The sampling pathlength is defined by the nature of TIR instead of the thickness of the loaded sample.

TIR occurs when the incidence angle exceeds the critical angle. A critical angle of a two-media system is the threshold angle of incidence that allows total reflection. For TIR to occur, the light waves must travel from a denser medium with refractive index n_1 into another rarer medium with refractive index n_2 (*i.e.*, $n_1 > n_2$). The relationship between the angle of incidence (θ_i) and the angles of refraction (θ_r) is described by Snell's law (Eq. 2.9):

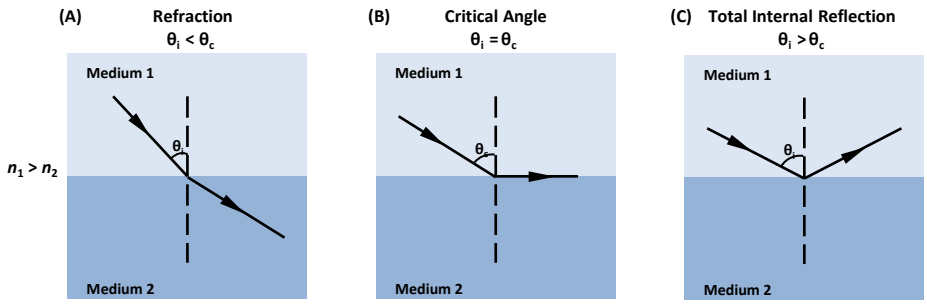

Figure 2.2: Three scenarios when light travels from a denser medium into a rarer medium. (A) $\theta_{\mathrm{i}} < \theta_{\mathrm{c}}$; (B) $\theta_{\mathrm{i}} =< \theta_{\mathrm{c}}$; and (C) $\theta_{\mathrm{i}} > \theta_{\mathrm{c}}$

$$\frac{sin\theta_{\mathrm{r}}}{sin\theta_{\mathrm{i}}} = \frac{v_2}{v_1} = \frac{n_1}{n_2} \tag{2.9}$$

where v represents the velocity of light in the respective medium and θ is measured with respect to the interface normal.

As we increase the incident angle θ_{i}, the refractive angle θ_{r} also increases and θ_{r} is bigger than θ_{i} at all times. Obviously, the angle of refraction cannot be larger than 90°. In this limiting condition, we define θ_{r} = 90°, and θ_{i} = θ_{c} in Eq. 2.9. The resulting equation defines the value for the critical angle:

$$\theta_{\mathrm{c}} = \arcsin(\frac{v_1}{v_2}) = \arcsin(\frac{n_2}{n_1}) \tag{2.10}$$

For incident angle $\theta_{\mathrm{i}} < \theta_{\mathrm{c}}$, the incident light wave is partly refracted as shown in Figure 2.2A. For $\theta_{\mathrm{i}} = \theta_{\mathrm{c}}$, the angle of refraction is 90° (Figure 2.2B). For $\theta_{\mathrm{i}} > \theta_{\mathrm{c}}$, the incident light wave undergoes TIR (Figure 2.2C).

In the electromagnetic theory, boundary conditions require the tangential components of the electric and magnetic fields to be continuous across the boundary [87]. To fulfill this requirement, a powerless transmitted field called evanescent wave must emerge at the boundary where TIR takes place. This evanescent wave propagates in parallel to the inter-

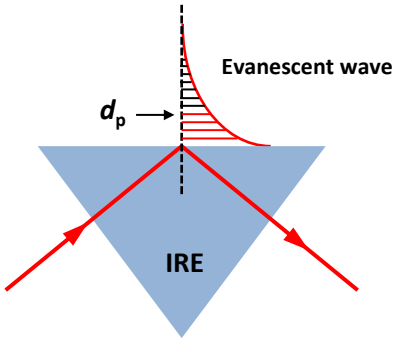

Figure 2.3: Evanescent wave at the interface. IRE denotes internal reflective element, d_{p} denotes the penetration depth. The red color represents the effective probing pathlength. This drawing is not true the to real scale.

face and decays exponentially into the other medium. The totally reflected light interacts with the sample via the evanescent wave. In areas where the sample interacts with the evanescent wave, specific parts of the IR beam are absorbed based on the samples composition. The totally reflected IR light lacks the absorbed parts and thus is attenuated, hence it is named "attenuated total reflectance" (ATR).

The sampling pathlength in ATR mode is termed the penetration depth (d_{p}). The depth of penetration is defined as the distance to the position at which the evanescent wave's amplitude has decreased to $1/e$ (*i.e.*, about 37%) of its maximum value. The penetration depth varies with the refractive indexes of the media, wavelength of the incident light, and angle of incidence (Eq. 2.11) :

$$d_{\mathrm{p}} = \frac{\lambda}{2\pi n_2 \sqrt{\sin^2\theta_{\mathrm{i}} - (\frac{n_2}{n_1})^2}} \tag{2.11}$$

A typical penetration depth for commonly used IRE is a few micron in the mid-IR range. Commonly used IREs include Si, ZnSe, Ge, and diamond. The selection of a certain IRE material depends on the sample to be probed.

There are two types of ATR configurations as shown in Figure 2.4. One is called

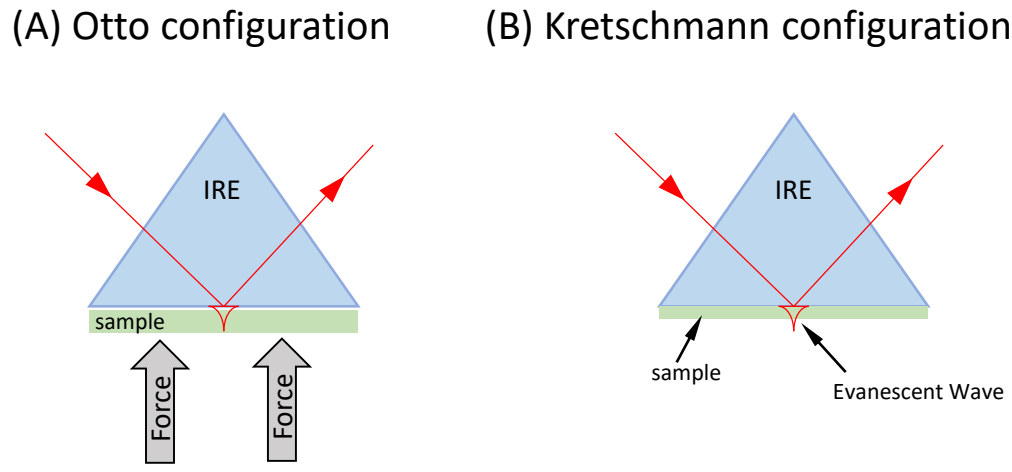

Figure 2.4: Two modes of ATR configuration. (A) Otto configuration, where the sample is positioned closely to the IRE with external applied force; (B) Kretschmann configuration, where the sample is deposited on the IRE. IRE denotes internal reflection element. This figure is not drawn to scale.

the Otto configuration, which requires positioning the sample close enough to the IRE, usually by applying force to the sample against the IRE (Figure 2.4(A)). The IR light comes in from the IRE, and the evanescent wave penetrates to reach the sample surface. The other is called Kretschmann configuration, which requires the deposition of sample (metal films) on to the IRE surface (Figure 2.4(B)). The IR light comes in from the back of the sample and internal reflection occurs at the sample surface.

2.2 CO Adsorption on the Transition Metal

2.2.1 Models of CO Adsorption on the Transition Metal

The adsorption of CO on transition metal surfaces is often considered as a benchmark system and has been the subject to many studies [88, 89]. The understanding of this adsorption facilitate the employment of CO absorption spectroscopy in investigating various

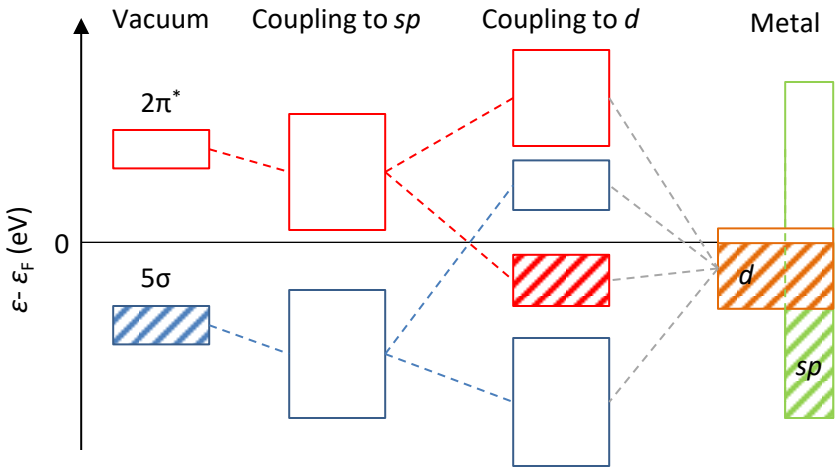

Figure 2.5: The coupling between CO and transition metal surface. Schematic illustration of 5σ and 2π* orbitals of CO molecule in vacuum and density of states (DOS) of transition metals (TMs) (right). Adapted with permission from Ref[91]. Copyright 1996 The Chemical Society of Japan.

catalytic interfaces [82, 84].

In the Blyholder model, the chemisorption of CO on transition metals can be rationalized with a frontier molecular orbital (FMO) theory. This interaction is usually described as the synergistic effect of two contributors [90].

One is the donation of electron density to the substrate with its bonding 5σ orbital (HOMO). This is referred to as σ-donation. The other is the reception of electron density from the substrate into its antibonding 2π* orbital (LUMO). This is termed π-backdonation. The degree of π-backdonation increases with increasing coordination number of the CO molecule, *i.e.*, hollow $>$ bridge $>$ atop. Hence, bridge-bound CO (CO_{bridge}) possesses a higher chemisorption energy than that atop-bound CO (CO_{atop}).

The trend of CO adsorption on transition metal was correctly predicted by Hammer, Morikawa, and Nørskov with the d-band model (HMN model) [91]. According to the HMN model, when a CO molecule is adsorbed on transition metal surface, the FMOs

of the adsorbate first broaden and shift down in energy through the interaction with the broad continuum of metal sp states Figure 2.5. This interaction renormalizes the states of the adsorbate. Upon interaction with the metal d-states, the 5σ and $2\pi^*$ orbitals are split into bonding and anti-bonding orbitals as a result of the hybridization of with the d-states. For late transition metals, the $2\pi^*$-d interaction is much stronger than that of the 5σ-d orbitals and the $2\pi^*$-d bonding orbital fall below the Fermi level, hence the contribution from these states to the surface bonding energy is relatively weak. A smaller energy gap between the $2\pi^*$ orbital and d-band center results in a stronger interaction and thus stronger chemisorption bond. This energy gap decreases when (1) the coordination number of the metal site decreases (*e.g.*, adsorption on metal defect sites); (2) from right to the left in a row of the periodic table (*e.g.*, Pt $>$ Au).

Using X-ray emission spectroscopy and ab initio calculations on cluster models, Föhlisch and co-workers developed another view of the CO-surface bond [89, 92]. They found that the CO-metal interaction gives rise to changes in the electronic structure of CO beyond the FMOs. In their model, the CO-surface bond on late transition metals is a result of π-attraction and σ-repulsion.

2.2.2 Vibrational Stark Effect

The vibrational Stark effect is a powerful tool to measure local electric fields at catalytic sites. It has been widely applied in quantifying the local electric field in chemical and biological systems [93]. Convenient molecular probes for this purpose include CO [31, 94, 95], CN [96], and NO [94] stretch modes.

For a diatomic molecule such as CO, the anharmonic molecular potential results in a slight lengthening of the bond length when it is excited to a higher vibrational energy level (Figure 2.6 (A)). Since CO molecule possesses a permanent dipole moment, the dipole moment of the excited state ($\vec{\mu}_1$) will be slightly larger than the one of ground state ($\vec{\mu}_0$) as

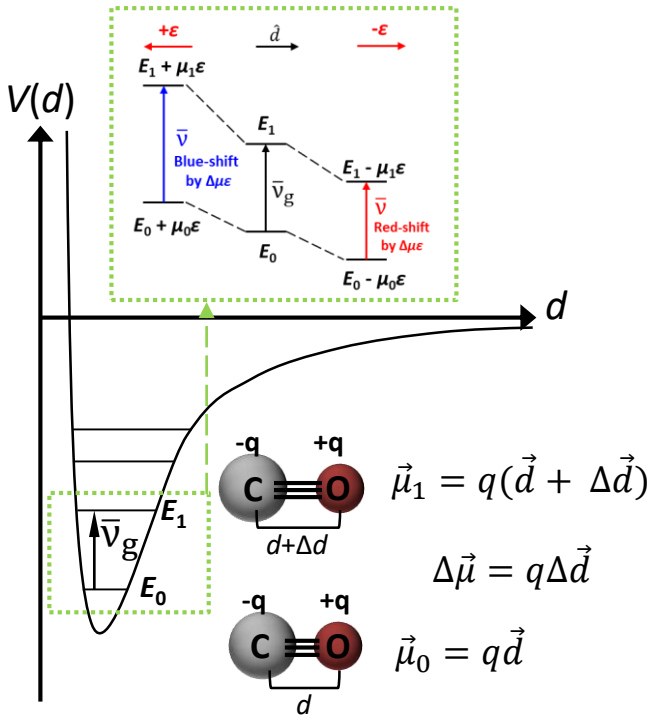

Figure 2.6: The vibrational Stark effect can be explained in terms of anharmonicity. The anharmonic form of molecular potential energy surface implies that bonds will be slightly longer (and so possess slightly larger dipole moments) in their vibrational excited states. The insert shows the ground and excited vibrational states that are stabilized differently by an electric field, resulting in a shift in the transition energy (vibrational frequency). $\hat{d}$ denotes the unit vector aligned with the CO bond axis. Adapted with permission from Ref[93]. Copyright 2015 American Chemical Society.

a result of the bond lengthening ($\Delta\vec{d}$).

$$\vec{\mu}_0 = q\vec{d} \tag{2.12}$$

$$\vec{\mu}_1 = q(\vec{d} + \Delta\vec{d}) \tag{2.13}$$

where q denotes the charge separation of the CO molecule and $\vec{d}$ is the bond length at ground state.

In an external electric field ($\vec{\mathcal{E}}_{\text{ext}}$), these states with different dipole moments will ex-

perience different (de)stabilization from the field. The field stabilizes or destabilizes the dipole depending on the orientation of the field and the dipole. Consequently, the external electric field will generate a shift in the vibrational transition energy that is proportional to the difference of the dipole moment of the two vibrational states.

The slight change of the molecule's dipole as a function of external electric field will directly affect the vibrational frequency, which can be detected by vibrational spectroscopy such as IR and Raman spectroscopy.

$$\Delta\vec{\nu} = -\Delta\vec{\mu} \cdot \vec{\mathcal{E}}_{\text{ext}} \tag{2.14}$$

The quantity $\Delta\vec{\mu}$ is referred to as the Stark tuning rate in the unit of cm^{-1}/(MV/cm). This difference dipole can be measured experimentally or calculated theoretically. The values of Stark tuning rate have been determined for many vibrational modes. For example,the vibrational Stark tuning rate for CO adsorbed on Cu is 1.3×10^{-6} cm^{-1}/(V cm^{-1}) [97].

The interfacial electric field at a electrode/electrolyte interface can be determined by performing vibrational Stark spectroscopy with an appropriate molecular probe (*e.g.*, CO). It is a powerful spectroscopic tool for probing the local environment at an electrified interface [98, 99] or inside biological systems [100, 101].

Chapter 3

Hydrogen Bonding Steers the Product Selectivity of Electrocatalytic CO Reduction

3.1 Introduction

The reaction environment profoundly impacts the kinetics of many chemical processes. Examples include the influence of the solvating environment on the rates of electron transfer [102], isomerization [103], peptide folding [104], and organic reactions [105], as well as the sensitivity of enzymatic catalysis to changes in the molecular structure of the active site [106]. For a chemical process that can lead to multiple reaction products, solvent effects can impact the relative rates of product formation, and therefore the product selectivity [107, 108]. These effects, which can have complex energetic and/or dynamical origins [102, 109, 110], are fundamentally rooted in intermolecular interactions between the reactants and their environment. In the context of heterogeneous electrocatalysis, the reaction environment is asymmetric, *i.e.* reactants at the electrochemical interface are interacting with the solid electrode and the liquid electrolyte. Understanding the interactions of intermediates with their interfacial environment is essential for controlling the reaction paths of electrocatalytic processes that exhibit poor product selectivity.

The reduction of CO_2 to hydrocarbons on Cu electrodes in an aqueous environment

is prototypical for a multi-electron electrochemical process whose reaction selectivity is poor. Products include CO, formate, methane, ethylene, and alcohols [7, 8, 111–115]. Hydrogen is a major product due to the competing water reduction reaction. This product spectrum sensitively depends on the properties of the electrocatalytic interface [116, 117]. These properties are jointly determined by the liquid electrolyte and the solid electrode. Most research to date has focused on understanding how the chemical composition and the surface morphology of the electrode give rise to catalytic reactivity. For example, quantitative correlations have been established between catalytic selectivity and grain-boundary density [11, 118–120], strain [121, 122], Cu nanocluster size [123–125], edge-site density [126–128], or single-crystal orientation [128–130]. These observations have provided deep insights into the interactions of key reaction intermediates, such as CO, with the electrode surface and how these interactions impact product selectivity.

The reactants on the electrode also interact with the liquid side of the reaction environment. Solvent composition [131–134], the identity and concentration of the supporting electrolyte's anions [135–137] and cations [27–29, 137–146], and the pH of the electrolyte [147–153] can greatly impact the product selectivity. For example, the rate of ethylene evolution during CO_2 reduction was found to increase by a factor of ≈ 15 when switching from Li^+- to Cs^+-containing electrolyte [29]. Clearly, careful control of the liquid-side properties of the interface is critical for improving the product selectivity of this process. However, a molecular-level understanding of the interactions between surface reactants and their liquid reaction environment is largely lacking to date. This knowledge gap hinders the design of novel interfaces with desired product selectivity. An improved understanding is expected to advance various design strategies, such as the decoration of the electrode surface with molecular co-catalysts [154–158].

Changing the cations of the electrolyte is a powerful means to alter the properties of the liquid reaction environment. Therefore, in principle, this method could be employed as

a tool for revealing selectivity-determining interactions between surface reactants and the electrolyte environment. However, cations can affect an electrocatalytic process in a number of different ways that are challenging to experimentally differentiate from each other. For example, cations can displace charged reactants from the interface and modulate the interfacial electric field, thereby altering the rates of electron-transfer from the electrode to surface species [138–141, 159]. More recently, density functional theory (DFT) calculations have shown that cations can impact the adsorption energy of reactants and/or the activation barriers of surface processes [29, 137, 143, 160, 161]. Cations can also block reaction sites [24, 135, 145, 162–165], chemically interact with surface species [25, 166–169], modulate the interfacial pH [27, 28], and/or alter the structure of interfacial water [170, 171]. Therefore, to unambiguously identify the principal interactions that alter the product selectivity, the number of possible interactions needs to be minimized by careful experimental design. Further, multimodal probes of the electrocatalytic interface need to be employed.

Herein, using a series of quaternary alkyl ammonium cations ($alkyl_4N^+$), we systematically manipulated the interfacial properties of the aqueous electrolyte/polycrystalline Cu interface. We chose these cations for two reasons: First, the ionic radius of an $alkyl_4N^+$ cation increases with increasing alkyl chain length [172]. This characteristic enabled us to tune the width of the electrochemical double layer and therefore the strength of the interfacial electric field for a given applied electrode potential. Second, compared to the more commonly employed alkali cations in CO_2 reduction studies, the use of these cations minimizes the number of possible interactions: Alkali cations are Lewis acids and their Lewis acid hardness decreases by a factor of three when going from Li^+ to Cs^+ [173]. Because of their Lewis acidity, hydrated alkali cations can buffer the interfacial pH [27, 28] and they could potentially chemically interact with intermediates such as surface-adsorbed CO (CO_{ads}) [174], which is a Lewis base. By contrast, $alkyl_4N^+$ cations are not Lewis acids

and their bulky alkyl chains minimize the chance of chemical interactions between these cations and intermediates.

Employing a combined DEMS and SEIRAS approach, we probed the effect of these cations on the reduction of CO_{ads} to ethylene on the polycrystalline Cu electrode. The reduction of CO_{ads} corresponds to the potential-determining step in the electrochemical reduction of CO_2 to hydrocarbons [175–179]. Understanding the influence of the liquid reaction environment on this process is therefore essential for developing a better mechanistic understanding of CO_2 reduction.

Using DEMS, we found that ethylene is produced in methyl$_4$N$^+$- and ethyl$_4$N$^+$-containing electrolytes, but ethylene is not formed in the presence of propyl$_4$N$^+$ and butyl$_4$N$^+$. With SEIRAS, we comprehensively analyzed the Cu/electrolyte interface. Irrespective of the identity of the alkyl$_4$N$^+$ cation of the electrolyte, we observed approximately the same CO-saturation coverage on the Cu electrode. This observation suggests that the cations do not block CO adsorption sites. Analyzing the dependence of the C≡O stretch frequency of CO_{ads} on applied electrode potential, we determined the electrochemical Stark tuning slopes and derived the potential-dependent interfacial electric fields in the presence of the four cations. At moderate applied potentials around -1.3 V vs. SHE, the interfacial electric field is on the order of 0.1 V Å^{-1}. On the basis of a simple electrostatic model, we found that the interfacial electric field does not appreciably affect the adsorption of CO on Cu under the experimental conditions employed in this work.

Analyzing the O−D stretch band of interfacial heavy water (D_2O) at the CO-covered Cu electrode, we found evidence for a layer of waters directly on top of CO_{ads} in methyl$_4$N$^+$- and ethyl$_4$N$^+$-containing electrolytes. These waters have their O−D bonds directed towards the terminal oxygens of the CO_{ads} molecules. Interestingly, this layer of waters is displaced by propyl$_4$N$^+$ and butyl$_4$N$^+$. These observations suggest that the CO_{ads}-D_2O interaction is essential for the formation of ethylene during the electrochemical reduc-

tion of CO. These waters are predisposed to stabilize the CO dimer, a key intermediate in ethylene formation, by hydrogen-bonding to its terminal oxygens. Theoretical work has recently predicted that this hydrogen bonding interaction is critical of the formation of this important intermediate [180]. To the best of our knowledge, our findings are the first experimental demonstration of the impact of this interaction on the selectivity of CO reduction.

3.2 Results and Discussion

Effects of Alkyl$_4$N$^+$ Cations on CO Reduction. With DEMS, we analyzed the product selectivity during the electrocatalytic reduction of CO to ethylene on polycrystalline Cu electrodes in four different electrolytes. The electrolytes were aqueous solutions of methyl$_4$N$^+$, ethyl$_4$N$^+$, propyl$_4$N$^+$, and butyl$_4$N$^+$ borates (0.1 M) and ethylenediaminetetraacetic acid disodium (EDTA-Na$_2$; 20 μM). EDTA-Na$_2$ prevents deactivation of the electrocatalytic interface by chelating trace metal impurities [181]. The electrolytes had a pH of 9.5, which is close to the pK$_a$ of boric acid (9.24). Therefore, the solutions were pH-buffered by the acid-base equilibrium between the anion (borate) and boric acid. Before the start of a DEMS measurement, the electrolyte was first saturated with CO. A 5 sccm flow rate of CO was maintained throughout the experiment. Detailed experimental procedures are given in the Materials and Methods section, and a scheme of the DEMS setup is provided in the Addendum (Figure A3.1).

Figure 3.1 shows the electrochemical current and the partial pressures of the two major products, hydrogen and ethylene, following two potential steps. The products were identified by their characteristic mass fragment/charge ratios (m/z) of 2 for H_2^+ and 26 for $C_2H_2^+$. Unless otherwise noted, all potentials in this work are referenced against the standard hydrogen electrode (SHE). The voltage was first stepped from -0.39 to -1.09 V (light gray

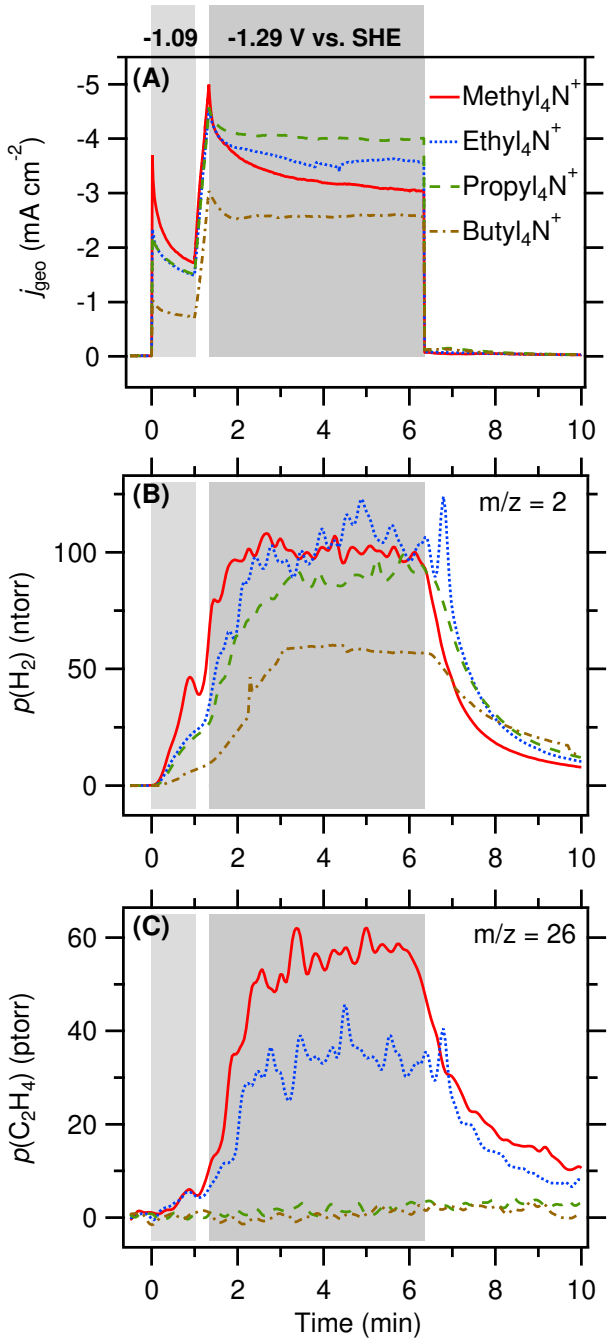

Figure 3.1: DEMS measurements. (A) Electrochemical current density based on the geometric area of the electrode, (B) H_2 partial pressure ($m/z = 2$ for H_2^+), and (C) C_2H_4 partial pressure ($m/z = 26$ for $C_2H_2^+$) recorded during the electroreduction of CO on Cu in the presence of different cations as indicated. The sequence of potential steps in these experiments is described in the text.

shaded area), the potential at which the CO-saturation coverage on the Cu electrode is IR-spectroscopically observed (vide infra). After holding this voltage for one minute, the potential was decreased at a rate of 10 mV s^{-1} to -1.29 V, which was maintained for five minutes (dark gray shaded area). As shown in Figure 3.1A, comparable electrochemical current densities are observed in the presence of methyl$_4$N$^+$, ethyl$_4$N$^+$, and propyl$_4$N$^+$, while a $\approx 30\%$ lower current is observed in the presence of butyl$_4$N$^+$. The hydrogen partial pressure (Figure 3.1B) detected by DEMS closely follows these trends, suggesting that hydrogen is the major reduction product. As shown in Figure 3.1C, ethylene is observed in methyl$_4$N$^+$- and ethyl$_4$N$^+$-containing electrolytes, but this product is not observed in the presence of the two larger cations.

Like similar setups [144, 182], our DEMS instrument is not capable of making fully quantitative measurements of the reaction rates: The product collection efficiency is dependent on the tip-electrode distance, which is difficult to accurately reproduce between independent experiments. Due to the low solubility of CO in water (≈ 1 mM), the measured rates may also be limited by mass transport of CO to the electrode. Despite these limitations, we could reproducibly determine that ethylene is formed at detectable rates in the presence of methyl$_4$N$^+$ and ethyl$_4$N$^+$, whereas we did not observe any ethylene in propyl$_4$N$^+$- and butyl$_4$N$^+$-containing electrolytes.

To confirm that the observed signal at $m/z = 26$ is due to ethylene formed by the reaction of CO and water at the Cu electrode, we carried out a series of control experiments: No ethylene signal ($m/z = 26$) is detected in the presence of methyl$_4$N$^+$ in Ar-purged electrolyte (Addendum, Figure A3.2) or in CO-purged methyl$_4$N$^+$-containing electrolyte when the electrode material is Pt (Addendum, Figure A3.3). Further, ethylene and hydrogen evolution are virtually unchanged when switching from methyl$_4$N$^+$ to its deuterated form, (CD$_3$)$_4$N$^+$ (Addendum, Figure A3.4).

These experiments conclusively demonstrate that the appearance of the $m/z = 26$

signal does not only require the presence of CO, but also necessitates the presence of a Cu electrode. Cu is the only pure metal that can reduce CO to ethylene at appreciable rates [7, 183, 184]. Therefore, the absence of this signal when a Pt electrode is used strongly supports its assignment to the $C_2H_2^+$ mass fragment of ethylene. Further, the experiments demonstrate that the signal is not due to the decomposition of the organic cations or their reaction with CO_{ads}.

To confirm further this assignment, we examined the mass spectrum. Because some reactants and products yield ions with m/z values that overlap with the mass spectrum of ethylene (*e.g.* CO^+ and $C_2H_4^+$ both have $m/z = 28$), its full mass spectrum cannot be observed during a DEMS measurement. However, ethylene's m/z values of 25, 26, and 27 do not overlap with the mass spectra of any other major reduction product of CO on copper. As shown in Figure A3.5 of the Addendum, the observed relative partial pressures at these three m/z values are in good agreement with those expected for ethylene. In addition, we confirmed the identity of ethylene with gas chromatography/mass spectrometry (GC-MS). An experiment with ^{13}C-labeled CO unequivocally established CO as the sole source of ethylene (Addendum, Figure A3.6).

Alteration of molecular diffusion coefficients by the cations could result in cation-dependent product collection efficiencies. However, the comparable decay times of the hydrogen partial pressure (Figure 3.1B) following the step from -1.39 to -0.39 V at $t \approx 6.3$ min suggest that molecular diffusion coefficients are similar in the four electrolytes. Taken together, the data unambiguously demonstrate that the identity of the $alkyl_4N^+$ cation of the electrolyte profoundly influences the selectivity of the CO reduction process on the polycrystalline Cu electrode.

SEIRAS of the Cu/Electrolyte Interface. To identify the principal mechanism giving rise to the observed selectivity trend, we characterized the Cu/electrolyte interface under operating conditions, using SEIRAS in an attenuated total reflection (ATR) geometry. An

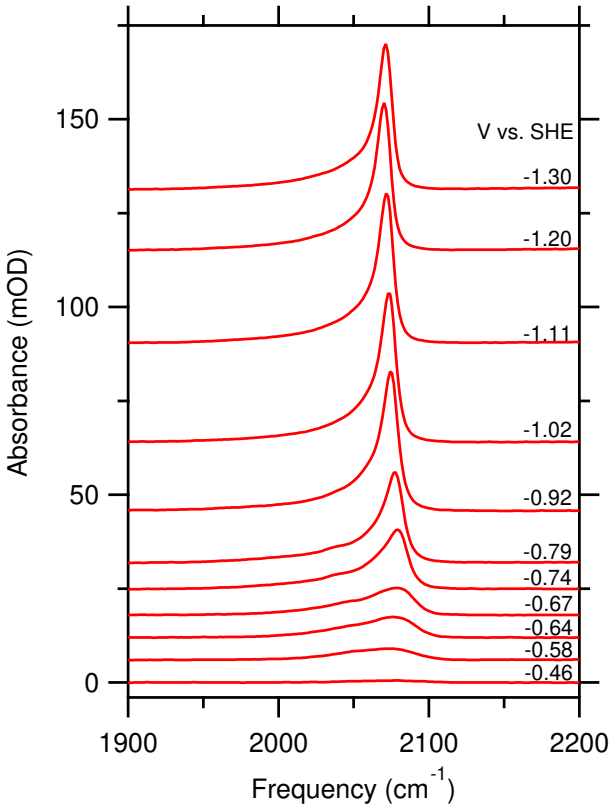

Figure 3.2: Representative C≡O stretch spectra of CO_{ads} as a function of applied potential in the presence of a solution of 0.1 M butyl$_4$N$^+$ chloride in D_2O.

electrolessly deposited polycrystalline Cu film on a Si ATR prism [76, 150, 185] formed the working electrode of a single-compartment spectro-electrochemical cell (Addendum, Figure A3.7). Characterization of the Cu film by cyclic voltammetry, capacitance measurements (Figure A3.8), and atomic force microscopy imaging (Figure A3.9) is reported in the Addendum.

We carried out the spectroscopic work in solutions of the chloride salts of the $alkyl_4N^+$ cations in heavy water (D_2O). Primarily, we chose these electrolyte conditions for the following reason: With increasing current density, the Cu thin films have an increasing propensity to delaminate from the Si crystal [150]. A significant component of the faradaic current originates from the hydrogen evolution reaction. To minimize the interference of hydrogen evolution with interfacial spectroscopy, we chose D_2O as the solvent. Due to the kinetic isotope effect, hydrogen evolution on Cu is substantially slower in D_2O compared to H_2O [186]. For DEMS, $alkyl_4N^+$ borate electrolytes were prepared by titration of the corresponding hydroxide solutions (see Materials and Methods). Because $alkyl_4N^+$ hydroxides are only available as H_2O solutions, we could not employ this electrolyte preparation procedure for the spectroscopic experiments. Therefore, we chose to directly dissolve $alkyl_4N^+$ chlorides in D_2O. The pH of these solutions slightly drifts during the measurements (see Materials and Methods). It is well-established that adsorption of CO on Cu is pH-independent [30, 150]. Further, our previous work has established that the CO stretch frequency is only slightly affected by pH [30]. Therefore, the following analyses are not impacted by this choice of electrolyte.

To connect rigorously the DEMS and spectroscopic experiments, we carried out the following control experiments: (1) DEMS results qualitatively similar to those presented above are also found in aqueous solutions of $alkyl_4N^+$ chlorides (Addendum, Figure A3.10). We emphasize that we only compare the qualitative trends because the reversible hydrogen electrode (RHE) potential is not well-defined in the latter measurements. (2) Addi-

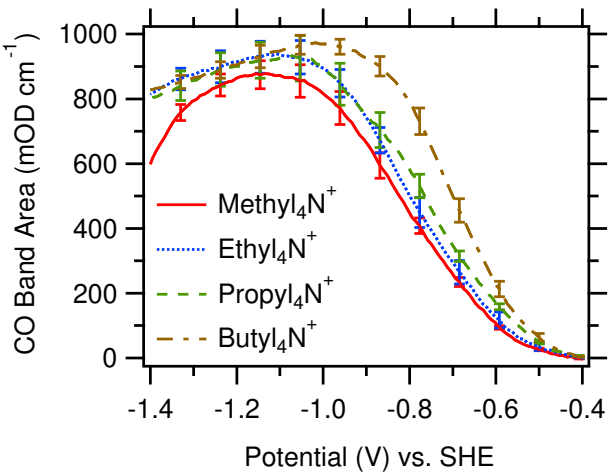

Figure 3.3: Integrated C≡O stretch band areas of CO_{ads} as a function of applied potential in the presence of different cations as indicated. Each trace is an average of three independent experiments. The standard errors are indicated.

tional spectroscopic experiments were carried out under electrolyte and potential conditions identical to those employed for the DEMS experiments (Addendum, Figure A3.11). These experiments confirm that the cation-dependent trends in the CO_{ads}-H_2O interaction hold for both electrolytes (vide infra). In the following, we evaluate the effects of the cations on CO surface coverage, interfacial electric field, and interfacial water structure.

Insensitivity of the CO Surface-Coverage on Alkyl$_4$N$^+$ Identity. Figure 3.2 shows representative spectra of the C≡O stretch band of CO_{ads} during a potential sweep from -0.39 to -1.39 V collected in butyl$_4$N$^+$-containing electrolyte. Additional spectra collected in the presence of the other cations and the corresponding current densities are provided in the Addendum (Figures A3.12 and A3.13).

Figure 3.3 shows the dependence of the integrated C≡O stretch band area of CO_{ads} on applied potential in the presence of the different alkyl$_4$N$^+$ cations. The integrated C≡O stretch band area is approximately proportional to the CO coverage on the electrode [187, 188]. Irrespective of the alkyl$_4$N$^+$ cation of the electrolyte, comparable integrated band areas are observed, indicating that the same CO-saturation coverage is reached within the

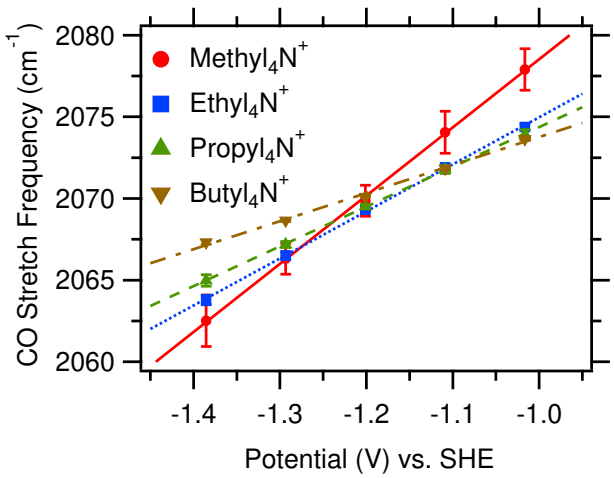

Figure 3.4: Peak frequencies of the C≡O stretch band of CO_{ads} as function of applied potential in the presence of different cations as indicated. The lines are linear fits to the data. The standard errors are indicated.

error of the measurement. It was suggested that organic cations, especially those with long hydrocarbon chains, may displace reactants from the electrode surface under certain conditions [135, 163]. Apparently, the Cu/CO interaction is sufficiently strong (compared to the Cu/alkyl$_4$N$^+$ interaction) to prevent such displacement effects. Further, in contrast of recent findings of CO on Pt electrodes [189], no displacement of atop-bound CO (center frequency ≈ 2080 cm^{-1}) to the bridge-bonded configuration (center frequency $\approx 1800 - 1880$ cm^{-1} [190]) is observed (Figure 3.2 and Addendum, Figure A3.12). The results demonstrate that the changes in the rate of ethylene evolution with cation identity are not due to blocking of CO adsorption sites.

Cation-Dependent Interfacial Electric Field. Figure 3.4 shows the dependence of the peak frequency of the C≡O stretch band of CO_{ads} on applied potential. To minimize coverage-dependent frequency shifts [191], the analysis was restricted to a potential range in which the CO coverage is approximately constant. The dependence of the frequency (ω) on the applied potential (ϕ) arises from the vibrational Stark effect, *i.e.* the influence

of the interfacial electric field ($\mathcal{E}(\phi)$) on the C≡O stretch mode [192–195]:

$$\omega(\phi) = \omega_{\mathrm{PZC}} - \Delta\mu\,\mathcal{E}(\phi), \tag{3.1}$$

where ω_{PZC} is the C≡O stretch frequency in the absence of the interfacial electric field and $\Delta\mu$ represents the vibrational Stark tuning rate. By writing $\Delta\mu$ and $\mathcal{E}$ in eq. 3.1 as scalar quantities, we implicitly assumed that the corresponding vectors are either parallel or antiparallel to each other. This assumption is reasonable for CO adsorbed on a metal surface [196]. However, it is an approximation as our electrodes are not atomically flat. We take $\Delta\mu$ and $\mathcal{E}$ as a positive quantities when the corresponding vectors point from the electrolyte towards the metal surface. The $\Delta\mu$ vector of CO_{ads} points from O to C.

The vibrational Stark tuning rate for CO adsorbed on Cu is 1.3×10^{-6} cm^{-1}/(V cm^{-1}) [97]. Although this value was derived from quantum mechanical calculations of CO on a Cu surface in vacuum, very similar values were estimated for CO adsorbed on various metal electrodes in an aqueous environment [196]. Further, experimental measurements of $\Delta\mu$ for CO adsorbed on various metals in vacuum also yielded comparable values [196].

The data in Figure 3.4 contain information on the structure of the electrochemical double layer. Inspection of this figure shows that the frequency linearly depends on the applied potential. This observation implies that the interfacial electric field is also linearly related to the applied potential (eq. 3.1). One model of the electrochemical double layer that is consistent with this finding is the Helmholtz model [197]:

$$\mathcal{E}(\phi) = -\frac{\Delta\phi_{\mathrm{M-El}}}{d_{\mathrm{H}}}, \tag{3.2}$$

where $\Delta\phi_{\mathrm{M-El}}$ is the interfacial potential drop, $\phi_{\mathrm{M}} - \phi_{\mathrm{El}}$ (ϕ_{M} and ϕ_{El} are the potentials of the metal and the bulk electrolyte, respectively). d_{H} is the width of the Helmholtz layer,

i.e. the distance between the negatively charged electrode surface and the plane of the cationic counter charge (outer Helmholtz plane). Combining eqs. 3.1 and 3.2, we obtain

$$\omega(\phi) = \omega_{\mathrm{PZC}} + \left(\frac{\Delta\mu}{d_{\mathrm{H}}}\right)\Delta\phi_{\mathrm{M-El}}. \tag{3.3}$$

The width of the Helmholtz layer (d_{H}) is expected to increase with increasing cation size: With increasing cation size, the outer Helmholtz plane shifts further away from the electrode surface. Consistent with this expectation, the slopes of the lines in Figure 3.4, the electrochemical Stark tuning rates ($\Delta\mu/d_{\mathrm{H}}$) [174, 198, 199], decrease with increasing cation size (Table 3.1). One may expect the extracted values of d_{H} to track the ionic radii of the cations. The radii of the cations (derived from the partial molar volumes of the cations in water [172]) are 3.2, 3.8, 4.4, and 4.7 Å for methyl$_4$N$^+$, ethyl$_4$N$^+$, propyl$_4$N$^+$, and butyl$_4$N$^+$, respectively. The extracted width increases at a larger rate with increasing cation size (Table 3.1) than that expected based on the radii of the cations. This observation suggests that the smaller cations fit between CO_{ads} molecules on the surface. This interpretation is reasonable because the CO-saturation coverage on Cu electrodes is estimated to be significantly less than one monolayer [137]. By contrast, the larger cations appear to reside at a distance from the electrode approximately equal to the distance between the surface of the electrode and the terminal oxygen of CO_{ads} (3.05 Å [200]) plus the radius of the cation. Clearly, based on eq. 3.2, we therefore expect the interfacial electric field to decrease with increasing cation size for the same applied potential.

To extract the interfacial electric field from eq. 3.1, knowledge of the C≡O stretch frequency of CO_{ads} in the absence of the field (ω_{PZC}) is required. The interfacial electric field strength vanishes at the potential of zero charge (PZC) of the electrode. This potential can be estimated from Figure 3.4 [199]. Inspection of this figure shows that the lines obtained for ethyl$_4$N$^+$, propyl$_4$N$^+$, and butyl$_4$N$^+$-containing electrolytes cross at ≈ -1.1 V. This

crossing point indicates that CO_{ads} experiences the same interfacial electric field at this potential, irrespective of the electrolyte's cation. This condition can only be fulfilled when the electrode does not carry any net charge, *i.e.* when $\Delta\phi_{\mathrm{M-El}} = 0$ V (eq. 3.3). Therefore, this crossing point is the approximate PZC of the CO-covered Cu electrode in alkyl$_4$N$^+$ chloride solutions. This PZC is more negative than the values obtained on Cu electrodes in contact with acidic and weakly adsorbing electrolytes (≈ -0.73 V; $\mathrm{pH} = 5.7$; 0.01 M $NaClO_4$) [201]. The more negative value obtained here is consistent with the expectation that the PZC shifts negatively by ≈ 60 mV per one unit increase in pH [202]. Additionally, the specific adsorption of Cl^- on Cu may contribute to the more negative value.

The frequency/potential relationship obtained in the presence of methyl$_4$N$^+$ does not cross with the other lines at ≈ -1.1 V (Figure 3.4). Although the measurement of the electrochemical Stark tuning slope in the presence of this cation was highly reproducible, the value of the y-axis intercept varied by as much as ≈ 5 cm^{-1} over independent experiments. Although the Cu thin films were stable for all the presented measurements, we noticed a higher propensity of film delamination in the presence of methyl$_4$N$^+$. Therefore, this cation may interact more strongly with the electrode than the other ones in this series. Because even a significant error of 0.2 V in the value of the PZC will not change our conclusions drawn from the analysis that follows, we will assume a PZC of ≈ -1.1 V of the Cu electrode for all of the four cations.

Using the extracted PZC and $\Delta\mu$, we evaluated the interfacial electric field ($\mathcal{E}$) according to eq. 3.1. We emphasize that the relationship between $\omega(\phi)$ and $\mathcal{E}(\phi)$ as defined in eq. 3.1 does not require the assumption of a particular model of the electrochemical double layer. Figure 3.5 shows the interfacial electric field experienced by CO_{ads} in the presence of different cations. The interfacial field decreases by a factor of ≈ 2.5 when going from methyl$_4$N$^+$ to butyl$_4$N$^+$-containing electrolyte. The obtained interfacial fields

Table 3.1: Electrochemical Stark tuning rates ($\Delta\mu/d_{\mathrm{H}}$) extracted from fitting a linear model to the data in Figure 3.4 and derived Helmholtz double layer widths (d_{H}). The standard deviations are indicated.

Cation	$\Delta\mu/d_{\mathrm{H}}$ ($\mathrm{V^{-1}\ cm^{-1}}$)	d_{H} (Å)
methyl$_4$N$^+$	41.8 ± 0.6	3.1 ± 0.0
ethyl$_4$N$^+$	28.8 ± 0.4	4.5 ± 0.1
propyl$_4$N$^+$	24.3 ± 0.2	5.4 ± 0.0
butyl$_4$N$^+$	17.2 ± 0.6	7.6 ± 0.3

are on the order of 0.1 V Å^{-1}. The electrostatic contribution to the CO-adsorption energy as a function of the local field is [143, 203]

$$E(\mathcal{E}) \approx -\mu\mathcal{E} - \frac{\alpha}{2}\mathcal{E}^2, \tag{3.4}$$

where μ, and α are the dipole moment and polarizability of $\mathrm{CO_{ads}}$, respectively. CO is only weakly adsorbed on Cu and therefore is expected to exhibit little change in its dipole moment and polarizability with respect to the values of CO in the gas phase. With the gas-phase values of 0.0244 eÅ and 0.124 eÅ^2 V^{-1} for the dipole moment and polarizability of CO [61], respectively, and an applied potential of -1.3 V, eq. 3.4 predicts a minute change in the CO adsorption energy of < 5 meV, which is negligible with respect to the adsorption energy of CO on Cu (≈ -0.6 eV [204, 205]).

The results suggest that the interfacial field at the Cu/electrolyte interface under the experimental conditions employed in this work are too small to have a significant effect on the CO adsorption energy. This conclusion is consistent with DFT calculations demonstrating that an electric field of 0.1 V Å^{-1} has negligible effect on the adsorption energy of CO on Cu [190].

The interfacial electric field will affect the rate of electron-transfer from the electrode to surface intermediates [159, 197]. However, ethylene is also not observed in the presence of butyl$_4$N$^+$ when a potential of -1.39 V is applied (Addendum, Figure A3.10). This ob-

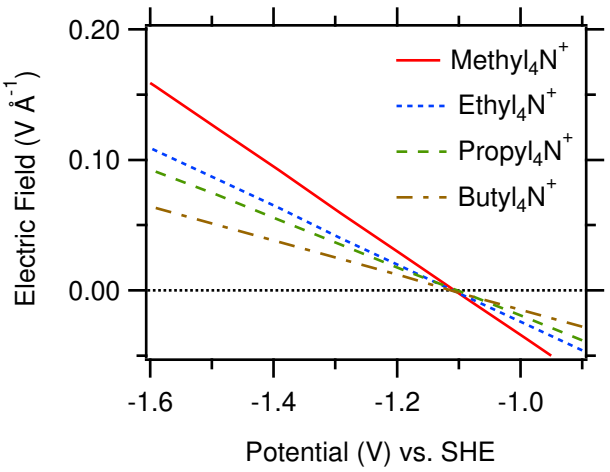

Figure 3.5: Dependence of the interfacial electric fields on applied potential in the presence of different electrolyte cations as indicated.

servation demonstrates that, in the present case, the cation-specific selectivity for ethylene is likely unrelated to the strength of the interfacial electric field.

Dependence of the $CO_{ads}-H_2O$ Interaction on Cation Identity. Interfacial water is the source of hydrogen in the electroreduction of CO_{ads} and provides the solvation environment for the reactants. Therefore, the structure and dynamics of interfacial water is expected to affect this process. To determine if the cations alter the structure of water near the electrode surface, we analyzed the dependence of the O−D stretch band of interfacial water at the CO-covered Cu electrode on the presence of the different cations (Figure 3.6). In the presence of methyl$_4$N$^+$ and ethyl$_4$N$^+$, a sharp and prominent band is observed at $\approx$ 2710 cm^{-1} on top of the broad O−D stretch band. The band is very weak in the presence of propyl$_4$N$^+$ and it is entirely absent in butyl$_4$N$^+$-containing electrolyte. To confirm that these trends are also observable under electrolyte conditions identical to those employed in the DEMS study, we collected spectra in H_2O solutions of methyl$_4$N$^+$ and butyl$_4$N$^+$ borates. As shown in Figure A3.11 of the Addendum, the spectrum collected in the presence of methyl$_4$N$^+$ borate exhibits a sharp band at 3675 cm^{-1}. The position of the band is in good agreement with the isotopic shift that is expected on the basis of a simple

harmonic oscillator model of the O−D/H stretch mode. By contrast, the band is absent in solutions of butyl$_4$N$^+$ borate (Addendum, Figure A3.11). These observations establish that the trends are also observable under the electrolyte conditions employed in the DEMS study.

Prior reports established that this band arises from interfacial waters that directly interact with CO_{ads} [75, 76, 171, 206–209]. These waters, which are not directly adsorbed on the electrode surface, have their O−D bonds pointed towards the terminal oxygen of CO_{ads} [75, 171]. The integrated area of this band tracks the CO surface coverage (Addendum, Figure A3.15). Further, the band is absent in Ar-purged methyl$_4$N$^+$-containing electrolyte (Addendum, Figure A3.14). These findings confirm that the band originates from interfacial waters that interact with CO_{ads}.

The center frequency of this band is slightly red-shifted by a few tens of wavenumbers with respect to the frequency of the O−D stretch of an isolated water molecule [207, 208]. On the basis of this observation, the interaction of water with CO_{ads} is often considered to be weak [75, 171] compared to the hydrogen bonding in bulk water. However, it was shown that this interaction affects the electronic structure of the metal−CO bond [208], and it was suggested that the CO_{ads}−H_2O interaction may be stronger than previously assumed [209]. Irrespective of this debate, our observations suggest that the two larger cations disrupt the CO_{ads}−H_2O interaction. Due to their larger size and more hydrophobic nature compared to methyl$_4$N$^+$ and ethyl$_4$N$^+$, they are expected to be more effective in displacing water molecules from the interface [170, 171].

Our findings suggest that ethylene evolution is shut down in the presence of propyl$_4$N$^+$ and butyl$_4$N$^+$ due to the disruption of the CO_{ads}−H_2O interaction by these two cations. At moderate overpotentials and basic pH, computational models [177–180, 210] and experimental evidence [144, 211] have suggested a surface-adsorbed CO dimer as an important intermediate in this reaction. Recent computational work predicts that hydrogen-bonding

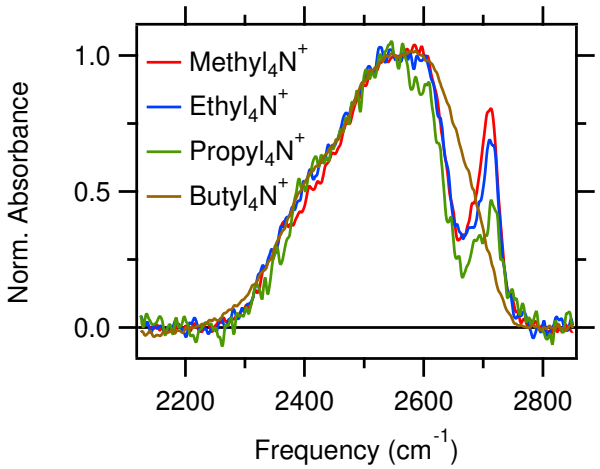

Figure 3.6: Normalized O−D stretch spectra recorded at a potential of -1.02 V in the presence of different cations as indicated. The unnormalized spectra are provided in the Addendum (Figure A3.14).

of interfacial waters to the oxygens of the CO dimer is required for its formation to be energetically favorable [180]. On the basis of these findings, we propose CO dimerization is impeded in the presence of propyl$_4$N$^+$ and butyl$_4$N$^+$ because these cations displace the water layer on top of CO$_{\text{ads}}$. Due to this displacement, these waters are not available to stabilize the CO dimer by hydrogen bonding to its terminal oxygens (Figure 3.7). This picture is also consistent with the cation-dependent structure of the double layer (Table 3.1). Our study provides the first experimental indication that this hydrogen bonding interaction is indeed critical for CO dimerization on Cu electrodes.

3.3 Conclusions

We investigated the effects of alkyl$_4$N$^+$ on the electroreduction of CO to ethylene on the polycrystalline Cu electrode in aqueous electrolytes. Using DEMS, we showed that ethylene is produced in the presence of methyl$_4$N$^+$ and ethyl$_4$N$^+$, but this product is not observed in propyl$_4$N$^+$- and butyl$_4$N$^+$-containing electrolytes. Using SEIRAS, we compre-

hensively characterized the properties of the electrocatalytic interface in the presence of the four alkyl$_4$N$^+$ cations. Our spectroscopic results suggest that the change in ethylene selectivity does not arise from blocking of CO adsorption sites or cation-dependent changes in the interfacial electric field strength. Analysis of the O−D stretch band of interfacial heavy water (D_2O) at the CO-covered electrode revealed a sharp band at ≈ 2710 cm^{-1} in methyl$_4$N$^+$- and ethyl$_4$N$^+$-containing electrolytes. This band, which is due to water with its O−D bond directed towards the terminal oxygen of CO_{ads}, is weak in the presence of propyl$_4$N$^+$ and entirely absent in butyl$_4$N$^+$-containing electrolyte. This observation demonstrates that these two cations displace the layer of waters on top of CO_{ads}. The waters identified by their characteristic O−D stretch frequency at ≈ 2710 cm^{-1} are predisposed to hydrogen bond to the terminal oxygens of the CO dimer, a key intermediate in the formation of ethylene [144, 177–180, 210, 211]. In line with recent theoretical predictions [180], our experimental results suggest that hydrogen bonding of water to the CO dimer is critical for its formation.

3.4 Experimental Procedures

Materials. For Cu thin film deposition on Si, NH_4F (40 wt.% in H_2O) and HF (48 wt.%) were purchased from Fisher Scientific (Waltham, MA). $CuSO_4 \cdot 5H_2O$ (99.999%; trace metal basis), EDTA-Na_2 (99.0 - 101.0%; ACS Reagent), 2,2-bipyridine (≥99%; ReagentPlus), HCHO (35 wt.%; 10% methanol as stabilizer), and NaOH (99.99%; trace metals basis) were acquired from Sigma Aldrich (St. Louis, MO). Polycrystalline diamond pastes were procured from Ted Pella (Redding, CA) or Electron Microscopy Sciences (Hartfield, PA).

For electrolyte preparation, tetramethylammonium chloride (≥98%; Acros Organics), tetraethylammonium chloride (98%; Alfa Aesar), tetramethylammonium hydroxide pen-

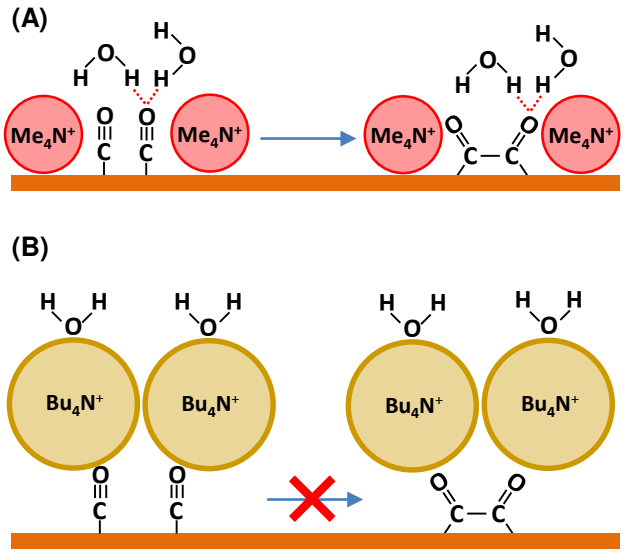

Figure 3.7: Possible CO_{ads} coupling mechanism on Cu(100), as proposed by Bagger *et al*. [180]. (A) In the presence of methyl$_4$N$^+$ (or ethyl$_4$N$^+$), interfacial waters are available to stabilize the CO dimer by hydrogen bonding. (B) In the presence of butyl$_4$N$^+$ (or propyl$_4$N$^+$), the formation of the CO dimer is blocked due to the displacement of interfacial water by these hydrophobic cations.

tahydrate (98%; Acros Organics), tetraethylammonium hydroxide (35 w/w% aq soln; Alfa Aesar), tetrapropylammonium hydroxide (25% in water; Acros Organics), tetrabutylammonium hydroxide (40 wt.%; Acros Organics), boric acid (Puratronic 99.9995%; Alfa Aesar), and deuterium oxide (99.8 atom% D; Acros Organics) were purchased from Fisher Scientific. Tetrapropylammonium chloride (98%), tetrabutylammonium chloride ($\geq$97%) were obtained from Sigma Aldrich. Deuterated tetramethylammonium chloride (D12, $\geq$98%) was obtained from Cambridge Isotope Laboratories (Tewksbury, MA).

Ar (ultra high purity), N_2 (ultra high purity), and CO (99.999%) were obtained from Air Gas (Radnor, PA).

DEMS System. The DEMS setup (Addendum, Figure A3.1) was designed on the basis of prior reports [212–214]. The reaction products that evolved from the electrode/electrolyte interface were collected by a sampling tip positioned $\approx$ 0.5 mm above the electrode surface. The sampling tip consisted of a PEEK tube plugged by a porous PTFE cylinder with

a pore size of ≈ 10 μm, a diameter of ≈ 3 mm, and a height of ≈ 2 mm (Genuine Porex; Fairburn, GA). To provide a water-tight seal, the cylinder was epoxied into the PEEK tube. A PTFE membrane of 20 nm pore size (PF-002HS; Cobetter Lab; Hangzhou, China) was wrapped around the PEEK tube/PTFE cylinder assembly and was fixated with epoxy and shrink tubing.

The tip was connected through PEEK tubing to a detection chamber that contained a residual gas analyzer (Microvision 2; MKS Instruments; Andover, MA) The chamber was pumped by a turbomolecular pump with a pumping speed of 67 L s^{-1} (HiCube 80 Eco; Pfeiffer Vacuum; Germany). A needle valve formed an adjustable orifice that separated the tip assembly from the vacuum chamber. The pressure before the needle valve (≈ 0.1 torr) was controlled by a dry scroll pump (Edwards nXDS 6i; Edwards Vacuum; Sanborn, NY). During the measurement, the pressure inside the detection chamber was $\approx 10^{-5}$ torr.

Cu Foil Preparation. Before each DEMS measurement, the copper foil (Puratronic 99.999%, 1.0 mm; Alfa Aesar) was first polished with a 1500-grit sand paper to remove surface oxides. The surface was then hand-polished with 1.0 and 0.3 μm alumina slurries. After each 10-min polishing step, the electrode was thoroughly rinsed with high purity water. After 10 min of sonication in high purity water, the copper foil was electropolished in a H_3PO_4, H_2O, and H_2SO_4 bath with volume ratio 10:5:2. The copper foil was subjected to a potential of 2.3 V vs. Cu for two sequential periods of 2 s, separated by an interval of 30 s at open circuit potential [215]. Finally, the copper foil was rinsed thoroughly with high purity water and blow-dried with N_2. Before each DEMS experiment, the copper foil was subjected to cleaning voltammetric cycles. A surface roughness factor of ≈ 3 compared to a smooth Cu surface[216] was determined on the basis of electrochemical capacitance measurements. The electrochemical protocols are detailed in our prior report [190].

Electrochemical Methods for DEMS.

Aqueous electrolytes containing 0.1 M alkyl$_4$N$^+$ hydroxide and 20 μM EDTA-Na_2 were

titrated with H_3BO_3 to a pH of 9.5. The pH after the experiments was 9.5 ± 0.1. Measurements were performed in a single-compartment electrochemical cell with an electrolyte volume of 3 mL (Addendum, Figure A3.1). A VersaStat3 potentiostat (AMETEK; Berwyn, PA) controlled the potential. A Pt foil (Premion 99.99%, 0.025 mm; Alfa Aesar) and a leak-free Ag/AgCl electrode (ET072, 3.4 M KCl; eDAQ; Colorado Springs, CO) were employed as the counter and reference electrodes, respectively. Before each experiment, the Pt foil was soaked in an aqueous acid solution (30 wt.% H_2SO_4, 30 wt.% HNO_3) for one hour, and was then rinsed with high purity water. The Ag/AgCl reference electrode was regularly calibrated with respect to a saturated calomel electrode (CHI 150; CH Instruments Inc.; Austin, TX). The measured potential was converted to the SHE scale according to $V_{\mathrm{SHE}} = V_{\mathrm{Ag/AgCl}} + 0.209\ \mathrm{V}$. 76% of the solution resistance was compensated *in situ* with the VersaStat3 potentiostat. The geometric surface area of the electrode was $\approx 1.9\ \mathrm{cm}^2$.

The sequence of potential steps during DEMS measurements is described in the main text. Prior to the potential jump ($t = 0$ s in Figure 3.1), the electrolyte was purged with Ar at a rate of 5 sccm for 10 min. A voltammetric cycle from -0.39 to -0.99 V with 10 mV s^{-1} was carried out, then the potential was held at -0.39 V for 20 min under CO purging at a rate of 5 sccm. Mass spectra were recorded with a time resolution of ≈ 3 s. For each partial pressure trace, the value that was recorded about 30 s before time zero (the time of the first potential step, Figure 3.1) was subtracted from the trace to zero out the baseline. Each trace in Figure 3.1 was smoothed by a binomial algorithm and is the average of two independent measurements. The background-subtracted, unsmoothed raw data are shown in the Addendum (Figures A3.16-A3.19).

Cu Thin Film Preparation for SEIRAS.

Thin polycrystalline Cu films were deposited on a reflecting facet of a 60° Si prism (Pike Technologies; Madison WI) by an electroless deposition procedure and characterized as

described in our previous report [190]. The film roughness factor was ≈ 13. The roughness of the films was maintained between $\pm 20\%$ of the original value after the spectroelectrochemical measurements. The typical surface morphology of the films was characterized by atomic force microscopy (Addendum, Figure A3.9). Characterization by X-ray photoelectron spectroscopy was reported in our prior study [190].

Electrochemical Methods for SEIRAS.

For the spectroelectrochemical measurements shown in the main text, the electrolyte was prepared with D_2O. The initial pH of the electrolyte was 9.7 ± 0.5. After the experiments, the pH typically decreased by $\approx 10\%$. Measurements were performed in a single-compartment electrochemical cell (Addendum, Figure A3.7) with 4 mL electrolyte. The electrical connection from the film to the potentiostat was made by sandwiching a ring of Cu foil (Puratronic 99.999%, 0.025 mm; Alfa Aesar) between the circular edge of the film and a Viton O-ring from the PEEK electrochemical cell. A Au wire (99.999%, 0.5 mm; Alfa Aesar) and a Ag/AgCl electrode (RE-5B, 3 M NaCl; BASi Inc; West Lafayette, IN) were employed as the counter and reference electrodes, respectively. The Cu ring and Au wire were polished with 0.3 μm alumina slurry for 5 min and were then rinsed with high purity water. The Ag/AgCl reference electrode was calibrated as described above. The geometric surface area of the Cu thin film was ≈ 1.9 cm^2. The Cu thin film was first held at -0.39 V for 20 min for CO saturation, and the potential was then linearly swept to -1.49 V at a rate of 2 mV s^{-1}. The cell resistance was not compensated.

SEIRAS Measurements.

The Si crystal coated with the Cu thin film was assembled into a PEEK electrochemical cell, which was placed on an ATR accessory (VeeMax III; Pike Technologies; Madison, WI). Spectra were recorded with a nitrogen-purged Bruker Vertex 70 FTIR spectrometer (Billerica, MA) equipped with a liquid nitrogen-cooled photoconductive MCT detector (FTIR-16; Infrared Associates; Stuart, FL). Spectra were collected every 4.61 s with a

spectral resolution of 4 cm^{-1} and a scanner velocity of 40 kHz. The change in optical density was calculated according to $\mathrm{mOD} = -10^3 \cdot \log(S/R)$, with S and R referring to the single beam sample spectrum and single beam reference spectrum, respectively. The reference potential was -0.39 V. To determine accurately the peak frequency, a cubic spline was employed to interpolate between recorded data points (SI Addendum, Figure A3.20).

3.5 Addendum

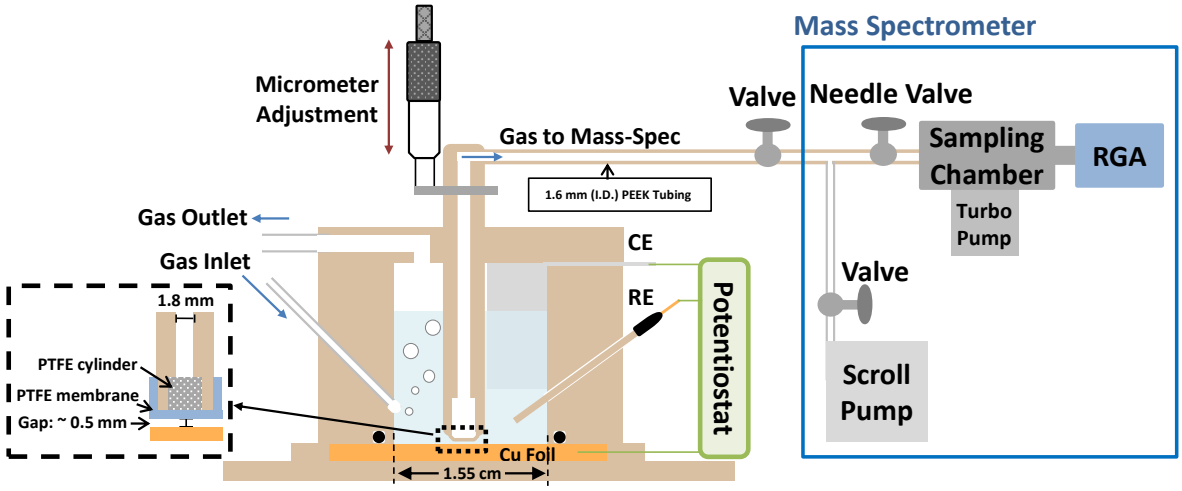

Figure A 3.1: DEMS setup. A description of the setup is given in the Materials and Methods section of the main text.

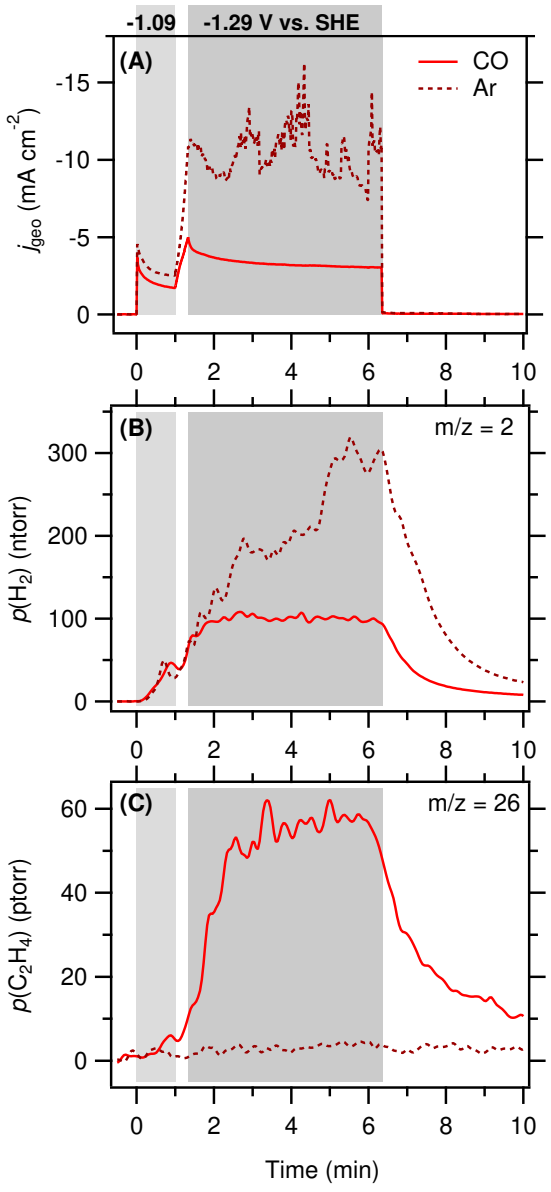

Figure A 3.2: The $m/z = 26$ signal is absent in Ar-purged electrolyte. (A) Electrochemical current density during the DEMS measurements. (B) H_2 partial pressure, and (C) C_2H_4 partial pressure in the presence of aqueous solutions of 0.1 M methyl$_4$N$^+$ borate under 1 atm of CO (solid line) or Ar (dashed line). At high current densities ($\approx$ 10 mA cm^{-2}), hydrogen bubbles cover the electrode within a few seconds. Stochastic desorption of the bubbles causes the observed current density fluctuations. A significant fraction of the bubbles does not interact with the sampling tip. Therefore, a fraction of the hydrogen escapes mass spectrometric detection, giving rise to discrepancies between current density and detected hydrogen partial pressure.

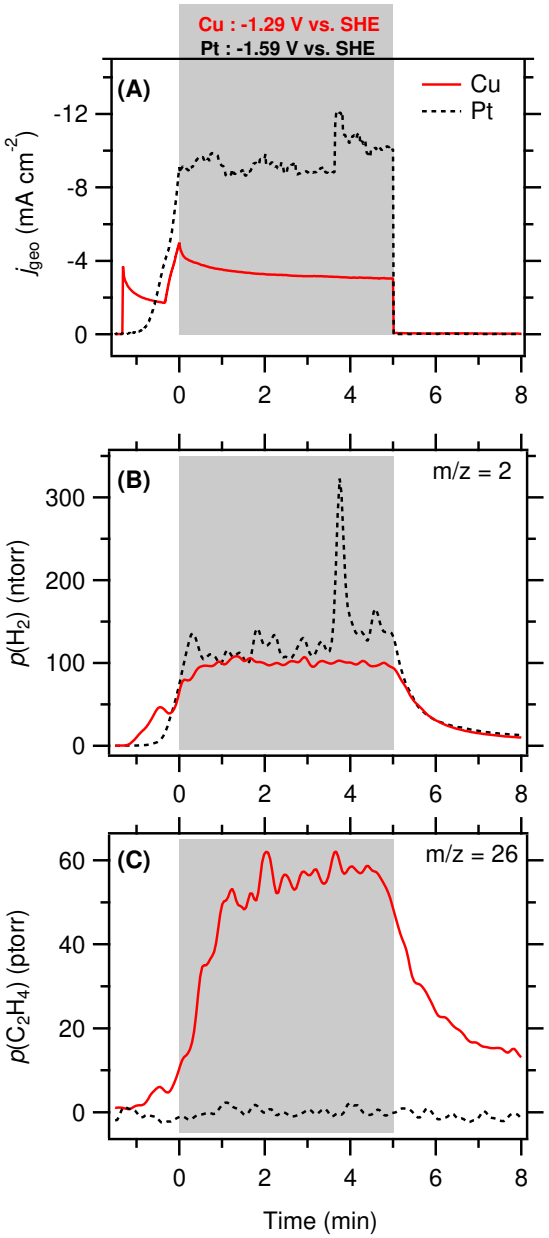

Figure A 3.3: The $m/z = 26$ signal is absent when a Pt electrode is used. (A) Electrochemical current density during the DEMS measurements. (B) H_2 partial pressure, and (C) C_2H_4 partial pressure in the presence of aqueous solutions of 0.1 M methyl$_4$N$^+$ borate under 1 atm of CO on Cu (solid line) or Pt (dashed line). Reaction potentials that gave the same amount of detected H_2 were chosen. The lower H_2 detection efficiency in the case of Pt compared to the experiments with Cu is attributed to differences in H_2 bubble nucleation, potentially due to differences in surface morphology. Further, the thin Pt foil has a higher propensity to warp (compared to the thick Cu sheet electrodes). Therefore, the electrode-sampling tip distance for the experiments with Pt could not be precisely controlled. This distance impacts the collection efficiency.

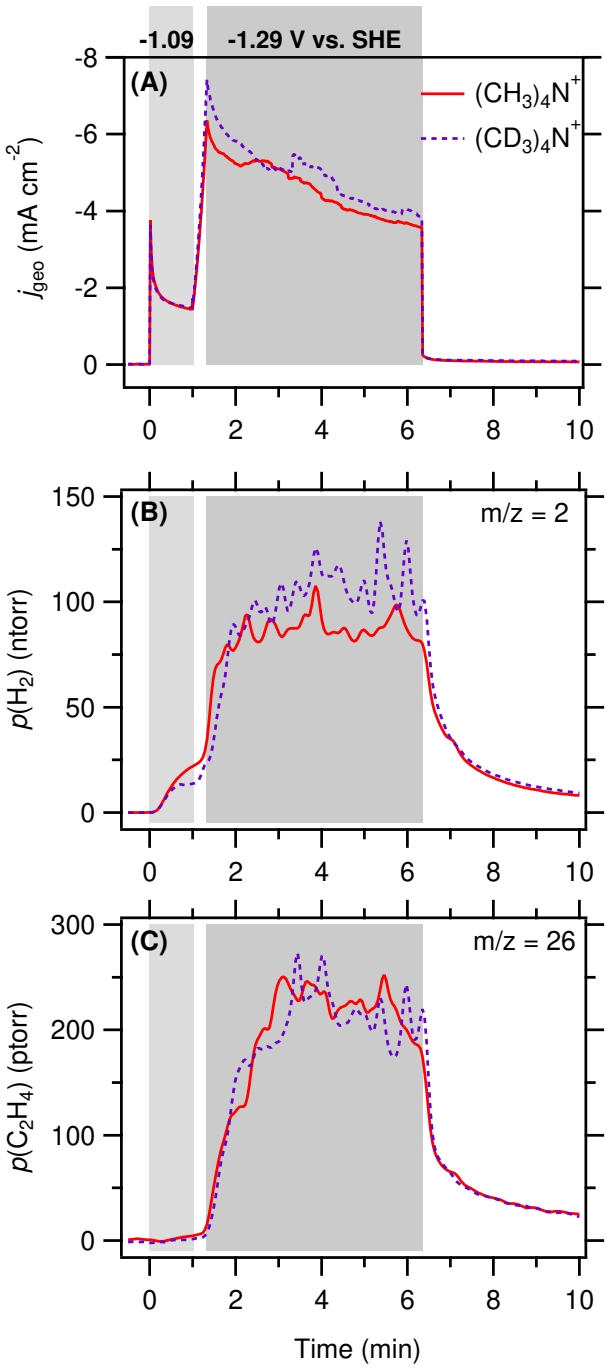

Figure A 3.4: The $m/z = 26$ signal is unaffected by the use of deuterated alkyl$_4$N$^+$. (A) Electrochemical current density during the DEMS measurements. (B) H_2 partial pressure, and (C) C_2H_4 partial pressure detected in the presence of aqueous solutions of 0.1 M $(CH_3)_4N^+$ (solid line) and $(CD_3)_4N^+$ chlorides (dashed line) under 1 atm CO.

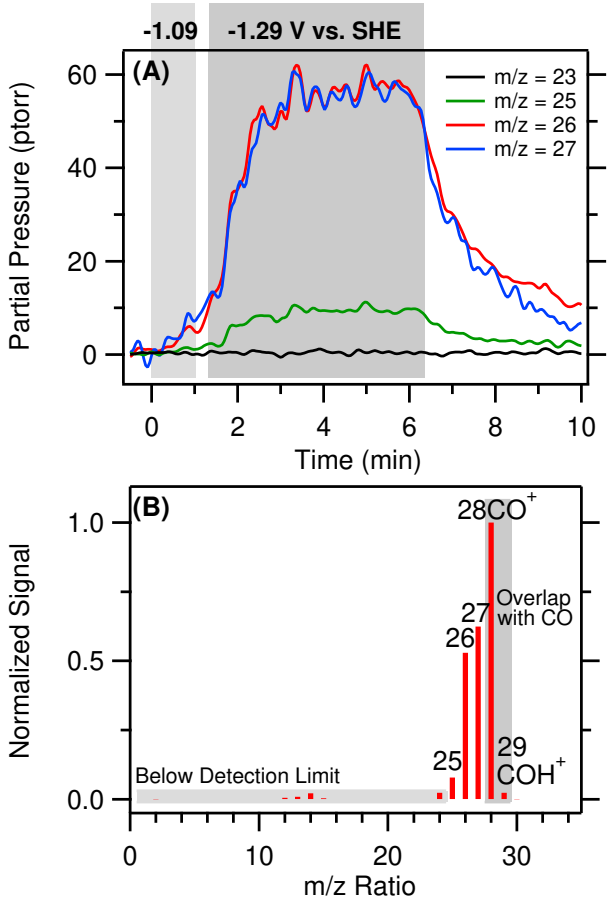

Figure A 3.5: The relative partial pressures of the observable m/z values are consistent with the relative signal intensities of the standard mass spectrum of C_2H_4. (A) $m/z = 23$, 25, 26, 27 signals for the 0.1 M methyl$_4$N$^+$-experiment presented in Figure 3.1C of this chapter. (B) Normalized standard mass spectrum of C_2H_4 from the NIST Chemistry Webbook.[217]

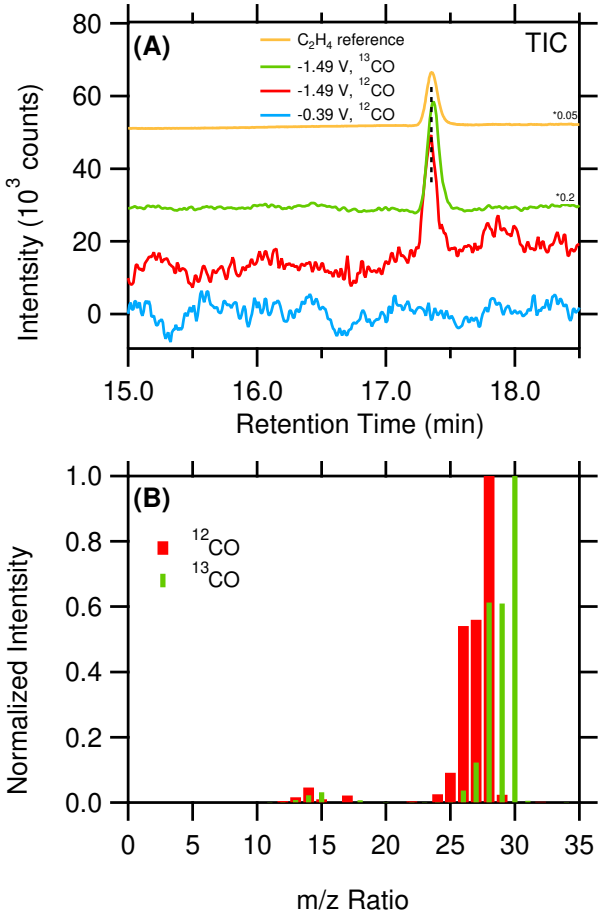

Figure A 3.6: GC-MS confirms of the formation of ethylene by CO reduction. (A) GC-MS total ion chromatograms (TIC) of a C_2H_4 standard sample and gaseous products of electrolysis in CO-saturated aqueous solutions of 0.1 M methyl$_4$N$^+$ borate as indicated. (B) Mass spectra of the chromatogram peaks at 17.35 min obtained from the gaseous products collected during electrolysis at -1.49 V vs. SHE. GC-MS experiments were carried out in an H-cell. The cathode and anode compartments were separated by a Selemion AMV anion-exchange membrane (AGC Engineering Co.; Chiba, Japan). Each compartment contained 10 mL of electrolyte. Prior to the start of electrolysis, the electrolyte was saturated with CO and the cell was sealed. 100 μL of gaseous sample from the headspace of the cell was injected into GC-MS after 40 min of electrolysis.

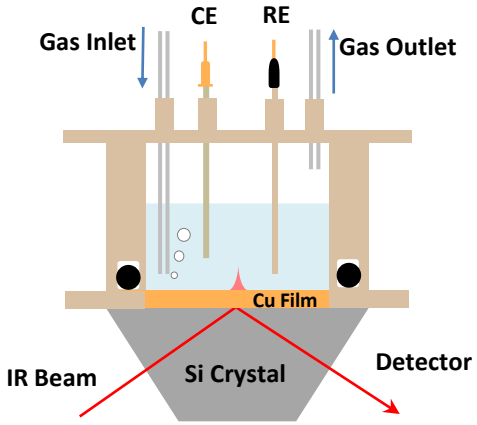

Figure A 3.7: Scheme of spectroelectrochemical cell.

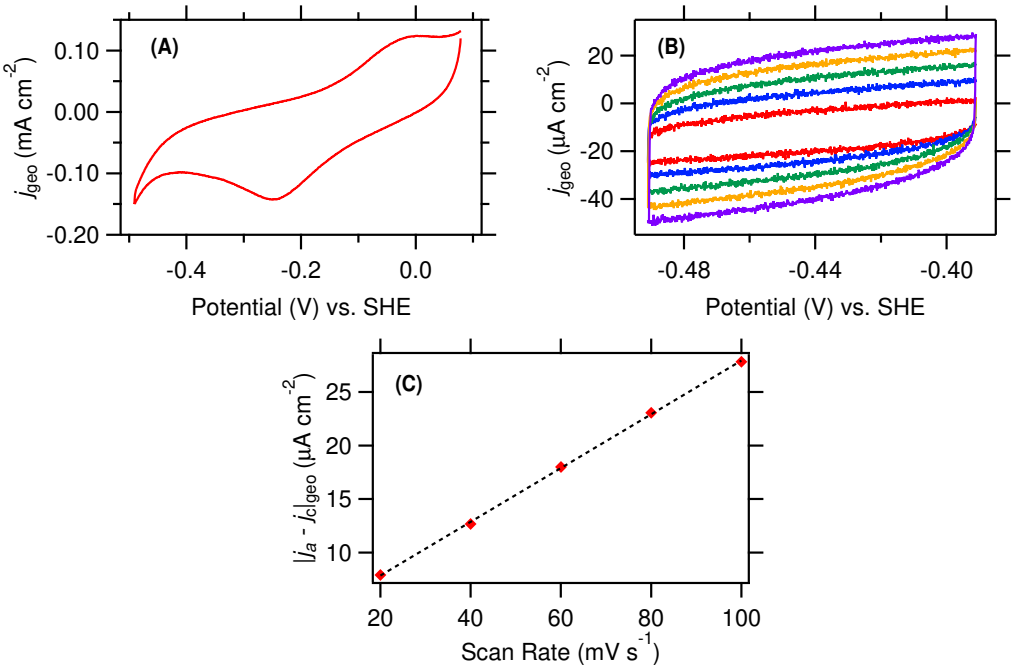

Figure A 3.8: (A) Representative cyclic voltammogram obtained following five Cu film cleaning cycles from 0.08 to -0.49 V at a scan rate of 50 mV s^{-1}. (B) Representative CVs taken at scan rates of 20 (red), 40 (blue), 60 (green), 80 (yellow), and 100 mV s^{-1} (purple) to measure the double layer capacitance. (C) The double layer charging current vs. scan rate for the data shown in graph (B) (red squares) and the linear fit (black dotted line) to the data. The roughness of the film was calculated by dividing the slope of the fitted line in graph (C) by a factor of two and a reference double layer capacitance value of 28 μF cm^{-2} for a smooth Cu surface.[216]

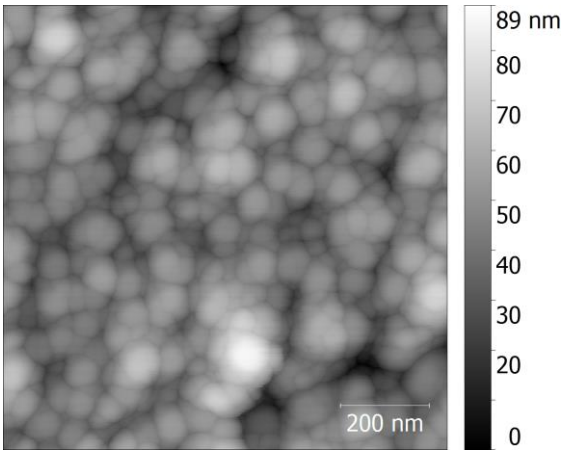

Figure A 3.9: AFM image of an as-synthesized Cu film on a Si ATR crystal.

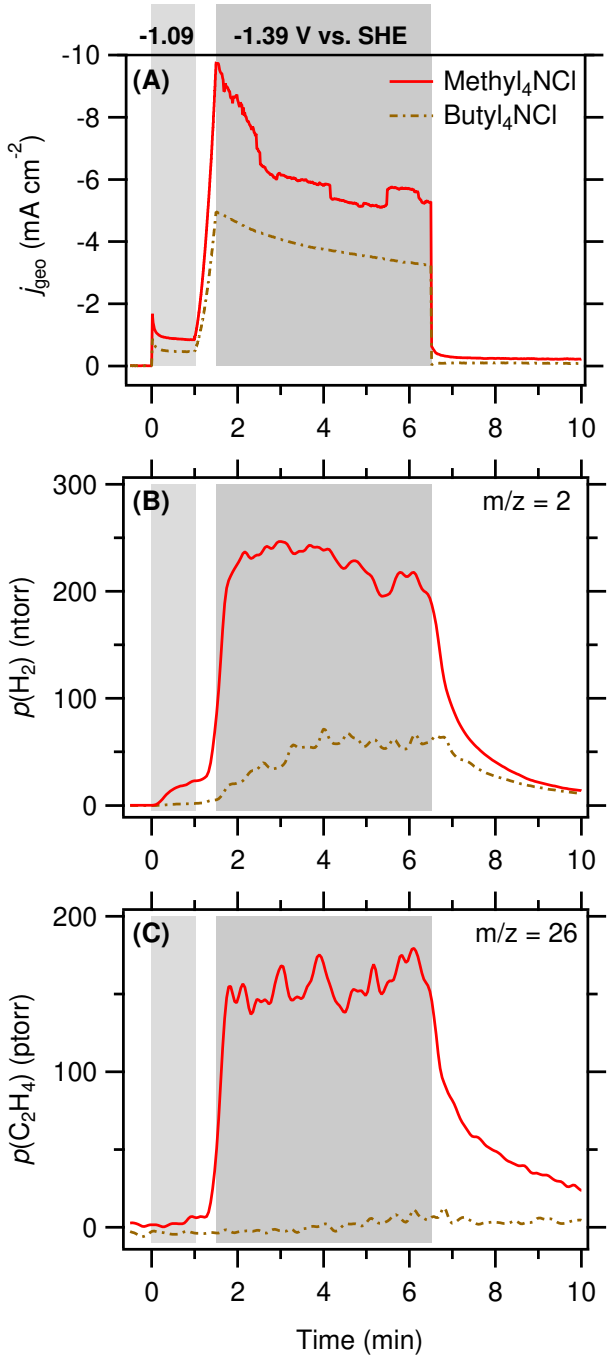

Figure A 3.10: The observed trends in the $m/z = 26$ signal are also obseved in the presence of the chloride anion. (A) Electrochemical current density during the DEMS measurements. (B) H_2 partial pressure, and (C) C_2H_4 partial pressure detected in the presence of aqueous solutions of 0.1 M methyl$_4$N$^+$ chloride (solid line) and butyl$_4$N$^+$ chloride (dashed line) under 1 atm CO.

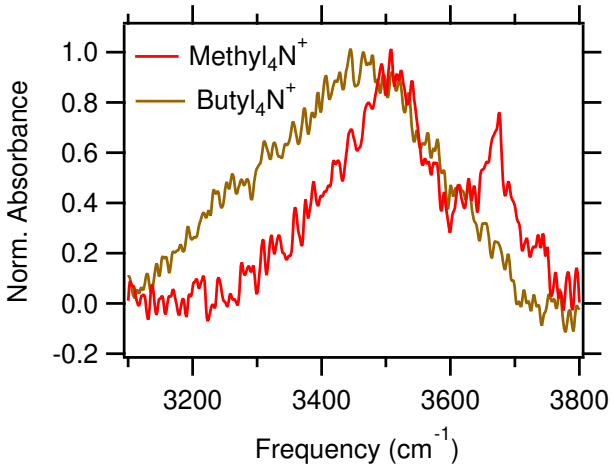

Figure A 3.11: The normalized O−H stretch spectra in the presence of aqueous solutions of 0.1 M methyl$_4$N$^+$ and butyl$_4$N$^+$ borate at -1.29 V. The 3675 cm^{-1} band is prominent in methyl$_4$N$^+$-containing electrolyte but absent in the presence of butyl$_4$N$^+$.

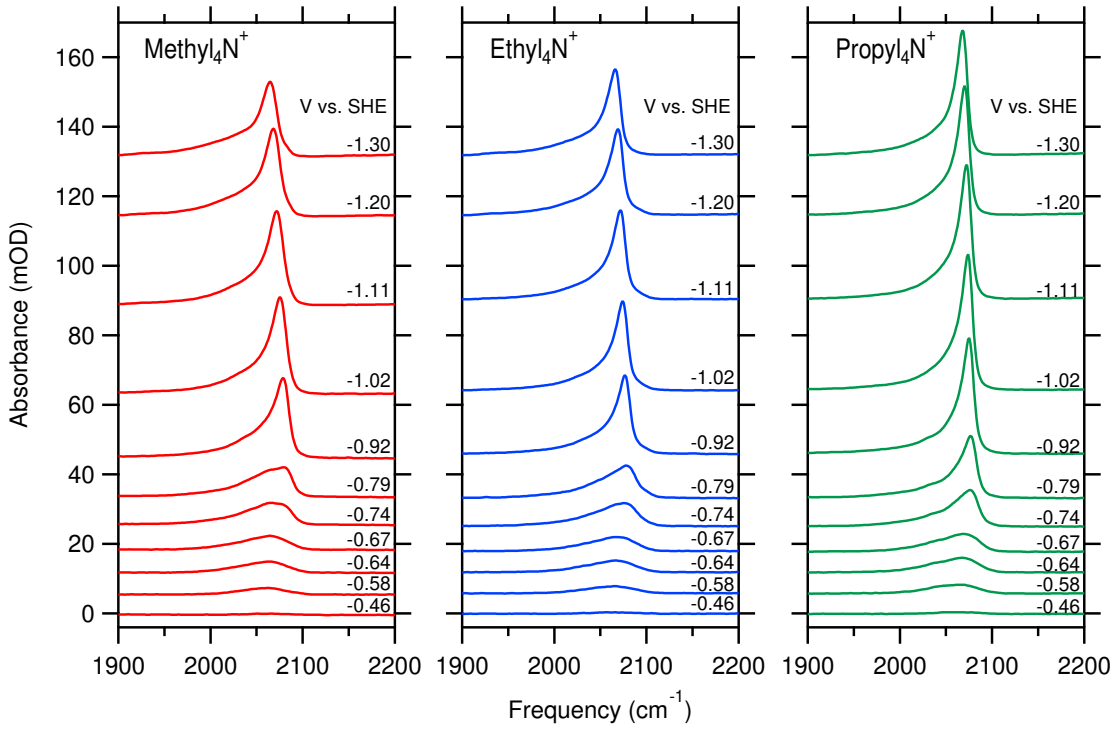

Figure A 3.12: Representative CO stretch spectra in solutions of 0.1 M methyl$_4$N$^+$, ethyl$_4$N$^+$, and propyl$_4$N$^+$ chloride in D_2O.

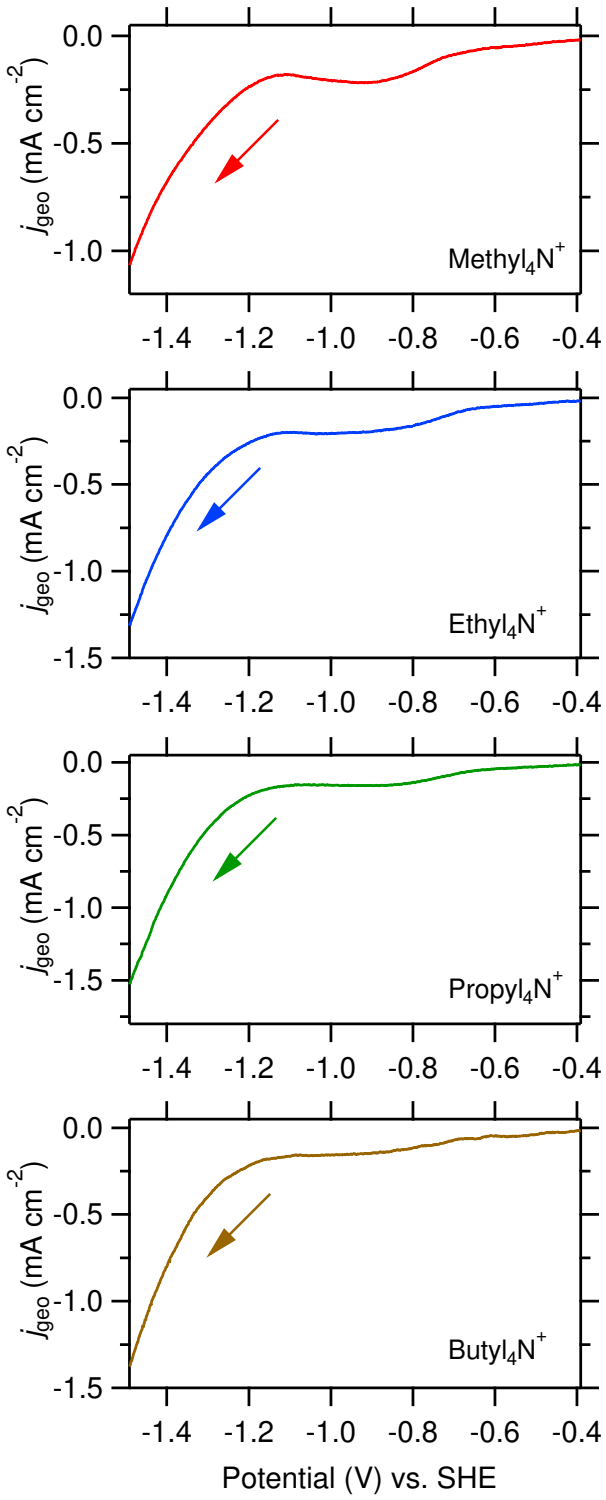

Figure A 3.13: Linear sweep voltammetry current-voltage curves for the spectroscopic data presented in the main text (Figure 3.2) and Figure A3.12. Arrows indicate the sweep direction.

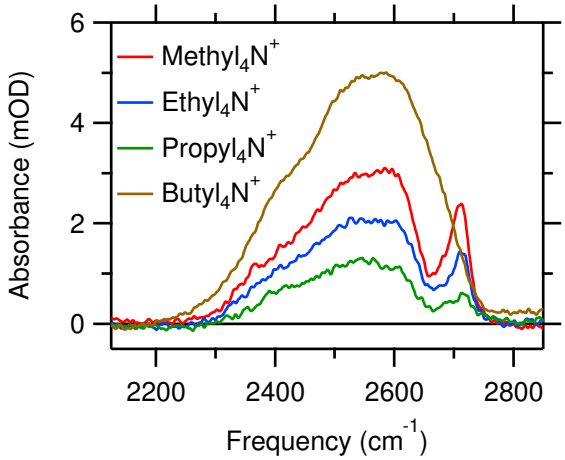

Figure A 3.14: Unnormalized O−D stretch spectra recorded at a potential of -1.02 V in the presence of the different cations as indicated.

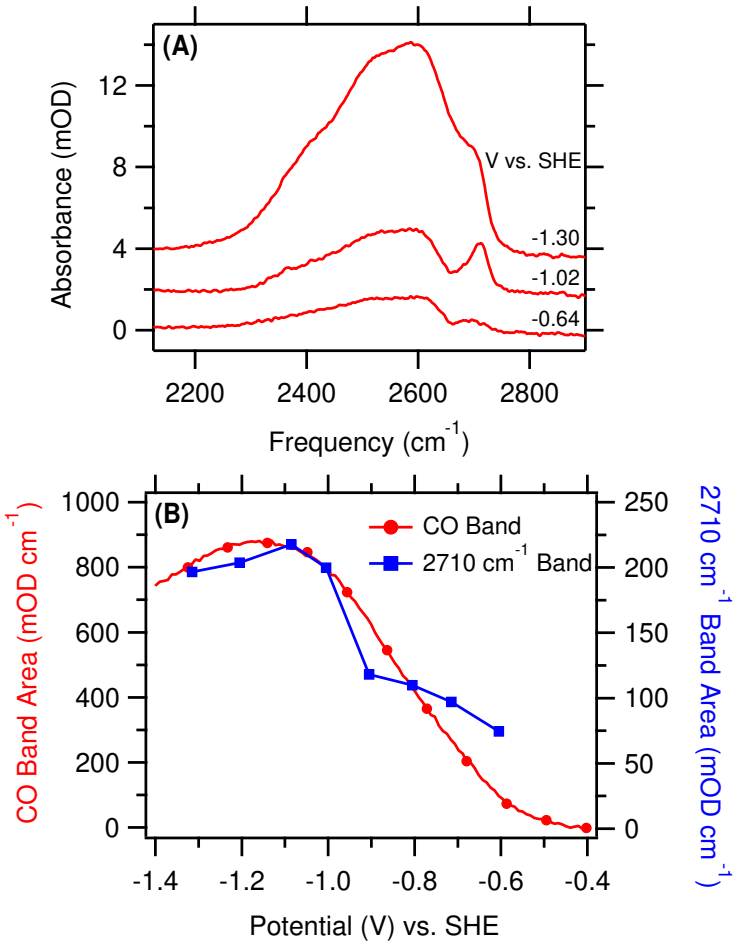

Figure A 3.15: (A) Representative O−D stretch spectra in 0.1 M methyl$_4$N$^+$ chloride in D_2O. (B) Integrated band areas of the C≡O stretch band (red circles) and O−D stretch band at 2710 cm^{-1} (blue squares) as a function of applied potential.

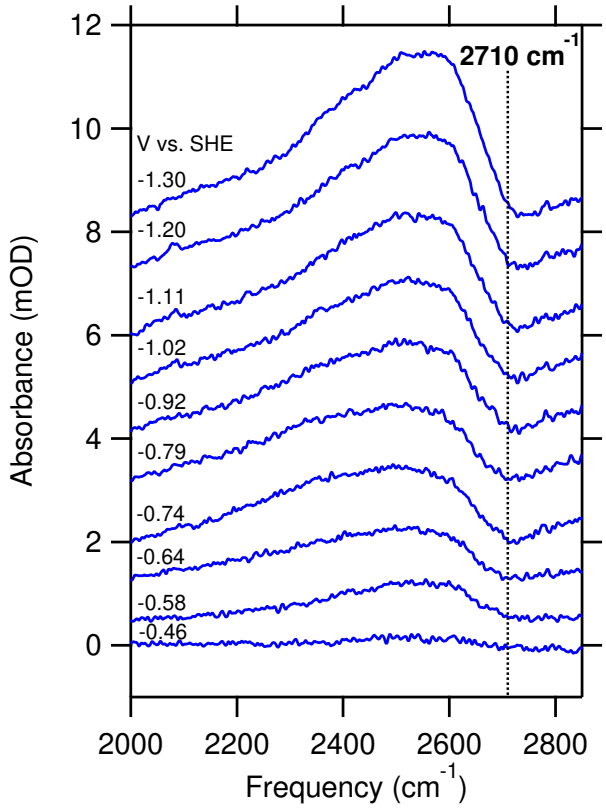
2710 cm-1
V vs. SHE
-1.30
-1.20
-1.11
-1.02
-0.92
-0.79
-0.74
-0.64
-0.58
-0.46
Absorbance (mOD)
Frequency (cm-1)
0
2
4
6
8
10
12
2000
2200
2400
2600
2800

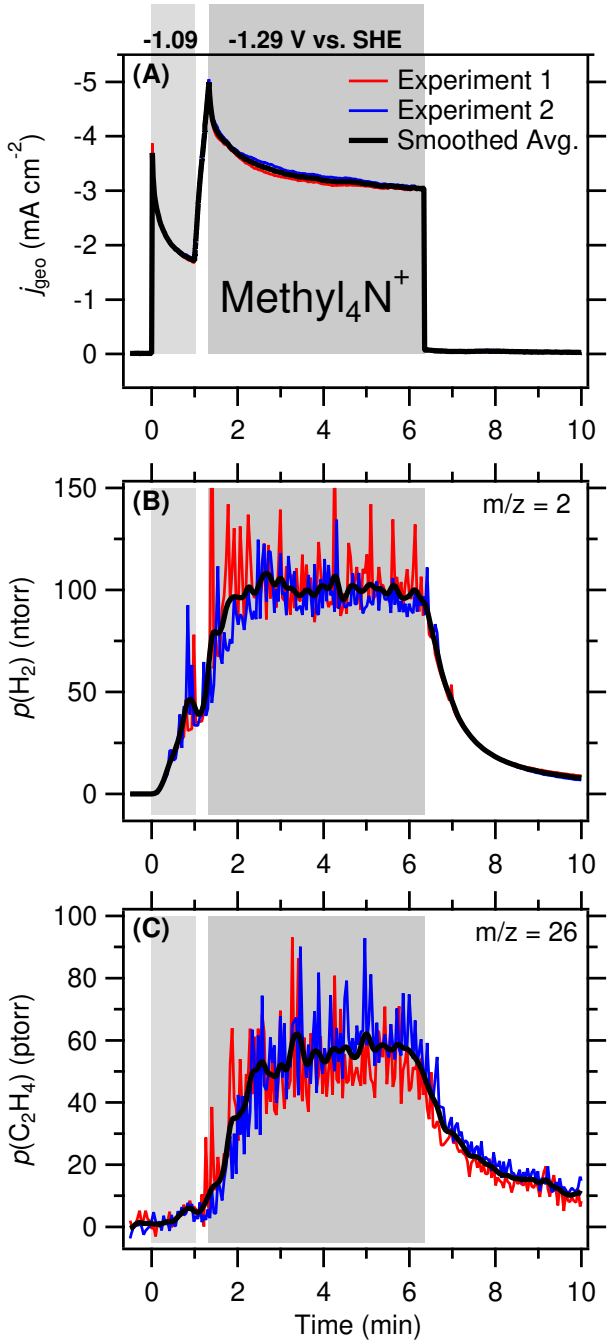

Figure A 3.16: Raw DEMS data for methyl$_4$N$^+$. (A) Electrochemical current density, (B) H_2 partial pressure, and (C) C_2H_4 partial pressure recorded during two independent experiments (thin red and blue traces) of CO electroreduction on Cu. The thick black trace represents the smoothed average of the two experiments.

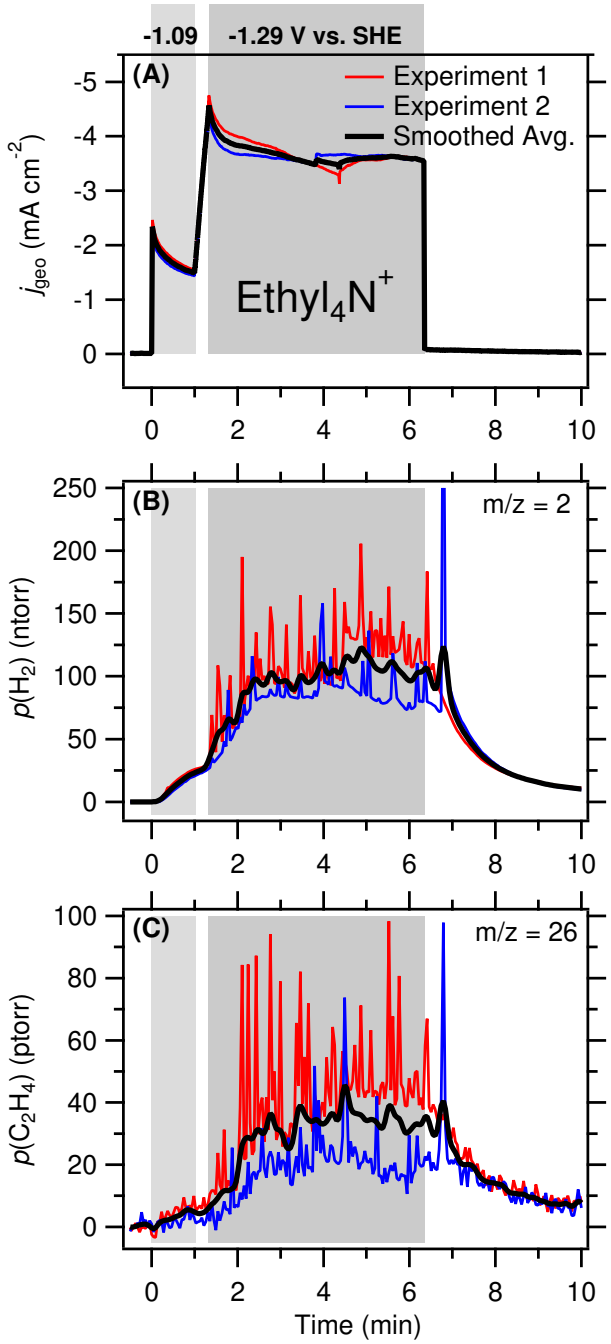

Figure A 3.17: Raw DEMS data for ethyl$_4$N$^+$. (A) Electrochemical current density, (B) H_2 partial pressure, and (C) C_2H_4 partial pressure recorded during two independent experiments (thin red and blue traces) of CO electroreduction on Cu. The thick black trace represents the smoothed average of the two experiments.

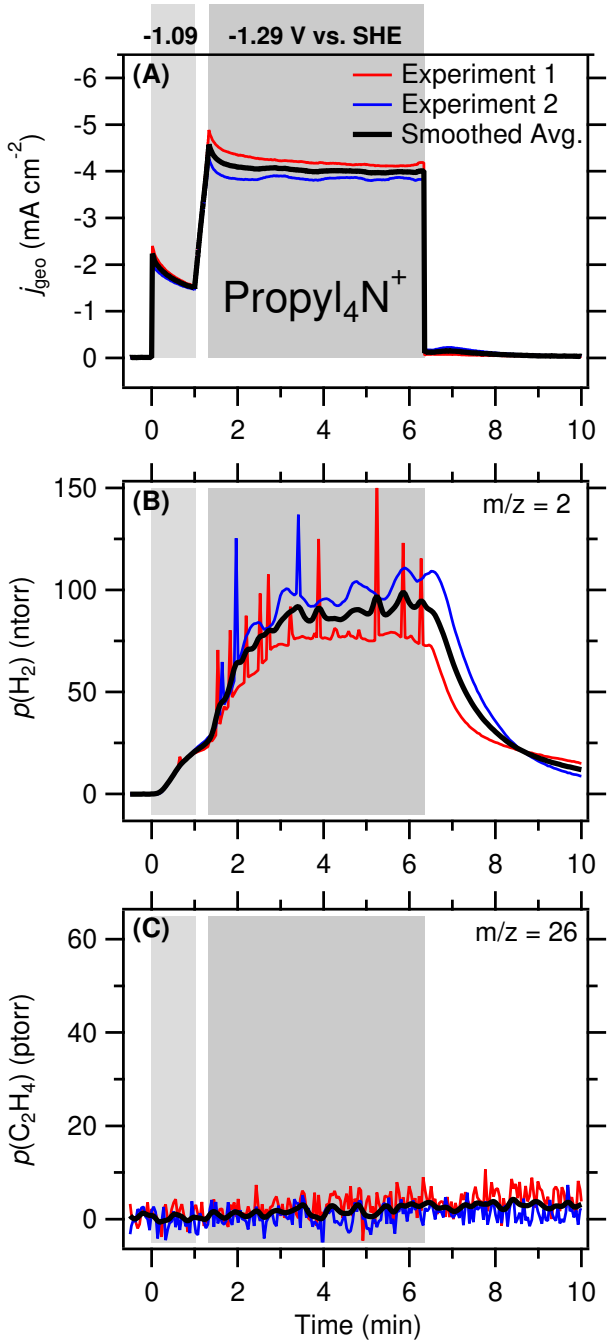

Figure A 3.18: Raw DEMS data for propyl$_4$N$^+$. (A) Electrochemical current density, (B) H_2 partial pressure, and (C) C_2H_4 partial pressure recorded during two independent experiments (thin red and blue traces) of CO electroreduction on Cu. The thick black trace represents the smoothed average of the two experiments.

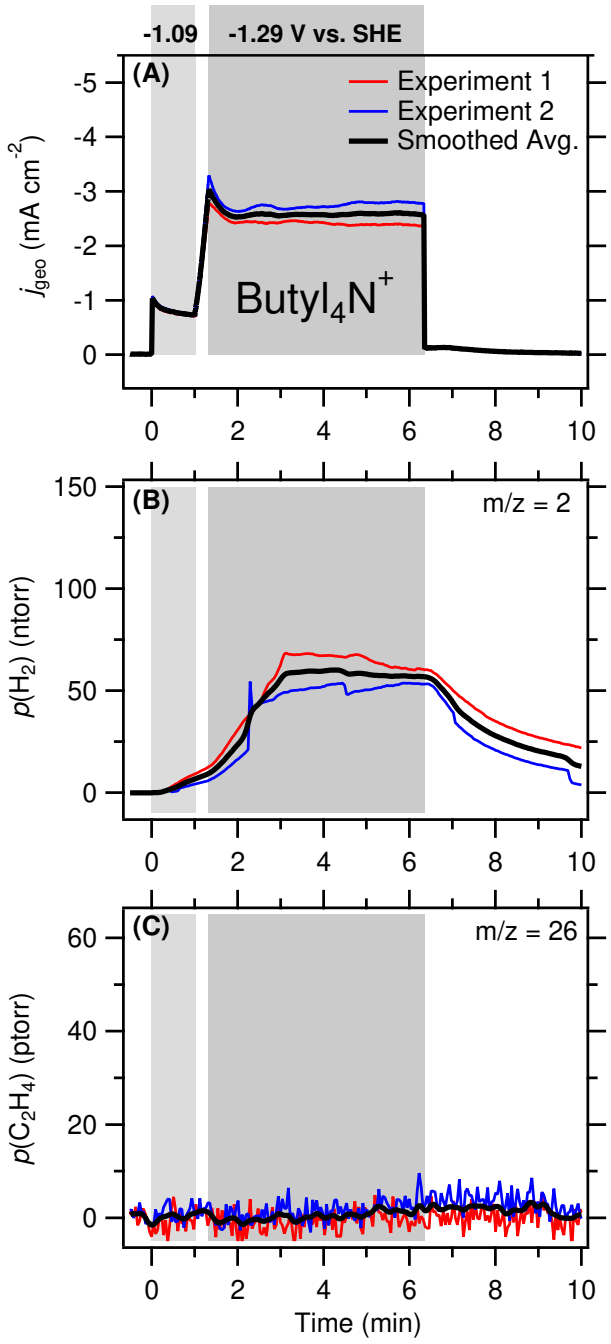

Figure A 3.19: Raw DEMS data for butyl$_4$N$^+$. (A) Electrochemical current density, (B) H_2 partial pressure, and (C) C_2H_4 partial pressure recorded during two independent experiments (thin red and blue traces) of CO electroreduction on Cu. The thick black trace represents the smoothed average of the two experiments.

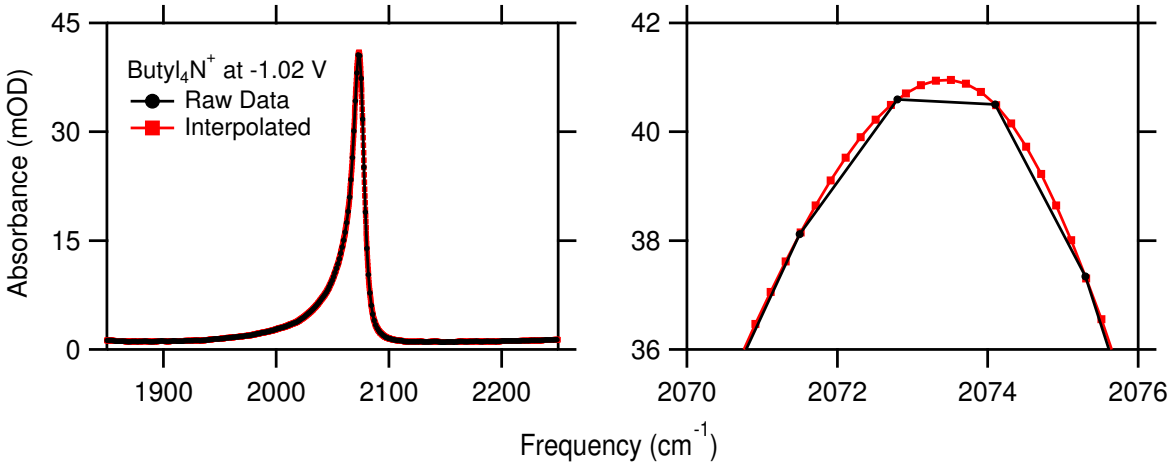

Figure A 3.20: An example of FTIR data interpolation. The data presented was collected in the presence of 0.1 M butyl$_4$N$^+$ in D_2O at potential of -1.02 V. The interpolated data (red) captures the CO peak frequency more accurately than the raw data (black).

3.6 Acknowledgement

This work was supported by the National Science Foundation (Award No.: CHE-1565948). We thank Prof. Udayan Mohanty for helpful discussions about the electrostatics of the electrochemical interface and Prof. Dunwei Wang for critically reading the manuscript.

3.7 Original Publication

Li,J.*, Li,X.*, Gunathunge, C. M. & Waegele, M. M. Hydrogen Bonding Steers the Product Selectivity of Electrocatalytic CO Reduction. *Proc. Natl. Acad. Sci. U.S.A* **116**, 92209229(2019).

*These authors contributed equally to this work.

Chapter 4

Revealing the Predominant Surface Facets of Rough Cu Electrodes Under Electrochemical Conditions

4.1 Introduction

Metal electrodes of high surface roughness often display high conversion rates for CO and CO_2 to desirable reduction products with good reaction selectivity. The strategies that have been employed for the preparation of high-surface area electrodes include the deposition of nanoparticles [124, 127, 218–220], reduction of variously prepared metal oxide phases [10, 120, 221–225], halide-induced surface reconstruction [182, 226–230], electrodeposition [161, 231–233], and the use of porous supports [234, 235].

The resulting electrodes are among the most selective and efficient catalysts for the reduction of CO and CO_2. For example, the electrodeposition of copper and copper alloy films in the presence of the nucleation inhibitor 3,5-diamino-1,2,4-triazole results in electrocatalysts with high surface area and tunable surface morphology [231, 232]. Copper nanowire electrodes produced by this method reduce CO_2 to ethylene with a Faradaic efficiency (F.E.) of $\approx 40\%$ at a potential of -0.5 V versus the reversible hydrogen electrode (RHE). By comparison, $\approx 1\%$ F.E. for ethylene was observed on a polycrystalline Cu foil at the same potential [231]. Similarly, oxide-derived copper electrodes convert

CO to C_{2+}-oxygenates with a F.E. of close to $\approx 60\%$ at moderate overpotentials (-0.25 to -0.5 V versus RHE), whereas only $\approx 10\%$ F.E. for these products was reported on a polycrystalline Cu foil in the same potential range [10].

The favorable catalytic properties of these electrodes are thought to arise from a combination of factors that include the predominance of certain surface facets [127, 182, 236], a suitable surface-density of edge and kink sites [124, 125, 127, 182, 237], the presence of subsurface oxygen or partially oxidized copper species [230, 233, 238], and a synergistic interplay between electrode morphology and electrolyte that brings about interfacial conditions favorable for the reduction of CO and CO_2 [161, 234, 239].

The attribution of the observed catalytic activity for CO and CO_2 reduction to specific atomic-level characteristics of high-surface area electrodes has proven challenging, though. For example, the high selectivity for C_{2+} hydrocarbons and oxygenates of oxide-derived copper electrodes have been variably attributed to the presence of metastable copper sites in the vicinity of grain boundaries [205], the preferential occurrence of (100) surface facets [236], or the presence of residual oxygen at or below the surface [238, 240]. Other studies suggested the absence of such oxygen species [241–243]. Further, a recent report indicated that high-surface area electrodes primarily bring about a favorable product spectrum through the suppression of the hydrogen evolution reaction rather than the promotion of the reduction of CO [225].

These diverging views highlight the great challenge that lies in identifying the key characteristics of rough electrodes that engender their high catalytic activity and selectivity. One of the key obstacles is the relative scarcity of methods that are suitable for the characterization of these complex materials under electrocatalytic conditions. While *ex situ* characterization techniques such as transmission electron microscopy (TEM), scanning electron microscopy (SEM), x-ray diffraction (XRD), or temperature programmed desorption (TPD) provide insightful structural information, they are mute on the structure

of the surface in the electrochemical environment. Electrochemical scanning tunneling microscopy (ESTM) is a powerful technique for probing flat electrode surfaces *in situ* [244, 245]. However, the method is of limited use for the characterization of rough electrodes. Though various x-ray techniques can probe electrode surfaces *in situ* [233, 235, 238, 246], these methods require synchrotron radiation and can therefore not be employed for routine measurements.

Infrared (IR) spectroscopy has been established as a useful complementary technique for probing the surface structure of heterogeneous catalysts. Specifically, the frequency of the C≡O stretch mode of atop-bound CO (CO_{atop}) is sensitive to the coordination and nature of the metal atom to which CO_{atop} is bound [247]. Therefore, by monitoring the peak frequency of the C≡O stretch band of CO_{atop}, atomic-level structural characteristics of the catalytic surface can be probed [185, 236, 248–252]. Because CO_{atop} is an on-pathway intermediate in the electroreduction of CO and CO_2 to hydrocarbons [140, 150, 190], the C≡O stretch frequency could provide atomic-level morphological information on rough metal electrodes under electrocatalytic conditions.

Correlating the C≡O stretch frequency with the structural properties of the electrode during electrolysis is complicated by three factors:

- First, due to experimental constraints, IR and Raman spectroscopies are often carried out under conditions disparate from those employed during electrolysis experiments for the detection of products. For example, in surface-enhanced infrared absorption spectroscopy (SEIRAS), spectra are often taken during a potential sweep on a timescale of a few minutes. By contrast, electrolysis is typically carried out on a timescale of tens of minutes. Electrocatalysts are well-known to undergo surface reconstructions under electrocatalytic conditions [185, 245, 253–255]. For this reason, spectroscopy often reports on the transient surface characteristics, whereas the measured product distributions are averaged over different states of the electrode

surface.

- Second, besides the coordination of the underlying metal atom, the C≡O stretch frequency of CO_{atop} is profoundly affected by the absolute CO coverage on the surface. The coverage affects the frequency in two distinct ways [247, 256]: (a) As the coverage changes, the bond energy between CO_{atop} and the surface is altered [257], thereby modifying the frequency. These effects are termed "chemical effects". (b) The coupling between the dynamical dipoles of CO_{atop} gives rise to new vibrational modes of the coupled system that can greatly affect the observed frequencies and band intensities. These coupling effects increase with increasing coverage. Although information on the surface structure from the C≡O stretch spectra can be obtained despite these coupling effects in certain cases, the extraction of this information can be very challenging and requires elaborate investigations with isotopic mixtures [258]. Therefore, the character of the adsorption site is most straightforwardly revealed by the C≡O stretch frequency of CO_{atop} in the limit of low coverage [259].

- Third, in the limit of low coverage, where coupling effects are expected to be small, the C≡O stretch frequency of CO_{atop} is generally determined by the character of the adsorption site. For example, in the limit of low coverage of CO_{atop} on copper, the C≡O stretch frequency typically increases with increasing CO_{atop} binding strength to the surface site (Figure A4.1, Addendum). However, CO_{atop} on copper (111) and (100) surface facets has virtually the same C≡O stretch frequency [247], even though the binding strength of CO_{atop} is about 40-100 meV larger on the (100) facet [204, 260]. Whereas the (111) facet is a poor catalyst for CO and CO_2 reduction, the (100) facet is one of the most active [126, 129, 261]. Therefore, it is not straightforward to distinguish between these two surface facets on polycrystalline

Cu catalysts on the basis of the C≡O stretch frequency [204].

Herein, we describe a strategy that overcomes these three challenges. We carried out time-resolved differential electrochemical mass spectrometry (DEMS) and SEIRAS on two types of rough copper electrodes during the reduction of CO. By simultaneously carrying out the two measurements on the same electrode, we were able to connect rigorously the structural information contained in the C≡O stretch spectra with the onset potentials for ethylene formation. Our key findings are as follows:

First, we examined two types of rough, SEIRAS-active electrodes: Electrochemically deposited copper films on Si-supported Au (CuAu-Si) and electrolessly deposited copper on Si (Cu-Si). The CuAu-Si film displays a $\approx 200 \pm 65$ mV more cathodic onset potential for the formation of ethylene in comparison to the Cu-Si film, which suggests that the surface morphologies of the films are distinct. It is often implicitly assumed that SEIRAS-active Cu thin films posses catalytic properties similar to those of polycrystalline Cu foils, which are routinely employed in electrolysis studies. Our finding shows that care has to be taken when comparing results from these Cu thin films with those from Cu foils.

Second, with isotope dilution experiments, we show that the lineshape of the C≡O stretch band at potentials more negative than ≈ -1.0 V versus the Ag/AgCl reference electrode is strongly dominated by the effects of dynamical dipole coupling on both types of SEIRAS-active films. Our finding demonstrates that the saturation coverage of CO_{atop} on the SEIRAS-active electrodes is sufficiently large to give rise to strong dynamical dipole coupling effects. Such effects should be thoroughly considered in the interpretation of future SEIRAS studies, because dynamical dipole coupling obscures surface-structural information contained in the C≡O stretch band.

Third, in contrast to the C≡O stretch band at potentials more negative than ≈ -1.0 V, the evolution of the lineshapes on the two types of films with increasing cathodic potential in the range of -0.6 to ≈ -1.0 V exhibits stark differences. We show that the disparate

potential-dependencies of the lineshapes can be explained with a simple Boltzmann model that considers the different binding energies of CO_{atop} on terrace and defect sites. On the basis of this model, we suggest that the different onset potentials for ethylene arise from distinct predominant surface facets on the two films. Specifically, our results indicate that (111) facets predominate on CuAu-Si films, whereas (100) facets are more ubiquitous on Cu-Si films.

Our analysis shows that the observation of the lineshape of the C≡O stretch as a function of applied potential can be utilized to gain insights into the atomic-level structure of rough metal electrodes under electrocatalytic conditions. While we applied this method to two types of SEIRAS-active copper films, it can be broadly applied to other rough metal electrodes. Therefore, the strategy established in this work could be employed to guide the development of preparation methods that yield rough metal electrodes with certain desired preferential surface facets.

4.2 Results

Choice and Characteristics of Thin Film Electrodes. Herein, we compare two distinct types of rough and SEIRAS-active thin film electrodes. The first type of copper film was electrolessly deposited on a Si attenuated total internal reflection (ATR) crystal (Cu-Si) [150, 185, 262]. The second type of copper film (≈ 8 nm thick) was electrodeposited onto a gold layer on a Si ATR crystal (CuAu-Si) [74, 263]. The detailed film preparation protocols are described in the Experimental Procedures section.

We chose to study these films because they represent the most commonly used copper thin films in SEIRAS studies. SEIRAS in an ATR configuration has become an indispensable technique for probing the electrode/electrolyte interface during CO and CO_2 reduction [81, 264]. The physical characteristics of the films enable the facile spectroscopic

interrogation of the electrode/electrolyte interface under a wide range of electrochemical conditions. However, because the films tend to peel off from the Si support and undergo surface reconstructions under extended periods of polarization, there is limited information on their catalytic properties [150, 190]. For this reason, it is often tacitly assumed that these thin polycrystalline copper films possess catalytic properties similar to those of the polycrystalline copper foils that are routinely employed in electrolysis studies. However, there is no rigorous scientific basis for this assumption. In this work, we characterize the CO reduction activity of these SEIRAS-active copper films.

The nanoscopic surface structures of the two types of films were characterized with atomic force microscopy (AFM) (Figure A4.2, Addendum). The AFM images show that Cu-Si films are composed of interconnected particles with an approximate average diameter of 80 nm. The CuAu-Si films show a similar nanoscopic structure, albeit with a smaller average particle size of about 40 nm. The roughness factor (RF) of each film under electrochemical conditions was determined by measuring the capacitance of the electric double layer (Figure A4.3, Addendum). The RF is the measured double layer capacitance of the electrode/electrolyte interface compared to that of the interface involving a smooth polycrystalline copper electrode (28 μF cm^{-2}) [216]. For Cu-Si and CuAu-Si, typical RFs are ≈ 10 and ≈ 5, respectively. The X-ray diffraction (XRD) spectra of the films show the characteristic peaks of Au, Cu, and Cu_2O (Figure A4.4, Addendum).

Onset Potentials for CO Reduction Products for Cu-Si and CuAu-Si. To connect rigorously the electrocatalytic and IR spectroscopic observations for each thin film, we simultaneously conducted DEMS and SEIRAS on the same electrode. The combined DEMS/SEIRAS setup is shown in Figure 4.1. Experiments were conducted in aqueous solutions of 0.1 M potassium phosphate at a pH of 7. Before the collection of DEMS/SEIRAS data, the Cu thin films were subjected to three potential cycles between -0.6 and -1.2 V at a scan rate of 0.01 V s^{-1}. This treatment was carried out to remove surface oxides and

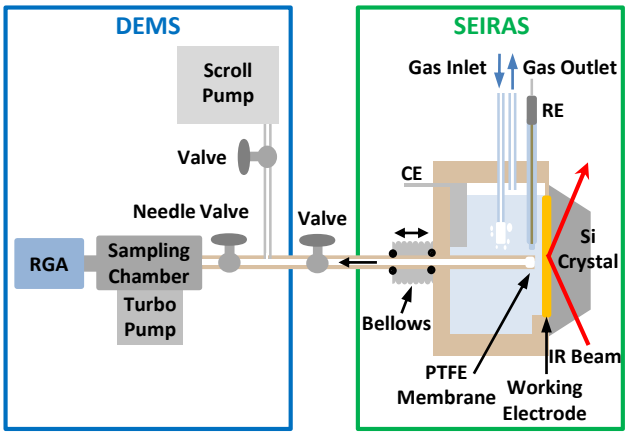

Figure 4.1: DEMS/SEIRAS setup. RGA, CE, and RE denote residual gas analyzer, counter electrode, and reference electrode, respectively. The sampling tip was inserted through a polytetrafluoroethylene (PTFE) bellows and connected to a micrometer, enabling the fine adjustment of the tip-electrode distance.

hydroxides [190, 265]. During an experiment, the electrolyte was purged with CO gas at a flow rate of 5 standard cubic centimeter per minute (sccm) and the electrode potential was scanned from -0.6 to -1.8 V at a rate of 0.001 V s^{-1}. Unless otherwise noted, all potentials herein are referenced against the Ag/AgCl electrode. During the scan, IR spectra of the interface and the mass spectra of volatile reduction products evolving from it were concurrently collected with a time resolution of a few seconds. Further experimental details are provided in the Experimental Procedures section.

Figure 4.2 shows the electrochemical current densities and partial pressures of the ions of hydrogen ($m/z = 2$), methane ($m/z = 15$), and ethylene ($m/z = 26$) for the two types of electrodes. m/z denotes the mass-to-charge ratio of the fragments detected by the mass spectrometer. To account for the differences in the electrochemically active surface areas of the two thin films, all signals in Figure 4.2 were divided by the RF of the respective electrode.

As shown in Figure 4.2B, the onset potential for H_2 evolution is ≈ -1.2 V for both types of thin films, indicating that they exhibit comparable water/proton reduction activity.

Similarly, the two films have comparable onset potentials for CH_4 evolution (≈ -1.7 V). By contrast, the onset potential for C_2H_4 is $\approx 200 \pm 65$ mV more cathodic for CuAu-Si compared to that for Cu-Si: On Cu-Si and CuAu-Si the onset potentials for C_2H_4 are ≈ -1.4 and ≈ -1.6 V, respectively. Herein, we defined the onset potential of each product as the potential at which the partial pressure of the product is 10% of that at -1.8 V. Choosing a different definition slightly affects the absolute values of the onset potentials, but has no impact on the general tends reported herein. The quoted values are based on four independent experiments for each film. The entire set of experiments is shown in Figure A4.5 of the Addendum.

We note that the absolute rates of product formation cannot be accurately determined with this DEMS setup: The partial pressures depend on the tip-electrode distance, which is difficult to precisely reproduce among independent experiments. Like in prior studies where similar setups were employed [144, 182], we therefore restrict the discussion to the onset potentials for the products. Further, our measured onset potentials are somewhat more cathodic than those reported for polycrystalline copper electrodes [215]. While these differences may arise from distinct surface morphologies, the absolute values of the determined onset potentials also depend on the time-resolution of the DEMS setup, which is a complex function of the mass transport of reduction products from the electrode surface to the detector [213]. The exact absolute value of the onset potential is not essential for the following discussion. The key observation herein is that there is a pronounced difference in the onset potentials for ethylene for Cu-Si and CuAu-Si thin film electrodes.

To ensure that the different onset potentials for ethylene are truly due to disparate properties that are intrinsic to the two thin film electrodes, we conducted the following control experiments: (1) The product selectivity for CO reduction is sensitive to the pH of the electrolyte in the vicinity of the electrode [266–268]. Because each electron transfer gives rise to the formation of a hydroxide anion, the interfacial pH may increase during electro-

catalysis [28, 148, 153, 239, 269, 270]. To test if the different onset potentials for ethylene arise from different interfacial pH conditions, we conducted DEMS experiments in aqueous solutions of potassium hydroxide at a pH of 12.85. In this electrolyte, no significant change in the interfacial pH is expected to occur during electrocatalysis. As shown in Figure A4.6 of the Addendum, the same trend in ethylene formation is observed. These results suggest that the disparate onset potentials for ethylene for the two types of films do not arise from local pH effects. (2) Exposed gold and/or the formation of a gold/copper alloy may impact the selectivity of the CO reduction reaction [271, 272]. To test if the underlying gold substrate is exposed in the CuAu-Si thin film under electrochemical conditions, we employed the C≡O stretch band of CO_{atop} as a probe of the electrochemically active surface. The center frequency of the C≡O stretch band sensitively depends on the chemical identity of the metal substrate and is therefore a suitable probe of exposed gold under electrochemical conditions [273, 274]. As shown in Figure A4.7 of the Addendum, SEIRAS does not show any evidence for exposed gold. (3) The DEMS signals for ethylene and methane are absent in Ar-purged electrolyte, demonstrating that the signals arise from the reduction of CO (Figure A4.8).

Taken together, the control experiments suggest that the difference in the onset potentials for ethylene formation on the two thin films arises from intrinsic differences in the copper surfaces. The product selectivity of the reduction of CO to hydrocarbons is sensitive to the surface structure of the electrode [126, 129, 261]. Therefore, the more cathodic ethylene onset potential for CuAu-Si compared to that for Cu-Si suggests that the two types of films possess different predominant surface facets.

Analysis of the C≡O Stretch Spectra of CO_{atop} on Cu-Si and CuAu-Si. To gain insights into the surface morphology of the two types of copper thin films, we analyzed the C≡O stretch band of CO_{atop}. The peak frequency of this band is sensitive to the coordination number of the metal atom to which CO_{atop} is bound [185, 236, 248–250,

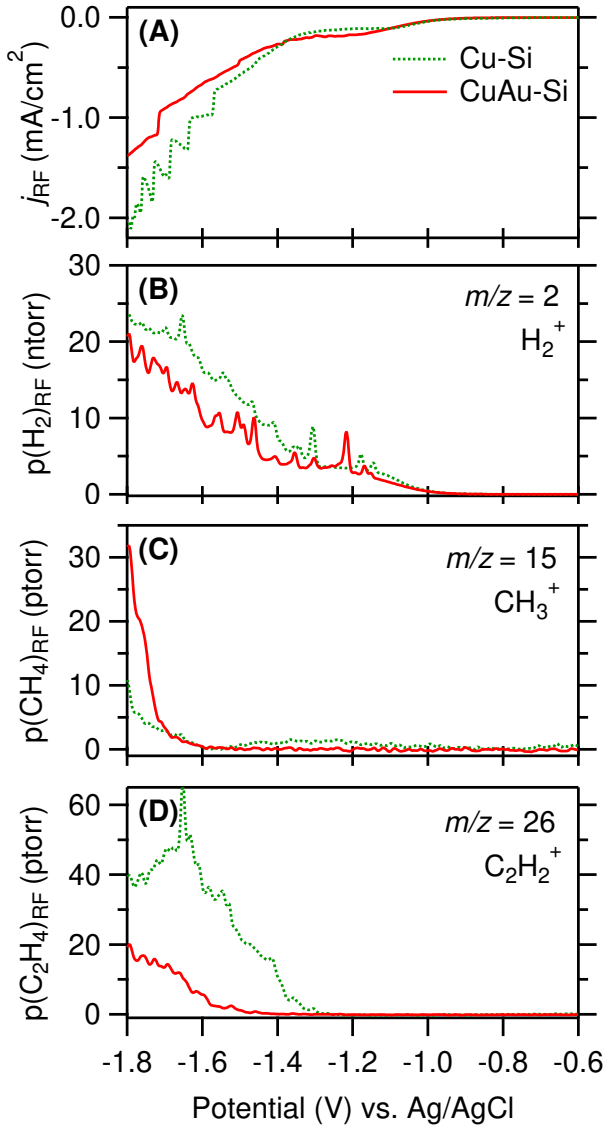

Figure 4.2: DEMS for Cu-Si and CuAu-Si in contact with CO-saturated 0.1 M potassium phosphate buffer at a pH of 7. (A) Electrochemical current densities. (B) H_2^+ ($m/z = 2$), (C) CH_3^+ ($m/z = 15$), and (D) $C_2H_2^+$ ($m/z = 26$) partial pressures. All signals in this figure were divided by the RF of the respective electrode.

252]. The adsorption of CO on late transition metals is partly controlled by the degree of hybridization of the d-band of the metal with the π^* orbital of CO [275–277]. The d-band shifts to more positive energies with decreasing coordination of the metal sites, resulting in a larger hybridization energy with the π^* orbital. Though a higher degree of hybridization weakens the intramolecular C≡O bond, it does not necessarily result in a lower C≡O stretch frequency: The C≡O stretch frequency of CO_{atop} on Cu blue-shifts with increasing strength of the surface bond (Figure A4.1, Addendum). Early theoretical studies suggested that with stronger binding, the surface bond becomes shorter and the carbon atom increasingly oscillates against the surface of the metal [278, 279]. This effect, termed the "wall effect", shifts the frequency to higher values. It has been proposed that the relative magnitude of these two opposing effects determines the overall shift [278].

Apart from the coordination number of the underlying metal atom, the peak frequency of the C≡O stretch band is also affected by "chemical effects" and dynamical dipole coupling [247, 256]. As the coverage of CO is modified, the chemical interaction of CO_{atop} with the surface changes. This change in the surface bond affects the frequency. On Cu, this "chemical effect" leads to a decrease in the C≡O stretch frequency with increasing coverage of CO_{atop} [256]. Additionally, the coupling of dynamical dipoles of CO_{atop} gives rise to new normal modes whose band frequencies and intensities are different from those of isolated CO_{atop} molecules in the absence of coupling [247]. "Chemical effects" and dynamical dipole coupling are functions of the surface coverage. We therefore monitored the lineshape as a function of cathodic potential, which changes the coverage of CO_{atop} on the electrode. Further, we conducted experiments with isotopically diluted CO mixtures, where dynamical dipole coupling is partly disrupted [247].

Figure 4.3 shows the potential-dependence of the C≡O stretch band of CO_{atop} from -0.87 to -1.05 V. Within this potential range, the most significant changes in the lineshape occur. At potentials close to the CO_{atop} saturation coverage (≈ -1.3 V), the changes in

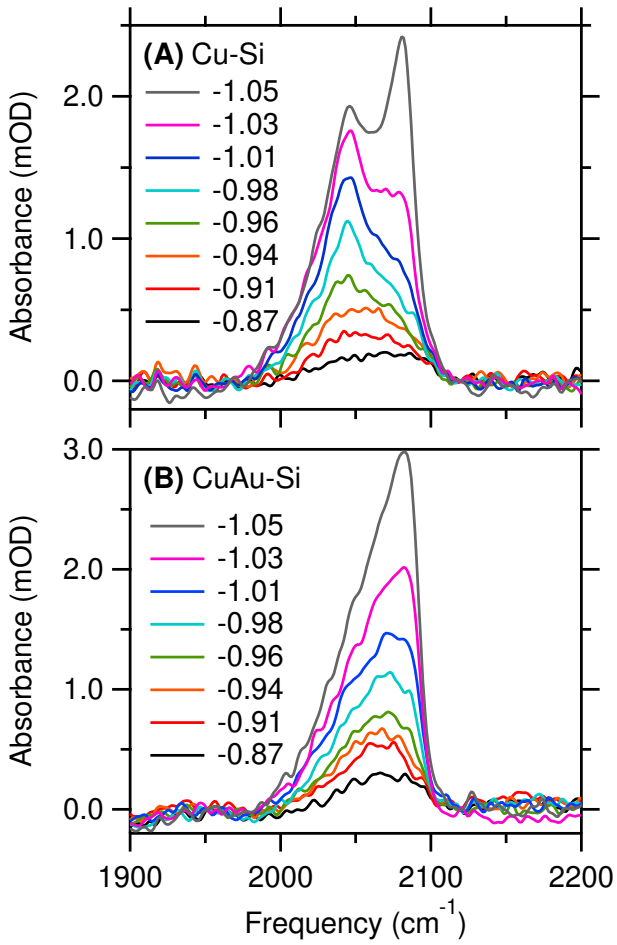

Figure 4.3: Potential-dependence of the C≡O stretch band of CO_{atop} on (A) Cu-Si and (B) CuAu-Si. The labels in the panels denote the electrode potential in volts versus the Ag/AgCl reference electrode. These spectra were concurrently collected with the DEMS data shown in Figure 4.2.

lineshape are comparatively small. The evolution of the spectra over the entire potential range is shown in Figure A4.9 of the Addendum. The change of the C≡O stretch band with potential is markedly specific to the type of the thin film: For Cu-Si, a prominent band peaked at ≈ 2045 cm^{-1} first develops before a band at ≈ 2080 cm^{-1} steeply gains amplitude with decreasing potential (Figure 4.3A). By contrast, for CuAu-Si, the band at ≈ 2080 cm^{-1} dominates at all potentials, whereas no distinct band appears at ≈ 2045 cm^{-1} at any potential (Figure 4.3B). We note that the exact peak positions of the bands depend on the applied potential. In the following, we refer to the band at ≈ 2045 cm^{-1} as the low frequency band (LFB) and the band at ≈ 2080 cm^{-1} as the high frequency band (HFB). Duplicate experiments confirm the reproducibility of the results (Figure A4.10, Addendum).

The LFB is attributable to CO_{atop} on terrace sites, whereas the HFB arises from CO_{atop} on defect sites. The peak assignments are well supported by spectroscopic studies on single crystalline copper electrodes: On the Cu(100) electrode in contact with phosphate buffer at neutral pH, the C≡O stretch band of CO_{atop} appears in the range 2040 to 2056 cm^{-1}, depending on the applied potential [280]. For example, the band is centered at a frequency of ≈ 2050 cm^{-1} at a potential of ≈ -1.0 V versus the Ag/AgCl reference electrode. This peak position is in good agreement with the LFB in our spectra (Figure 4.3A). On polycrystalline Cu, it has been suggested that Cu(100) is the predominant facet under electrochemical conditions [129, 245]. It is therefore reasonable to attribute the LFB to CO_{atop} on terrace sites. However, as discussed above, we emphasize that on the basis of the C≡O stretch frequency, it is difficult to distinguish between Cu(100) and Cu(111) terraces. We address the question of the prevalent surface facet further below and in the Discussion section.

On stepped single crystal Cu electrodes in phosphate buffer at neutral pH, the C≡O stretch band of CO_{atop} appears at $\approx 2080 \pm 7$ cm^{-1}, depending on the stepped crystal

facet and the applied potential [188]. This band was assigned to CO_{atop} on step sites on the basis of two observations [188]: (a) On Cu(111) single crystal electrodes, the C≡O stretch band of CO_{atop} was not observable. Therefore, for the n(111)-(100) single crystal electrodes, the C≡O stretch band could only originate from step sites. (b) The integrated C≡O stretch band area scaled linearly with the step-site density.

Taken together, on the basis of these prior studies of Cu single crystal electrodes under electrolyte and potential conditions similar to those employed in this study, we can confidently assign the LFB and HFB to CO_{atop} on terrace and step (defect) sites, respectively.

The coverage of CO on the electrode is dependent on the mass transport conditions at the electrocatalytic interface. The spectra in Figures 4.3 were collected in a static electrolyte to enable simultaneous product detection with DEMS (Figure 4.2). To test if the distinct potential-dependencies of the lineshapes are also observed under different mass transport conditions, we conducted additional experiments in a spectro-electrochemical cell in which the electrolyte was stirred (Figure A4.11, Addendum). During these experiments, the potential was scanned from -0.6 to -1.4 V at a rate of 0.002 V s^{-1}. As shown in Figures A4.12 and A4.13 of the Addendum, the same trends were observed. Further, for these experiments, we recorded the spectra for two consecutive cyclic voltammorgams (CV) for each film. No major differences in the lineshapes are noticeable between consecutive cycles. These results demonstrate that the distinct potential-dependencies shown in Figure 4.3 are observable over a wide range of mass transport conditions and are not due to irreversible processes at the interface (such as irreversible surface reconstructions). These control experiments suggest that at the onset potential for ethylene formation on Cu-Si (≈ -1.4 V), no irreversible surface reconstruction takes place on either of the two thin film electrodes. Although irreversible reconstructions may occur at more cathodic potentials, we can exclude those reconstructions as the origin for the different ethylene onset potentials for the two films on the basis of these experiments. Therefore, the distinct

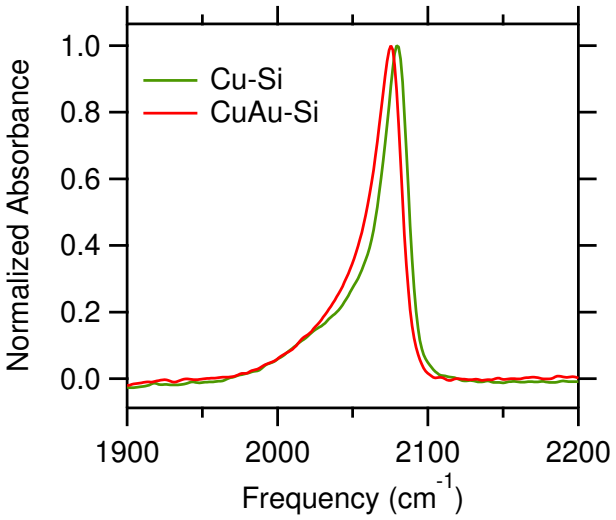

Figure 4.4: Peak-normalized C≡O stretch band of CO_{atop} on Cu-Si and CuAu-Si at a potential of -1.3 V. The peak amplitudes are 17.2 and 15.2 mOD for the spectra of CO_{atop} on Cu-Si and CuAu-Si, respectively. These spectra were concurrently collected with the DEMS data shown in Figure 4.2.

potential-dependencies of the spectra in Figure 4.3 provide insights into the origin of the different onset potentials for this product on the two types of films.

Effect of Dynamical Dipole Coupling on the C≡O Stretch Band of CO_{atop}.

Figure 4.4 shows the peak-normalized C≡O stretch bands of CO_{atop} on the two types of films at a potential of -1.3 V, that is, at a potential close to the onset for ethylene formation on Cu-Si. Comparison of the spectra reveals only minute differences: The HFB of CO_{atop} on Cu-Si exhibits a small blue shift of ≈ 5 cm^{-1} with respect to that for CuAu-Si. Further, at ≈ 2045 cm^{-1}, the LFB appears as a shoulder on the HFB in the spectrum of CO_{atop} on Cu-Si. We previously showed that the C≡O stretch band of CO_{atop} can indeed be modeled by the sum of two (skewed) Gaussian functions [185]. Fits of these Gaussian functions to the spectra are shown in Figure A4.14 of the Addendum. Given the significant difference in the onset potentials for ethylene formation, the strong similarity between the two spectra may seem surprising. However, as detailed below, dynamical dipole coupling

strongly impacts the spectra in the vicinity of this potential.

The amplitudes of the two Gaussian functions corresponding to the LFB and HFB do not necessarily reflect the relative populations of CO_{atop} on terrace and defect sites: Dynamical dipole coupling can greatly enhance the intensity of the high frequency modes at the expense of the low frequency modes of the coupled system [247, 281]. This intensity borrowing amplifies the band that predominantly arises from CO_{atop} on defect sites and attenuates that of CO_{atop} on terrace sites. The strength of dynamical dipole coupling decreases with increasing separation of the singleton frequencies of CO_{atop} (the frequencies in the absence of coupling) [247]. Therefore, $^{12}C^{16}O_{atop}$ that is primarily surrounded by $^{13}C^{18}O_{atop}$ will exhibit a lesser degree of dynamical dipole coupling with its neighbors, because the singleton frequencies of the two isotopes are separated by ≈ 100 cm^{-1}.

To assess the degree of dynamical dipole coupling within CO_{atop} adlayers on Cu-Si and CuAu-Si, we conducted SEIRAS of isotopic mixtures of CO. Figure 4.5A shows the peak-normalized C≡O stretch band of isotopically pure $^{12}C^{16}O_{atop}$ (dashed line) and that of a mixture of 10% $^{12}C^{16}O_{atop}$ and 90% $^{13}C^{18}O_{atop}$ (solid line) on Cu-Si at a potential of -1.3 V. These experiments were carried out in a two-compartment spectro-electrochemical cell under stirring of the electrolyte (Figure A4.11, Addendum). The spectrum of the isotopically pure $^{12}C^{16}O_{atop}$ adlayer exhibits the sharp HFB and the broader LFB as a shoulder. As indicated in the figure, the spectrum of the isotopic mixture shows similar bands, labeled HFB_{HI} and LFB_{HI} (the subscript stands for "heavy isotope"). Because these two features primarily arise from $^{13}C^{18}O_{atop}$, they are red-shifted by ≈ 100 cm^{-1} compared to the corresponding bands of the isotopically pure $^{12}C^{16}O_{atop}$ adlayer. Additionally, the spectrum of the isotopic mixture also contains a band centered at ≈ 2045 cm^{-1} (labeled with a star symbol, *), which primarily arises from $^{12}C^{16}O_{atop}$. Clearly, the isotopic mixture does not show a HFB due to the light isotope ($^{12}C^{16}O_{atop}$). This observation indicates that the large amplitude of the HFB in the case of isotopically pure $^{12}C^{16}O_{atop}$ is primarily

a result of intensity borrowing due to dynamical dipole coupling. Similar observations can be made for the lineshape of CO_{atop} on CuAu-Si (Figure 4.5B). Taken together, these results show that dynamical dipole coupling greatly impacts the C≡O stretch band of CO_{atop} on both types of films in a potential range that gives rise to a CO coverage at or close to saturation.

Assessment of Relative CO_{atop} Coverage on Cu-Si and CuAu-Si. We assessed the CO_{atop} coverage on the thin film electrodes. Unfortunately, it is not possible to determine the absolute CO_{atop} coverage on the films: In the case of CO adsorbed on Pt, the absolute coverage of CO is easily determined by electrostripping of the CO adlayer (oxidation of adsorbed CO to CO_2) [282]. This method is not applicable here because CO_{atop} on copper is in dynamic equilibrium with solution-phase CO [140, 150, 185]. Comparison of the integrated C≡O stretch band areas also does not necessarily provide insight into the relative coverages: The surface-enhancement factors may be significantly different between the two types of films. The accurate determination of surface-enhancement factors is a non-trivial task. Further, dynamical dipole coupling leads to deviations from Beer's law [247, 281].

Although the absolute coverage cannot be determined, the relative coverage between the two films can be estimated from the isotope dilution experiments: While dynamical dipole coupling between $^{12}C^{16}O_{atop}$ and $^{13}C^{18}O_{atop}$ is weak, it still occurs because of the broadness of the bands. Dynamical dipole coupling between CO_{atop} molecules of different isotopic composition typically leads to negligible frequency shifts but manifests itself through intensity borrowing [247]. Specifically, the degree of intensity transfer from the bands primarily due to $^{13}C^{18}O_{atop}$ (LFB_{HI} and HFB_{HI} in Figure 4.5) to the one mostly due to $^{12}C^{16}O_{atop}$ (* in Figure 4.5) increases with increasing CO_{atop} coverage. Therefore, the ratio of the peak amplitude of HFB_{HI} to that of the (*) band is a semi-quantitative measure of the CO_{atop} coverage. Because this method requires only comparison of relative

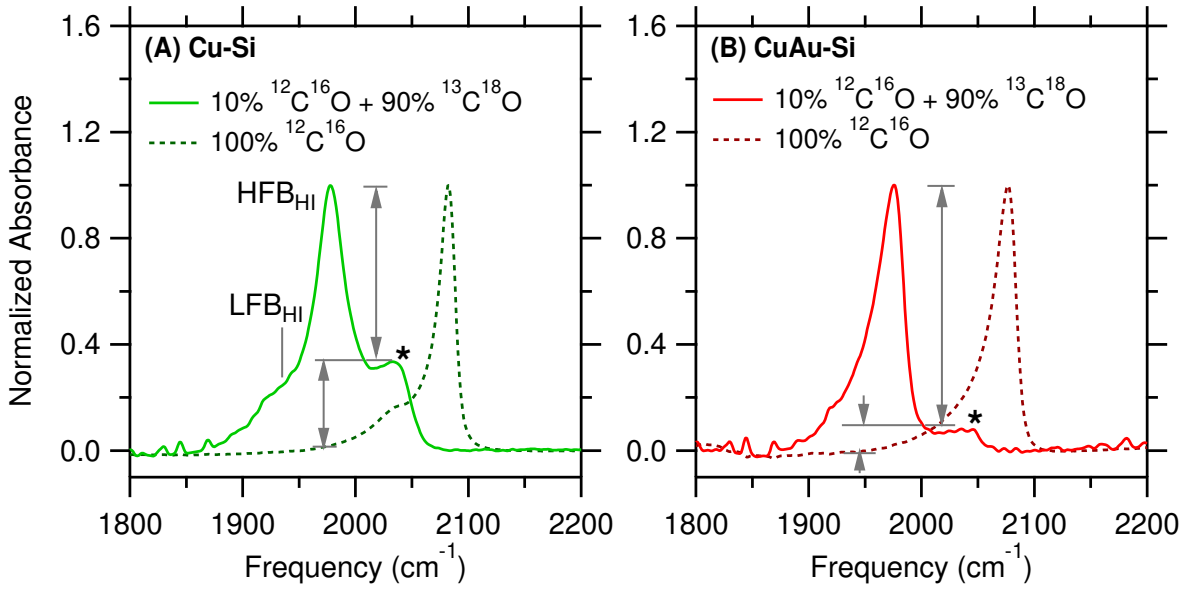

Figure 4.5: Comparison of the peak-normalized C≡O stretch bands of isotopically pure $^{12}C^{16}O$ and a mixture of 10% $^{12}C^{16}O$ and 90% $^{13}C^{18}O$ adsorbed in the atop configuration on (A) Cu-Si and (B) CuAu-Si at a potential of -1.3 V.

peak amplitudes within the same spectrum, variation of the absolute intensity of the spectra from film to film does not affect the following analysis.

Inspection of the spectrum of the isotopic mixture of CO_{atop} on Cu-Si shows that the amplitude of the band primarily associated with $^{12}C^{16}O_{atop}$ (*) is $\approx$ 30% relative to the amplitude of the HFB_{HI} (Figure 4.5A; arrows). By contrast, the corresponding band of CO_{atop} on CuAu-Si (*) has only an amplitude of $\approx$ 10% with respect to the HFB_{HI} peak maximum of the same spectrum (Figure 4.5B; arrows). This result shows that dynamical dipole coupling is stronger in the case of Cu-Si. We conclude that the saturation coverage of CO_{atop} on Cu-Si is higher in comparison to the coverage on CuAu-Si. Duplicate experiments confirm the reproducibility of the isotope dilution experiments (Figure A4.15, Addendum).

Cyclic Voltammetric Characterization of the Surface Facets of Cu-Si and CuAu-Si. The mass spectrometric and spectroscopic data suggest that the two types of films

posses distinct predominant crystallographic surface facets. To characterize further the surface facets, we employed cyclic voltammetry (CV). In the CVs of copper single crystals in contact with basic electrolyte, the adsorption and desorption of hydroxide give rise to voltammetric waves whose peak potentials are specific to a certain crystallographic facet [283–286].

Figures 4.6A and B respectively show the CVs of Cu(100) and Cu(111) single crystals in contact with Ar-saturated aqueous solutions of 0.1 M KOH. The CVs are not centered around zero on the current density axis because of residual oxygen in the electrolyte [284]. For comparison with prior studies, the potentials in Figure 4.6 are referenced against the reversible hydrogen electrode (RHE). The peaks in the underpotential region of Cu_2O formation (-0.25 to 0.2 V) are attributable to the adsorption and desorption of hydroxide. The observed peak potentials for the adsorption/desorption of hydroxide are clearly distinct for the two surface facets. Additionally, the magnitude of the oxidation/reduction current density at potentials > 0.3 V is smaller for Cu(111) than for Cu(100). These observations are in good agreement with prior reports [283–286]. Taken together, these features characterize the Cu(111) and Cu(100) surface facets.

Figures 4.6C and D respectively show the CVs of the Cu-Si and CuAu-Si electrodes. The cathodic scan of the CV for Cu-Si displays a peak at -0.17 V (labeled with a star symbol, *), consistent with the potential of the hydroxide desorption peak for the Cu(100) single crystal. By contrast, the CV for CuAu-Si shows a peak at $+0.07$ V (*) during the anodic scan. This peak falls within the potential range of the hydroxide adsorption peaks for Cu(111). The peaks are not observable on the respective reverse scans, likely because of the sloping baselines and the small amplitudes of these features. At potentials > 0.3 V, the Cu surface is oxidized to Cu_2O. In that region, the shape of the CV for Cu-Si bears a resemblance to that for Cu(100), whereas the shape of the CV for CuAu-Si in that same region is more similar to that for Cu(111).

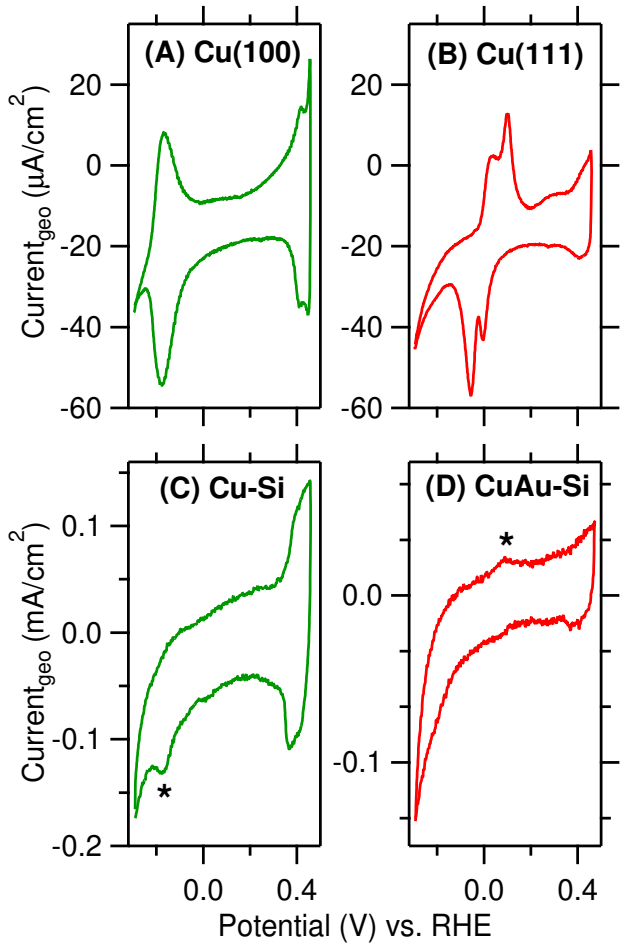

Figure 4.6: CVs for (A) Cu(100), (B) Cu(111), (C) Cu-Si, and (D) CuAu-Si. The CVs were collected in Ar-saturated 0.1 M KOH at a scan rate of 0.05 V s^{-1}. The panels show the geometric current densities.

The CV data suggest that the predominant surface facet on Cu-Si is Cu(100). This conclusion is further supported by prior reports, which showed that the electrocatalytic properties of polycrystalline Cu electrodes are similar to those of Cu(100) [287]. Further, electrochemical STEM studies revealed that Cu(100) is a stable facet on polycrystalline Cu under electrocatalytic conditions [245]. By contrast, the CV data indicate that the major facet on CuAu-Si is Cu(111). The predominance of the Cu(111) surface facet on CuAu-Si is likely a result of semi-epitaxial growth of the Cu layer on the Au substrate. As shown in Figure A4.16 of the Addendum, the CV of the electrolessly deposited Au film electrode resembles that of a Au(111) electrode [288]. This finding is consistent with prior studies, which found that the electroless deposition of Au on Si results in films that preferentially expose their (111) facet [288]. Epitaxial growth of Cu(111) with a thickness of $\approx$ 30 nm on Au(111) has been demonstrated for core-shell nanoparticles [289]. Therefore, it is probable that the preferential (111) orientation of the electrochemically deposited Cu layer ($\approx$ 8 nm thick) of the CuAu-Si films arises from its semi-epitaxial growth on the Au(111) substrate. Possible interfacial Cu/Au alloying and surface reconstruction are considered in the Discussion section. In summary, the CV characterization indicates that Cu(100) is the major facet on Cu-Si, whereas Cu(111) is predominant on CuAu-Si.

The *in situ* characterization of the electrode surfaces with the CV method requires alkaline electrolyte. Cu electrodes may undergo reconstruction under alkaline conditions [245]. However, our mass spectrometric control experiments show that the distinct selectivity of Cu-Si and CuAu-Si for ethylene is also observed under alkaline conditions (Figure A4.6, Addendum). Further, the distinct potential-dependence of the C$\equiv$O stretch spectrum of CO_{atop} is also observed at high pH (Figure A4.17, Addendum). On the basis of these control experiments, we conclude that the information on the surface characterization obtained at high pH can be employed for the interpretation of the experiments conducted at neutral pH.

4.3 Discussion

The CV characterization suggests that the Cu-Si surface consists mostly of (100) facets, whereas the CuAu-Si surface exhibits mainly (111) facets. On the basis of this result, we can rationalize the potential-dependence of the spectra. The following analysis is based on a simple framework in which we consider only two types of surface sites with different binding affinities for CO_{atop}. Of course, on the polycrystalline electrode, there are many different types of surface sites (edges, kinks, various terraces) that give rise to a distribution of CO_{atop} binding energies. However, this added complexity does not affect the core of our argument. Further, the assumption is justified because the lineshape of the C≡O stretch band at saturation coverage can be modeled by the sum of two Gaussian functions, one representing CO_{atop} on terrace sites, the other CO_{atop} on defect sites (Figure A4.14, Addendum).

The relative occupancy of CO_{atop} on defect and terrace sites is governed by the Boltzmann equation:

$$\frac{N_{\text{defect}}}{N_{\text{terrace}}} = \frac{g_{\text{defect}}}{g_{\text{terrace}}} \exp\left(+\frac{\Delta E}{kT}\right), \tag{4.1}$$

where g_{defect} and g_{terrace} are the degeneracies of the two types of sites, k is the Boltzmann constant, and T the absolute temperature. $\Delta E = E_{\text{defect}} - E_{\text{terrace}} > 0$ is the difference between the binding energies of CO_{atop} on defect and terrace sites (Herein, we define the binding energies as positive quantities). From eq. (4.1), it is clear that the relative occupancy is determined by two factors: The relative abundance of defect to terrace sites, $\frac{g_{\text{defect}}}{g_{\text{terrace}}}$, and the difference in the CO_{atop} binding energy between the two types of sites, ΔE.

We first consider the possibility that the ratio $\frac{g_{\text{defect}}}{g_{\text{terrace}}}$ could be significantly different

for the two types of films. Specifically, the C≡O stretch spectrum of CO_{atop} on CuAu-Si at potentials > -1.0 V may be a result of a higher density of defect sites on that film in comparison to Cu-Si, that is, the ratio $\frac{g_{\text{defect}}}{g_{\text{terrace}}}$ in eq. (4.1) may be higher. If CuAu-Si had a substantially higher density of defect sites and an otherwise similar composition of surface facets, a higher CO_{atop} saturation coverage would be observed (relative to that on Cu-Si, because defect sites bind CO_{atop} more strongly). However, the isotope dilution experiments show that the opposite is the case (Figure 4.5). On the basis of these data, it is unlikely that CuAu-Si possesses a significantly higher defect site density compared to Cu-Si. Therefore, the distinct potential-dependencies of the C≡O stretch spectra on the two types of films likely arise from differences in the exponential term in eq. (4.1) rather than from different values of $\frac{g_{\text{defect}}}{g_{\text{terrace}}}$.

By considering the differences in the exponential term in eq. (4.1), we can understand why the lineshapes of the C≡O stretch exhibit starkly different potential-dependencies for the two types of films. As described in the Results section, the CV characterization indicates that on CuAu-Si, Cu(111) facets predominate, whereas Cu(100) facets prevail on Cu-Si. The experimental energies for the desorption of CO_{atop} from Cu(111) and Cu(100) are 0.49 and 0.53 eV, respectively [204]. DFT calculations predict the same trend for the CO_{atop} binding energies, though the predicted energy difference is about twice as large [260]. On both films, we assume that the binding energy of CO_{atop} on defect sites is 0.60 eV, the experimentally determined desorption energy of CO_{atop} from polycrystalline copper surfaces as determined by temperature programmed desorption [204]. This assumption is justified because this value is similar to that observed for CO_{atop} desorption from step edges on Cu(211) [204].

On the basis of these values, ΔE in eq. (4.1) is smaller for Cu-Si than for CuAu-Si. As a result, according to eq. (4.1), the probability for CO to occupy a terrace site is about five times higher on Cu-Si than that on CuAu-Si at room temperature. This population of

CO_{atop} on (100) terrace sites manifests itself in the IR spectrum as the C≡O stretch band at 2045 cm^{-1}, which dominates the spectrum at potentials > -1.0 V (Figure 4.3A). Once a certain threshold coverage has been reached, dynamical dipole coupling amplifies the band associated with CO_{atop} on defect sites, producing the marked change in lineshape around -1.0 V. By contrast, on CuAu-Si, the large difference in binding energies between (111) terrace and defect sites prevents the buildup of a significant population of CO_{atop} on terrace sites. As a result, even at relatively anodic potentials, the band exhibits a higher peak frequency due to the binding of CO to defect sites (Figure 4.3B). Figure 4.7 summarizes this analysis.

The model provides a simple explanation for the disparate evolution of the C≡O stretch spectrum on the two film types. Importantly, the analysis establishes the potential-dependence of the C≡O stretch band of CO_{atop} as a suitable probe of the atomic-level surface morphology of rough electrodes. As discussed above, the peak frequency of the C≡O stretch band is often a complex function of coupling effects and the applied potential. Because our analysis presented here focuses on general trends of the lineshape rather than exact numerical values, we expect this method to be more robust and versatile than an analysis that solely focuses on peak frequencies.

Taken as a whole, the CV characterization and the spectroscopic data indicate that (100) terraces are prevalent on Cu-Si, whereas (111) terraces are more ubiquitous on CuAu-Si. This finding is consistent with our DEMS results that show that the onset potential for ethylene is $\approx 200 \pm 65$ mV more cathodic for CuAu-Si compared to that for Cu-Si: In prior studies, DEMS on single crystalline copper electrodes in phosphate buffer at a pH of 7 showed that the onset potential for ethylene formation on Cu(111) is about 200 mV more cathodic than that on Cu(100) [129, 261, 266]. This trend does not only hold for Cu(111) and Cu(100), but it is more general. Single crystals on which the (111) facet predominates exhibit more cathodic onset potentials for ethylene formation than crystals

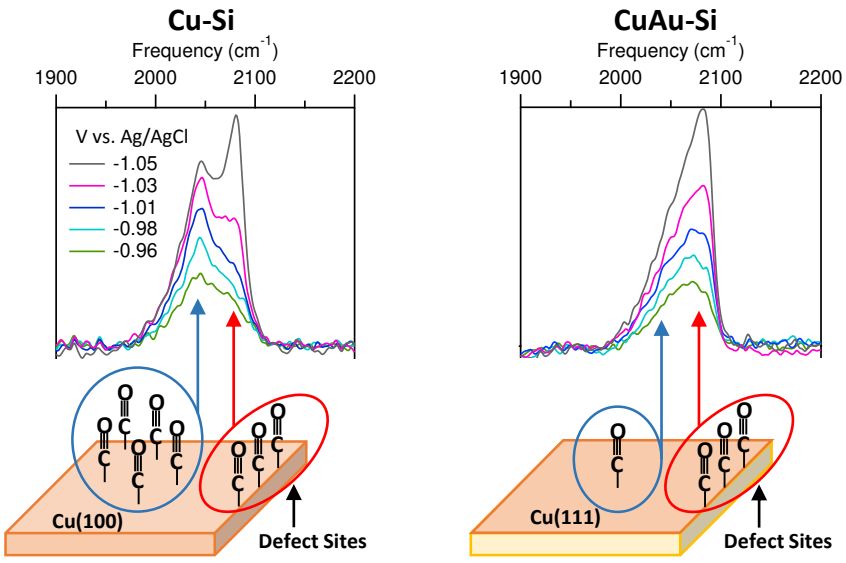

Figure 4.7: Cartoon summarizing the key findings. Cu-Si (Left): Because the difference in CO_{atop} binding energy between (100) terrace and defect sites is relatively small, a significant CO_{atop} population develops on the terraces. This CO population gives rise to the band at 2045 cm^{-1}. CuAu-Si (Right): The difference in CO_{atop} adsorption energy between (111) terrace and defect sites is comparatively large for CuAu-Si. As a result, the CO_{atop} population on terraces remains small, preventing the development of a distinct band at 2045 cm^{-1}.

on which the (100) facet is more abundant [261]. Similarly, the F.E. for ethylene during the reduction of CO_2 in 0.1 M $KHCO_3$ on Cu(111) electrodes is about five times lower than that on Cu(100) [126].

Consideration of Alternative Explanations. The relatively high C≡O stretch frequency on CuAu-Si at potentials > -1.0 V could also arise from the formation of CO islands, that is, a non-uniform distribution of CO on the surface. Such island formation would enable dynamical dipole coupling even at low absolute coverage. Islands of CO were observed on single crystalline Pt electrodes when the coverage was lowered from saturation by partial oxidation of the CO adlayer [282]. Spatially non-uniform oxidation of the CO adlayer then results in patches of CO on the electrode. In the case of CO_{atop} on Cu-Si, island formation is unlikely: DFT calculations and experiment work showed that the interaction between neighboring CO molecules is highly repulsive [257, 290]. Unlike

in the case of Pt, CO_{atop} is reversibly bound to copper and in dynamic equilibrium with solution-phase CO [140, 150, 185]. Therefore, CO_{atop} island formation on Cu is less likely than on Pt electrodes.

To confirm this notion, we monitored the potential-dependence of the C≡O stretch band of the light isotope in a mixture of 50% $^{12}C^{16}O_{atop}$ and 50% $^{13}C^{18}O_{atop}$. In this mixture, we can observe the band of the light isotope at potentials > -1.0 V. As shown in Figure A4.18 of the Addendum, at a potential of -0.93 V, isotopic dilution has essentially no effect on the peak frequency of the band arising from $^{12}C^{16}O_{atop}$. This experiment confirms that the comparatively high frequency of this band at potentials > -1.0 V is mostly due to adsorption of CO on defect sites. Dynamical dipole coupling does not make a major contribution at these relatively anodic potentials.

We note that in a recent study on the mass transport effects of CO on the spectrum of CO_{atop}, Malkani *et al.* concluded that CO adsorbs on Cu in islands [291]. The spectra of Malkani *et al.* exhibit different lineshapes in comparison to ours. This observation indicates that their film morphology is different from those of our films. Further, they conducted their work at a more cathodic potential (-0.6 V versus RHE). It is entirely possible that CO island formation occurs on their electrodes and experimental conditions, whereas it does not in our experiments. Therefore, our findings do not contradict their conclusions. The possibility that the formation of CO_{atop} islands on Cu could be potential-dependent is intriguing and warrants further investigation.

The isotope dilution experiments presented here show that dynamical dipole coupling strongly influences the lineshape at potentials more cathodic than ≈ -1.0 V. However, it is not the sole contributing factor. In an earlier publication [185], we presented evidence that a CO-induced, reversible surface reconstruction process also contributes to the change in lineshape with decreasing potential. For example, the concurrent enhancement of the metal-adsorbate bands and the HFB in the surface-enhanced Raman spectra reported in

that work cannot be explained with a dynamical dipole coupling picture, but is consistent with an adsorbate-induced reconstruction process. While such a reconstruction process adds complexity to the picture, it does not impact the qualitative aspects of the model presented herein.

Recently, it was suggested that co-adsorbed hydroxide on Cu electrodes lowers the C≡O stretch frequency and influences the binding energy of adsorbed CO [265, 292]. Specifically, Iijima *et al.* showed that the lineshape of the C≡O stretch mode of CO_{atop} on Cu electrodes is profoundly dependent on the number of CVs (-0.13 and -0.7 V) that are performed as a pre-treatment prior to spectroscopic measurements [265]. With an increasing number of CVs (from zero to 15), they observed an increase in the C≡O stretch frequency. They attributed this observation to a decrease in the coverage of hydroxide with increasing number of CV pre-treatments.

In our experiments, we pre-treated each electrode with five cleaning CVs between -0.13 and -0.7 V, followed by three CVs with turning potentials of -0.6 and -1.2 V prior to the collection of SEIRAS/DEMS data (see Experimental Procedures Section for details). Following these steps, we ensured that the electrode was never returned to oxidizing potentials until the end of the experiment. The following observations suggest that this protocol is effective in minimizing the impact of hydroxide on the C≡O stretch spectrum: First, to test if the spectra are sensitive to the number of CV pre-treatments, we collected additional SEIRAS data in which we increased the number of cleaning CVs (-0.13 and -0.7 V) from 5 to 15. All other steps of the protocol were left unchanged. Iijima *et al.* suggested that this treatment minimizes the amount of hydroxide on the surface [265]. As shown in Figure A4.19 of the Addendum, the potential-dependencies of the spectra shown in Figure 4.3 (5 CV pre-treatments) are also observed after 15 CV pre-treatments. Second, to probe if the spectra change with an increase in the bulk hydroxide concentration, we carried out SEIRAS on the two films in contact with 0.1 M phosphate buffer at a pH of 12.

As shown in Figure A4.17 of the Addendum, we observed similar potential-dependencies of the spectra as reported in Figure 4.3. This finding shows that an increase of the bulk hydroxide concentration by five orders of magnitude does not significantly impact the lineshape. Third, the changes in lineshape with potential are reversible on both types of films and are also observed during consecutive CV cycles (Figures A4.12 and A4.13, Addendum). Fourth, from the hydroxide desorption waves in the CVs in Figure 4.6, the hydroxide desorption potentials for Cu(100) and Cu(111) are -0.78 and -0.67 V vs. Ag/AgCl at neutral pH, respectively. Because we examined the potential-dependence of the spectra at more negative potentials, the amount of hydroxide on the surface is expected to be minimal.

Taken together, these observations suggest that the impact of hydroxide on the lineshape of the C≡O stretch band of CO_{atop} on Cu is minimal under our experimental conditions. However, it is possible that co-adsorbed hydroxide is a small contributing factor. Indeed, a possible contribution of hydroxide would be consistent with our conclusion that on Cu-Si, the major surface facet is (100). As shown in Figure 4.6, the desorption potential of hydroxide is ≈ 0.1 V more cathodic for Cu(100) compared to that for Cu(111). Therefore, the appearance of the LFB band on Cu-Si may be in part because of co-adsorbed hydroxide, but this effect is expected to be small on the bases of the observations discussed in the preceding paragraph.

Different coverages of bridge-bonded CO (CO_{bridge}, referring to adsorbed CO interacting with two or three Cu surface atoms) on Cu-Si and CuAu-Si could influence the onset potential of ethylene. Recent studies showed that CO_{bridge} on Cu electrodes is an electrochemically inactive species under CORR/CO_2RR conditions [84, 190]. For the data presented herein, the amplitude of the band of CO_{bridge} was close to the detection limit on both types of films during the cathodic forward scans under neutral pH conditions, suggesting that CO_{bridge} does not give rise to the different catalytic activities of the films.

Lastly, we consider the possibility that the Cu overlayer may be affected by strain and ligand effects [121, 293, 294]. Our CV characterization of CuAu-Si suggests that the surface is of Cu(111) character (Figure 4.6). Indeed, pseudomorphic Cu overlayers on Au(111) substrates have been imaged with electrochemical STM [295]. However, overlayers of Cu on Au have a tendency to coalesce into islands and to form interfacial Cu/Au alloys under cathodic polarization [251, 295, 296]. Although our SEIRAS control experiments did not reveal the presence of Au on the surface (Figure A4.7, Addendum), the amount of Au at the surface may be below the detection limit of the method. Because Cu/Au alloys bind CO less strongly than pure Cu [251, 297], the incorporation of Au into Cu terraces of the CuAu-Si films is an alternative explanation for the absence of a distinct LFB on that electrode.

Semi-epitaxial growth of Cu on Au(111) and any strain or ligand effects are expected to be limited to thin overlayers. Indeed, for CuAu-Si electrode with a 16 nm thick Cu overlayer, the potential-dependence of the C≡O stretch band resembles that observed for Cu-Si (Figure A4.20, Addendum), suggesting the CuAu-Si system as a convenient SEIRAS platform to study the impact of Cu overlayer thickness on catalyst selectivity.

4.4 Conclusions

We showed that the two most commonly used methods for the deposition of SEIRAS-active copper films on Si result in electrode surfaces that exhibit greatly different catalytic activities towards the reduction of CO to ethylene: Films produced by the electrochemical deposition of copper on Si-supported Au thin films (CuAu-Si) display a $\approx 200 \pm 65$ mV more cathodic onset potential for the formation of ethylene compared to that of Cu thin films that are electrolessly deposited on the Si support (Cu-Si).

Despite the great difference in CO reduction activity, in the vicinity of the potential of

CO_{atop} saturation coverage (-1.3 V), the C≡O stretch bands of CO_{atop} on CuAu-Si and Cu-Si are remarkably similar. SEIRAS of isotopically diluted mixture of CO_{atop} show that the C≡O stretch lineshape at the saturation coverage is profoundly influenced by dynamical dipole coupling on both films. However, the degree of dynamical dipole coupling on CuAu-Si is lower than in the case of Cu-Si, suggesting a higher CO_{atop} surface coverage on the latter film. Further, the potential-dependence of the lineshape of the C≡O stretch band at potentials > -1.0 V is remarkably different for the two thin films. We rationalize the potential-dependence of the spectra with a Boltzmann model that considers the difference in CO adsorption energy on defect sites and the sites of the prevalent crystallographic surface facet. On the basis of this model, we conclude that the major surface facet on Cu-Si binds CO more strongly than that on CuAu-Si. Based on our CV characterization of the electrodes and our electrocatalytic results, we suggest that the prevalent crystallographic facet on CuAu-Si is (111), whereas that on Cu-Si is (100). Our study highlights the complexities involved in the interpretation of the C≡O stretch band of CO_{atop} on polycrystalline copper electrodes. Further, our work shows that the analysis of the potential-dependence of the C≡O stretch lineshape can reveal differences in the surface structure of electrocatalysts under electrocatalytic conditions. This strategy could be employed to guide the design of rough electrodes with certain desired surface facets.

4.5 Experimental Procedures

Materials. Chemicals for Cu or Au thin film deposition on Si: NH_4F (40 wt.% in H_2O), HF (48 wt.%), $NaAuCl_4 \cdot 2H_2O$ (99.99%; metals basis), Na_2SO_3 (98.5%; for analysis, anhydrous), $Na_2S_2O_3 \cdot 2H_2O$ (99.999%; trace metal basis), and NH_4Cl (99.999%; metal basis) were purchased from Fisher Scientific (Waltham, MA). $CuSO_4 \cdot 5H_2O$ (99.999%; trace metal basis), EDTA-Na_2 ($99.0 - 101.0\%$; ACS Reagent), 2,2-bipyridine ($\geq$ 99%;

ReagentPlus), HCHO (35 wt.%; 10% methanol as stabilizer), and NaOH (99.99%; trace metals basis) were acquired from Sigma Aldrich (St. Louis, MO). Polycrystalline diamond pastes and alumina slurry were procured from Ted Pella (Redding, CA) or Electron Microscopy Sciences (Hartfield, PA).

Chemicals for electrochemical measurements: (KH_2PO_3, $\geq$ 99.995%, TraceSELECT, metals basis; K_2HPO_3, $\geq$ 99.999%, TraceSELECT, metals basis; KOH, 99.99%, trace metals basis, Sigma Aldrich). High-purity water for electrolyte preparation was derived from a Barnstead Nanopure Diamond system.

Ar (ultra high purity), N_2 (ultra high purity), and CO (99.999%) were obtained from Air Gas (Radnor, PA). Doubly labeled $^{13}C^{18}O$ (99 atom % ^{13}C, 95 atom % ^{18}O) was purchased from Sigma Aldrich.

Cu(100) and Cu(111) single crystals ($5 \times 5 \times 1$ mm) were purchased from MTI Corporation (Richmond, CA).

Cu-Si Film Deposition. Thin polycrystalline Cu-Si films were deposited in an electroless manner on the reflecting surface of a 60° Si prism (Pike Technologies; Madison, WI) as previously described [31]. The thin Cu films had a resistance of $3 - 5\ \Omega$.

CuAu-Si Film Deposition. Thin polycrystalline Au films were first deposited in an electroless manner on the reflecting surface of a 60° Si prism (Pike Technologies; Madison, WI) according to established procedures [74, 263]. The Si crystal was cleaned with aqua regia solution to remove Au residue prior to each deposition. To prepare the Si crystal surface, it was successively polished with 6 and 1 μm diamond pastes and 1 μm alumina slurry on a polishing pad. Then, the crystal was rinsed under high-purity water and sonicated in water or acetone alternately for 5 times. For deposition, the Si crystal was first etched in 40 % NH_4F for 90 s to remove surface oxides and to terminate the surface with hydrogen. A gold nanofilm was plated by immersing the Si crystal in a 2 : 1 mixture of a plating solution and 2% HF at 60°C for 120 s. The plating solution contained 15 mM

$NaAuCl_4 \cdot 2H_2O$, 150 mM Na_2SO_3, 50 mM $Na_2S_2O_3 \cdot 2H_2O$, and 50 mM NH_4Cl. To improve Au film adhesion to the Si crystal, the deposited Au film was removed by placing a few drops of aqua regia on the film [288]. Then, the Si crystal was thoroughly washed with high-purity water and dried with ultra high-purity nitrogen. On this Si crystal, a second gold nanofilm was plated by immersing the crystal in the plating solution as described above. Removal and re-deposition of the Au film was repeated until a homogeneous film was obtained. Typically, the second or third re-deposition yielded a stable gold nanofilm on the Si crystal. The deposited Au thin films had a resistance of $8 - 10\ \Omega$.

The Au film was cleaned with five CVs in 0.1 M H_2SO_4 solution from 0 to 1.5 V at a scan rate of 0.05 V s^{-1} under 5 sccm Ar purging. Then, the Cu electrodeposition was carried out with an addition of 5.75 mM $CuSO_4$ to the solution. The film was held at a potential of -0.2 V until the desired amount of charge ($\approx$ 40 mC) was passed. The thickness of the film was calculated according to: $t_{\mathrm{Cu}} = \frac{Q_{\mathrm{Cu}} \cdot m_{\mathrm{Cu}}}{zFA\rho}$, where Q_{Cu}, $\mathrm{m_{Cu}}$, z, F, A, and ρ represent the total charge during deposition, Cu atomic mass, electrons needed per Cu atom deposition, Faraday constant, deposition area, and Cu film density, respectively. The CuAu-Si film was then rinsed with high-purity water.

Pre-treatment of Cu-Si and CuAu-Si Films Prior to DEMS and SEIRAS Experiments. Prior to the collection of DEMS and SEIRAS data, Cu-Si and CuAu-Si were pre-treated according to the following protocol: With the cell at open circuit, the electrolyte was purged with Ar for 20 minutes at a rate of 5 sccm. The electrode was then treated with five CVs from -0.13 to -0.7 V vs. Ag/AgCl at a scan rate of 0.05 V s^{-1} followed by the RF determination. To determine the RF of the film, the capacitance of the electrochemical double layer in Ar saturated electrolyte (Figure A4.3, Addendum) was measured as previously described [31]. Immediately after this step, Cu film was subjected to three CVs from -0.6 to -1.2 V at a 0.01 V s^{-1} scan rate. Following this step, the Cu electrode was never returned to oxidizing potentials until the end of the DEMS/SEIRAS

experiments. After completion of the CVs, potential was held at -0.6 V in the 0.1 M phosphate buffer electrolytes and at -0.8 V in 0.1 M KOH for 20 min while CO was purged at a rate of 5 sccm.

DEMS/SEIRAS Measurements. The components of the DEMS setup were described previously [31]. The DEMS setup in this work only differed in the configuration and positioning mechanism of the sampling tip within the spectro-electrochemical cell (Figure 4.1). The sampling tip was positioned ≈ 100 μm above the electrode surface. A single compartment spectro-electrochemical cell was used as shown in Figure 4.1. The catholyte volume was 6 mL. Prior to each experiment, the cell was cleaned for 1 h in an acid solution (30 wt.% H_2SO_4, 30 wt.% HNO_3) and afterwards sonicated for 1 h in Nanopure water. A Ag/AgCl (RE-5B, 3 M NaCl; BASi Inc.; West Lafayette, IN) and a Pt foil (Premion 99.99%, 0.025 mm; Alfa Aesar) were utilized as the reference and counter electrodes, respectively. The Ag/AgCl reference electrode was regularly checked against a saturated calomel electrode (CHI 150; CH Instruments Inc.; Austin, TX). The spectroscopic methods were described previously [31]. Following the pre-treatment steps described above, the DEMS/SEIRAS experiments were conducted. For the combined DEMS/SEIRAS experiments in 0.1 M phosphate buffer, the potential was scanned from -0.6 to -1.8 V at a rate of 0.001 V s^{-1}. In 0.1 M KOH, the potential was scanned from -0.8 to -1.8 V at the same rate.

Isotope Dilution Measurements. Isotope dilution experiments were carried out with gas mixtures of either 90% $^{13}C^{18}O$ + 10% $^{12}C^{16}O$ or 50% $^{13}C^{18}O$ + 50% $^{12}C^{16}O$. The electrolyte was purged with 4.5 sccm of $^{13}C^{18}O$ and 0.5 sccm of $^{12}C^{16}O$ to produce a 90% : 10% mixture. To obtain the 50% : 50% mixture both $^{13}C^{18}O$ and $^{12}C^{16}O$ were purged at a rate of 2.5 sccm. Then, the potential was scanned from -0.6 to -1.4 V at a rate of 0.002 V s^{-1} in CO-saturated electrolyte while SEIRAS spectra were collected. These experiments were carried out in the spectro-electrochemical cell shown in Figure A4.11 of

the Addendum under stirring of the electrolyte.

Cyclic Voltammetric Characterization of Cu Surfaces. The backsides of the Cu(100) and Cu(111) single crystals were covered with epoxy. Prior to CV characterization, the single crystal electrodes were cleaned electrochemically in an acid solution of H_3PO_4:H_2SO_4:H_2O = $10:5:2$. A potential of 2.3 V vs. Cu was applied for 2 s followed by 30 s at open circuit potential and another 2 s at 2.3 V. The electrodes were then thoroughly rinsed with high-purity water before they were immersed in an Ar saturated 0.1 M KOH solution. CVs of Cu(100) and Cu(111) were collected in a single compartment cell while the electrolyte was purged with Ar gas at a rate of 5 sccm. The electrolyte was stirred. Ten CV cycles were collected from -0.3 to 0.45 V vs. RHE at a 0.05 V s^{-1} scan rate and the 10^{th} cycle is shown in Figure 4.6. CVs of the Cu-Si and CuAu-Si films were collected in Ar saturated 0.1 M KOH in the cell shown in Figure A4.11 of Addendum under stirring of the electrolyte. The Cu-Si and CuAu-Si films were pre-treated by applying five CVs with turning potentials of -0.13 and -0.7 V at a scan rate of 0.05 V s^{-1}. This step was followed by capacitance measurements to determined the RF of each film (Figure A4.3, Addendum). Then, 10 CVs were collected from -0.3 to 0.45 V versus RHE at a 0.05 V s^{-1} scan rate while Ar was purged at a rate of 5 sccm. The 10^{th} cycle is shown in Figure 4.6. Similar CV shapes as those shown in Figure 4.6 were also observed in the other cycles.

4.6 Addendum

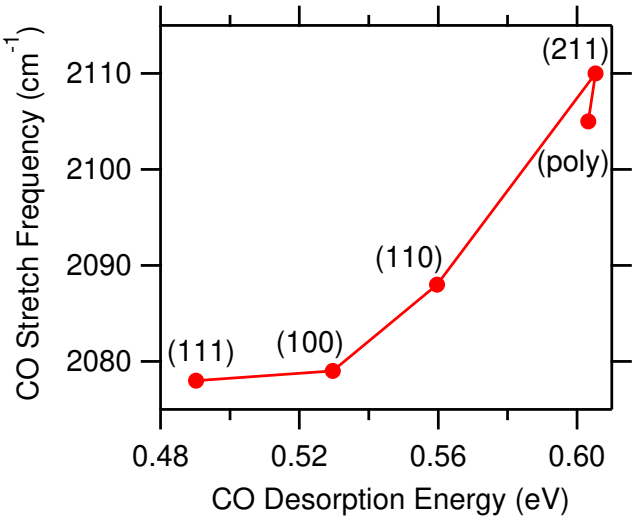

Figure A 4.1: Dependence of the C≡O stretch frequency on the CO_{atop} desorption energy on different Cu surfaces. The frequencies and desorption energies were taken from Hollins *et al.* [247] and Vollmer *et al.* [204], respectively. Both measurements were carried out at low CO coverage, where coupling effects are weak and the C≡O stretch frequency is most representative of the adsorption site [247, 259].

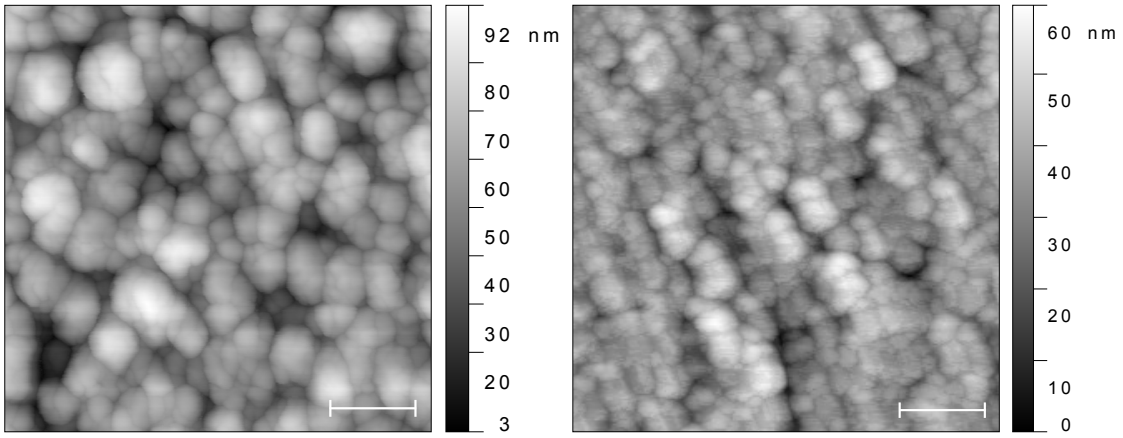

Figure A 4.2: AFM images of Cu-Si (left) and CuAu-Si (right). The scale bar is 200 nm. Images were acquired in a 1×1 μm^2 area with a Si cantilever (Nanosensors; Neuchatel, Switzerland; PPP-NCHR 10 M, 7 nm tip radius, 330 kHz resonance frequency, and 42 N m^{-1} spring constant) at a 0.5 Hz scan rate in non-contact mode on a Park XE-100 AFM system (Park Americas; Santa Clara, CA). The left figure is reproduced with permission from Gunathunge *et al.* [190] Copyright 2018, American Chemical Society.

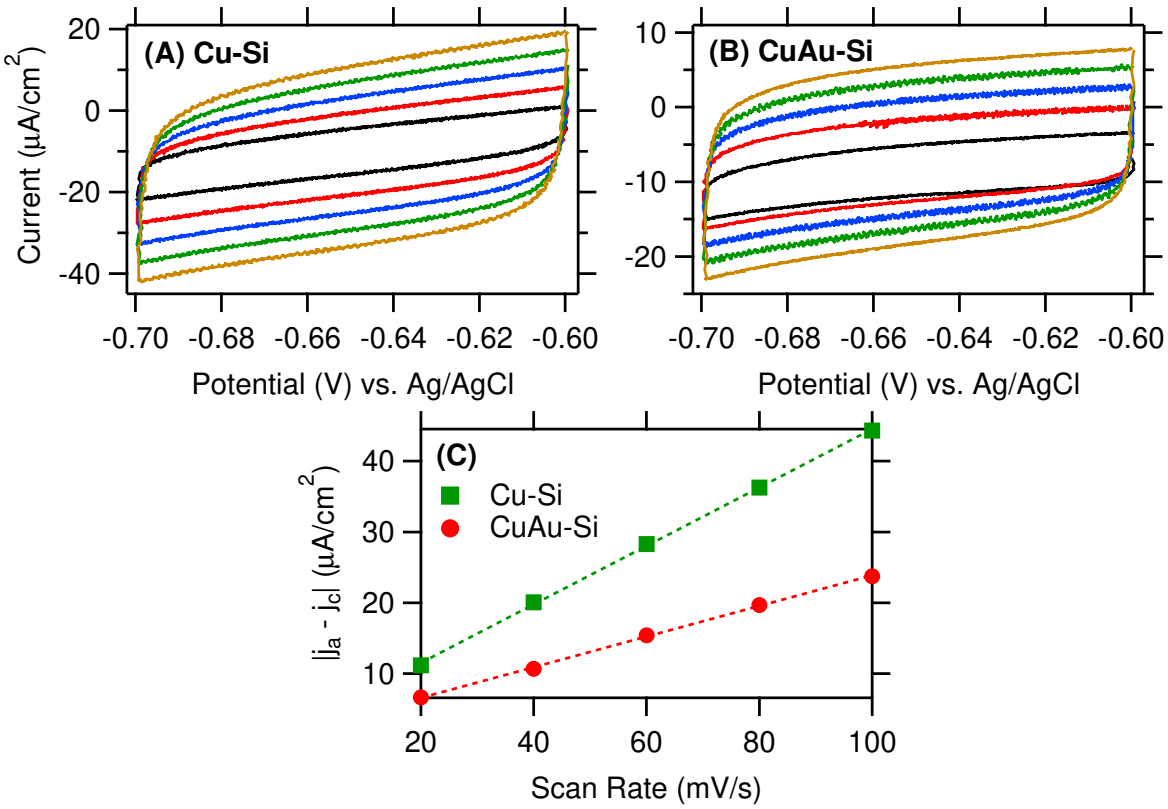

Figure A 4.3: Representative CVs for the determination of the electric double layer capacitances of (A) Cu-Si and (B) CuAu-Si in 0.1 M phosphate buffer at pH = 7. CVs were taken at 20 (black), 40 (red), 60 (blue), 80 (green) and 100 (yellow) mV s^{-1} scan rates. (C) Double layer charging current densities for Cu-Si (green squares) and CuAu-Si (red circles) versus the scan rate. The dashed lines represent linear fits to the data.

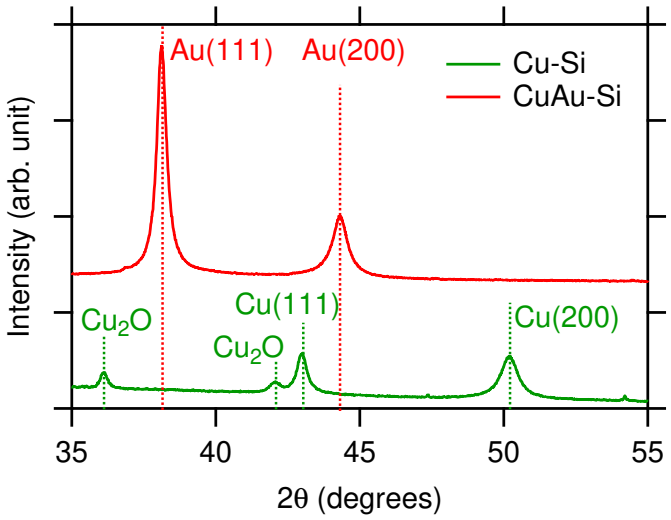

Figure A 4.4: XRD patterns for Cu-Si and CuAu-Si. Because the Cu layer was only ≈ 8 nm thick for the CuAu-Si sample, no Cu peaks were detectable. A Bruker D2 Phaser XRD system (Billerica, MA; Cu Kα radiation, λ = 1.5418 Å) was used for data collection.

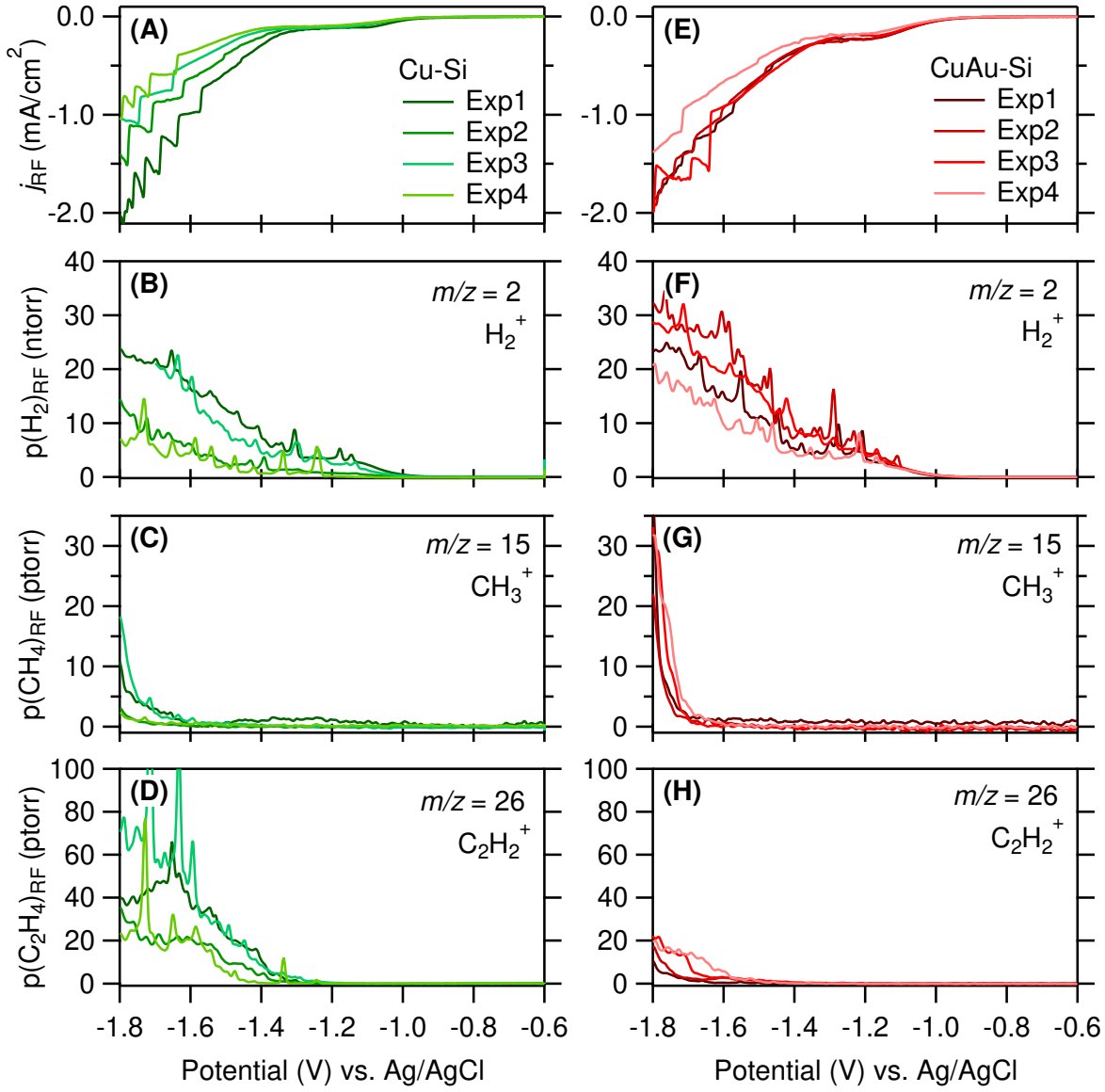

Figure A 4.5: Set of DEMS measurements from which the onset potentials of the products were determined. (A) Electrochemical current densities, (B) H_2^+ ($m/z = 2$), (C) CH_3^+ ($m/z = 15$), and (D) $C_2H_2^+$ ($m/z = 26$) partial pressures for Cu-Si. (E) Electrochemical current densities, (F) H_2^+ ($m/z = 2$), (G) CH_3^+ ($m/z = 15$), and (H) $C_2H_2^+$ ($m/z = 26$) partial pressures for CuAu-Si. All signals in this figure were divided by the RF of the respective electrode.

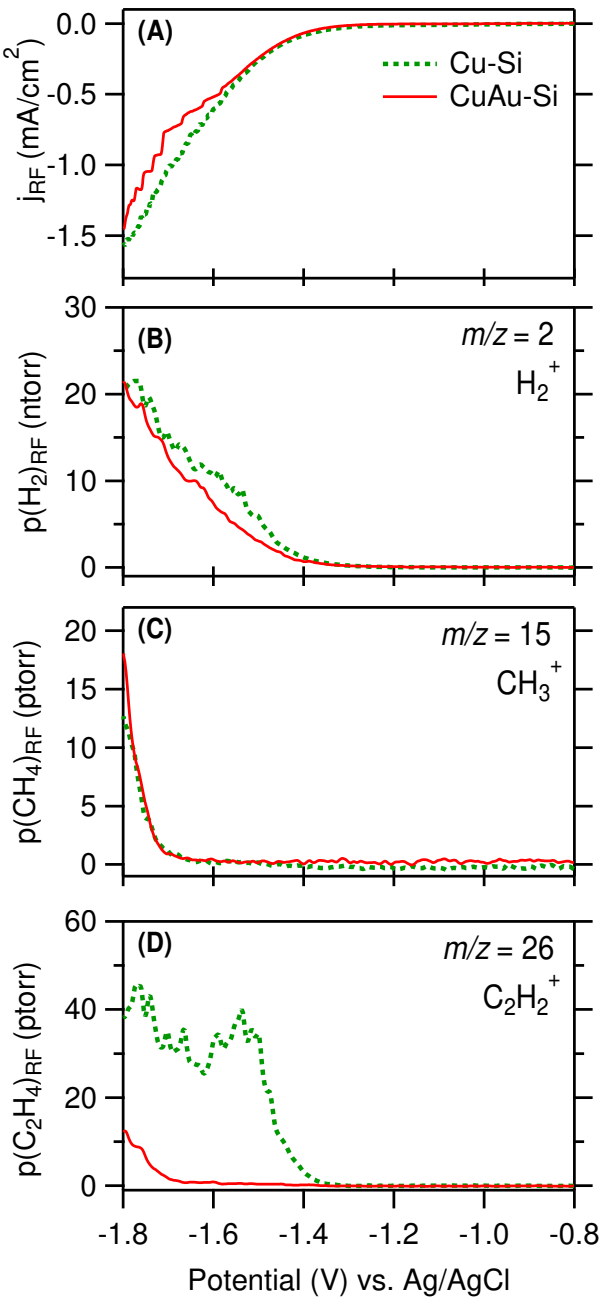

Figure A 4.6: Control experiment at high pH to exclude local pH effects. DEMS measurement for Cu-Si and CuAu-Si thin film electrodes in contact with CO-saturated 0.1 M KOH at a pH of 12.85 during a potential scan from -0.8 to -1.8 V with a 0.001 V s^{-1} scan rate. (A) Electrochemical current densities. (B) H_2^+ ($m/z = 2$), (C) CH_3^+ ($m/z = 15$), and (D) $C_2H_2^+$ ($m/z = 26$) partial pressures. All signals in this figure were divided by the RF of the respective electrode.

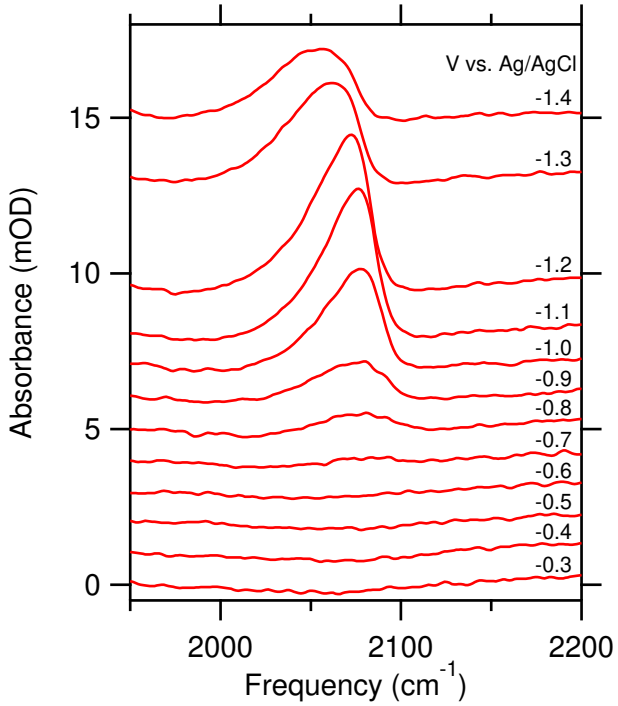

Figure A 4.7: Control experiment to exclude the possibility of Au exposure: C≡O stretch band of CO_{atop} on CuAu-Si from -0.3 to -1.4 V with -0.3 V as the reference spectrum. The absence of a C≡O stretch band above 2100 cm^{-1} and at potentials > -0.6 V indicates that gold is not exposed. CO_{atop} on Au is stable in the potential range from ≈ -0.7 to 0 V vs. Ag/AgCl [274].

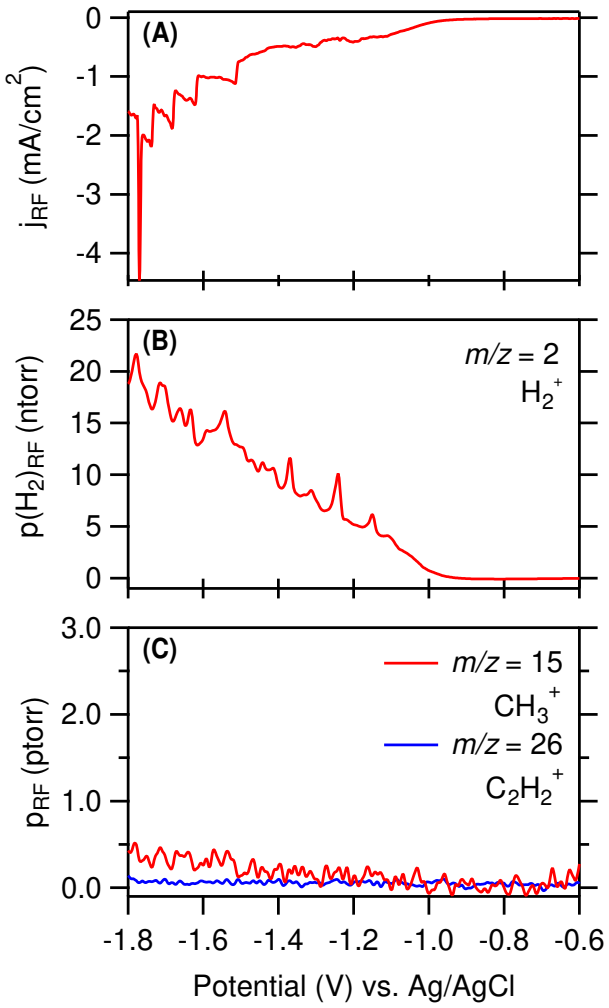

Figure A 4.8: Control experiment to verify CO as the source for the detected hydrocarbons: DEMS for Cu-Si thin film electrodes in contact with Ar-saturated 0.1 M potassium phosphate buffer at a pH of 7. (A) Electrochemical current density. (B) H_2^+ ($m/z = 2$), (C) CH_3^+ ($m/z = 15$), and $C_2H_2^+$ ($m/z = 26$) partial pressures. All signals in this figure were divided by the roughness factor (RF) of the Cu-Si film electrode.

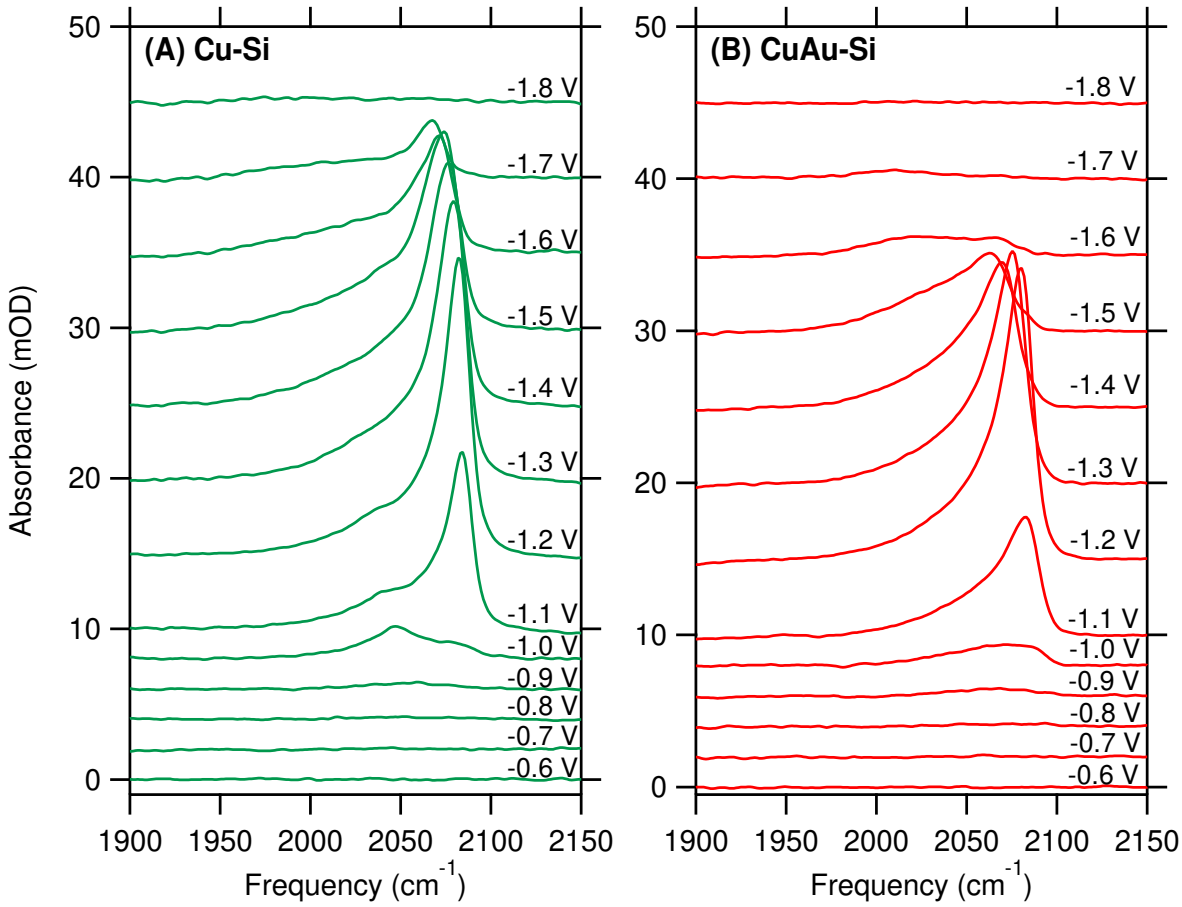

Figure A 4.9: Potential-dependence of the C≡O stretch band of CO_{atop} on (A) Cu-Si and (B) CuAu-Si from -0.6 to -1.8 V. These experiments correspond to the experimental data shown in Figures 4.1, 4.2, and 4.3 of this chapter.

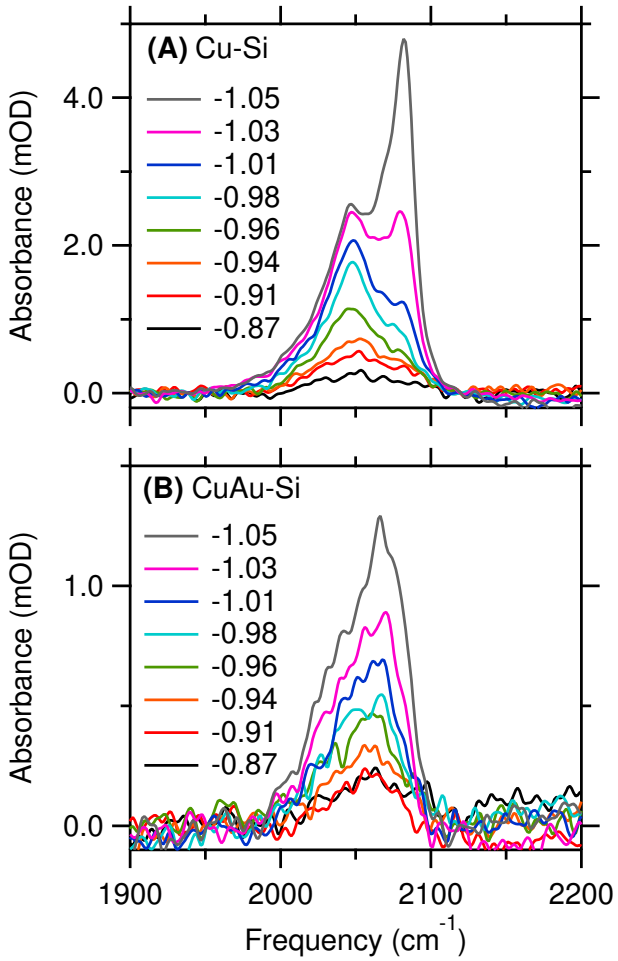

Figure A 4.10: Potential-dependence of the C≡O stretch band of CO_{atop} on (A) Cu-Si, and (B) CuAu-Si films from -0.87 to -1.05 V for two selected data sets from the data shown in Figure S4.5.

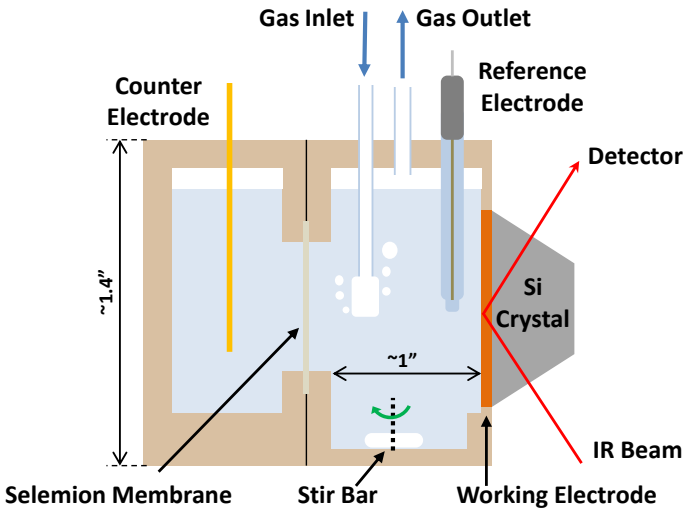

Figure A 4.11: Custom-built two-compartment SEIRAS cell. The working compartment capacity is about 6 mL, while the counter compartment volume is about 4 mL.

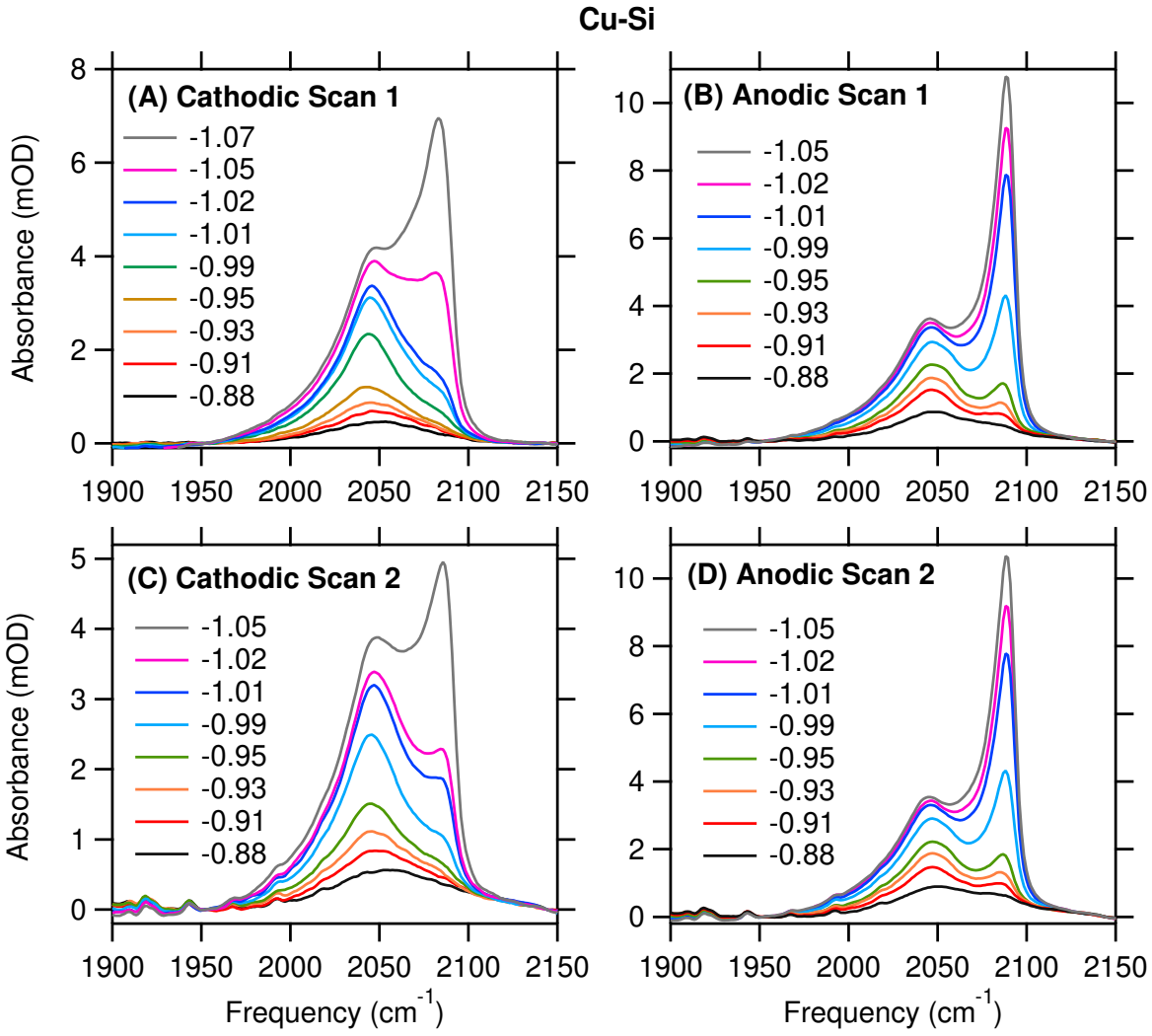

Figure A 4.12: Potential-dependence of the C≡O stretch band of CO_{atop} on Cu-Si during (A), (C) cathodic and (B), (D) anodic scans of two consecutive CVs as indicated in the panels. The labels in the panels denote the electrode potential in volts versus the Ag/AgCl reference electrode. Spectra were collected from -0.6 to -1.4 V at a 0.002 V s^{-1} scan rate under stirring of the electrolyte in the spectro-electrochemical cell shown in Figure A 4.11.

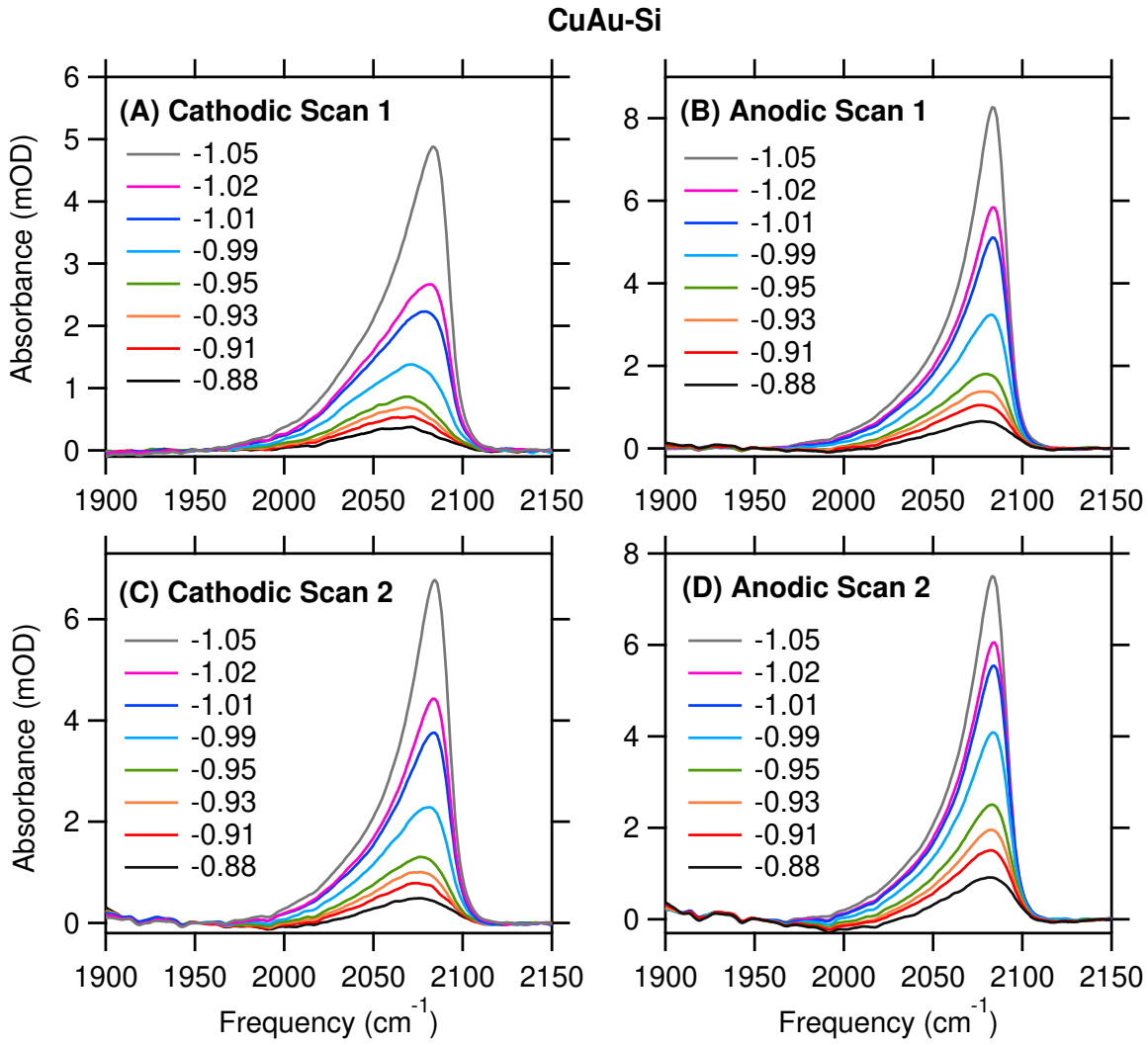

Figure A 4.13: Potential-dependence of the C≡O stretch band of CO_{atop} on CuAu-Si during (A), (C) cathodic and (B), (D) anodic scans of two consecutive CVs as indicated in the panels. The labels in the panels denote the electrode potential in volts versus the Ag/AgCl reference electrode. Spectra were collected from -0.6 to -1.4 V at a 0.002 V s^{-1} scan rate under stirring of the electrolyte in the spectro-electrochemical cell shown in Figure A4.11.

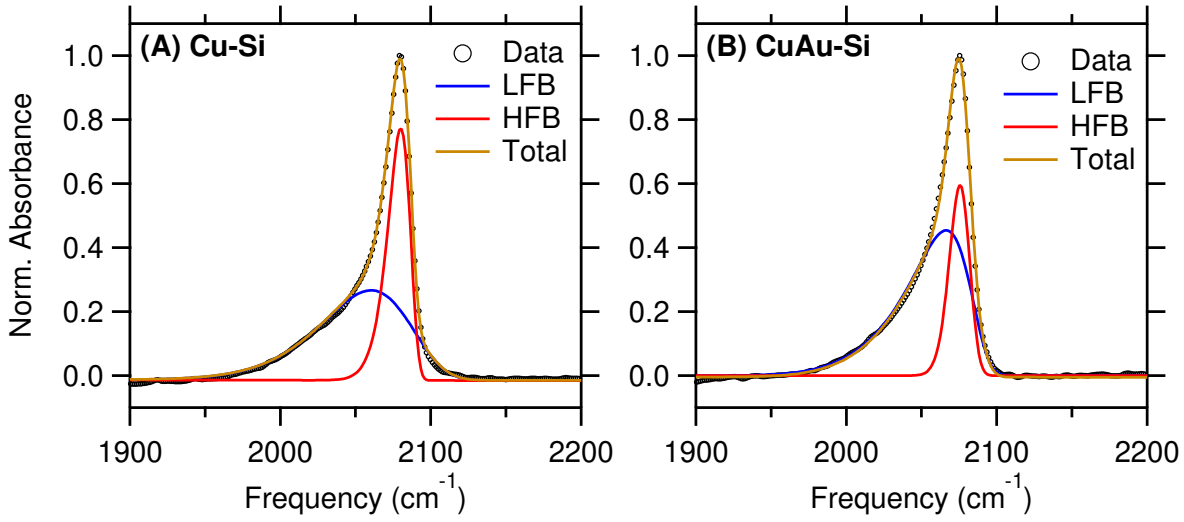

Figure A 4.14: C≡O stretch band of CO_{atop} on (A) Cu-Si and (B) CuAu-Si at a potential of -1.3 V modeled by the sum of two (skewed) Gaussian functions. LFB and HFB denote low frequency band and high frequency band, respectively.

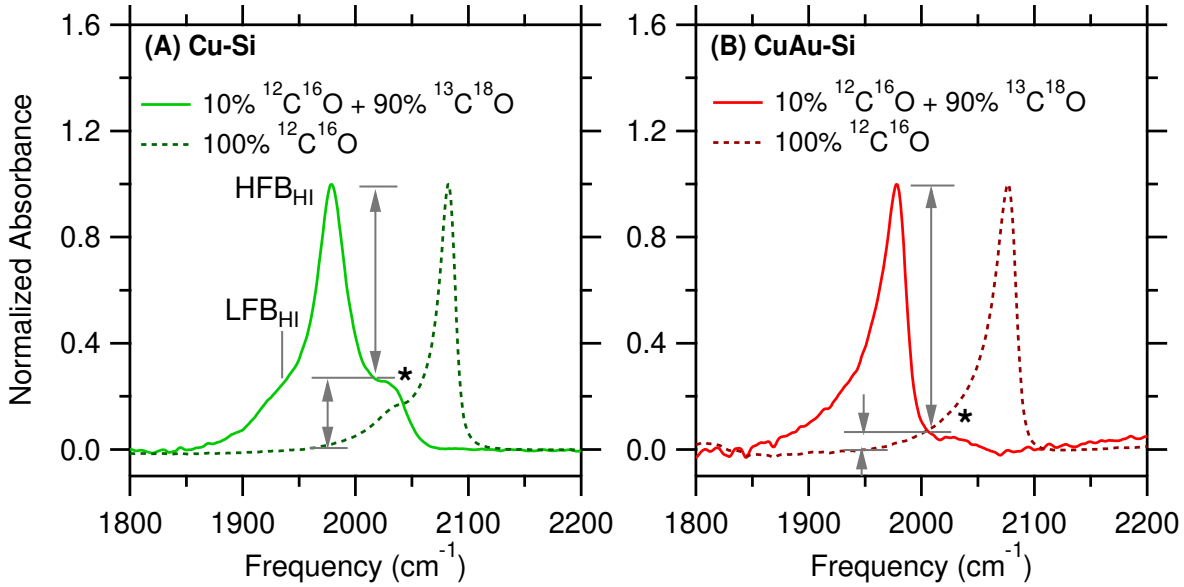

Figure A 4.15: Duplicate experiments of isotopic mixtures (Figure 4.4 of this chapter). Spectra of CO adsorbed in the atop configuration on (A) Cu-Si and (B) CuAu-Si at a potential of -1.3 V. The high-frequency and low-frequency bands of $^{13}C^{18}O$ are denoted by HFB_{HI} and LFB_{HI}, respectively. The subscript HI denotes "heavy isotope". The LFB of the $^{12}C^{16}O$ is denoted by a star symbol (*). Arrows indicate the relative amplitudes of the HFB_{HI} and (*) bands.

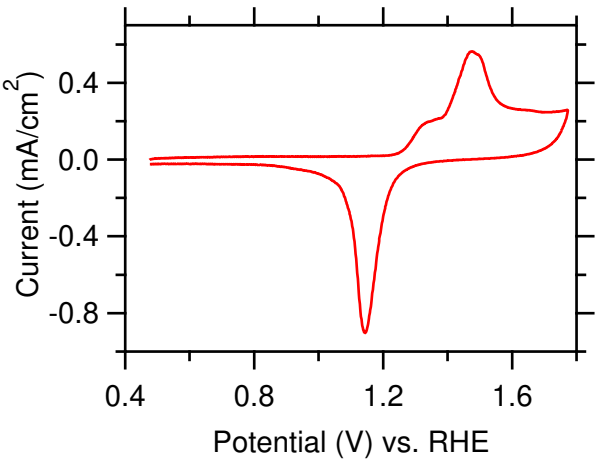

Figure A 4.16: CV of an electrolessly deposited Au film in Ar-saturated 0.1 M H_2SO_4. The scan rate was 0.05 V s^{-1}. The figure shows the geometric current density.

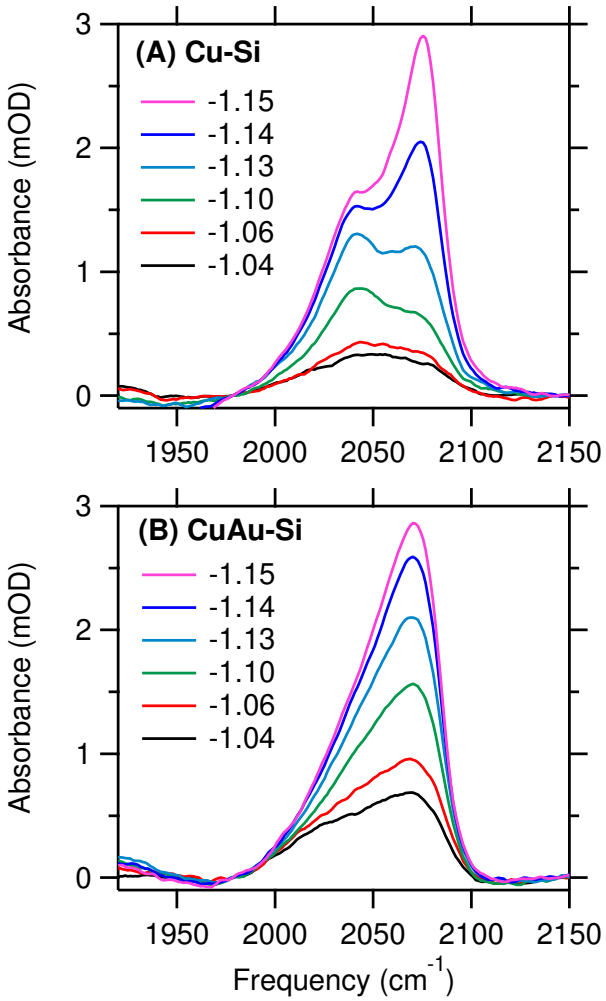

Figure A 4.17: Potential-dependence of the C≡O stretch band of CO_{atop} on (A) Cu-Si and (B) CuAu-Si in 0.1 M phosphate buffer at a pH of 12 in the cell shown in Figure S4.11. Spectra were collected from -0.6 to -1.4 V at a 0.002 V s^{-1} scan rate. The onset potential of CO_{atop} is shifted to cathodic potential by ≈ 150 mV. However, the potential dependence of the C≡O stretch of CO_{atop} follows the same trend as observed at a pH of 7. The labels in the panels denote the electrode potential in volts versus the Ag/AgCl reference electrode.

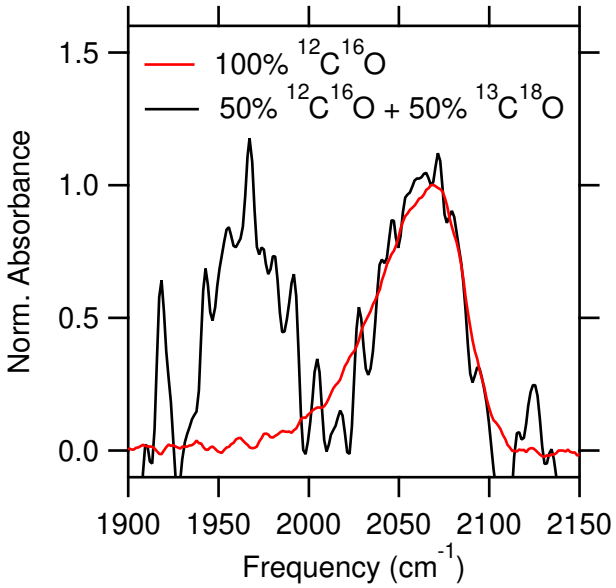

Figure A 4.18: Comparison of the C≡O stretch band of CO_{atop} in a mixture of 50% $^{12}C^{16}O$/50% $^{13}C^{18}O$ with that of isotopically pure $^{12}C^{16}O_{atop}$ on CuAu-Si at -0.93 V.

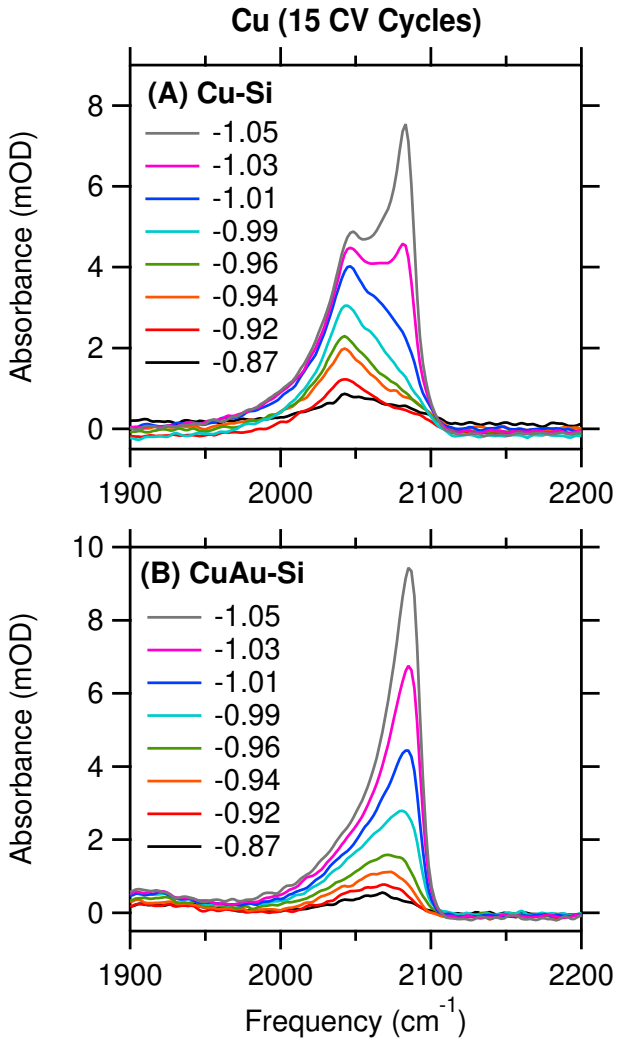

Figure A 4.19: Potential-dependence of the C≡O stretch band of CO_{atop} on (A) Cu-Si and (B) CuAu-Si after subjecting the electrode to 15 pre-treatment CVs between -0.13 to -0.7 V at a scan rate of 0.05 V s^{-1}. The electrolyte was 0.1 M potassium phosphate buffer at pH = 7. The labels in the panels denote the electrode potential in volts versus the Ag/AgCl reference electrode. The experiments were carried out with the cell shown in Figure S4.11.

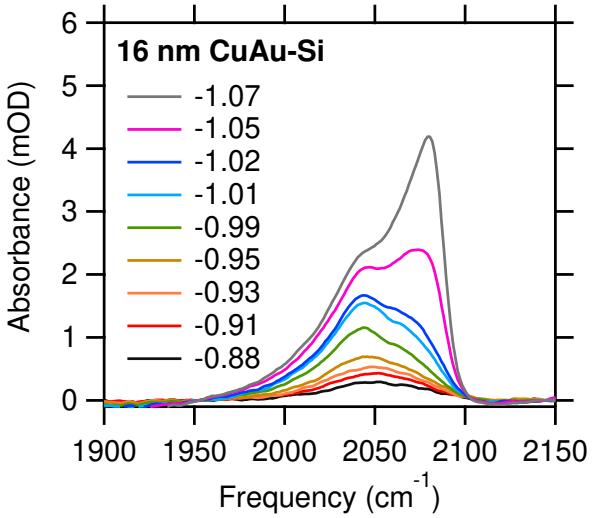

Figure A 4.20: Potential-dependence of the C≡O stretch band of CO_{atop} on CuAu-Si with a Cu overlayer thickness of 16 nm in 0.1 M potassium phosphate buffer at pH = 7. The labels in the panels denote the electrode potential in volts versus the Ag/AgCl reference electrode. The experiment was conducted in the spectro-electrochemical cell shown in Figure S4.11.

4.7 Acknowledgement

This work was supported by a CAREER award from the National Science Foundation (Award No.: CHE-1847841). J.L. was partly supported by the US Department of Energy's Basic Energy Sciences - Solar Photochemistry Program (Award No.: DE-SC0020261). We thank Professor Eric Borguet for suggesting the experiments with doubly labeled carbon monoxide.

4.8 Original Publication

This chapter has been published: Gunathunge, C. M., Li, J., Li, X., Hong, J. J. & Waegele, M. M. Revealing the Predominant Surface Facets of Rough Cu Electrodes Under Electrochemical Conditions. *ACS Catal.* **10**, 69086923 (2020).

Chapter 5

Observation of a Potential-Dependent Switch of Water Oxidation Mechanism on Co-Oxide-Based Catalysts

5.1 Introduction

Intense research on the water oxidation catalyst (WOC) center in photosystem II (PSII) over the last decades has revealed deep insights on the mechanisms by which Nature liberates electrons and protons from H_2O, two critical ingredients for downstream reactions such as CO_2 reduction and N_2 fixation [298, 299]. This knowledge has propelled research on using molecular catalysts to oxidize water, and impressive progress has been made in terms of catalyst performance as measured by turn-over frequencies (TOFs) and turn-over numbers (TONs) [42, 300]. From a technological development perspective, there is a strong incentive to carry out the reaction on heterogeneous catalysts, especially on those of low-cost and outstanding stability. Indeed, recent years have witnessed a surge of such research activities [47, 301–305]. Despite the apparent variety of these catalysts, they share important commonalities in the chemical mechanisms. For instance, it is generally believed that the reaction proceeds through a series of proton-coupled electron transfer (PCET) steps that lead to the formation of M=O (where M represents an active metal center) intermediates [306, 307]. It is also agreed upon that the subsequent O-O bond for-

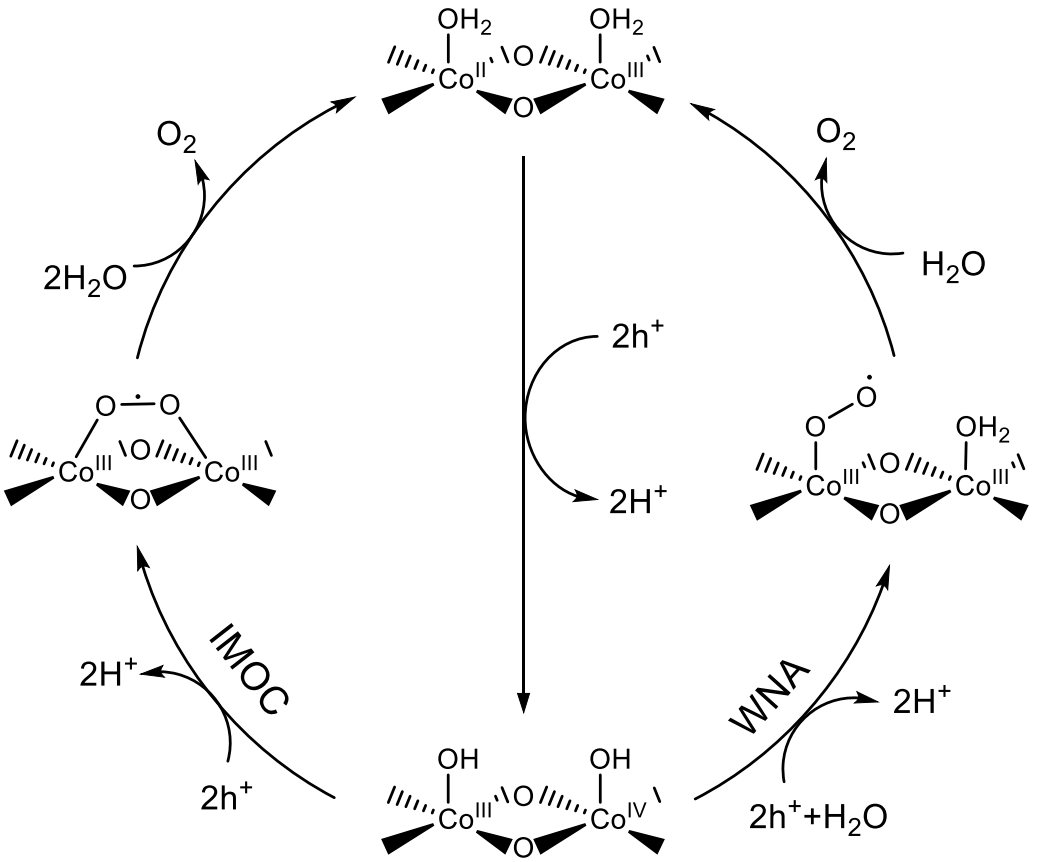

Figure 5.1: Proposed water oxidation mechanisms by heterogeneous Co phosphate (Co-Pi) catalysts. Two possibilities have been proposed, the intramolecular oxygen coupling pathway (IMOC, left) and the water nucleophilic attack route (WNA, right).

mation is of critical importance to the overall reaction [308]. The details of the O-O formation and the subsequent steps, however, have been the subject of diverging views. At least two possible pathways have been proposed and supported [309–312]. One involves direct nucleophilic attack of water, followed by O_2 release and regeneration of the catalyst. In the literature, this mechanism is referred to as water nucleophilic attack (WNA,Figure 5.1, right pathway) [300, 309]. The other involves the coupling of two metal-oxo intermediates followed by O_2 release, which is referred to as intramolecular oxygen coupling (IMOC, Figure 5.1, left pathway [309].

For Ir- and Ru-based molecular catalysts, density-functional theory (DFT) calculations

predicted that the IMOC pathway dominates at low overpotentials, whereas the WNA pathway becomes accessible at higher overpotentials [311, 313]. The two pathways were also predicted to be competitive on a heterogenized dinuclear Ir oxide cluster [311]. With optical pump-probe spectroscopy, Cuk *et al.* monitored the microsecond decay of oxyl (Ti-O) and bridge (Ti-O-Ti) intermediates on $SrTiO_3$ photoelectrodes [312]. They found that the two species decay with distinct reaction rates on a microsecond timescale. It was suggested that Ti-O's convert to Ti-O-O-Ti by dimerization (IMOC pathway) and Ti-O-Ti converts to Ti-OOH by nucleophilic attack of water (WNA pathway). Furthermore, it was found that the relative predominance of the two pathways was controlled by the ionic strength of the electrolyte, with the WNA pathway dominating at low ionic strength. However, how the relative predominance of these mechanisms depends on the applied electrode potential has not been investigated in experiments. Herein, we address this central question.

Inspiration on how to further this understanding could be drawn from progress made in molecular WOC-based studies. To discern different pathways for the water oxidation reaction by molecular catalysts, researchers have resorted to a strategy of correlating the reaction rate with the catalyst concentrations [300]. With the help of additional experiments such as isotope labelling, significant knowledge has been gained [45, 314, 315]. Similar approaches are challenging to implement for heterogeneous catalysts, however, because the active sites, including their structures and densities, are often poorly defined on a heterogeneous catalyst. The challenge could be circumvented using clever experimental designs. For instance, Durrant *et al.* have identified a change of reaction orders relative to the hole concentration from the first to the third order on Fe_2O_3 using photoinduced absorption spectroscopy [316]. Frei *et al.* have succeeded in observing both the metal-oxo, and superoxo species, using an infrared spectroscopy technique [307]. In both studies, different reaction mechanisms were proposed for different light intensities. Nevertheless, due to the lack of detailed information on the active centers, particularly their

density under different conditions, it remains difficult to directly corroborate these early observations for an unambiguous understanding of water oxidation on heterogeneous catalysts. While it is possible to address this challenge by synthesizing heterogeneous catalysts with well-defined active centers, as has been demonstrated recently by others and us [317, 318], the catalyst library remains limited, and significant work is needed before the values of such catalysts can be materialized. An alternative approach is to study how the reaction kinetics changes as a function of water activity, which is the main strategy for this present work.

To appreciate the significance of this strategy, it helps to examine the proposed WNA and IMOC pathways on a heterogeneous Co phosphate (Co-Pi) catalyst (Figure 5.1). Prior studies have suggested that the initial electron/proton transfer steps (vertical arrow in the center) are fast in comparison to the O-O formation. Therefore, these steps are quasi-equilibrated, whereas O-O formation limits the rate of the reaction. From the oxidized state of the catalyst shown on the bottom of the scheme, the water oxidation process can proceed through two distinct pathways: The WNA pathway involves a water molecule within the electric double layer in the rate-determining O-O forming step (right arrow). By contrast, the IMOC pathway only involves surface species in the rate-determining step (RDS) (left arrow). On the basis of this simplified mechanistic picture, the water oxidation reaction is expected to be (pseudo) first order in the water activity when proceeding through the WNA pathway, whereas it is (pseudo) zeroth order when proceeding through the IMOC pathway. This simplified view assumes that the change in the water activity does not significantly affect the positions of the quasi-equilibria prior to the presumed RDS of O-O bond formation, as discussed later. It is, therefore, possible to discern the reaction mechanisms even without detailed knowledge of the active centers by altering the water activity, which has not been investigated previously.

The problem is now reduced to how to alter water activity in a water oxidation reac-

tion. Indeed, most prior studies on this subject have treated water as a substrate of invariant activity, such that it was excluded in most kinetic considerations [319, 320]. Only recently did we see advances where the water activity could be suppressed significantly in aqueous solutions [321–323]. The so-called "water-in-salt" electrolyte containing high concentrations of salts (*e.g.*, up to 21 m (mole per kg of H_2O)) represents one such system. The strong solvation effect of the high-concentration ions renders its H_2O behaviors drastically different from those in bulk H_2O. It becomes possible to perform water oxidation reactions in an aqueous system where the water activity is no longer unity. We are, therefore, offered an opportunity to test the hypothesis proposed in the previous paragraph. That is, we expect a different sensitivity of the kinetics on the water activity for different mechanisms.

To prove this concept, we have chosen Co-oxide-based catalysts as a study platform because they represent a class of most studied heterogeneous WOCs, with Co phosphate (Co-Pi) receiving arguably the most attention. A broad knowledge base has already been generated [309, 320, 324–330]. For example, the coordination environment of Co has been identified by a suite of spectroscopic techniques [327]. That the O-O formation is the RDS has been supported by numerous studies [309, 320, 324, 325, 328, 329]. Both WNA and IMOC mechanisms have been proposed and supported by either experimental or computational studies for this catalyst [309, 325, 328, 329, 331–333]. Herein, we report the new observation of a switch from the IMOC pathway at low applied potentials to the WNA mechanism at high applied potentials.

5.2 Results and Discussion

5.2.1 Detection of water oxidation intermediates

Prior studies have shown that various implementations of infrared and surface-enhanced Raman spectroscopies are powerful probes of water oxidation intermediates [306, 307, 312, 334–342]. To examine the mechanistic proposal (Figure 5.1), we employed surface-enhanced infrared absorption spectroscopy (SEIRAS) in the attenuated total reflection (ATR) geometry. In SEIRAS-ATR, the surface plasmon resonance of rough metal films locally enhances the evanescent field, rendering the technique sensitive to sub-monolayers of species adsorbed on the electrode [343]. With this work, we establish SEIRAS-ATR in the Kretschmann configuration as a tool for probing water oxidation intermediates on metal oxide catalysts. For this purpose, we first electrochemically deposited a thin layer of $CoO_x(OH)_y$ [324] onto a chemically deposited Au thin film ($CoO_x(OH)_y$-Au) [74] on a micro-machined Si-ATR crystal, which affords high infrared transparency below 1200 cm^{-1}. A scheme of the setup is shown in Figure A5.1 in the Addendum. For SEIRAS-ATR, $CoO_x(OH)_y$ instead of Co-Pi was employed as the prototypical catalyst because the latter would greatly complicate the interpretation of the IR spectra in the region around 1000 cm^{-1} due to the phosphate anion and its response to the applied potentials. As will be discussed in detail later in this work, the electrochemical behaviors of $CoO_x(OH)_y$ are comparable to Co-Pi. It also features structurally similar active sites and the same cobalt oxidation states under water oxidation conditions as Co-Pi [324, 344]. The $CoO_x(OH)_y$-Au film exhibits a large activity for water oxidation in comparison with the Au substrate (Figure A5.2).

Figure 5.2 shows the steady-state spectra of the $CoO_x(OH)_y$-Au electrode in 0.1 M potassium phosphate (KPi) in D_2O, H_2O, and $H_2{}^{18}O$. The absorbance was calculated ac-

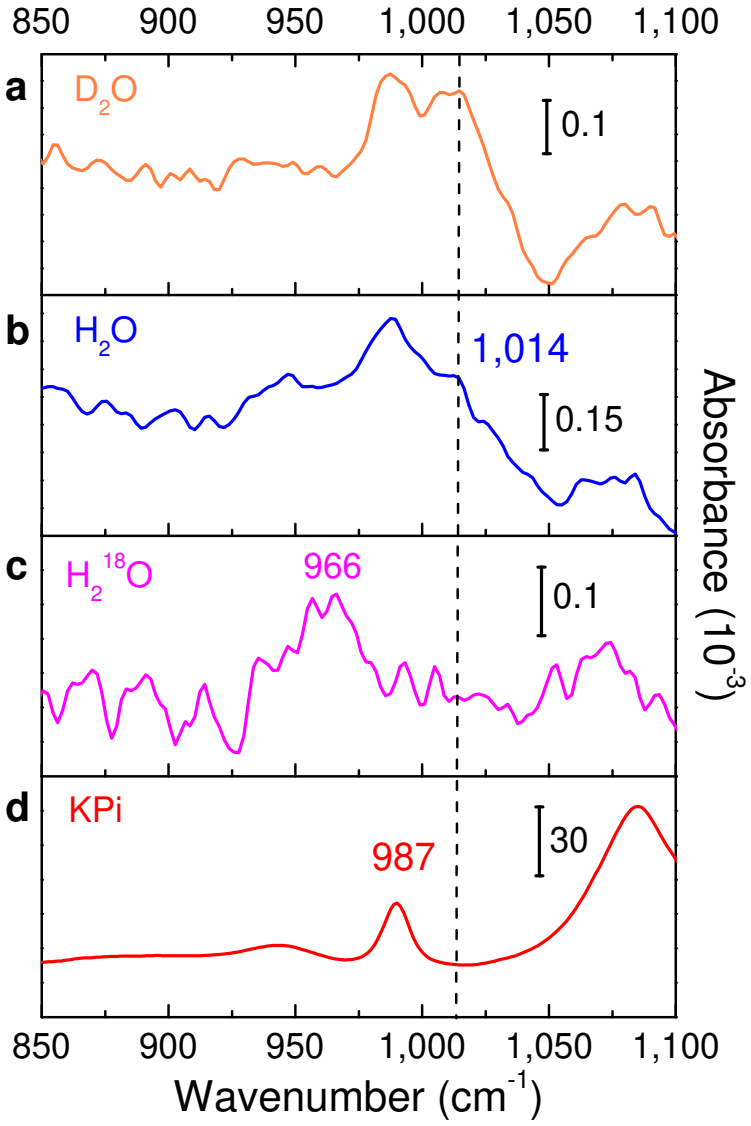

Figure 5.2: Observation of a superoxo intermediate by SEIRAS-ATR on a $CoO_x(OH)_y$-Au electrode. Spectra collected on electrodes in contact with 0.1 M solutions of KPi in: (a) D_2O, (b) H_2O, and (c) $H_2{}^{18}O$ at a sample potential of 2.21 V. A spectrum at 1.61 V served as a reference spectrum. The band of the superoxo species is centered at 1,014 cm^{-1} in the presence of D_2O and H_2O and occurs at 966 cm^{-1} in the presence of $H_2{}^{18}O$. All other spectral changes are attributed to KPi. (d) Spectrum of a bulk KPi solution.

cording to Absorbance = -log(S/R), where S and R refer to the sample and reference spectra respectively taken at 2.21 V and 1.61 V. Unless otherwise noted, all potentials in this work are relative to the reversible hydrogen electrode (RHE). The spectrum in the D_2O-based electrolyte exhibited a band centered at 1,014 cm^{-1} (at 2.21 V; Figure 5.2a). The intensity of this band increased with increasing applied potential (Figure A5.3), suggesting that it is due to a water oxidation intermediate. To assign the band to a water oxidation intermediate, we carried out the following control experiments: First, to exclude the possibility that the band (1,014 cm^{-1}) arises from a phosphate species in solution, we confirmed that the band also appears when the electrolyte is 0.1 M KCl in D_2O and in H_2O (Figure A5.4). Second, the band is absent on an Au electrode without the $CoO_x(OH)_y$ film (Figure A5.4).

These observations strongly suggest that the band centered at 1,014 cm^{-1} is a water oxidation intermediate on $CoO_x(OH)_y$-Au. According to the proposed mechanism, this spectral feature can be associated with either Co-O-O$^{\cdot}$-Co from the IMOC pathway or Co-O-O$^{\cdot}$ or Co-O-OH from the WNA pathway (Figure 5.1). To further assign this band, we conducted isotopic labelling experiments with H_2O and $H_2{}^{18}O$. The lack of an isotopic shift when the solvent was switched from D_2O to H_2O implies that the vibrational mode of the species does not involve a hydrogen atom (Figure 5.2b). Upon switching to the $H_2{}^{18}O$ electrolyte, this band shifts to 966 cm^{-1} (Figure 5.2c). The 48 cm^{-1} difference (from 1,014 to 966 cm^{-1}) indicates that the intermediate involves an O-containing motif. These experimental observations support the conclusion that the 1,014 cm^{-1} band is associated with the superoxide intermediates (Co-O-O$^{\cdot}$-Co or Co-O-O$^{\cdot}$) [307, 330, 336]. The other possible water oxidation intermediate, hydroperoxide (Co-O-OH), would feature characteristic bands in the 740-920 cm^{-1} region [336, 338, 345, 346]. Due to the absorption by the H_2O librational mode, the signals were too weak to be discernable in that spectral range. The other bands in the spectra in Figure 5.2a-c are due to the enrichment and depletion of electrolyte phosphate species at the interface with changes in applied potential. The

magnitude of those spectral changes depend on the characteristics of a specific electrode, such as film thickness and homogeneity, and the electrolyte system. The negative band at $\sim$1050 cm^{-1} in Figure 5.2a,b is likely due to a surface-adsorbed phosphate species [347]. The spectrum of a bulk KPi solution is shown in Figure 5.2d. Duplicate experiments confirm the reproducibility of the spectroscopic results (Figure A5.5). Taken together, this set of experiments demonstrates the utility of the SEIRAS-ATR technique for the detection of water oxidation intermediates under operating conditions. Importantly, the result confirms the presence of a superoxo species, consistent with the mechanistic proposal (Figure 5.1). Future research should be directed to further distinguish between Co-O-O$^{\cdot}$-Co and Co-O-O$^{\cdot}$.

5.2.2 Electrochemical Characterization with Varying Water Activities

To further probe the mechanisms as shown in Figure 5.1, we monitored the electrochemical water oxidation current as a function of electrode potential in water-in-salt electrolytes of varying water activities. As noted above, different reaction orders with respect to water activity are expected from the two competing mechanisms: A (pseudo) first-order dependence on H_2O activity (a_w) is expected for the WNA route, whereas a (pseudo) zeroth-order dependence on a_w is expected for the IMOC pathway. In a practical electrochemical system, the dependence of the kinetics on a_w is likely more complicated because of a number of other factors, including the participation of H_2O as a solvent; these potential complications notwithstanding, the value of quantitatively analyzing the reaction rates as a function of water activity becomes obvious.

Figure 5.3a compares the steady-state electrochemical current densities due to the oxidation of water on Co-Pi in contact with 0.1 M KPi containing 0, 2, 4, and 7 m $NaNO_3$.

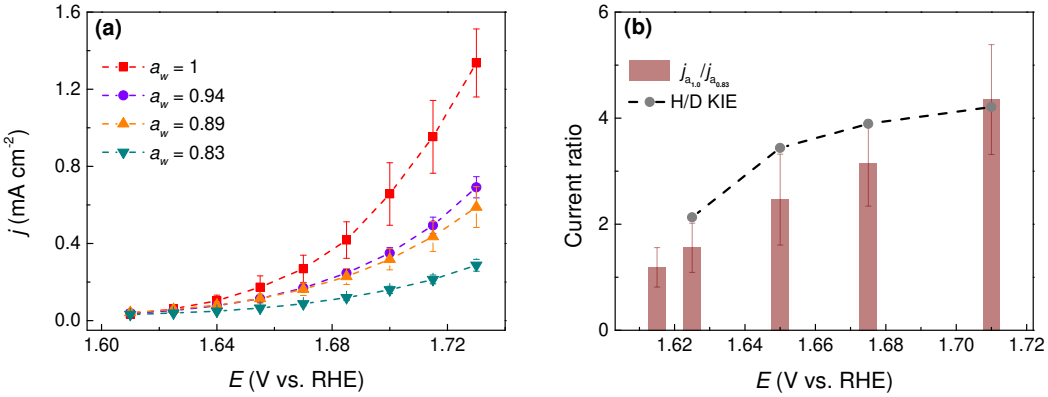

Figure 5.3: Potential-dependence of the current modulation ratio for different water activities and solvents. (a) Suppression of the current density due to the water oxidation reaction on Co-Pi when a_w was decreased from 1 to 0.83. The water activity was altered by setting the $NaNO_3$ concentration in a 0.1 M KPi buffer at neutral pH to 0 m, 2 m, 4 m, 7 m. The data were collected on a Co-Pi film on an FTO substrate under steady-state conditions and under stirring of the electrolyte. The data were derived from an average of three independent experiments for each a_w. Error bars denote the standard deviation of three individual measurements. The potential was corrected for the iR-drop. Further experimental details are provided in the Addendum. (b) $j_{a1.0}/j_{a0.83}$ is the ratio of the water oxidation current densities on the Co-Pi catalyst observed in electrolytes with water activities of 1 and 0.83. The ratio $j_{a1.0}/j_{a0.83}$ was calculated from the data in Figure 5.3a. H/D refers to the ratio of the current densities of the Co-Pi catalyst in 0.1 M KPi in H_2O and D_2O.

The corresponding water activities are shown in the legend and were calculated on the basis of empirical equations [348]. These values describe the activity of bulk water in these water-in-salt electrolytes. We caution that the activity of water at the electrocatalytic interface may be different from those values. Nevertheless, the activities of interfacial water are expected to qualitatively follow the same trend with increasing water-in-salt concentration. All electrolytes were at neutral pH and were stirred during measurements, which were carried out on electrodeposited Co-Pi on fluorine-doped tin oxide (FTO) substrates in a single-compartment electrochemical cell. The potential window was carefully chosen so as to avoid mass transport limitations (*i.e.*, $>$1.71 V) or large experimental errors due to low current densities (*i.e.*, $<$1.62 V). Details of the data collection protocol are given in the SI, and a representative data set is shown in Figure A5.6. As shown, with increasing molality of $NaNO_3$ and, hence, decreasing a_w, the current density of water oxidation is increasingly suppressed. A similar trend was observed for $CoO_x(OH)_y$ (Figure A5.7), suggesting that the observed trend is a more general feature of cobalt oxide-based catalysts. This finding further corroborates our assertion made above that $CoO_x(OH)_y$is an appropriate alternative model system for Co-Pi.

The observed suppression of the water oxidation reaction could arise from a number of different physical phenomena. First, to test if the catalyst undergoes irreversible structural changes in the different electrolytes, we recorded the CVs of the same Co-Pi electrode in 0.1 M KPi before and after collection of 3 cycles of CVs in the four electrolytes (of molalities 0, 2, 4, 7 m). As shown in Figure A5.8, the CVs in 0.1 M KPi before and after catalysis in the water-in-salt electrolytes overlap. These data suggest that no irreversible changes in catalytic activity occur during water oxidation in the water-in-salt electrolytes.

Second, to test if the mass transport of water to the electrode limits the reaction rate at high salt concentrations, we collected the steady-state electrochemical current densities of a CoPi-coated Pt rotating disk electrode (RDE) at rotation rates of 2,000 rpm (Figure A5.9)

and 0 rpm (Figure A5.10). Comparison of the two figures reveals that the recorded current densities on the RDE exhibit the same trend with increasing salt concentration, irrespective of the rotation rate. Moreover, as demonstrated in Table A5.1, the increase in the thickness of the stagnant layer with electrolyte concentration is expected to be small. Collectively, these results suggest that the suppression of the water oxidation reaction is not caused by limited mass transport of water to the electrode.

Third, at high concentrations of $NaNO_3$, nitrate anions are expected to limit the enrichment of phosphate anions in the electric double layer with increasing potential. As a result, the pH buffer capacity at the electrocatalytic interface might decrease with increasing $NaNO_3$ concentration. Changes in the pH in the vicinity of the electrode (local pH) could impact the reaction rate and mechanism [320, 349]. To exclude local pH effects as a possible reason for the reactivity trends with increasing $NaNO_3$ concentration, we carried out three different control experiments: (1) We monitored the electrochemical current density as a function of solution pH at a fixed (absolute) electrode potential. As shown in Figures A5.11-5.13, the pH-dependence of the current density was independent of the rotation rate of the RDE. (2) We carried out galvanostatic titration experiments. The potential shows an approximately Nernstian shift of 60 mV/pH for all electrolytes (Figures A5.11-5.13). (3) We varied the concentration of KPi in the electrolytes containing 4 and 7 m $NaNO_3$. As shown in Figure A5.14, the potential-dependence of the reaction rate is insensitive to the concentration of KPi. Taken together, these control experiments suggest that the local pH does not significantly depend on the concentration of $NaNO_3$.

Fourth, to test if nitrate anions block catalytic sites, we recorded the electrochemical current density as a function of potential in 7 m $NaClO_4$. Perchlorate typically does not chemisorb on electrodes [350]. As shown in Figure A5.15, the impact of 7 m $NaClO_4$ on the current density is similar to that of 7 m $NaNO_3$. This result indicates that nitrate anions do not block catalytic sites of Co-Pi.

Fifth, alkali metal cations are known to influence the rate of the water oxidation reaction on various electrocatalysts [168, 351–354]. In the case of Ni oxyhydroxides, intercalated electrolyte cations have been proposed to stabilize reaction intermediates [352, 353]. To test if the catalytic activity is affected by the identity of the cation, we conducted additional control experiments in 2 m KNO_3. As shown in Figure A5.16, the current modulation ratio virtually overlaps with the one obtained in 2 m $NaNO_3$ (higher concentrations of KNO_3 could not be tested because of the lower solubility of that salt relative to $NaNO_3$). This result is consistent with earlier work [355] showing that the substitution of K^+ in Co-Pi by Na^+ has no significant impact on the catalytic activity of this catalyst. On the basis of this finding and our observation that the catalytic activity of Co-Pi is retained after a sequence of CVs in three water-in-salt electrolytes (Figure A5.8), we can exclude the incorporation of Na^+ into the Co-Pi film as the origin of the change in catalytic activity with increasing electrolyte concentration. Cations can also influence an electrocatalytic process by altering the properties of the electric double layer in a number of distinct ways [32], which are not fully understood to date. One of the principal ways in which cations can impact the catalytic activity is by altering the structure and dynamics of water at the interface [32, 354]. This possibility is included in our interpretation of these results in terms of the decreasing activity of water with increasing concentration of the water-in-salt electrolytes.

Sixth, to exclude the possibility that impurities, *e.g.* Fe, incorporate into the catalyst [356] with increasing salt concentration, we performed CV tests in electrolytes with reagent grade and trace metal grade salts. As shown in Figure A5.17, the same water oxidation activity was observed in both electrolytes.

Lastly, to test if the electrochemical currents arise from the oxidation of water to molecular oxygen, we conducted gas chromatography measurements. Figure A5.18 shows that O_2 is produced with near-unity Faradaic efficiency. This measurement demonstrates

that (1) other possible oxidation products (such as H_2O_2) are not produced in appreciable amounts and (2) parasitic chemical reactions (such as the oxidation of nitrate) do not occur.

Taken as a whole, this set of results indicates that the observed suppression of the water oxidation reaction is most likely due to the decrease of water activity (a_w) from 1 to 0.83 as the concentration of $NaNO_3$ increases from 0 to 7 m.

To further analyze the data shown in Figure 5.3a, we plotted the ratio of the current density at a_w =1 over that at a_w =0.83 at different potentials (Figure 5.3b). This ratio quantifies the extent to which the reaction rate is modulated by the water activity. It is clear that the impact of the water activity strongly depends on the electrode potential: At 1.71 V, the rate is suppressed by a factor of ≈4.3. By contrast, at a potential of 1.615 V, the modulation factor is only ≈1.2, indicating that the rate of the reaction is less sensitive to the change in water activity at that potential. Identical trends were obvious for the other a_w's (*i.e.*, 0.94 and 0.89), albeit with different magnitudes.

That the reaction rate is suppressed by up to a factor of 4.3 by an a_w change from 1 to 0.83 at 1.71 V strongly suggests that H_2O is involved in the rate-determining step at that potential. Conversely, for the same a_w, the modulation is close to unity at 1.615 V, indicating that H_2O involvement in the rate-determining step is less likely. Taken as a whole, the data suggest that a mechanistic switch occurs between 1.615 V and 1.71 V. A possible mechanistic switch that is consistent with our observations is the transition from the IMOC pathway ((pseudo) zeroth-order in a_w) to the WNA route ((pseudo) first-order in a_w) as the electrode potential is increased from 1.615 to 1.71 V.

To corroborate further this assertion, we measured the steady-state current density on the FTO-supported Co-Pi electrode in 0.1 M KPi in heavy water (D_2O) as a function of electrode potential. The ratio of the current density of the corresponding measurement in light water over that in heavy water is the apparent kinetic isotope effect (KIE). The

apparent KIE is close to 2 at 1.625 V and increases to ≈4.2 as the potential is tuned to 1.71 V. Because the IMOC pathway does not involve water in the rate-determining step, we expect the rate of the reaction to be insensitive to H/D substitution. By contrast, the WNA involves a water molecule in the rate-determining step. Therefore, a dependence of the rate on the isotope of hydrogen is expected. Collectively, the KIE measurements further corroborate our notion that the mechanism switches from the IMOC route to the WNA pathway with increasing potential.

We note that the interpretation of KIE effects can be highly complex. For example, a similar KIE dependence on potential might be explained by a switch of the oxidized substrates from OH^- to H_2O, as has been reported by Zhao *et al.* on Fe_2O_3 [357]. That mechanism, however, is not applicable to the Co-Pi catalyst because OH^- is unlikely to be the oxidized substrate at pH 7. Furthermore, Hammes-Schiffer *et al.* demonstrated that the relative contributions that specific reactant/product vibronic states make to the current density are dependent on the isotope [358]. They showed that this effect could give rise to a potential-dependence of the KIE. While we cannot fully rule out that such effects contribute to the potential-dependence of the KIE in the present case, the corroboration between the KIE data and the potential-dependent impact of the water activity on the reaction rate supports the conclusion of a potential-induced switch from the IMOC mechanism to the WNA pathway with increasing potential. A KIE on the WNA pathway was also reported by Cuk *et al.* during the photocatalytic oxidation of water on $SrTiO_3$ [312].

As far as the KIE effect is concerned, it is noted that Dau and co-workers also found a suppression of the water oxidation reaction in D_2O relative to that in H_2O [325]. Their electrokinetic results were similar to those reported herein. However, they interpreted these data differently. Specifically, the authors found that the redox-potential of the pre-equilibrium $[Co^{III}\text{-}OH] \leftrightharpoons [Co^{IV}\text{-}O] + H^+ + e^-$ shifts by about 60 mV in the anodic direction upon switching the solvent from H_2O to D_2O. Because galvanostatic measurements

for water oxidation in H_2O and D_2O show a similar shift, they suggested that the suppression of the water oxidation reaction is due to the shift in this pre-equilibrium (rather than a KIE on the rate-determining step of the water oxidation reaction). This pre-equilibrium is a critical factor determining the activity of Co-oxide based catalysts [320, 324, 359]. This alternative interpretation could also account for the observed suppression of the water oxidation in D_2O. However, we note that on the basis of the cyclic voltammograms of Co-Pi in H_2O and D_2O (Figure A5.19), we estimated a shift of $\approx$28 mV in the Co(II)/Co(III) redox half-wave potential. The relatively small shift in the pre-equilibrium suggests that it may not be the sole reason for the observed dependence of the rate of the water oxidation on the H/D isotope. Most importantly, this interpretation cannot account for the suppression of the current with increasing salt concentration (Figure 5.3). As discussed above, our control experiments in which we varied the rotation rate of the RDE (Figures A5.9-5.10), the pH of the electrolyte (Figures A5.11-5.13), and the concentration of KPi (Figure A5.14) confirm that the buffer capacity is sufficient to maintain the $[Co^{III}\text{-}OH] \leftrightharpoons [Co^{IV}\text{-}O] + H^+ + e^-$ equilibrium in the water-in-salt electrolytes. To further corroborate this notion, we analyzed the Co(II)/Co(III) redox equilibrium of Co-Pi in contact with the water-in-salt electrolytes with cyclic voltammetry. As shown in Figure A5.20, the Co(II)/Co(III) redox half-wave potential is shifted by only 10-20 mV in the cathodic direction with increasing salt concentration. This small shift indicates the pre-equilibrium is not significantly affected by the presence of water-in-salt electrolytes. Therefore, when the isotope effect results are viewed in the context of the electrokinetic results for the water-in-salt electrolytes, our interpretation provides a cohesive, self-consistent picture, whereas the hypothesis of the shift in the pre-equilibrium can only partly explain the collective results. Although the shift may be a contributing factor, we conclude that it is not the dominating effect.

5.2.3 Rationalization of the Potential-Induced Mechanistic Switch

In the following section, we discuss two possible molecular origins for our proposed potential-induced mechanistic switch. First, we show that the interfacial electric field at the electrocatalyst/electrolyte contact may affect the relative activation barriers of the two pathways, and, thus, the relative weight of each route as the potential is altered. Second, we performed a density functional theory (DFT) study of the two routes. These calculations show that only at high potentials does the WNA mechanism become thermodynamically accessible. In a practical system, the two effects may synergistically combine to favor the WNA pathway at high electrode potentials. Next, we first discuss the impact of the interfacial electric field on the activation barriers; then we describe the insights derived from the DFT modeling.

The key distinction between the IMOC and WNA pathways is the involvement of water in the rate-determining step of the latter one (Figure 5.1). On the basis of this observation, we expect the energetics of the two pathways to exhibit distinct sensitivity to the interfacial electric field. The magnitude of the interfacial electric field of the electric double layer increases as the potential of the electrode is increased. It is well established that electric fields can profoundly impact the rates and selectivity of chemical reactions [143, 203, 360–362]. Reaction intermediates with sufficiently large dipole moments and polarizabilities can interact with the electric fields. As a result of this interaction, the free energy profile of the reaction processes can be altered [143, 203]. Nørskov *et al.* have shown that the impact of electric fields on surface-bound water oxidation intermediates (M-OOH, M-OH, M=O) is typically very small because these species have small dipole moments and polarizabilities [361]. On the basis of these findings, it is likely that the interfacial electric field has negligible impact on the IMOC pathway. Because the rate-determining O-O bond formation step is a chemical step, we expect the principal activation barrier of the IMOC

pathway to be independent of the electrode potential. By contrast, because water has a relatively large dipole moment and polarizability, the orientation and dynamics of water molecules at electrified interfaces may strongly depend on the electrode potential [362–364]. It has been suggested that the water dynamics and structure at interfaces affect the rates of various electrocatalytic processes, such as water oxidation and reduction [354, 362]. Therefore, even though O-O coupling in the WNA as hypothesized in Figure 5.1 is a chemical step, we expect the activation barrier of this process to depend on the electrode potential: $\Delta G^{\neq}_{\mathrm{WNA}} = \Delta G^{\neq}_{\mathrm{WNA}} - \Delta\overrightarrow{\mu} \cdot \overrightarrow{E}$, where $\Delta G^{\neq}_{\mathrm{WNA}}$is the standard chemical free energy of activation in the absence of an electric field; $\Delta\overrightarrow{\mu}$ represents the change in the surface dipole when going from the reactant to the activated complex state; and $\overrightarrow{E}$ is the interfacial electric field, which depends on the electrode potential. These qualitative considerations show that because of the participation of water in the rate-determining chemical step of O-O bond formation for the WNA mechanism, the activation barrier of this step is a function of electrode potential. Nevertheless, without knowledge of the molecular-level structure of the electrocatalyst/electrolyte interface at the present time, our considerations must remain qualitative in nature at the present stage. Irrespective, this model describes one possible origin of the observed mechanistic switch from the IMOC route to the WNA pathway with increasing potential.

To explore further other possible causes of the potential-induced switch, we studied the energetics of the two pathways with DFT. All calculations were performed with the B3LYP functional and def2-SV(P) and def2-TZVP basis set implemented in the Gaussian 16 software package. Further computational details are provided in the Appendix. We constructed atomic models on the basis of previous EXAFS [327] and X-ray pair distribution function analysis. The $Co_7O_{24}H_{27}$ cluster has a Co ion surrounded by 6 Co ions at the edge which are connected to the center Co ion by μ_3-O bridges (Figure A5.21). The energetics of the water oxidation reaction is sensitive to the protonation state of the clus-

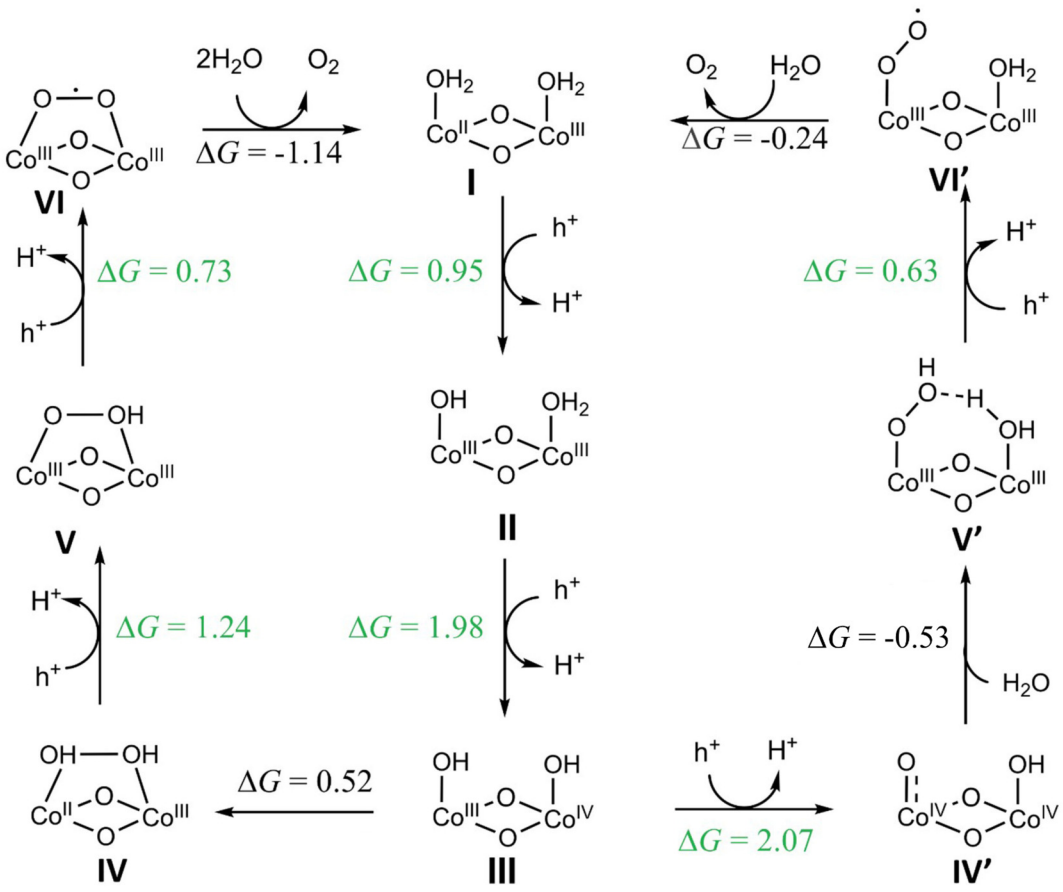

Figure 5.4: Possible routes of water oxidation suggested by the DFT calculations. Left: the IMOC mechanism under low overpotential (thermodynamically favored pathway); right: the WNA mechanism under high overpotential. The calculated free energy changes (ΔG) are given in the unit of eV. The numbers shown in green are the free energy changes of electrochemical steps vs. the computed hydrogen electrode.

ter [328, 329]. We considered different protonation states and found that the lowest energy protonation state is a highly symmetric cluster with one side of the μ_3-O being protonated, and each pair of edge Co ions having strong hydrogen bonds between nearby hydroxide and water ligands (Figure A5.22). The protonation of the hydroxide ligand of the edge Co atoms is energetically unfavorable since it destroys the strong hydrogen bond interaction between OH^- and nearby H_2O. However, the edge OH^- group can be protonated by reducing the corresponding edge Co(III) to Co(II) (Figure A5.23).

On the basis of this structural model, we investigated the water oxidation mechanism (Figure 5.4) starting from the H_2O-Co(II)-($\mu-O)_2$-Co(III)-OH_2 intermediates (I). We note that our computational method overestimates the oxidation potential of Co(III) to Co(IV) by $\sim$0.3 V (Figure A5.24). All potentials quoted herein are not corrected for this systematic error. The oxidation of Co(II) to Co(III) requires 0.95 V, which is much lower than the applied potential during catalysis. The second oxidation requires 1.98 V to generate intermediate III with one Co oxidized to Co(IV). This oxidation is a metal-center oxidation, consistent with XANES results of the Co-Pi catalyst under catalytic conditions, which suggest a valence of Co greater than 3 [327]. When the overestimation of the redox potential is accounted for, this intermediate is predicted to be prevalent under water oxidation conditions. Consistent with the prediction, the resting state of the catalyst has been assigned to intermediate III in prior reports [309, 320, 324, 325, 349, 365]. The hydroxide coordinated to the Co(IV) center in intermediate III has a partial radical character as indicated by a Mulliken spin population of 0.21 (Figure A5.25). Therefore, the two hydroxides can couple to form hydroperoxide through the IMOC mechanism. Thermodynamically, this pathway is favored over the WNA pathway under low applied potentials. The following two oxidations require low potentials. Therefore, it is fairly easy to form intermediate VI. The release of O_2 and binding of two water molecules complete the catalytic cycle.

Under high applied potential, intermediate III can be further oxidized to form intermediate IV' with two nearby Co being oxidized to Co(IV). The terminal O atom coordinated to Co(IV) is best described as an oxyl radical since the Mulliken spin population on the O atom is 0.89 (Figure A5.25), close to 1 for a perfect radical. The intermediate IV' can react with a water molecule from the solution to form intermediate V' through the WNA mechanism. The incoming H_2O forms hydroperoxide with the oxyl radical and releases a proton to the nearby OH^- group. Intermediate V' can be further oxidized to intermediate VI', which releases O_2 and adsorbs a water molecule to complete the catalytic cycle.

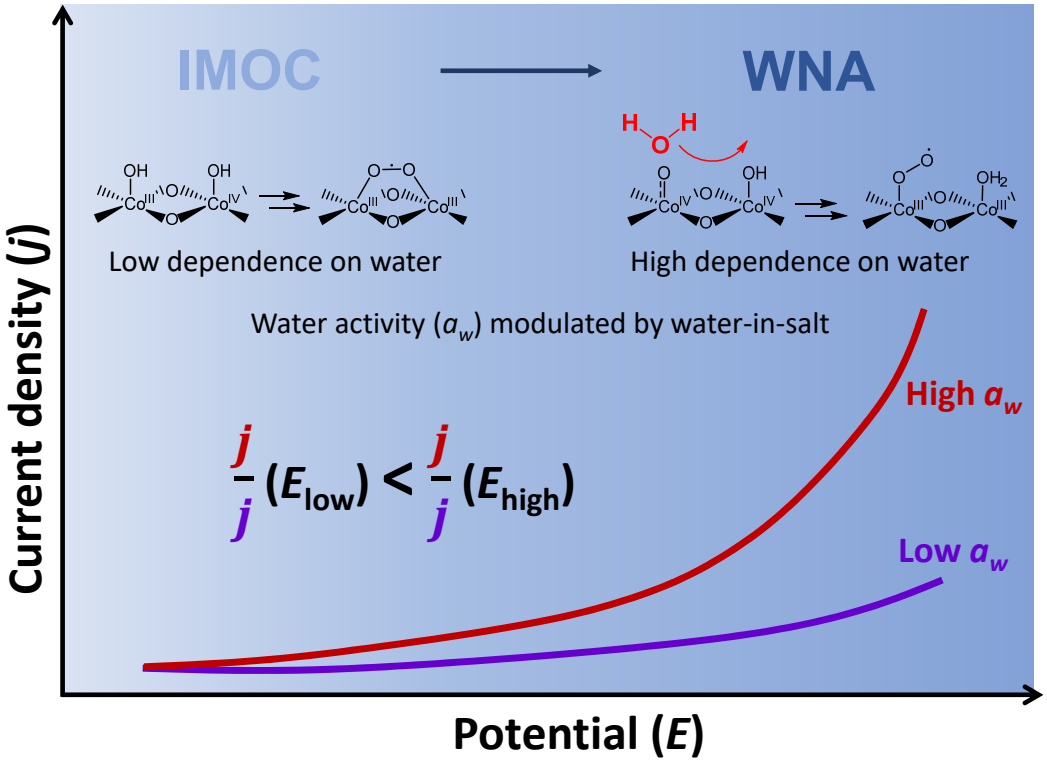

Figure 5.5: Schematic representation of the key findings and conclusions of this work.

We note that both IMOC and WNA mechanisms feature a superoxo intermediate (VI and VI', respectively). This prediction is consistent with our spectroscopic results, which indicate the presence of a superoxo species. On the basis of the simulated O-O vibrational frequencies (Figure A5.26) alone, we cannot identify which of the two species gives rise to the vibrational band at 1,014 cm^{-1} (Figure 5.2). We reserve a more detailed assignment for future investigations.

Although alternative reaction pathways may be available [329, 366], the DFT computations show that (1) the IMOC and WNA pathways are feasible from a thermodynamic perspective and (2) their energetics are consistent with the proposed mechanistic framework (Figure 5.1) and the interpretation of our electrokinetic results (Figure 5.3): At low overpotential, the IMOC pathway predominates, whereas the WNA pathway becomes ac-

cessible at high overpotential. Lastly, it is noted that, in line with prior precedence, we only considered the thermodynamics of the pathways [313, 366]. The calculation of the activation barriers is complicated by spin-state changes during the conversion of intermediate III to IV. Further, the activation barriers are sensitive to the protonation state of the catalyst, which is a complex function of applied electrode potential and reaction conditions. Fully accounting for these complications will require additional research that is beyond of the scope of the current work.

Taken as a whole, the thermodynamic description of the two pathways and the qualitative considerations of the impact of the interfacial field on the relative magnitude of activation barriers of the O-O bond-forming steps provide strong support for the conclusion of a potential-dependent mechanistic switch. The DFT modeling predicts that a certain threshold potential for the WNA pathway needs to be surpassed before this pathway becomes thermodynamically feasible. In addition, the involvement of water in the rate-determining step may further lower the activation barrier for the O-O bond formation step for the WNA route, leading to a further acceleration of the reaction rate. Our conclusions are graphically summarized in Figure 5.5.

5.2.4 Broader Implications

Prior research on homogeneous water oxidation mechanisms has revealed that the 4-proton, 4-electron process of water oxidation can take place on a mononuclear or a dinuclear catalyst. Whether WNA or oxygen-coupling is the preferred mechanism has been at the center of intense studies for the natural photosystem II, as well as for molecular catalysts. In testing the various hypotheses for the reaction mechanisms, researchers mainly relied on kinetic models that depend on the information of key species, such as the concentration of the catalyst and the turn-over frequencies. In principle, the same methodology could be applied for the establishment of a similar knowledge base for heterogeneous wa-

ter oxidation reactions. However, the lack of knowledge on the detailed information of the catalytically active centers creates a critical challenge for such an approach. Our strategy of probing the kinetics of heterogeneous water oxidation by varying water activities is new. It generates information that permits the verification of hypotheses that are difficult or impossible to obtain by other methods. How the water oxidation reaction proceeds is sensitive to a number of factors, including the local catalytic environment (*e.g.*, the availability of mononuclear, dinuclear or multinuclear active centers), substrate concentration, as well as the driving forces. While our studies suggest that the WNA mechanism is favored at high driving force, we are inspired to understand that in a practical water oxidation system (such as the Oxygen Evolution Catalyst in Photosystem II or in an electrolyzer), both mechanisms may co-exist. The fact that this switch is observed on Co-Pi and $CoO_x(OH)_y$ (Figures A5.7 and A5.27) suggests that the potential-induced changes in pathway may be a more general phenomenon of Co-oxide based electrocatalytsts. The dynamic switch of the mechanisms could help to explain how Nature ensures the most efficient route for the utilization of solar energy to liberate electrons and protons; it also implies that future designs and optimization of heterogeneous catalysts for large-scale engineering implementations of water oxidation should consider the facile switch of reaction mechanisms. It is noted that the WNA mechanism could proceed through a mononuclear site or a dinuclear site depending on the catalytic conditions [307, 367, 368]. However, it likely makes only a minor contribution to our study because of the narrow and low overpotential regime investigated, as well as the equivalent involvement of water molecule in the rate-determining step on both sites. Lastly, while we envision that studying water oxidation by varying water activities indeed adds a new dimension to the tool kit, it faces limitations for systems at highly alkaline conditions where OH^- but not H_2O is being oxidized.

5.3 Conclusion

In conclusion, this work introduced two key innovations. Using SEIRAS-ATR, we detected a key intermediate corresponding to O-O bond formation in Co-based water oxidation. This information lends support to the proposed mechanisms. By varying the water activity, we established a kinetic model that allowed us to verify the two competing mechanisms of water oxidation. We found that the dinuclear route (*i.e.*, IMOC) is favored at relatively low driving forces, whereas the mononuclear route (*i.e.*, WNA) is preferred at relatively high driving forces. The results contribute significantly to the understanding of water oxidation by heterogeneous catalysts.

5.4 Experimental Procedurest

5.4.1 Materials

$Co(NO_3)_2$ (99.999%, Alfa Aesar), KOH (85%, VWR International), $NaNO_3$ (99.0% min., Alfa Aesar), $NaClO_4$ (99.0% min., Alfa Aesar), KNO_3 (99.0% min., Sigma-Aldrich), K_2HPO_4 (98.0% min., Alf Aesar), KH_2PO_4 (98.0% min., Alf Aesar), Na_2HPO_4 (99.0% min., Fisher chemical) and $C_2H_3NaO_2$ (99.0% min., Sigma-Aldrich) were used as received. HF (48 wt.%), $NaAuCl_4 2H_2O$ (99.99%; metals basis), Na_2SO_3 (98.5%; for analysis, anhydrous), $Na_2S_2O_3 2H_2O$ (99.999%; trace metal basis), NH_4Cl (99.999%; metal basis), and KNO_3 (99.999%, trace metal basis) were used as received from Fisher Scientific. All electrolyte solutions were prepared with deionized water (Barnstead, 18 MΩ-cm resistivity). $H_2{}^{18}O$ (97% enriched) was used as received from Medical Isotopes, NH. D_2O (99.9%) was used as received from Aldrich.

5.4.2 Au Nanofilm Preparation

The gold nanofilm was electrolessly deposited onto Si wafers (IRUBIS GmbH, Germany) following the reported method [74]. The reflective surface of the Si wafer was polished on a mat using 6 and 1 m diamond slurries (Ted Pella; Redding, CA), then 0.05 m alumina paste (Electron Microscopy Sciences; Hatfield, PA) with cotton swabs, for 5 min respectively. Then, the Si wafer was cleaned with five consecutive 5 min sonication in ultrapure water and acetone alternately. For the deposition, the Si wafer was first etched in 40% NH_4F for 90 s to remove surface oxide and terminate the surface with hydrogen atoms. Au nanofilm was plated by immersing the Si wafer into a 2:1 mixture of a plating solution and 2% HF at 60 °C for 120 s. The plating solution contains 15 mM $NaAuCl_4 2H_2O$, 150 mM Na_2SO_3, 50 mM $Na_2S_2O_3 2H_2O$, and 50 mM NH_4Cl. The resulted resistance of the gold film is 5-10 Ω.

5.4.3 Co-Pi or $CoO_x(OH)_y$ Film Deposition

Co-Pi catalysts were electrodeposited onto substrates in a solution of 0.5 mM $Co(NO_3)_2$ and 0.1 M phosphate buffer (KPi) (pH=7.0) using a Solartron analytical potentiostat by potentiastatical deposition at a potential of 1.14 V vs. the normal hydrogen electrode (NHE) with the passage of 20 mC cm^{-2} [320]. $CoO_x(OH)_y$ electrodes were electrodeposited onto the Pt substrates or Au films in a solution of 10 mM $Co(NO_3)_2$ and 0.1 M $NaCH_3CO_2$ using a VersaStat3 potentiostat (AMETEK; Berwyn, PA). The galvanostatical deposition was set at an anodic current density of 0.05 mA cm^{-2} vs. Pt counter electrode for 5 min [366].

5.4.4 General Electrochemical Methods

All electrochemical experiments were conducted using a CH Instruments or Solartron analytical potentiostat, a Ag/AgCl reference electrode (0.197 V) or a saturated calomel electrode (SCE, 0.242 V), and a Pt counter electrode. Two types of substrates were used for working electrodes: fluorine-doped tin oxide (FTO) electrode and Pt rotating disk electrode. All the electrochemical measurements were conducted on Co-Pi-coated FTO electrodes in a single cell unless otherwise stated. Rotating disk electrode measurements were conducted using a Pine Instruments MSR rotator and a 5 mm diameter Pt-disk rotating electrode. All electrochemical experiments were performed using a three-electrode electrochemical cell containing a $\sim$15 mL electrolyte solution. Unless otherwise stated, all experiments were performed at ambient temperature and electrode potentials were converted to the reversible hydrogen electrode (RHE) scale using an equation: E(RHE) = E(RE) + $E^{\emptyset}$(RE) + 0.059 $\times$ pH, E(RHE) and E(RE) are the potential versus RHE and reference electrode, $E^{\emptyset}$(RE) is the potential of reference electrode. The electrolyte resistance between working electrode (WE) and RE was measured by electrochemical impedance spectroscopy (EIS) and the resistance was used for *iR* compensation. $E(\mathrm{RE})_{actual} = E(\mathrm{RE})_{measured} - iR$ (i and R are the values of current and solution resistance, respectively)

All the water-in-salt (WiS) electrolyte solutions used in the experiments were freshly prepared before every single test. To make the water-in-salt solutions, we first prepared KPi buffer solutions and then added salts into the KPi buffer solutions. pH of all the solutions was adjusted to 7.0 with a freshly prepared 6 M KOH solution in order to prevent the influence of pH on water oxidation activity. Based on the previous literature [348], water activities (a_w) in 0 m $NaNO_3$ @ 0.1 M KPi , 2 m $NaNO_3$ @ 0.1 M KPi, 4 m $NaNO_3$ @ 0.1 M KPi, 7 m $NaNO_3$ @ 0.1 M KPi are calculated as 1, 0.94, 0.89, 0.83, respectively.

5.4.5 Details of the Electrochemical Measurements

The data in Figures 5.3a and 5.3b were collected under steady-state condition, each set of data were repeated three times with a freshly prepared catalyst of similar activity. During the data collection process, the steady-state measurement was performed for about 5 minutes until the current was stable, and then the data was processed by making an average of the last 20 raw data points in steady-state current density vs. potential (*j*-*E*) plots (Figure A5.6 is a representative example of data collection). The data in Figures A5.7 and A5.9-A5.16 were collected under steady-state condition for 3 to 5 min depending on the experiment. The data was processed by making an average of the last 20 raw data points. For Figures A5.17 and A5.20, the samples were subjected to 3 consecutive CV measurements. The second and third CV cycles show consistent result, so the third CV cycles were shown. For Figure A5.19: The data was collected with the same catalyst; we first measured the cyclic voltammetry (CV) plot in D_2O at a scan rate of 20 mV s^{-1} and then performed the same measurement in H_2O.

5.4.6 SEIRAS-ATR Measurement

All *in situ* surface-enhanced infrared absorption spectroscopy in attenuated total reflection mode (SEIRAS-ATR) measurements were carried out using nitrogen-purged Bruker Vertex 70 FTIR spectrometer (Billerica, MA) equipped with a liquid-nitrogen-cooled MCT detector (FTIR-16; Infrared Associates; Stuart, FL). The catalyst coated Si wafer was assembled into a customized polyether ether ketone (PEEK) spectroelectrochemical cell, and coupled vertically with an ATR accessory (VeeMax III; Pike Technologies; Madison, WI). All experiments were run with an incident angle of 50°, a resolution of 4 cm^{-1}, and a scanner velocity of 40 kHz. For all spectra shown, change in optical density was calculated according to Absorbance = -log(*S*/*R*), with *S* and *R* referring to the single beam

sample spectrum and single beam reference spectrum, respectively.

Before and after spectroscopic measurements, the quality of the film electrodes was confirmed by carrying out a CV from 1.0 to 1.6 V vs. Ag/AgCl (1.61 to 2.21 V vs. RHE) at a scan rate of 20 mV s^{-1}. All presented spectra were collected with electrodes that exhibited Co(II)/Co(III) redox peaks in the CVs and a water oxidation current (Figure A5.2).

For spectroscopic measurements, the $CoO_x(OH)_y$ electrode potential was stepped in 0.1 V increments from 2.21 to 1.61 V vs. RHE. The steps were connected by potential ramps of 20 mV s^{-1}. Each potential was held for 120 s. During this time, infrared spectra were collected. Spectra collected at 2.21 and 2.01 V (sample potentials) are shown in Figures 5.2 and A5.3-A5.5. The single beam spectra collected at 1.61 V vs. RHE served as the reference spectrum. A leakless Ag/AgCl (ET072-1; eDAQ, Colorado Springs, CO) and Pt wire (99.95%; BASi Inc.; West Lafayette, IN) were used as reference electrode and counter electrode, respectively. The electrolyte was prepared with 0.1 M KPi in D_2O, H_2O, or H_2 ^{18}O at pH = 7, and the solution pD value was corrected with a factor of 0.4 from the reading of a pH meter [369].

5.4.7 Faraday Efficiency Measurement

Faradaic efficiency (FE) was measured with gas chromatography-online method (GCMS-QP2010, Shimadzu). A piece of FTO (1×3 cm^2) was used for growing Co-Pi catalyst. The method for growing the catalyst is the same as that described in the Co-Pi or $CoO_x(OH)_y$ Film Deposition part. O_2 gas was detected. During the experiment, the Co-Pi-coated FTO electrode was immersed into a reaction cell containing about 20 mL 0.1 M KPi neutral electrolyte. A constant current (3 mA) was applied to the electrode in order to generate O_2 bubbles. Then, the O_2 gas was further purged into the gas line of gas chromatography-mass spectrometry (GC-MS) for FE measurement. The equation for calculating FE is

given below:

$$FE = \frac{4 \times Oxygen\ amount\ (umol \cdot\ s^{-1})}{Charge\ (umol \cdot\ s^{-1})} \times 100\%$$

5.4.8 Computational Details

All DFT calculations were performed with Gaussian 16 Revision C01 software package [370]. We used the B3LYP functional [371, 372] in conjugation with the def2-SV(P) basis set [373] for all atoms in the geometry optimization. Frequency analysis was performed to verify the nature of obtained stationary points and obtain harmonic frequencies to calculate the zero-point energies and thermal correction to the entropy and free energy. We used the def2-TZVP basis set [373] for single-point energy calculation to final composite free energy changes. The solvation effect was considered the SMD implicit solvation model [374] and the dispersion correction was considered using Grimme's empirical dispersion correction version 3 with Becke-Johnson damping [375]. We performed geometry optimization in both gas phase and dielectric continuum with SMD. We found that the geometry relaxation in the solvation is quite significant (Figure A5.22), therefore, all the geometries except H_2 and O_2 used in the manuscript were optimized with the SMD implicit solvation model.

We considered different sizes of Co clusters and found the planar $Co_7O_{24}H_{27}$ cluster with edge-sharing CoO_6 octahedral is the most stable structure, which is consistent with the structure model suggested by EXAFS study [327]. We considered different protonation state of the $Co_7O_{24}H_{27}$ cluster by placing protons at different O positions and found the most stable configuration corresponds to protonated μ_2-O and μ_3-O bridges, which was used for our mechanistic investigation. We simulated the O-O vibrational frequency of the O-O bond in possible intermediates. We used the atomic masses of specified isotopes and diagonal the Hessian matrix in the mass-weighted coordinates to obtain the vibrational

frequency for different isotopes.

The free energy changes of proton-coupled electron transfer steps were calculated with Nørskov's computational hydrogen electrode (CHE) approach [376] to get the free energy change with respect to the reversible hydrogen electrode (RHE) to avoid the explicit use of the hydrated proton and to include the pH effect naturally. Its procedure is given below:

1. Calculate the free energy change (ΔG_1) with respect to the release of equivalence of H_2(g):

$$RH \rightarrow Ox + \frac{1}{2}H_2\left(g\right),\ \Delta G_1$$

2. Use the definition of RHE:

$$\frac{1}{2}H_2\left(g\right) \rightarrow H^+\left(aq\right) + \ e^-,\ \Delta G_2$$

3. Free energy change of a proton-coupled electron transfer step (ΔG_3) with respect to RHE can be calculated by adding ΔG_1 and ΔG_2:

$$RH \rightarrow Ox + \ H^+ + \ e^-,\ \ \Delta G_3 = \Delta G_1 + \Delta G_2$$

We also considered the water oxidation mechanisms on CoOOH. Given the nature of this system, we applied periodic boundary condition to study the catalytic mechanism on CoOOH surfaces. All calculations for the CoOOH system were performed with the Vienna Ab initio Simulation Package (VASP) [377–380]. We use the Perdew-Burke-Ernzerhof (PBE) exchange-correlation functional [381] in conjugation with the projected-augmented wave (PAW) method [382, 383] to describe the ion-electrons interactions. A cutoff energy of 500 eV was chosen for the plane wave basis set in all calculations. We used the Gaussian smearing method to accelerate SCF convergence and the σ value was chosen to be 0.1 eV. The standard GGAs fail for strongly correlated systems such as the d electrons of Co. All

calculations involving Ir and Ce atoms were performed with the spin-polarized DFT+U method, using the rotational-invariant formalism developed by Dudarev *et al.* [384]. The empirical U_{eff} parameters were chosen to be 3.4 eV for Co 3d electrons [385].

A 9 $\times$ 9 $\times$ 9 Monckhorst-Pack type k-point grid [386] was chosen for the optimization of bulk ceria. The energy convergence criterion was set to be 10^{-6} eV per unit cell and the geometry convergence criterion was set to be 10^{-5} eV per unit cell for energy difference between two consecutive ionic steps. The optimized lattice constants $a = b = 2.88$ Å and $c = 13.17$ Å are in good agreement with experimental lattice constant of $a = b = 2.85$ Å and $c = 13.15$ Å [387].

We prepared slab models for the CoOOH (012) surface to study the water oxidation mechanisms on the the CoOOH (012) surface. CoOOH (012) surface with 3 layers of Co atoms with both sides terminated by water ligands are used in the study (Figure A5.21). A vacuum layer of $\sim$ 15 Å was used to minimize the artificial interactions between periodic images. A supercell of 13.52 Å $\times$ 31.54 Å $\times$ 14.37 Å was used to model the CoOOH (012) surface. The atoms in the bottom one layers were fixed at their optimized positions, while the atoms in the top two layers, as well as the adsorbates, were allowed to relax during geometry optimization. A 1 $\times$ 1 $\times$ 1 Monckhorst-Pack type k-point grid was used for all surface structure relaxations unless otherwise noted. The energy convergence criterion was set to be 10^{-5} eV per super cell and the force convergence criterion of 0.03 eV Å^{-1}.

The calculations of isolated small molecules were performed with a supercell of 15.0 Å $\times$ 15.0 Å $\times$ 15.0 Å. The Gaussian smearing method and a σ value of 0.1 eV were used in the calculations. A 1 $\times$ 1 $\times$ 1 Monckhorst-Pack type k-point grid was used to sample the Brillouin zone and the SCF convergence criterion was set to be 10^{-5} eV per unit cell.

The energy changes obtained from the periodic boundary calculations were corrected by the thermo-correction from the cluster model to obtain the free energy changes given in Figure A5.27. The saturated vapor pressure of water at 298.15 K (3.169 kPa) was used to

obtain the free energy changes of $H_2O(g)$ $H_2O(l)$.

5.5 Addendum

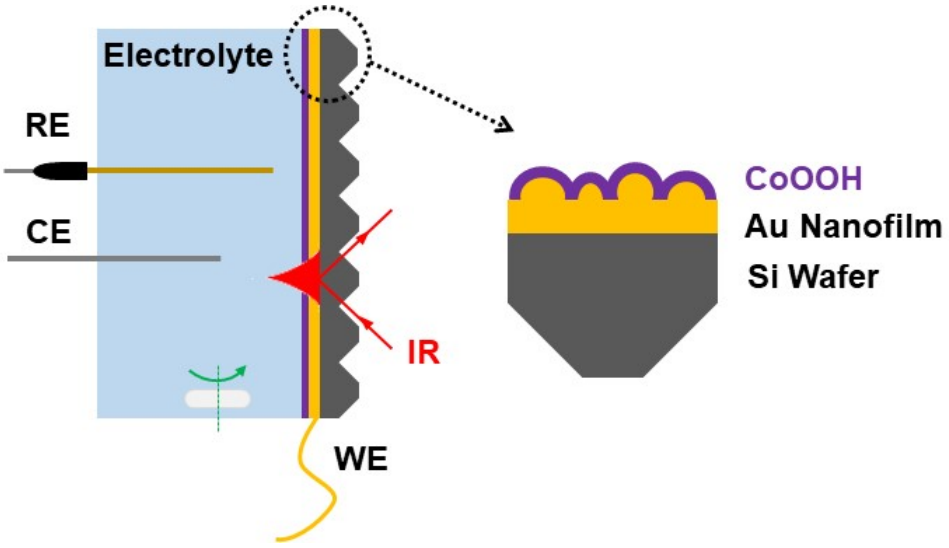

Figure A 5.1: Experimental configuration for SEIRAS. WE, CE, and RE denote the working electrode, counter electrode, and reference electrode, respectively.

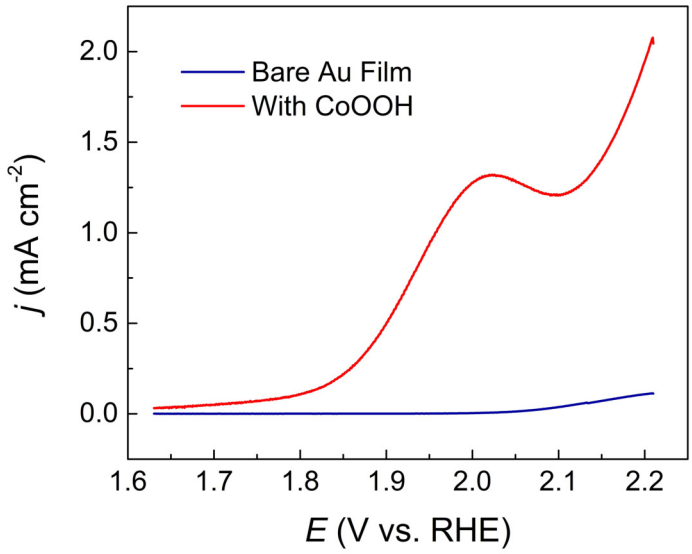

Figure A 5.2: Water oxidation activity comparison between bare Au film and $CoO_x(OH)_y$-Au sample. The CVs were collected from 1.61 to 2.21 V at a scan rate of 20 mV s^{-1}. The current data are from the third forward scan of the catalyst. All the data were corrected with *iR* compensation.

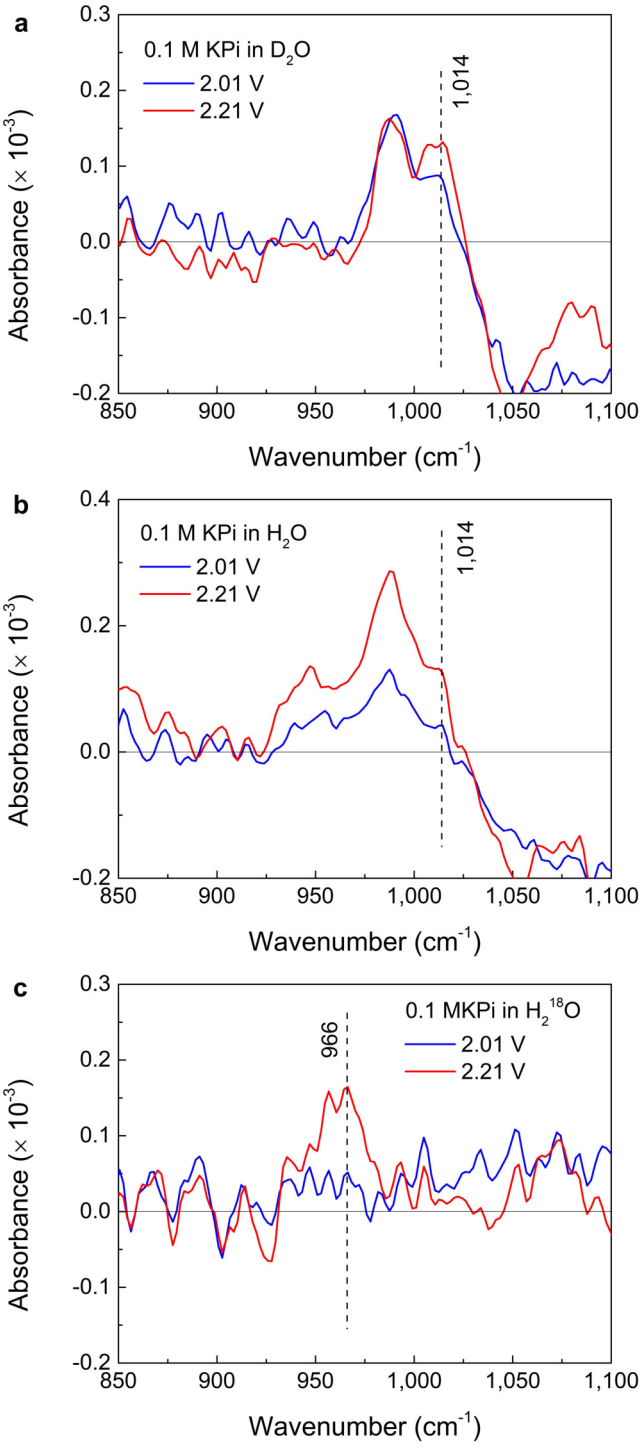

Figure A 5.3: The intensity of the band centered at 1,014 cm^{-1} at 2.21 V increases with increasing applied potential in 0.1 M KPi with (**a**) D_2O, (**b**) H_2O, and (**c**) $H_2{}^{18}O$.

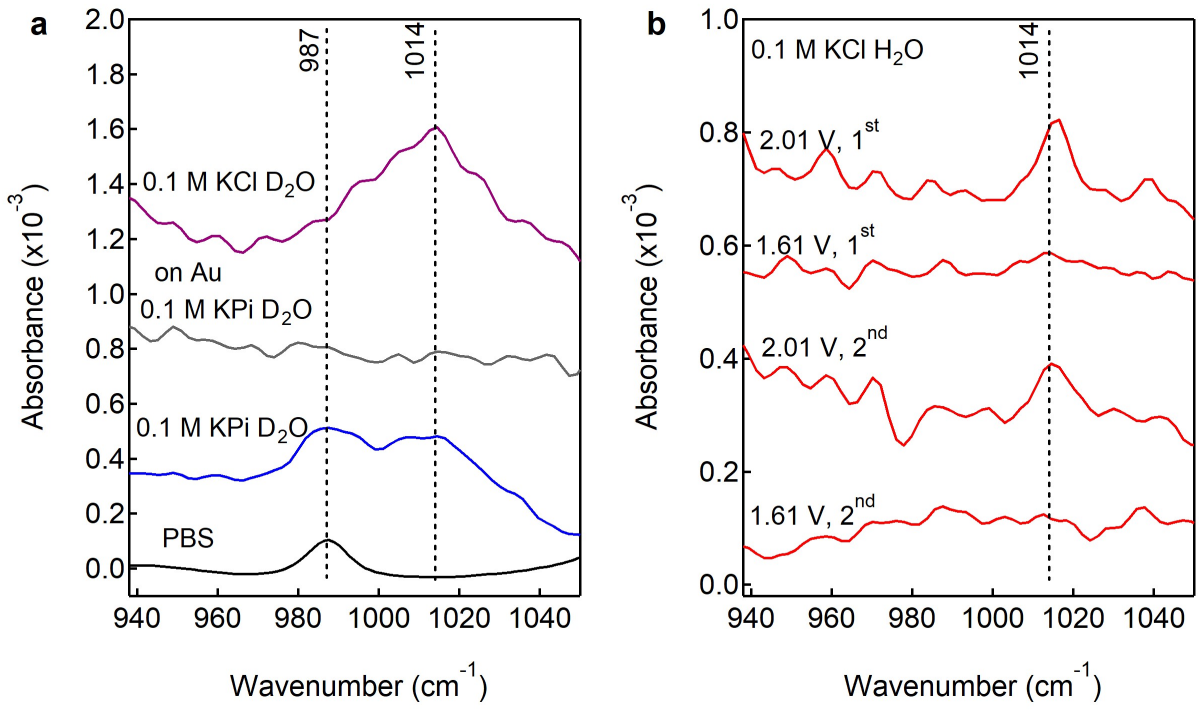

Figure A 5.4: Control experiments for ruling out the complication brought up by solution species: (**a**) A prominent band at 1,014 cm^{-1} is observable in 0.1 M KCl with D_2O at 2.21 V, while the band does not appear on a bare Au at the same potential. PBS indicates the spectrum of a bulk phosphate solution. (**b**) The band at 1014 cm^{-1} shows a potential-dependent reversibility as potential is switched between 2.01 V and 1.61 V (two cycles are shown labeled as "1^{st}" and "2^{nd}".

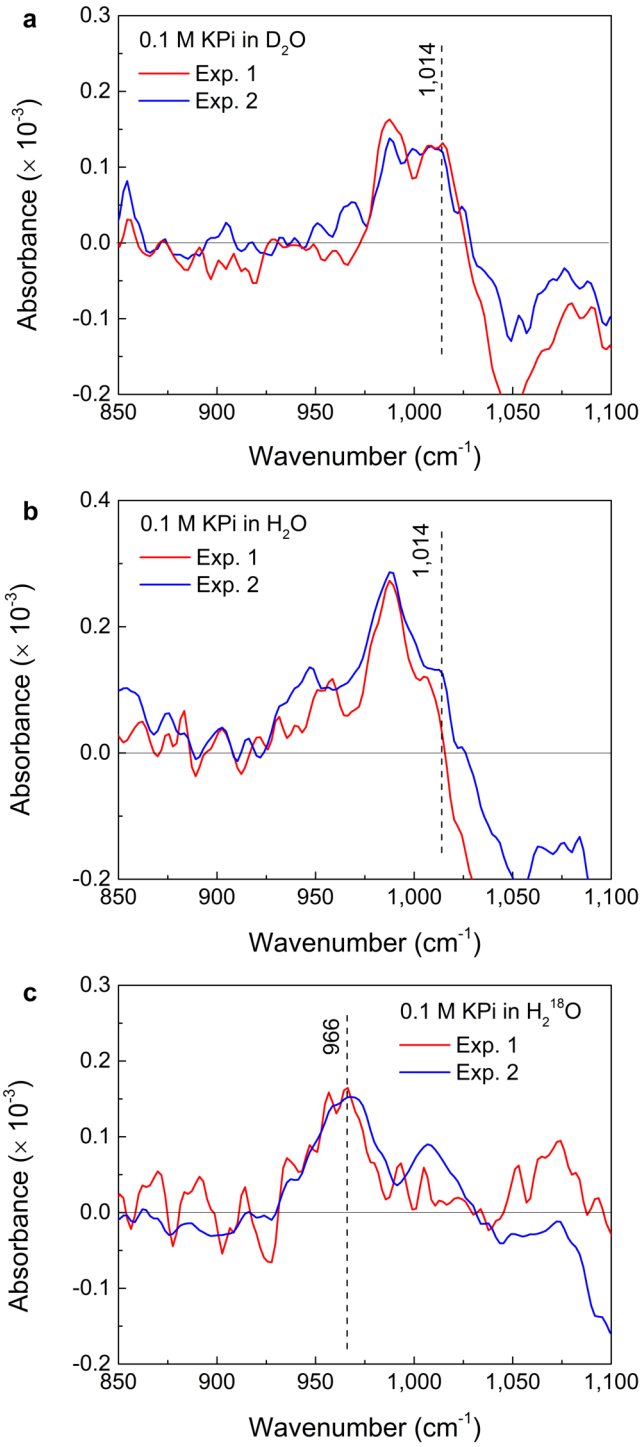

Figure A 5.5: SEIRAS data collected on different samples in 0.1 M KPi with (**a**) D_2O, (**b**) H_2O, and (**c**) $H_2{}^{18}O$, to demonstrate reproducibility at 2.21 V. Reference spectra were taken at 1.61 V

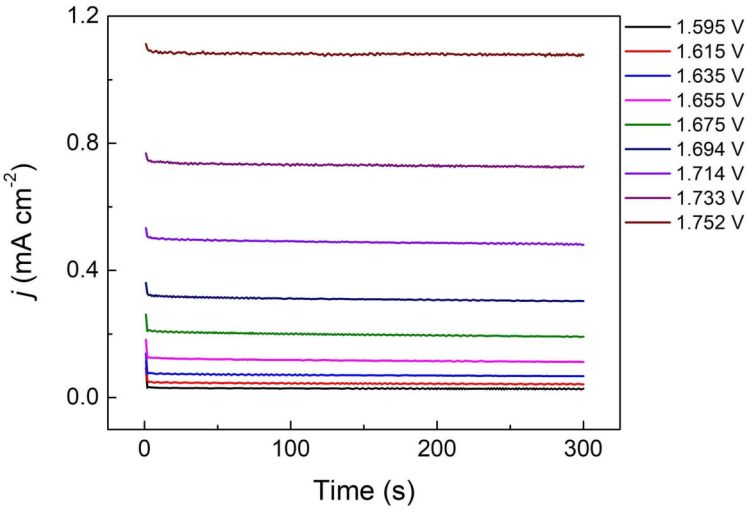

Figure A 5.6: Representative steady-state electrochemical *j*-*t* plots of water oxidation on Co-Pi catalysts in 0.1 M KPi containing 2 m $NaNO_3$ electrolyte (a_w= 0.94) at various potentials as indicated. The electrode potential was corrected for the *iR* drop.

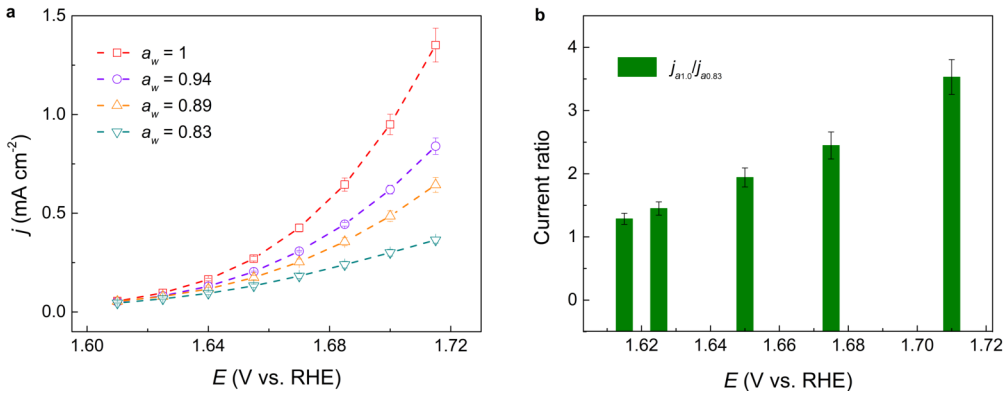

Figure A 5.7: Steady-state water oxidation current density as in Figures 5.3a and b, but collected on a $CoO_x(OH)_y$-coated Pt electrode under stirring condition. The data were derived from an average of three independent experiments for each a_w. Error bars denote the standard deviation of three individual measurements. Error bars denote the standard deviation of three individual measurements. The electrode potential was corrected for the *iR* drop.

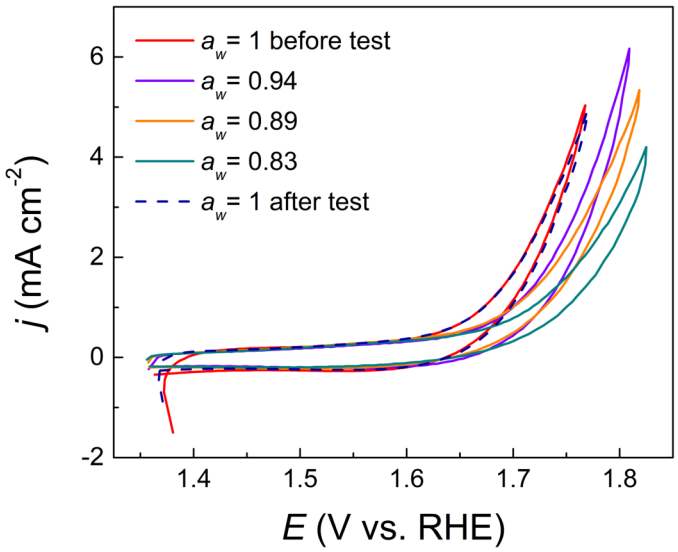

Figure A 5.8: CV stability test of the same Co-Pi catalyst before and after a series of CVs in water-in-salt electrolytes at a scan rate of 20 mV s^{-1}. The CV measurements are from the first cycle of the catalyst. The electrode potential was corrected for the *iR* drop.

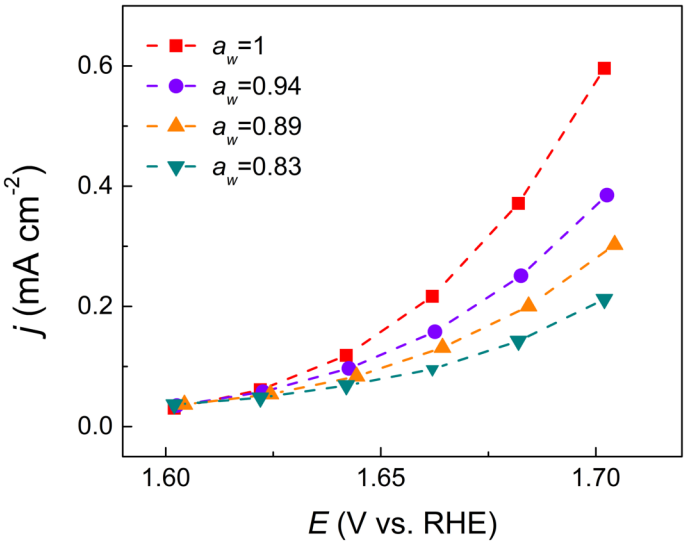

Figure A 5.9: Steady-state water oxidation current density as in Figure 5.3a, but collected on a Co-Pi-coated Pt RDE at a rotation rate of 2,000 rpm. The electrode potential was corrected for the *iR* drop.

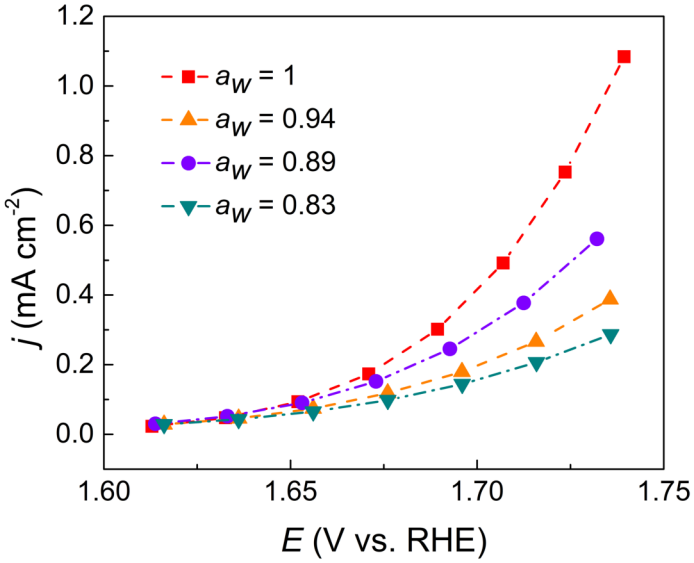

Figure A 5.10: Steady-state water oxidation current density on a Co-Pi-coated Pt RDE as that in Figure A5.9 but collected at a rotation rate of 0 rpm. The electrode potential was corrected for the *iR* drop.

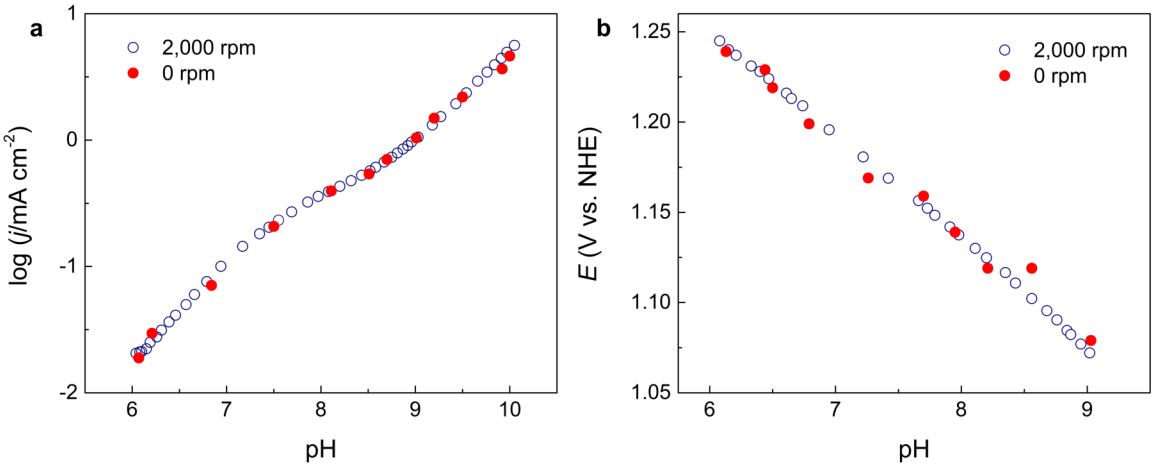

Figure A 5.11: pH titration under (**a**) controlled-potential (1.237 V vs. NHE) and (**b**) controlled-current (30 A cm^{-2}) for a Co-Pi-coated Pt RDE in 2 m $NaNO_3$@0.1 M KPi (a_w= 0.94) at two different rotation rates, as indicated. These data were collected under steady state conditions.

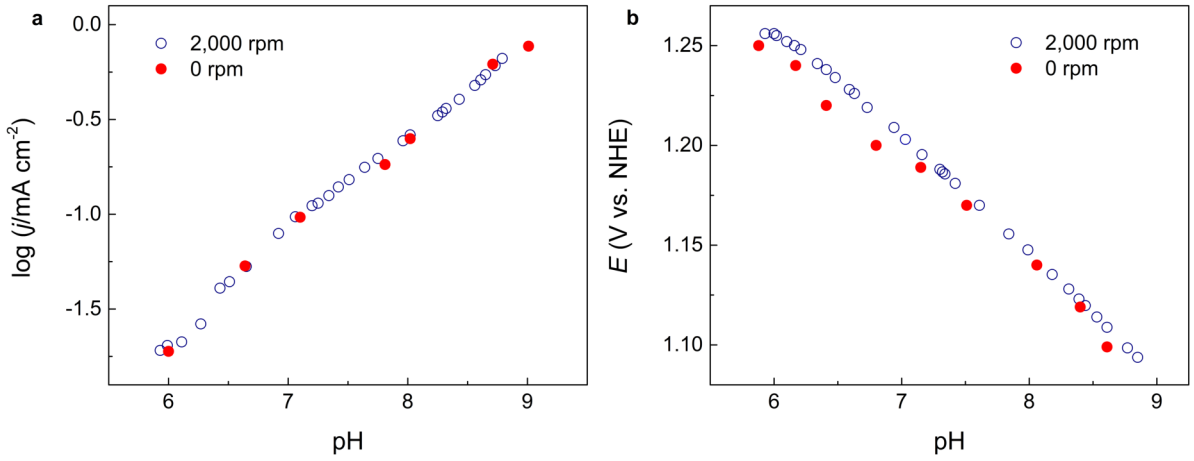

Figure A 5.12: pH titration under (**a**) controlled-potential (1.237 V vs. NHE) and (**b**) controlled-current (30 A cm^{-2}) for a Co-Pi-coated Pt RDE in 4 m $NaNO_3$@0.1 M KPi (a_w= 0.89) at two different rotation rates, as indicated. These data were collected under steady state conditions.

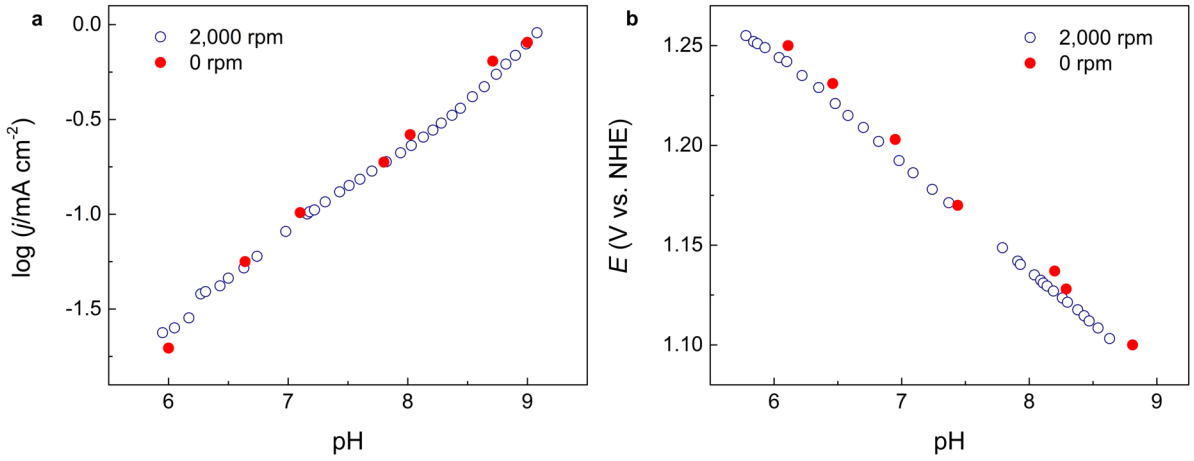

Figure A 5.13: pH titration under (**a**) controlled-potential (1.237 V vs. NHE) and (**b**) controlled-current (30 A cm^{-2}) for a Co-Pi-coated Pt RDE in 7 m $NaNO_3$@0.1 M KPi (a_w= 0.89) at two different rotation rates, as indicated. These data were collected under steady state conditions.

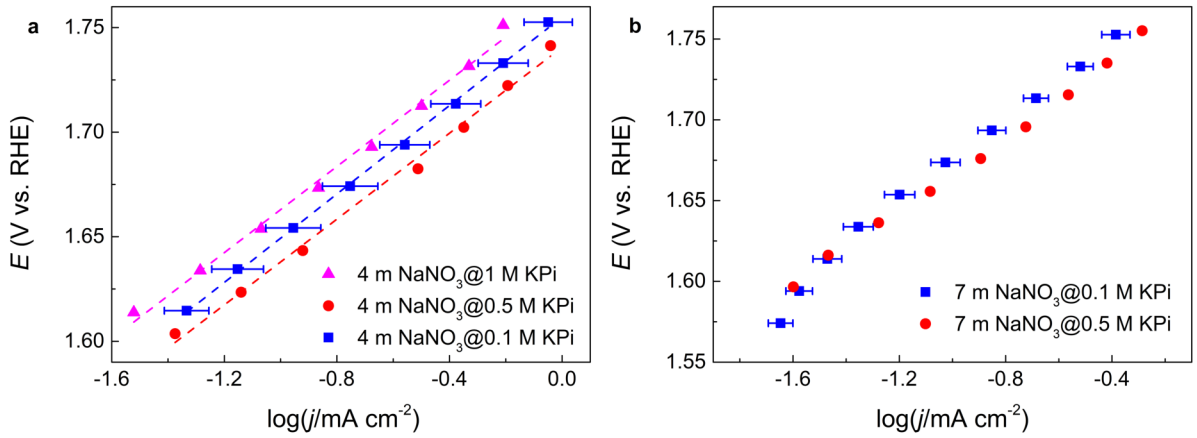

Figure A 5.14: Tafel data for (**a**) 4 m $NaNO_3$ (**b**) 7 m $NaNO_3$ containing different concentrations of KPi indicate that there is no significant dependence of the slope and reaction rate on KPi concentration. These data were collected under steady state conditions. The electrode potential was corrected for the *iR* drop. Error bars denote the standard deviation of three independent measurements.

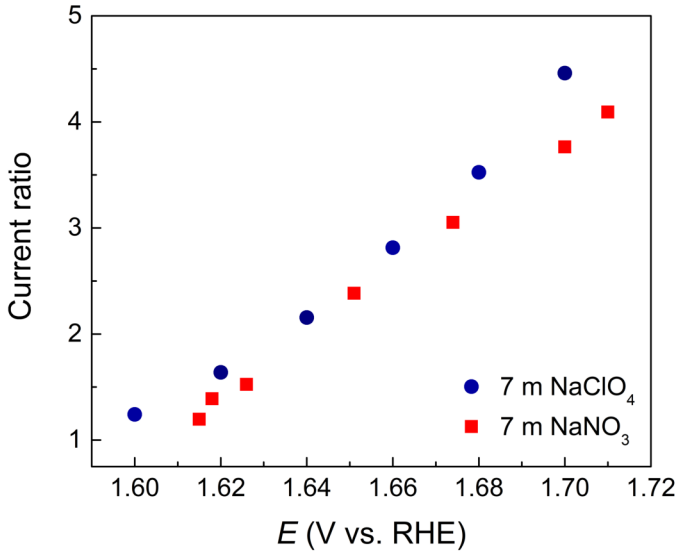

Figure A 5.15: To study the influence of the anion on the electrocatalytic activity, we replaced $NaNO_3$ with $NaClO_4$ to perform a similar potentiostatic measurement. The buffer solution was 0.1 M NaPi to avoid precipitation of $KClO_4$. These data were collected under steady state 0.2 M conditions. The electrode potential was corrected for the *iR* drop.

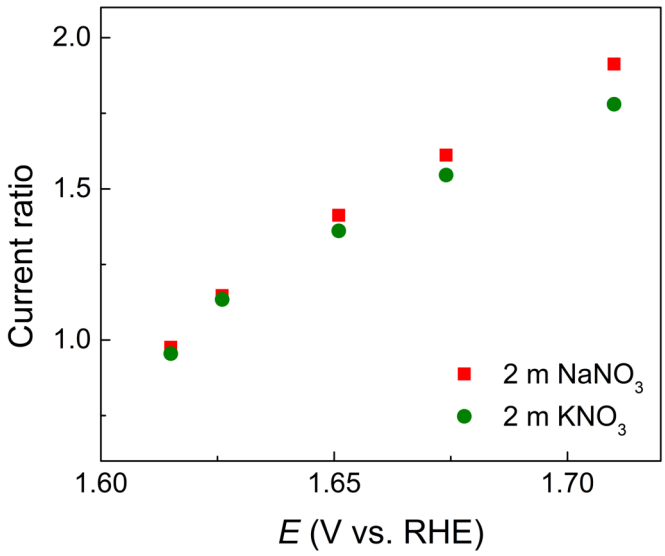

Figure A 5.16: Current modulation ratios in a_w = 0.94 with different cations. The concentration is limited by the KNO_3 solubility. These data were collected under steady-state conditions. The electrode potential was corrected for the *iR* drop.

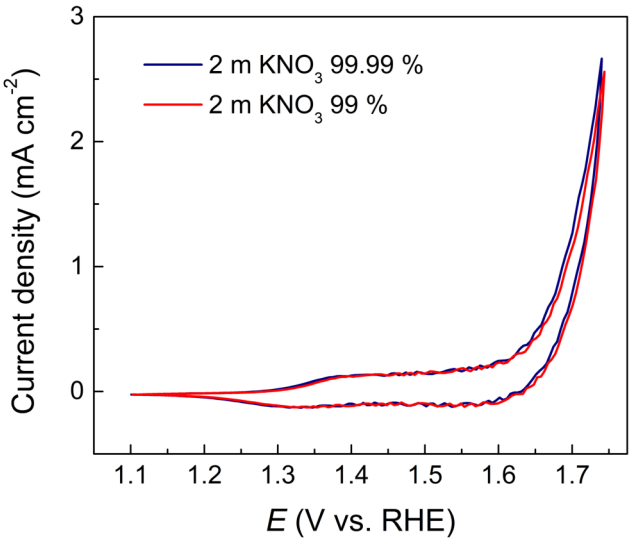

Figure A 5.17: Comparison of CV data collected in 2 m 99% KNO_3 and 2 m 99.99% KNO_3, at a scan rate of 20 mV s^{-1}. The CV measurements are from the third cycle of the catalyst. The electrode potential was corrected for the *iR* drop.

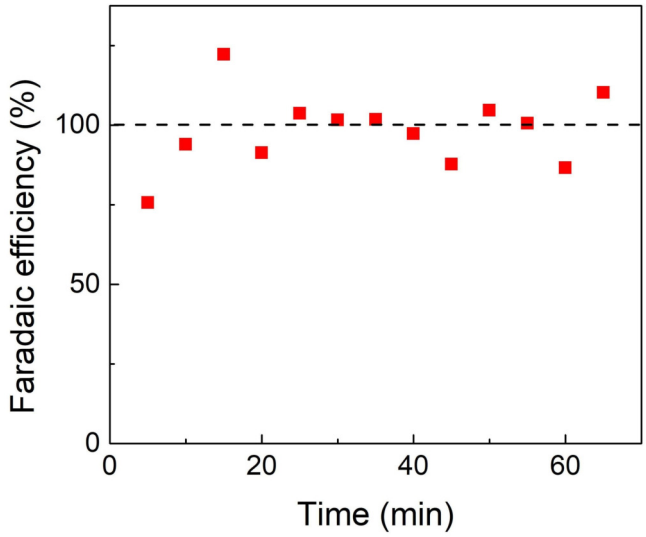

Figure A 5.18: The Faradaic efficiency for O_2 was measured at a current of 3 mA in 7 m $NaNO_3$ solution containing 0.1 M KPi buffer with gas chromatography.

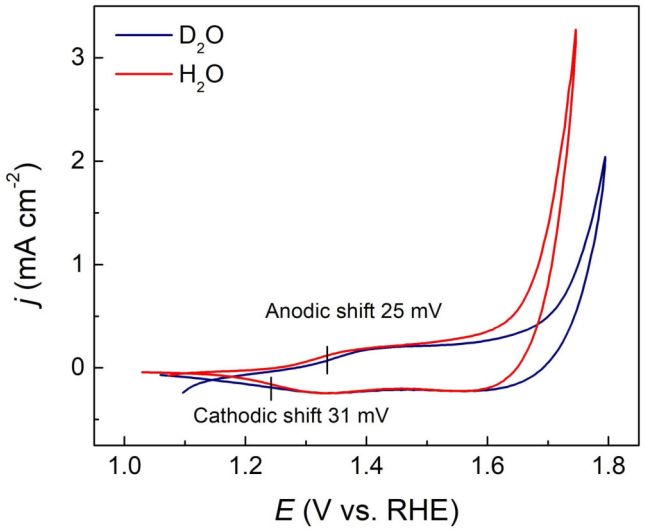

Figure A 5.19: Comparison of CV data collected in D_2O and H_2O, at a scan rate of 20 mV s^{-1}. The electrode potential was corrected for the *iR* drop. The CV measurements are from the first cycle of the catalyst. The shift of the half-wave potential was calculated according to the following equation:

Shift of redox half wave-potential

= (Shift of anodic feature + Shift of cathodic feature) / 2 = (25 mV + 31 mV) / 2 =28 mV

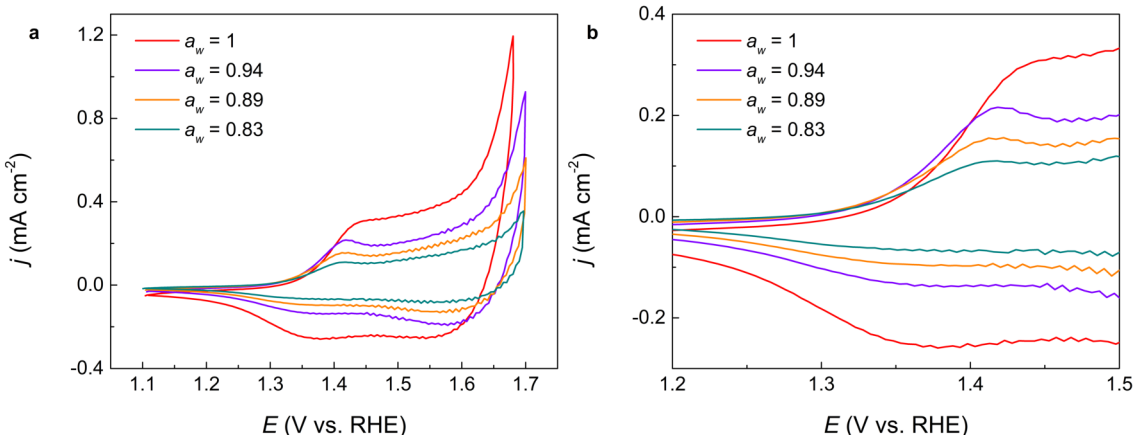

Figure A 5.20: A series of CVs of the Co-Pi catalyst in water-in-salt electrolytes at a scan rate of 20 mV s^{-1} in (**a**) full range and (**b**) zoomed range. The CV measurements are from the third cycle of the catalyst. The electrode potential was corrected for the *iR* drop.

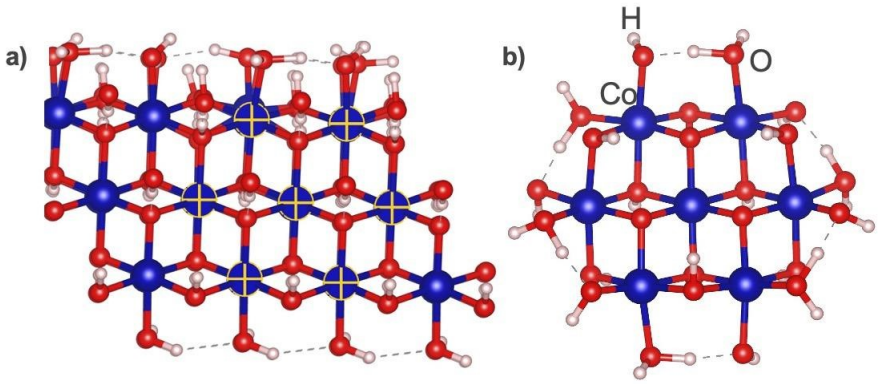

Figure A 5.21: The structural models of (**a**) the CoOOH (012) surface and (**b**) the Co-Pi catalyst. The cluster model of the Co-Pi catalyst is based on previous EXAFS study [327]. The Co7 core in the cluster model resemble the highlighted Co7 unit in the CoOOH structure. The atomic model of Co cluster ($Co_7O_{24}H_{27}$) is constructed for our theoretical study with the water and hydroxides ligands. The blue, red, and white spheres represent Co, O, and H atoms, respectively.

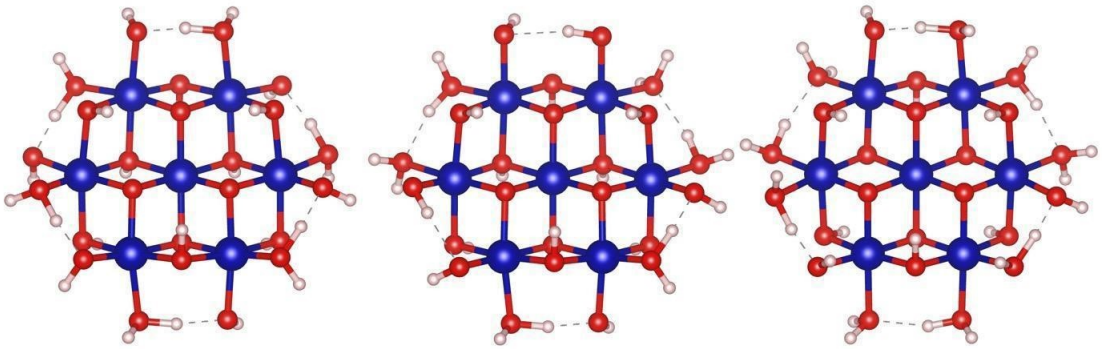

Figure A 5.22: Relative free energies of the $Co_7O_{24}H_{27}$ cluster with different protonation states in gas phase and in aqueous solution. The most stable protonation state (left) has alternative HO—H_2O hydrogen bond interactions at peripheric Co pairs and the bottom μ_3-O bridges being protonated. Destroying the alternative HO—H_2O hydrogen bond interaction by preparing H_2O—H_2O and HO—HO hydrogen bonding pattern increases the energy (middle). Removing the protons from μ_3-O bridges to terminal OH^- increases the energy (right) since it disturbs the strong HO—H_2O hydrogen bond interactions. We choose the most stable protonation state (left) for our mechanistic study. It is worth pointing out that the free energy different in the solution is much smaller than in the gas phase due to a large geometry relaxation due to the high dielectric solvation environment. Therefore, we optimized all geometries in the SMD implicit solvation model.

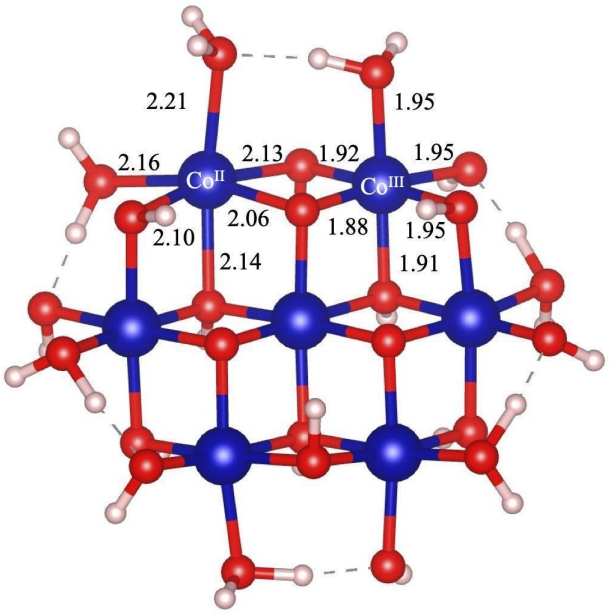

Figure A 5.23: Optimized Co–O bond lengths around the Co(II) and Co(III) centers in intermediate **I**. The Co–O bond lengths are somewhat longer around the Co(II) center since the ground state of Co(II) is a high-spin quartet. In contrast, the low-spin Co(III) center has much shorter Co–O bond lengths and stronger metal-ligand interactions which are crucial for the stability of the molecular-like Co-Pi water oxidation catalyst.

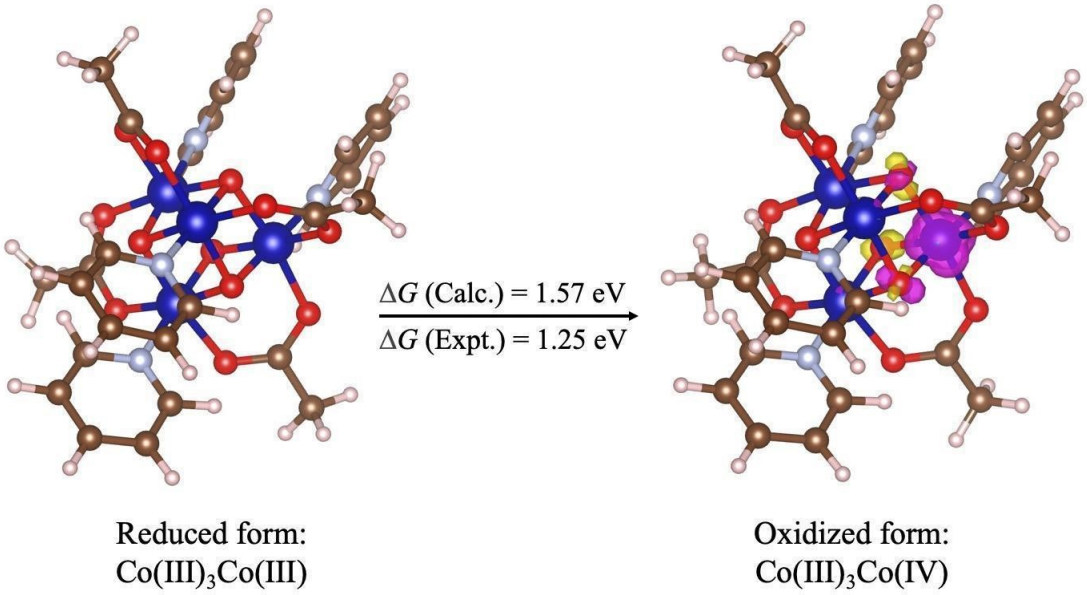

Figure A 5.24: Optimized structures of the $Co_4O_4(OAc)_4(Py)_4$ complex in its reduced and oxidized form. Magenta and yellow isosurfaces show the alpha and beta spin density distribution and are plotted with an isovalue of 0.01 $Å^{-3}$. The calculated and experimental [388] free energy changes with respect to the normal hydrogen electrode (NHE) are 1.57 and 1.25 eV, respectively. Our calculation using the B3LYP functional overestimates the potential for oxidation potential of Co(III) to Co(IV) by 0.3 eV, which is consistent with a recent benchmark study [389], highlighting the difficulty to describe the high oxidation Co complex.

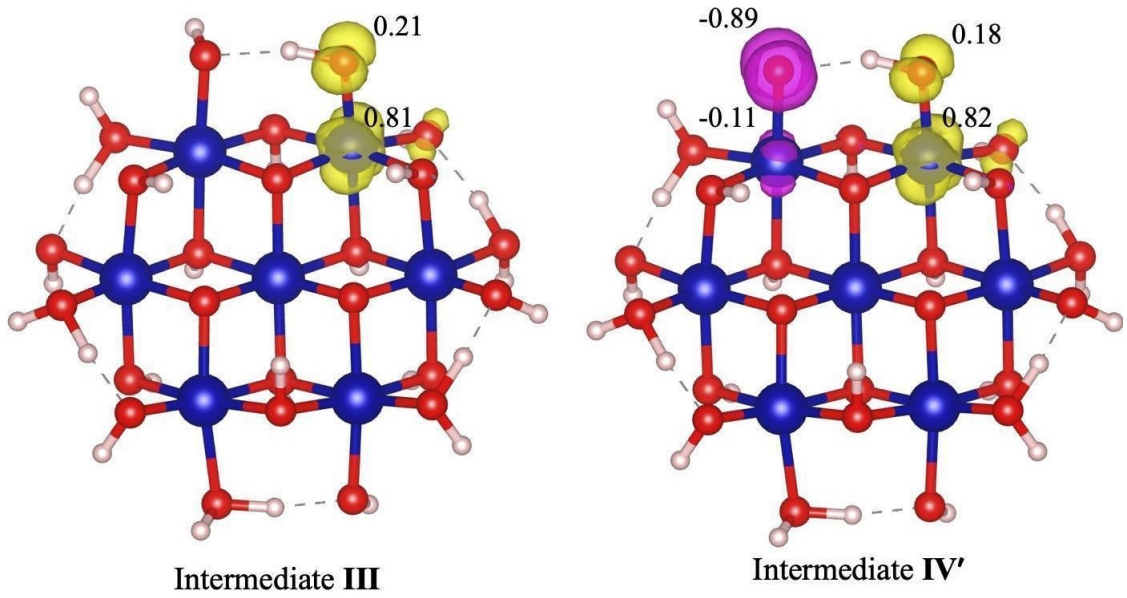

Figure A 5.25: Optimized structures of intermediates **III** and **IV′**.Magenta and yellow isosurfaces show the alpha and beta spin density distribution and are plotted with an isovalue of 0.01 $Å^{-3}$. The numbers next to Co and O ions indicate their Mulliken spin density population. It can be seen clearly that the OH^{-} coordinated to the Co(IV) center has significant radical character while the Co(IV)=O in intermediate **IV′** is best described as Co(III)–O.

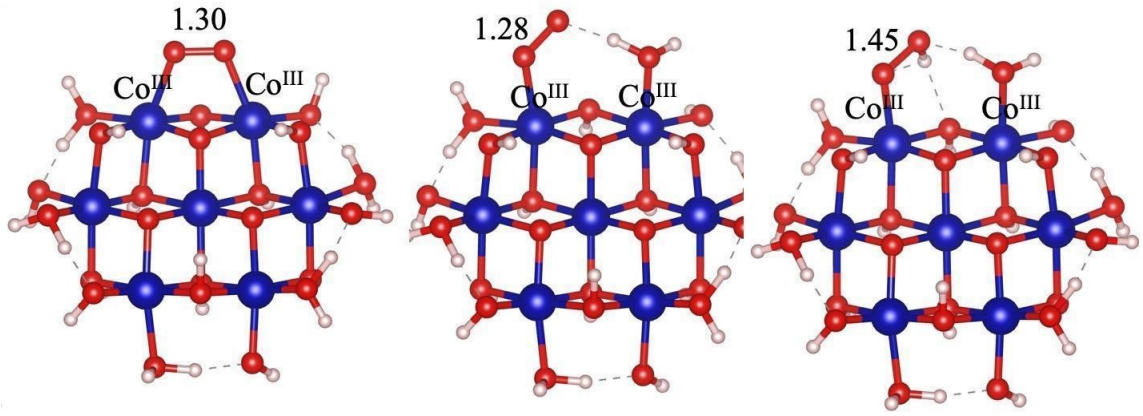

Figure A 5.26: Calculated O–O vibrational frequencies and associated isotope shifts for possible intermediates.

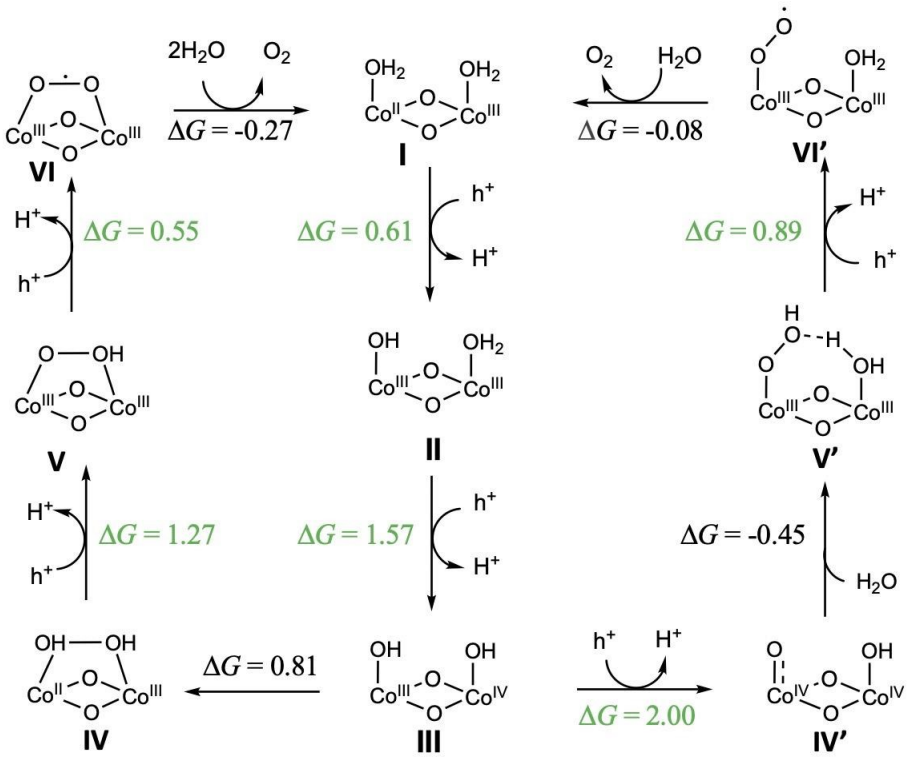

Figure A 5.27: Possible routes of water oxidation on the CoOOH (012) surface suggested by the DFT calculations. Similar to the results of Co-cluster model for Co-Pi system, the IMOC mechanism is possible under low applied potential while the WNA mechanism require higher potential to be accessible. The calculated free energy changes (ΔG) are given in the unit of eV. The numbers shown in green are the free energy changes of electrochemical steps vs. the computed hydrogen electrode.

Table A 5.1: Viscosities (η), densities (d), and stagnant layer thickness (y_s) of water-in-salt electrolytes.

m (mol/kg)	η (cP)	d (g/mL)	y_s at f =2000 rpm (m)
0[a]	1	1	249
2.14[b]	1.04	1.11	241
3.32[b]	1.19	1.16	252
4.62[b]	1.30	1.21	258
6.02[b]	1.62	1.26	283
7.56[b]	1.92	1.30	302

[a] Based on the assumption that the viscosity and density of 0 m solution are 1 cP and 1g/mL.

[b] Based on Ref [390].

The stagnant layer thickness (y_s) is calculated based on

$$y_s = 3.6 \times \left(\frac{\upsilon}{\omega}\right)^{\frac{1}{2}}$$

where $\upsilon = \eta/d$ is the kinematic viscosity, and $\omega = 2\pi f/60$ is the angular rotation rate at f (rotation rate in revolutions per minute) [391].

The viscosity of water-in-salt solutions are expected to increase from 1 to $\sim$ 2 cP when increasing the molality from 0 to 7.56 m [390]. The stagnant layer thicknesses at all molalities fall in the range of 200-300 m, which are expected for conventional RDE measurements at a rotating rate of 2000 rpm. The thickness first decreases with the addition of high molality salt, then it increases as the molality increases. When the molality increases from 2 to 7.56 m, the thickness increases ca. 25%.

5.6 Acknowledgement

The work at Boston College is supported by the U.S. Department of Energy (DOE), Office of Science, Office of Basic Energy Sciences, Chemical Sciences, Geosciences, and Biosciences Division (DE-SC0020261). Work at Yale University was supported by the U.S. Department of Energy (DOE), Office of Science, Office of Basic Energy Sciences, Chemical Sciences, Geosciences, and Biosciences Division (DE-FG02-07ER15909). V.S.B. acknowledges the computer time from the National Energy Research Scientific Computing Center (NERSC) and Yale Center for Research Computing (YCRC).

5.7 Original Publication

This chapter has been published: Lang, C.*, Li, J.*, Yang, K. R.*, Wang, Y.*, He, D., Thorne, J. E., Croslow, S., Dong, Q., Zhao, Y., Prostko, G., Brudvig, G. W., Batista, V. S., Waegele, M. M. & Wang, D. Observation of a Potential-Dependent Switch of Water Oxidation Mechanism on Co-Oxide-Based Catalysts. *Chem*, **7**, 1 (2021).

*These authors contributed equally to this work.

Chapter 6

Conclusions and Outlook

In this dissertation, we demonstrated the application of surface-enhanced infrared absorption spectroscopy (SEIRAS) for probing interfacial properties and reaction intermediates at electrocatalytic interfaces.

In Chapter 3, we detected ethylene formation on Cu during CO reduction in the presence of different quaternary alkyl ammonium cations. We found a strong dependence of the ethylene production rate on cation size. To rationalize this different catalytic performance, we employed CO_{ads} as the molecular probe to quantify the interfacial electric field strength at the Cu electrode. We found these differently-sized cations induced small changes in the interfacial electric field, which are unlikely to give rise to the observed modulation of the catalytic activity. By contrast, we found that an interaction between interfacial water and CO_{ads} is disrupted in the presence of the more hydrophobic cations. On the basis of this observation, we concluded that this water-CO_{ads} intermediate is an important precursor of ethylene formation on Cu electrodes during CO reduction.

In Chapter 4, by coupling SEIRAS to DEMS, we further illustrated a broader potential of this technique in connecting catalytic activity to a certain interfacial condition. On two differently prepared Cu electrode (*i.e.*, Cu-Si and CuAu-Si), we monitored the evolution of ethylene and the C≡O stretching band of CO_{ads} with applied potential. We found that the Cu-Si is more active in ethylene formation than CuAu-Si. Potential dependent CO_{ads} lineshape analysis revealed that Cu(100) is predominant on Cu-Si, while Cu(111) prevails

CuAu-Si. This preference of the crystallographic facets is responsible for the observed differences in catalytic behavior.

SEIRAS can also be employed to understand oxidation reactions, *e.g*, CO oxidation and oxygen evolution reaction. In Chapter 5, we observed a superoxo species, a key reaction intermediate on Co-oxide based catalysts during the water oxidation reaction. Further, employing water-in-salt electrolytes, we systematically altered the water activity, which enabled us to quantify the impact of the water activity on the rate of the reaction. We discovered that the water oxidation mechanism is sensitive to the applied electrode potential: At relatively low driving force, the reaction proceeds through the IMOC pathway, whereas the WNA mechanism prevails at high driving force.

These examples demonstrate the great potential of SEIRAS in *operando* mechanistic investigations. Moving forward, SEIRAS can be generalized to study a diversity of other exciting systems.

- SEIRAS relies on nanostructured metal thin films that are deposited on an ATR crystal, which in most cases is Si due to the good adhesion of metal films and wide pH compatibility. As a result of the strong absorption of Si below 1400 cm^{-1}, obtaining spectral information of this region is largely hindered. The employment of micromachined Si wafers is a promising way to overcome this limitation. The ultra-thin Si wafer (ca. 500 μm) minimizes the strong absorption of Si, extending the observable spectral window. [392] As demonstrated in Chapter 5, we were able to detect a water oxidation intermediate by taking advantages of these thin Si wafers. We anticipate that this approach can be applied to a wide range of other reactions and interfaces.

- The stability of the SEIRAS-active film still remains challenging. These thin metal films attached to the ATR element tend to delaminate under harsh experimental conditions. While certain treatments have been reported to increase the adhesion ability

of the metal thin film to the ATR crystal, *e.g.*, annealing [393] or repeating deposition, [288], the community should continue to discover more reliable protocols to obtain more robust metal thin films.

- The best time resolution obtained with SEIRAS to date is tens of millisecond time scale via time-resolved rapid scan measurements, [394–396] and hundreds of microsecond through step-scan measurements. [395, 397] The step-scan technique is capable of monitoring a reaction or a process at a sub-microsecond to nanosecond time resolution. Combined with step-scan, SEIRAS broadens its potential to detect the molecular-level information for a fast reaction process.

- The materials of SEIRAS active metal film have been largely restricted in single pure metal composition (see Chapter 2) while only a few examples of alloy materials have been reported. [398, 399] As demonstrated by us in Chapter 5 and others, [236, 342, 400, 401] other materials can be deposited on to nanostructured metal films as the substrate for SEIRAS measurement. These examples show that SEIRAS can be applied to a wide variety of electrocatalysts.

Bibliography

1. Höök, M. & Tang, X. Depletion of Fossil Fuels and Anthropogenic Climate Change–A Review. *Energy Policy* **52,** 797–809 (2013).

2. Shafiee, S. & Topal, E. When Will Fossil Fuel Reserves Be Diminished? *Energy Policy* **37,** 181–189 (2009).

3. Betts, R. A., Jones, C. D., Knight, J. R., Keeling, R. F. & Kennedy, J. J. El Niño and a Record CO_2 Rise. *Nat. Clim. Change* **6,** 806–810 (2016).

4. Climate Change Science Program (US). *Climate Change Impacts in the United States, Highlights: US National Climate Assessment* (US Global Change Research Program, 2014).

5. Chu, S., Cui, Y. & Liu, N. The Path towards Sustainable Energy. *Nat. Mater.* **16,** 16–22 (2017).

6. Hori, Y., Kikuchi, K. & Suzuki, S. Production of CO and CH_4 in Electrochemical Reduction of CO_2 at Metal Electrodes in Aqueous Hydrogencarbonate Solution. *Chem. Lett.* **14,** 1695–1698 (1985).

7. Kuhl, K. P., Cave, E. R., Abram, D. N. & Jaramillo, T. F. New Insights into the Electrochemical Reduction of Carbon Dioxide on Metallic Copper Surfaces. *Energy Environ. Sci.* **5,** 7050–7059 (5 2012).

8. Hori, Y. *Electrochemical CO_2 Reduction on Metal Electrodes* (eds Vayenas, C. G., White, R. E. & Gamboa-Aldeco, M. E.) 89–189 (Springer New York, New York, NY, 2008).

9. Peterson, A. A., Abild-Pedersen, F., Studt, F., Rossmeisl, J. & Nørskov, J. K. How Copper Catalyzes the Electroreduction of Carbon Dioxide into Hydrocarbon Fuels. *Energy Environ. Sci.* **3,** 1311–1315 (2010).

10. Li, C. W. & Kanan, M. W. CO_2 Reduction at Low Overpotential on Cu Electrodes Resulting from the Reduction of Thick Cu_2O Films. *J. Am. Chem. Soc.* **134,** 7231–7234 (2012).

11. Li, C. W., Ciston, J. & Kanan, M. W. Electroreduction of Carbon Monoxide to Liquid Fuel on Oxide-Derived Nanocrystalline Copper. *Nature* **508,** 504–507 (2014).

12. Mariano, R. G., McKelvey, K., White, H. S. & Kanan, M. W. Selective Increase in CO_2 Electroreduction Activity at Grain-Boundary Surface Terminations. *Science* **358,** 1187–1192 (2017).

13. Feng, X., Jiang, K., Fan, S. & Kanan, M. W. A Direct Grain-Boundary-Activity Correlation for CO Electroreduction on Cu Nanoparticles. *ACS Cent. Sci.* **2,** 169–174 (2016).

14. Cheng, D., Zhao, Z.-J., Zhang, G., Yang, P., Li, L., Gao, H., Liu, S., Chang, X., Chen, S., Wang, T., *et al.* The Nature of Active Sites For Carbon Dioxide Electroreduction over Oxide-derived Copper Catalysts. *Nat. Commun.* **12,** 1–8 (2021).

15. Watanabe, M., Shibata, M., Katoh, A., Sakata, T. & Azuma, M. Design of Alloy Electrocatalysts for CO_2 Reduction: Improved Energy Efficiency, Selectivity, and Reaction Rate for The CO_2 Electroreduction on Cu Alloy Electrodes. *J. Electroanal. Chem. Interf. Electrochem.* **305,** 319–328 (1991).

16. Kim, D., Resasco, J., Yu, Y., Asiri, A. M. & Yang, P. Synergistic Geometric and Electronic Effects for Electrochemical Reduction of Carbon Dioxide Using Gold-Copper Bimetallic Nanoparticles. *Nat. Commun.* **5,** 1–8 (2014).

17. Choi, J., Kim, M. J., Ahn, S. H., Choi, I., Jang, J. H., Ham, Y. S., Kim, J. J. & Kim, S.-K. Electrochemical CO_2 Reduction to CO on Dendritic Ag-Cu Electrocatalysts Prepared by Electrodeposition. *Chem. Eng. J.* **299,** 37–44 (2016).

18. Ren, D., Ang, B. S.-H. & Yeo, B. S. Tuning the Selectivity of Carbon Dioxide Electroreduction toward Ethanol on Oxide-Derived Cu_xZn Catalysts. *ACS Catal.* **6,** 8239–8247 (2016).

19. Sarfraz, S., Garcia-Esparza, A. T., Jedidi, A., Cavallo, L. & Takanabe, K. CuSn Bimetallic Catalyst for Selective Aqueous Electroreduction of CO_2 to CO. *ACS Catal.* **6,** 2842–2851 (2016).

20. Hoang, T. T., Verma, S., Ma, S., Fister, T. T., Timoshenko, J., Frenkel, A. I., Kenis, P. J. & Gewirth, A. A. Nanoporous Copper-Silver Alloys by Additive-Controlled Electrodeposition for the Selective Electroreduction of CO_2 to Ethylene and Ethanol. *J. Am. Chem. Soc.* **140,** 5791–5797 (2018).

21. Morales-Guio, C. G., Cave, E. R., Nitopi, S. A., Feaster, J. T., Wang, L., Kuhl, K. P., Jackson, A., Johnson, N. C., Abram, D. N., Hatsukade, T., *et al.* Improved CO_2 Reduction Activity towards C_2+ Alcohols on A Tandem Gold on Copper Electrocatalyst. *Nat. Catal.* **1,** 764–771 (2018).

22. Zhu, W., Tackett, B. M., Chen, J. G. & Jiao, F. Bimetallic Electrocatalysts for CO_2 Reduction. *Top. Curr. Chem.* **376,** 41 (2018).

23. Hori, Y., Murata, A., Takahashi, R. & Suzuki, S. Enhanced Formation of Ethylene and Alcohols at Ambient Temperature and Pressure in Electrochemical Reduction of Carbon Dioxide at A Copper Electrode. *J. Chem. Soc., Chem. Commun.,* 17–19 (1988).

24. Strmcnik, D., Kodama, K., van der Vliet, D., Greeley, J., Stamenkovic, V. R. & Marković, N. M. The Role of Non-Covalent Interactions in Electrocatalytic Fuel-Cell Reactions on Platinum. *Nat. Chem.* **1,** 466–472 (2009).

25. Stoffelsma, C., Rodriguez, P., Garcia, G., Garcia-Araez, N., Strmcnik, D., Marković, N. M. & Koper, M. T. M. Promotion of the Oxidation of Carbon Monoxide at Stepped Platinum Single-Crystal Electrodes in Alkaline Media by Lithium and Beryllium Cations. *J. Am. Chem. Soc.* **132,** 16127–16133 (2010).

26. Roberts, F. S., Kuhl, K. P. & Nilsson, A. High Selectivity for Ethylene from Carbon Dioxide Reduction over Copper Nanocube Electrocatalysts. *Angew. Chem. Int. Ed.* **54,** 5179–5182 (2015).

27. Singh, M. R., Kwon, Y., Lum, Y., Ager, J. W. & Bell, A. T. Hydrolysis of Electrolyte Cations Enhances the Electrochemical Reduction of CO_2 over Ag and Cu. *J. Am. Chem. Soc.* **138,** 13006–13012 (2016).

28. Ayemoba, O. & Cuesta, A. Spectroscopic Evidence of Size-Dependent Buffering of Interfacial pH by Cation Hydrolysis during CO_2 Electroreduction. *ACS Appl. Mater. Interfaces* **9,** 27377–27382 (2017).

29. Resasco, J., Chen, L. D., Clark, E., Tsai, C., Hahn, C., Jaramillo, T. F., Chan, K. & Bell, A. T. Promoter Effects of Alkali Metal Cations on the Electrochemical Reduction of Carbon Dioxide. *J. Am. Chem. Soc.* **139,** 11277–11287 (2017).

30. Gunathunge, C. M., Ovalle, V. J. & Waegele, M. M. Probing Promoting Effects of Alkali Cations on the Reduction of CO at the Aqueous Electrolyte/Copper Interface. *Phys. Chem. Chem. Phys.* **19,** 30166–30172 (2017).

31. Li, J., Li, X., Gunathunge, C. M. & Waegele, M. M. Hydrogen Bonding Steers the Product Selectivity of Electrocatalytic CO Reduction. *Proc. Natl. Acad. Sci. U.S.A* **116,** 9220–9229 (2019).

32. Waegele, M. M., Gunathunge, C. M., Li, J. & Li, X. How Cations Affect the Electric Double Layer and the Rates and Selectivity of Electrocatalytic Processes. *J. Chem. Phys.* **151,** 160902 (2019).

33. Ovalle, V. J. & Waegele, M. M. Impact of Electrolyte Anions on the Adsorption of CO on Cu Electrodes. *J. Phys. Chem. C* **124,** 14713–14721 (2020).

34. Suntivich, J., May, K. J., Gasteiger, H. A., Goodenough, J. B. & Shao-Horn, Y. A Perovskite Oxide Optimized for Oxygen Evolution Catalysis from Molecular Orbital Principles. *Science* **334,** 1383–1385 (2011).

35. Kibria, M. G., Edwards, J. P., Gabardo, C. M., Dinh, C.-T., Seifitokaldani, A., Sinton, D. & Sargent, E. H. Electrochemical CO2 Reduction into Chemical Feedstocks: From Mechanistic Electrocatalysis Models to System Design. *Adv. Mater.* **31,** 1807166 (2019).

36. Qing, G., Ghazfar, R., Jackowski, S. T., Habibzadeh, F., Ashtiani, M. M., Chen, C.-P., Smith, M. R. & Hamann, T. W. Recent Advances and Challenges of Electrocatalytic N_2 Reduction to Ammonia. *Chem. Rev.* **120,** 5437–5516 (2020).

37. Chen, G., Bare, S. R. & Mallouk, T. E. Development of Supported Bifunctional Electrocatalysts for Unitized Regenerative Fuel Cells. *J. Electrochem. Soc.* **149,** A1092 (2002).

38. Wang, Z.-L., Xu, D., Xu, J.-J. & Zhang, X.-B. Oxygen Electrocatalysts in MetalAir Batteries: From Aqueous to Nonaqueous Electrolytes. *Chem. Soc. Rev.* **43,** 7746–7786 (2014).

39. Tahir, M., Pan, L., Idrees, F., Zhang, X., Wang, L., Zou, J.-J. & Wang, Z. L. Electrocatalytic Oxygen Evolution Reaction for Energy Conversion and Storage: A Comprehensive Review. *Nano Energy* **37,** 136–157 (2017).

40. Zouni, A., Witt, H.-T., Kern, J., Fromme, P., Krauss, N., Saenger, W. & Orth, P. Crystal Structure of Photosystem II from Synechococcus Elongatus at 3.8 Å Resolution. *Nature* **409,** 739–743 (2001).

41. Gust, D., Moore, T. A. & Moore, A. L. Solar Fuels via Artificial Photosynthesis. *Acc. Chem. Res.* **42,** 1890–1898 (2009).

42. Blakemore, J. D., Crabtree, R. H. & Brudvig, G. W. Molecular Catalysts for Water Oxidation. *Chem. Rev.* **115,** 12974–13005 (2015).

43. Garrido-Barros, P., Gimbert-Suriñach, C., Matheu, R., Sala, X. & Llobet, A. How to Make an Efficient and Robust Molecular Catalyst for Water Oxidation. *Chem. Soc. Rev.* **46,** 6088–6098 (2017).

44. Dogutan, D. K. & Nocera, D. G. Artificial Photosynthesis at Efficiencies Greatly Exceeding That of Natural Photosynthesis. *Acc. Chem. Res.* **52,** 3143–3148 (2019).

45. Duan, L., Bozoglian, F., Mandal, S., Stewart, B., Privalov, T., Llobet, A. & Sun, L. A Molecular Ruthenium Catalyst with Water-Oxidation Activity Comparable to That of Photosystem II. *Nat. Chem.* **4,** 418–423 (2012).

46. Limburg, B., Bouwman, E. & Bonnet, S. Molecular Water Oxidation Catalysts Based on Transition Metals and Their Decomposition Pathways. *Coord. Chem. Rev.* **256,** 1451–1467 (2012).

47. Hunter, B. M., Gray, H. B. & Mller, A. M. Earth-Abundant Heterogeneous Water Oxidation Catalysts. *Chem. Rev.* **116,** 14120–14136 (2016).

48. Harriman, A., Pickering, I. J., Thomas, J. M. & Christensen, P. A. Metal Oxides as Heterogeneous Catalysts for Oxygen Evolution under Photochemical Conditions. *J. Chem. Soc., Faraday Trans. 1* **84,** 2795–2806 (1988).

49. Trotochaud, L., Ranney, J. K., Williams, K. N. & Boettcher, S. W. Solution-Cast Metal Oxide Thin Film Electrocatalysts for Oxygen Evolution. *J. Am. Chem. Soc.* **134,** 17253–17261 (2012).

50. McCrory, C. C. L., Jung, S., Peters, J. C. & Jaramillo, T. F. Benchmarking Heterogeneous Electrocatalysts for the Oxygen Evolution Reaction. *J. Am. Chem. Soc.* **135,** 16977–16987 (2013).

51. Cherevko, S., Geiger, S., Kasian, O., Kulyk, N., Grote, J.-P., Savan, A., Shrestha, B. R., Merzlikin, S., Breitbach, B., Ludwig, A. & Mayrhofer, K. J. Oxygen and Hydrogen Evolution Reactions on Ru, RuO_2, Ir, and IrO_2 Thin Film Electrodes in Acidic and Alkaline Electrolytes: A Comparative Study on Activity and Stability. *Catal. Today* **262,** 170–180 (2016).

52. Gong, M. & Dai, H. A Mini Review of NiFe-Based Materials as Highly Active Oxygen Evolution Reaction Electrocatalysts. *Nano Res.* **8,** 23–39 (2015).

53. Lyons, M. E., Doyle, R. L., Browne, M. P., Godwin, I. J. & Rovetta, A. A. Recent Developments in Electrochemical Water Oxidation. *Curr. Opin. Electrochem.* **1,** 40–45 (2017).

54. Li, J., Triana, C. A., Wan, W., Adiyeri Saseendran, D. P., Zhao, Y., Balaghi, S. E., Heidari, S. & Patzke, G. R. Molecular and heterogeneous water oxidation catalysts: recent progress and joint perspectives. *Chem. Soc. Rev.* **50,** 2444–2485 (2021).

55. Yang, X., Wang, Y., Li, C. M. & Wang, D. Mechanisms of Water Oxidation on Heterogeneous Catalyst Surfaces. *Nano Res.* (2021).

56. Spurgeon, J. M. & Kumar, B. A Comparative Technoeconomic Analysis of Pathways for Commercial Electrochemical CO_2 Reduction to Liquid Products. *Energy Environ. Sci.* **11,** 1536–1551 (2018).

57. Jouny, M., Luc, W. & Jiao, F. General Techno-Economic Analysis of CO_2 Electrolysis Systems. *Ind. Eng. Chem. Res.* **57,** 2165–2177 (2018).

58. Verma, S., Kim, B., Jhong, H.-R.., Ma, S. & Kenis, P. J. A. A Gross-Margin Model for Defining Technoeconomic Benchmarks in the Electroreduction of CO_2. *ChemSusChem* **9,** 1972–1979 (2016).

59. Ayers, K. E., Capuano, C. & Anderson, E. B. Recent Advances in Cell Cost and Efficiency for PEM-based Water Electrolysis. *ECS Trans.* **41,** 15 (2012).

60. Spöri, C., Kwan, J. T. H., Bonakdarpour, A., Wilkinson, D. P. & Strasser, P. The Stability Challenges of Oxygen Evolving Catalysts: Towards a Common Fundamental Understanding and Mitigation of Catalyst Degradation. *Angew. Chem. Int. Ed.* **56,** 5994–6021 (2017).

61. Atkins, P. & de Paula, J. *Atkins' Physical Chemistry; Oxford University Press; Oxford, United Kingdom* (2002).

62. Osawa, M. & Ikeda, M. Surface-Enhanced Infrared Absorption of p-Nitrobenzoic Acid Deposited on Silver Island Films: Contributions of Electromagnetic and Chemical Mechanisms. *J. Phys. Chem.* **95,** 9914–9919 (1991).

63. Hartstein, A., Kirtley, J. R. & Tsang, J. C. Enhancement of the Infrared Absorption from Molecular Monolayers with Thin Metal Overlayers. *Phys. Rev. Lett.* **45,** 201–204 (1980).

64. Osawa, M., Ataka, K.-i., Yoshii, K. & Yotsuyanagi, T. Surface-Enhanced Infrared ATR Spectroscopy for In Situ Studies of Electrode/Electrolyte Interfaces. *J. Electron. Spectros. Relat. Phenom.* **64-65,** 371–379 (1993).

65. Nishikawa, Y., Fujiwara, K., Ataka, K. & Osawa, M. Surface-Enhanced Infrared External Reflection Spectroscopy at Low Reflective Surfaces and Its Application

to Surface Analysis of Semiconductors, Glasses, and Polymers. *Anal. Chem.* **65,** 556–562 (1993).

66. Lee, S. J. & Kim, K. Diffuse Reflectance Infrared Spectra of Stearic Acid Self-Assembled on fine silver particles. *Vib. Spectrosc.* **18,** 187–201 (1998).

67. Osawa, M. Dynamic Processes in Electrochemical Reactions Studied by Surface-Enhanced Infrared Absorption Spectroscopy (SEIRAS). *Bull. Chem. Soc. Jpn.* **70,** 2861–2880 (1997).

68. Aroca, R. F., Ross, D. J. & Domingo, C. Surface-Enhanced Infrared Spectroscopy. *Appl. Spectrosc.* **58,** 324A–338A (2004).

69. Osawa, M. & ichi Ataka, K. Electromagnetic Mechanism of Enhanced Infrared Absorption of Molecules Adsorbed on Metal Island Films. *Surf. Sci.* **262,** L118–L122 (1992).

70. Jensen, T. R., Van Duyne, R. P., Johnson, S. A. & Maroni, V. A. Surface-Enhanced Infrared Spectroscopy: A Comparison of Metal Island Films with Discrete and Nondiscrete Surface Plasmons. *Appl. Spectrosc.* **54,** 371–377 (2000).

71. Petryayeva, E. & Krull, U. J. Localized Surface Plasmon Resonance: Nanostructures, Bioassays and Biosensing—A Review. *Anal. Chim. Acta* **706,** 8–24 (2011).

72. Hatta, A., Ohshima, T. & Suëtaka, W. Observation of the Enhanced Infrared Absorption of p-Nitrobenzoate on Ag Island Films with an ATR Technique. *Appl. Phys. A* **29,** 71–75 (1982).

73. Ferri, D., Bürgi, T. & Baiker, A. Pt and Pt/Al_2O_3 Thin Films for Investigation of Catalytic SolidLiquid Interfaces by ATR-IR Spectroscopy: CO Adsorption, H_2-Induced Reconstruction and Surface-Enhanced Absorption. *J. Phys. Chem. B* **105,** 3187–3195 (2001).

74. Miyake, H., Ye, S. & Osawa, M. Electroless Deposition of Gold Thin Films on Silicon for Surface-Enhanced Infrared Spectroelectrochemistry. *Electrochem. Commun.* **4,** 973–977 (2002).

75. Yan, Y.-G., Li, Q.-X., Huo, S.-J., Ma, M., Cai, W.-B. & Osawa, M. Ubiquitous Strategy for Probing ATR Surface-Enhanced Infrared Absorption at Platinum Group Metal-Electrolyte Interfaces. *J. Phys. Chem. B* **109,** 7900–7906 (2005).

76. Wang, H.-F., Yan, Y.-G., Huo, S.-J., Cai, W.-B., Xu, Q.-J. & Osawa, M. Seeded Growth Fabrication of Cu-on-Si Electrodes for *in situ* ATR-SEIRAS Applications. *Electrochim. Acta* **52,** 5950–5957 (2007).

77. Etchegoin, P. G. & Le Ru, E. C. A Perspective on Single Molecule SERS: Current Status and Future Challenges. *Phys. Chem. Chem. Phys.* **10,** 6079–6089 (2008).

78. Merklin, G. T. & Griffiths, P. R. Influence of Chemical Interactions on the Surface-Enhanced Infrared Absorption Spectrometry of Nitrophenols on Copper and Silver Films. *Langmuir* **13,** 6159–6163 (1997).

79. Li, J.-T., Zhou, Z.-Y., Broadwell, I. & Sun, S.-G. In-Situ Infrared Spectroscopic Studies of Electrochemical Energy Conversion and Storage. *Acc. Chem. Res.* **45,** 485–494 (2012).

80. Ye, J.-Y., Jiang, Y.-X., Sheng, T. & Sun, S.-G. In-Situ FTIR Spectroscopic Studies of Electrocatalytic Reactions and Processes. *Nano Energy* **29,** 414–427 (2016).

81. Kas, R., Ayemoba, O., Firet, N. J., Middelkoop, J., Smith, W. A. & Cuesta, A. In-Situ Infrared Spectroscopy Applied to the Study of the Electrocatalytic Reduction of CO_2: Theory, Practice and Challenges. *ChemPhysChem* **20,** 2904–2925 (2019).

82. Gunathunge, C. M., Li, J., Li, X. & Waegele, M. M. Surface-Adsorbed CO as an Infrared Probe of Electrocatalytic Interfaces. *ACS Catal.* **10,** 11700–11711 (2020).

83. Viinikanoja, A., Wang, Z., Kauppila, J. & Kvarnström, C. Electrochemical Reduction of Graphene Oxide and Its In Situ Spectroelectrochemical characterization. *Phys. Chem. Chem. Phys.* **14,** 14003–14009 (2012).

84. Chou, T.-C., Chang, C.-C., Yu, H.-L., Yu, W.-Y., Dong, C.-L., Velasco-Vlez, J.-J., Chuang, C.-H., Chen, L.-C., Lee, J.-F., Chen, J.-M. & Wu, H.-L. Controlling the Oxidation State of the Cu Electrode and Reaction Intermediates for Electrochemical CO_2 Reduction to Ethylene. *J. Am. Chem. Soc.* **142,** 2857–2867 (2020).

85. Huo, S.-J., Xue, X.-K., Yan, Li, Q.-X., Ma, M., Cai, W.-B., Xu, Q.-J. & Osawa, M. Extending in Situ Attenuated-Total-Reflection Surface-Enhanced Infrared Absorption Spectroscopy to Ni Electrodes. *J. Phys. Chem. B* **110,** 4162–4169 (2006).

86. Huo, S.-J., Wang, J.-Y., Yao, J.-L. & Cai, W.-B. Exploring Electrosorption at Iron Electrode with in Situ Surface-Enhanced Infrared Absorption Spectroscopy. *Anal. Chem.* **82,** 5117–5124 (2010).

87. Harrick, N. J. & Beckmann, K. H. in *Characterization of Solid Surfaces* (eds Kane, P. F. & Larrabee, G. B.) 215–245 (Springer US, Boston, MA, 1974).

88. Hoffmann, F. M. Infrared Reflection-Absorption Spectroscopy of Adsorbed Molecules. *Surf. Sci. Rep.* **3,** 107–192 (1983).

89. Föhlisch, A., Nyberg, M., Hasselström, J., Karis, O., Pettersson, L. G. M. & Nilsson, A. How Carbon Monoxide Adsorbs in Different Sites. *Phys. Rev. Lett.* **85,** 3309–3312 (2000).

90. Blyholder, G. Molecular Orbital View of Chemisorbed Carbon Monoxide. *J. Phys. Chem.* **68,** 2772–2777 (1964).

91. Hammer, B., Morikawa, Y. & Nørskov, J. K. CO Chemisorption at Metal Surfaces and Overlayers. *Phys. Rev. Lett.* **76,** 2141–2144 (1996).

92. Föhlisch, A., Nyberg, M., Bennich, P., Triguero, L., Hasselstrm, J., Karis, O., Pettersson, L. G. M. & Nilsson, A. The Bonding of CO to Metal Surfaces. *J. Chem. Phys.* **112,** 1946–1958 (2000).

93. Fried, S. D. & Boxer, S. G. Measuring Electric Fields and Noncovalent Interactions Using the Vibrational Stark Effect. *Acc. Chem. Res.* **48,** 998–1006 (2015).

94. Park, E. S., Andrews, S. S., Hu, R. B. & Boxer, S. G. Vibrational Stark Spectroscopy in Proteins: A Probe and Calibration for Electrostatic Fields. *J. Phys. Chem. B* **103,** 9813–9817 (1999).

95. Dunwell, M., Wang, J., Yan, Y. & Xu, B. Surface Enhanced Spectroscopic Investigations of Adsorption of Cations on Electrochemical Interfaces. *Phys. Chem. Chem. Phys.s* **19,** 971–975 (2017).

96. Suydam, I. T. & Boxer, S. G. Vibrational Stark Effects Calibrate the Sensitivity of Vibrational Probes for Electric Fields in Proteins. *Biochemistry* **42,** 12050–12055 (2003).

97. Bagus, P. S., Nelin, C. J., Müller, W., Philpott, M. R. & Seki, H. Field-Induced Vibrational Frequency Shifts of CO and CN Chemisorbed on Cu(100). *Phys. Rev. Lett.* **58,** 559–562 (1987).

98. Zou, S. & Weaver, M. J. Potential-Dependent MetalAdsorbate Stretching Frequencies for Carbon Monoxide on Transition-Metal Electrodes: Chemical Bonding versus Electrostatic Field Effects. *J. Phys. Chem.* **100,** 4237–4242 (1996).

99. Weaver, M. J. & Wasileski, S. A. Influence of Double-Layer Solvation on Local versus Macroscopic Surface Potentials on Ordered Platinum-Group Metals as Sensed by the Vibrational Stark Effect. *Langmuir* **17,** 3039–3043 (2001).

100. Sigala, P. A., Fafarman, A. T., Bogard, P. E., Boxer, S. G. & Herschlag, D. Do Ligand Binding and Solvent Exclusion Alter the Electrostatic Character within the Oxyanion Hole of an Enzymatic Active Site? *J. Am. Chem. Soc.* **129,** 12104–12105 (2007).

101. Stafford, A. J., Ensign, D. L. & Webb, L. J. Vibrational Stark Effect Spectroscopy at the Interface of Ras and Rap1A Bound to the Ras Binding Domain of RalGDS Reveals an Electrostatic Mechanism for ProteinProtein Interaction. *J. Phys. Chem. B* **114,** 15331–15344 (2010).

102. Chen, P. & Meyer, T. J. Medium Effects on Charge Transfer in Metal Complexes. *Chem. Rev.* **98,** 1439–1478 (1998).

103. Velsko, S. P., Waldeck, D. H. & Fleming, G. R. Breakdown of Kramers theory description of photochemical isomerization and the possible involvement of frequency dependent friction. *J. Chem. Phys.* **78,** 249–258 (1983).

104. Mukherjee, S., Waegele, M. M., Chowdhury, P., Guo, L. & Gai, F. Effect of Macromolecular Crowding on Protein Folding Dynamics at the Secondary Structure Level. *J. Mol. Biol.* **393,** 227–236 (2009).

105. Jorgensen, W. L., Blake, J. F., Lim, D. & Severance, D. L. Investigation of Solvent Effects on Pericyclic Reactions by Computer Simulations. *J. Chem. Soc., Faraday Trans.* **90,** 1727–1732 (1994).

106. Suydam, I. T., Snow, C. D., Pande, V. S. & Boxer, S. G. Electric Fields at the Active Site of an Enzyme: Direct Comparison of Experiment with Theory. *Science* **313,** 200–204 (2006).

107. Breslow, R. & Maitra, U. On the Origin of Product Selectivity in Aqueous Diels-Alder Reactions. *Tetrahedron Lett.* **25,** 1239–1240 (1984).

108. Rybtchinski, B. & Milstein, D. Solvent-Controlled Selectivity toward Exclusive C-C or C-H Bond Activation by a Cationic Metal Center. *J. Am. Chem. Soc.* **121,** 4528–4529 (1999).

109. Grote, R. F., Van der Zwan, G. & Hynes, J. T. Frequency-Dependent Friction and Solution Reaction Rates. *J. Phys. Chem.* **88,** 4676–4684 (1984).

110. Weaver, M. J. Dynamical solvent effects on activated electron-transfer reactions: principles, pitfalls, and progress. *Chem. Rev.* **92,** 463–480 (1992).

111. Hori, Y., Murata, A. & Takahashi, R. Formation of Hydrocarbons in the Electrochemical Reduction of Carbon Dioxide at a Copper Electrode in Aqueous Solution. *J. Chem. Soc., Faraday Trans. 1* **85,** 2309–2326 (1989).

112. Gattrell, M., Gupta, N. & Co, A. A Review of the Aqueous Electrochemical Reduction of CO_2 to Hydrocarbons at Copper. *J. Electroanal. Chem.* **594,** 1–19 (2006).

113. Kuhl, K. P., Hatsukade, T., Cave, E. R., Abram, D. N., Kibsgaard, J. & Jaramillo, T. F. Electrocatalytic Conversion of Carbon Dioxide to Methane and Methanol on Transition Metal Surfaces. *J. Am. Chem. Soc.* **136,** 14107–14113 (2014).

114. Hoang, T. T. H., Ma, S., Gold, J. I., Kenis, P. J. A. & Gewirth, A. A. Nanoporous Copper Films by Additive-Controlled Electrodeposition: CO_2 Reduction Catalysis. *ACS Catal.* **7,** 3313–3321 (2017).

115. Weng, Z., Zhang, X., Wu, Y., Huo, S., Jiang, J., Liu, W., He, G., Liang, Y. & Wang, H. Self-Cleaning Catalyst Electrodes for Stabilized CO_2 Reduction to Hydrocarbons. *Angew. Chem. Inter. Ed.* **56,** 13135–13139 (2017).

116. Dunwell, M., Yan, Y. & Xu, B. Understanding the Influence of the Electrochemical Double-Layer on Heterogeneous Electrochemical Reactions. *Curr. Opin. Chem. Eng.* **20,** 151–158 (2018).

117. Arán-Ais, R. M., Gao, D. & Roldan Cuenya, B. Structure- and Electrolyte-Sensitivity in CO_2 Electroreduction. *Acc. Chem. Res.* **51,** 2906–2917 (2018).

118. Mariano, R. G., McKelvey, K., White, H. S. & Kanan, M. W. Selective Increase in CO_2 Electroreduction Activity at Grain-Boundary Surface Terminations. **358,** 1187–1192 (2017).

119. Cao, L., Raciti, D., Li, C., Livi, K. J. T., Rottmann, P. F., Hemker, K. J., Mueller, T. & Wang, C. Mechanistic Insights for Low-Overpotential Electroreduction of CO_2 to CO on Copper Nanowires. *ACS Catal.* **7,** 8578–8587 (2017).

120. Raciti, D., Cao, L., Livi, K. J. T., Rottmann, P. F., Tang, X., Li, C., Hicks, Z., Bowen, K. H., Hemker, K. J., Mueller, T. & Wang, C. Low-Overpotential Electroreduction of Carbon Monoxide Using Copper Nanowires. *ACS Catal.* **7,** 4467–4472 (2017).

121. Clark, E. L., Hahn, C., Jaramillo, T. F. & Bell, A. T. Electrochemical CO_2 Reduction over Compressively Strained CuAg Surface Alloys with Enhanced Multi-Carbon Oxygenate Selectivity. *J. Am. Chem. Soc.* **139,** 15848–15857 (2017).

122. Choi, C., Cheng, T., Flores Espinosa, M., Fei, H., Duan, X., Goddard, W. A. & Huang, Y. A Highly Active Star Decahedron Cu Nanocatalyst for Hydrocarbon Production at Low Overpotentials. *Adv. Mater.,* 1805405 (2018).

123. Mistry, H., Reske, R., Zeng, Z., Zhao, Z.-J., Greeley, J., Strasser, P. & Cuenya, B. R. Exceptional Size-Dependent Activity Enhancement in the Electroreduction of CO_2 over Au Nanoparticles. *J. Am. Chem. Soc.* **136,** 16473–16476 (2014).

124. Manthiram, K., Beberwyck, B. J. & Alivisatos, A. P. Enhanced Electrochemical Methanation of Carbon Dioxide with a Dispersible Nanoscale Copper Catalyst. *J. Am. Chem. Soc.* **136,** 13319–13325 (2014).

125. Reske, R., Mistry, H., Behafarid, F., Cuenya, B. R. & Strasser, P. Particle Size Effects in the Catalytic Electroreduction of CO_2 on Cu Nanoparticles. *J. Am. Chem. Soc.* **136,** 6978–6986 (2014).

126. Hori, Y., Takahashi, I., Koga, O. & Hoshi, N. Electrochemical Reduction of Carbon Dioxide at Various Series of Copper Single Crystal Electrodes. *J. Mol. Catal. A: Chem.* **199,** 39–47 (2003).

127. Loiudice, A., Lobaccaro, P., Kamali, E. A., Thao, T., Huang, B. H., Ager, J. W. & Buonsanti, R. Tailoring Copper Nanocrystals Towards C_2 Products in Electrochemical CO_2 Reduction. *Angew. Chem. Int. Ed.* **55,** 5789–5792 (2016).

128. Hahn, C., Hatsukade, T., Kim, Y.-G., Vailionis, A., Baricuatro, J. H., Higgins, D. C., Nitopi, S. A., Soriaga, M. P. & Jaramillo, T. F. Engineering Cu Surfaces for the Electrocatalytic Conversion of CO_2: Controlling Selectivity Toward Oxygenates and Hydrocarbons. *Proc. Natl. Acad. Sci. U. S. A.* **114,** 5918–5923 (2017).

129. Schouten, K., Qin, Z., Pérez Gallent, E. & Koper, M. T. M. Two Pathways for the Formation of Ethylene in CO Reduction on Single-Crystal Copper Electrodes. *J. Am. Chem. Soc.* **134,** 9864–9867 (2012).

130. Huang, Y., Handoko, A. D., Hirunsit, P. & Yeo, B. S. Electrochemical Reduction of CO_2 Using Copper Single-Crystal Surfaces: Effects of CO* Coverage on the Selective Formation of Ethylene. *ACS Catal.* **7,** 1749–1756 (2017).

131. Rosen, B. A., Salehi-Khojin, A., Thorson, M. R., Zhu, W., Whipple, D. T., Kenis, P. J. A. & Masel, R. I. Ionic Liquid–Mediated Selective Conversion of CO_2 to CO at Low Overpotentials. *Science* **334,** 643–644 (2011).

132. Figueiredo, M. C., Ledezma-Yanez, I. & Koper, M. T. M. In Situ Spectroscopic Study of CO_2 Electroreduction at Copper Electrodes in Acetonitrile. *ACS Catal.* **6,** 2382–2392 (2016).

133. García Rey, N. & Dlott, D. D. Effects of Water on Low-Overpotential CO_2 Reduction in Ionic Liquid Studied by Sum-Frequency Generation Spectroscopy. *Phys. Chem. Chem. Phys.* **19,** 10491–10501 (2017).

134. Schreier, M., Yoon, Y., Jackson, M. N. & Surendranath, Y. Competition between H and CO for Active Sites Governs Copper-Mediated Electrosynthesis of Hydrocarbon Fuels. *Angew. Chem. Int. Ed.* **57,** 10221–10225 (2018).

135. McCrum, I. T., Hickner, M. A. & Janik, M. J. Quaternary Ammonium Cation Specific Adsorption on Platinum Electrodes: A Combined Experimental and Density Functional Theory Study. *J. Electrochem. Soc.* **165,** F114–F121 (2018).

136. Varela, A. S., Ju, W., Reier, T. & Strasser, P. Tuning the Catalytic Activity and Selectivity of Cu for CO_2 Electroreduction in the Presence of Halides. *ACS Catal.* **6,** 2136–2144 (2016).

137. Akhade, S. A., McCrum, I. T. & Janik, M. J. The Impact of Specifically Adsorbed Ions on the Copper-Catalyzed Electroreduction of CO_2. *J. Electrochem. Soc.* **163,** F477–F484 (2016).

138. Paik, W., Andersen, T. & Eyring, H. Kinetic Studies of the Electrolytic Reduction of Carbon Dioxide on the Mercury Electrode. *Electrochim. Acta* **14,** 1217–1232 (1969).

139. Hori, Y. & Suzuki, S. Electrolytic Reduction of Carbon Dioxide at Mercury Electrode in Aqueous Solution. *Bull. Chem. Soc. Jpn.* **55,** 660–665 (1982).

140. Murata, A. & Hori, Y. Product Selectivity Affected by Cationic Species in Electrochemical Reduction of CO_2 and CO at a Cu Electrode. *Bull. Chem. Soc. Jpn.* **64,** 123–127 (1991).

141. Thorson, M. R., Siil, K. I. & Kenis, P. J. A. Effect of Cations on the Electrochemical Conversion of CO_2 to CO. *J. Electrochem. Soc.* **160,** F69–F74 (2013).

142. Sun, L., Ramesha, G. K., Kamat, P. V. & Brennecke, J. F. Switching the Reaction Course of Electrochemical CO_2 Reduction with Ionic Liquids. *Langmuir* **30,** 6302–6308 (2014).

143. Chen, L. D., Urushihara, M., Chan, K. & Nørskov, J. K. Electric Field Effects in Electrochemical CO_2 Reduction. *ACS Catal.* **6,** 7133–7139 (2016).

144. Pérez-Gallent, E., Marcandalli, G., Figueiredo, M. C., Calle-Vallejo, F. & Koper, M. T. M. Structure- and Potential-Dependent Cation Effects on CO Reduction at Copper Single-Crystal Electrodes. *J. Am. Chem. Soc.* **139,** 16412–16419 (2017).

145. Feaster, J. T., Jongerius, A. L., Liu, X., Urushihara, M., Nitopi, S. A., Hahn, C., Chan, K., Nørskov, J. K. & Jaramillo, T. F. Understanding the Influence of [EMIM]Cl on the Suppression of the Hydrogen Evolution Reaction on Transition Metal Electrodes. *Langmuir* **33,** 9464–9471 (2017).

146. Sartin, M. M., Yu, Z., Chen, W., He, F., Sun, Z., Chen, Y.-X. & Huang, W. Effect of Particle Shape and Electrolyte Cation on CO Adsorption to Copper Oxide Nanoparticle Electrocatalysts. *J. Phys. Chem. C* **122,** 26489–26498 (2018).

147. Hori, Y., Takahashi, R., Yoshinami, Y. & Murata, A. Electrochemical Reduction of CO at a Copper Electrode. *J. Phys. Chem. B* **101,** 7075–7081 (1997).

148. Singh, M. R., Clark, E. L. & Bell, A. T. Effects of Electrolyte, Catalyst, and Membrane Composition and Operating Conditions on the Performance of Solar-Driven Electrochemical Reduction of Carbon Dioxide. *Phys. Chem. Chem. Phys.* **17,** 18924–18936 (2015).

149. Varela, A. S., Kroschel, M., Reier, T. & Strasser, P. Controlling the Selectivity of CO_2 Electroreduction on Copper: The Effect of the Electrolyte Concentration and the Importance of the Local pH. *Catal. Today* **260,** 8–13 (2016).

150. Wuttig, A., Liu, C., Peng, Q., Yaguchi, M., Hendon, C. H., Motobayashi, K., Ye, S., Osawa, M. & Surendranath, Y. Tracking a Common Surface-Bound Intermediate During CO_2-to-Fuels Catalysis. *ACS Cent. Sci.* **2,** 522–528 (2016).

151. Seifitokaldani, A., Gabardo, C. M., Burdyny, T., Dinh, C.-T., Edwards, J. P., Kibria, M. G., Bushuyev, O. S., Kelley, S. O., Sinton, D. & Sargent, E. H. Hydronium-Induced Switching between CO_2 Electroreduction Pathways. *J. Am. Chem. Soc.* **140,** 3833–3837 (2018).

152. Wang, L., Nitopi, S. A., Bertheussen, E., Orazov, M., Morales-Guio, C. G., Liu, X., Higgins, D. C., Chan, K., Nørskov, J. K., Hahn, C., *et al.* Electrochemical Carbon Monoxide Reduction on Polycrystalline Copper: Effects of Potential, Pressure, and pH on Selectivity Toward Multicarbon and Oxygenated Products. *ACS Catal.* **8,** 7445–7454 (2018).

153. Dunwell, M., Yang, X., Setzler, B. P., Anibal, J., Yan, Y. & Xu, B. Examination of Near-Electrode Concentration Gradients and Kinetic Impacts on the Electrochemical Reduction of CO_2 using Surface-Enhanced Infrared Spectroscopy. *ACS Catal.* **8,** 3999–4008 (2018).

154. Barton Cole, E., Lakkaraju, P. S., Rampulla, D. M., Morris, A. J., Abelev, E. & Bocarsly, A. B. Using a One-Electron Shuttle for the Multielectron Reduction of CO_2 to Methanol: Kinetic, Mechanistic, and Structural Insights. *J. Am. Chem. Soc.* **132,** 11539–11551 (2010).

155. Oberst, J. L., Jhong, H.-R., Kenis, P. J. A. & Gewirth, A. A. Insight into the Electrochemical Reduction of CO_2 on Gold via Surface-Enhanced Raman Spectroscopy and N-Containing Additives. *J. Solid State Electrochem.* **20,** 1149–1154 (2016).

156. Fang, Y. & Flake, J. C. Electrochemical Reduction of CO_2 at Functionalized Au Electrodes. *J. Am. Chem. Soc.* **139,** 3399–3405 (2017).

157. Ahn, S., Klyukin, K., Wakeham, R. J., Rudd, J. A., Lewis, A. R., Alexander, S., Carla, F., Alexandrov, V. & Andreoli, E. Poly-Amide Modified Copper Foam Electrodes for Enhanced Electrochemical Reduction of Carbon Dioxide. *ACS Catal.* **8,** 4132–4142 (2018).

158. Atifi, A., Boyce, D. W., DiMeglio, J. L. & Rosenthal, J. Directing the Outcome of CO_2 Reduction at Bismuth Cathodes Using Varied Ionic Liquid Promoters. *ACS Catal.* **8,** 2857–2863 (2018).

159. Frumkin, A. N. Influence of Cation Adsorption on the Kinetics of Electrode Processes. *Trans. Faraday Soc.* **55,** 156–167 (1959).

160. Mills, J. N., McCrum, I. T. & Janik, M. J. Alkali Cation Specific Adsorption onto fcc(111) Transition Metal Electrodes. *Phys. Chem. Chem. Phys.* **16,** 13699–13707 (2014).

161. Liu, M., Pang, Y., Zhang, B., De Luna, P., Voznyy, O., Xu, J., Zheng, X., Dinh, C. T., Fan, F., Cao, C., de Arquer, F. P. G., Safaei, T. S., Mepham, A., Klinkova, A., Kumacheva, E., Filleter, T., Sinton, D., Kelley, S. O. & Sargent, E. H. Enhanced Electrocatalytic CO_2 Reduction via Field-Induced Reagent Concentration. *Nature* **537,** 382–386 (2016).

162. Herasymenko, P. & Šlendyk, I. Wasserstoffüberspannung und Adsorption der Ionen. *Z. Phys. Chem. A* **149,** 123–139 (1930).

163. Ikeda, O., Tamura, H. & Matsuda, Y. Specific Adsorption Effects of Organic Cation on the Electroreduction of Dimethylfumarate. *J. Electroanal. Chem.* **111,** 345–358 (1980).

164. Fawcett, W. R., Fedurco, M. & Opallo, M. The Inhibiting Effects of Tetraalkylammonium Cations on Simple Heterogeneous Electron Transfer Reactions in Polar Aprotic Solvents. *J. Phys. Chem.* **96,** 9959–9964 (1992).

165. Strmcnik, D., van der Vliet, D. F., Chang, K.-C., Komanicky, V., Kodama, K., You, H., Stamenkovic, V. R. & Marković, N. M. Effects of Li^+, K^+, and Ba^{2+} Cations on the ORR at Model and High Surface Area Pt and Au Surfaces in Alkaline Solutions. *J. Phys. Chem. Lett.* **2,** 2733–2736 (2011).

166. Fedurco, M., Kedzierzawski, P. & Augustynski, J. Effect of Multivalent Cations upon Reduction of Nitrate Ions at the Ag Electrode. *J. Electrochem. Soc.* **146,** 2569–2572 (1999).

167. Subbaraman, R., Tripkovic, D., Strmcnik, D., Chang, K.-C., Uchimura, M., Paulikas, A. P., Stamenkovic, V. & Marković, N. M. Enhancing Hydrogen Evolution Activity in Water Splitting by Tailoring Li^+-$Ni(OH)_2$-Pt Interfaces. *Science* **334,** 1256–1260 (2011).

168. Suntivich, J., Perry, E. E., Gasteiger, H. A. & Shao-Horn, Y. The Influence of the Cation on the Oxygen Reduction and Evolution Activities of Oxide Surfaces in Alkaline Electrolyte. *Electrocatal.* **4,** 49–55 (2013).

169. Van der Vliet, D. F. & Koper, M. T. M. Electrochemistry of Pt (100) in Alkaline Media: A Voltammetric Study. *Surf. Sci.* **604,** 1912–1918 (2010).

170. Yamakata, A., Soeta, E., Ishiyama, T., Osawa, M. & Morita, A. Real-Time Observation of the Destruction of Hydration Shells under Electrochemical Force. *J. Am. Chem. Soc.* **135,** 15033–15039 (2013).

171. Yamakata, A. & Osawa, M. Cation-Dependent Restructure of the Electric Double Layer on CO-covered Pt Electrodes: Difference Between Hydrophilic and Hydrophobic Cations. *J. Electroanal. Chem.* **800,** 19–24 (2017).

172. Marcus, Y. Tetraalkylammonium Ions in Aqueous and Non-Aqueous Solutions. *J. Solution Chem.* **37,** 1071–1098 (2008).

173. Pearson, R. G. Absolute Electronegativity and Hardness: Application to Inorganic Chemistry. *Inorg. Chem.* **27,** 734–740 (1988).

174. Roth, J. D. & Weaver, M. J. Role of the Double-Layer Cation on the Potential-Dependent Stretching Frequencies and Binding Geometries of Carbon Monoxide at Platinum-Nonaqueous Interfaces. *Langmuir* **8,** 1451–1458 (1992).

175. Durand, W. J., Peterson, A. A., Studt, F., Abild-Pedersen, F. & Nørskov, J. K. Structure Effects on the Energetics of the Electrochemical Reduction of CO_2 by Copper Surfaces. *Surf. Sci.* **605,** 1354–1359 (2011).

176. Nie, X., Esopi, M. R., Janik, M. J. & Asthagiri, A. Selectivity of CO_2 Reduction on Copper Electrodes: The Role of the Kinetics of Elementary Steps. *Angew. Chem. Int. Ed.* **52,** 2459–2462 (2013).

177. Calle-Vallejo, F. & Koper, M. Theoretical Considerations on the Electroreduction of CO to C_2 Species on Cu(100) Electrodes. *Angew. Chem. Int. Ed.* **52,** 7282–7285 (2013).

178. Goodpaster, J. D., Bell, A. T. & Head-Gordon, M. Identification of Possible Pathways for C−C Bond Formation during Electrochemical Reduction of CO_2: New Theoretical Insights from an Improved Electrochemical Model. *J. Phys. Chem. Lett.* **7,** 1471–1477 (2016).

179. Xiao, H., Cheng, T. & Goddard, W. A. Atomistic Mechanisms Underlying Selectivities in C_1 and C_2 Products from Electrochemical Reduction of CO on Cu(111). *J. Am. Chem. Soc.* **139,** 130–136 (2017).

180. Bagger, A., Arnarson, L., Hansen, M. H., Spohr, E. & Rossmeisl, J. Electrochemical CO Reduction: A Property of the Electrochemical Interface. *J. Am. Chem. Soc.* **141,** 1506–1514 (2019).

181. Wuttig, A. & Surendranath, Y. Impurity Ion Complexation Enhances Carbon Dioxide Reduction Catalysis. *ACS Catal.* **5,** 4479–4484 (2015).

182. Roberts, F. S., Kuhl, K. P. & Nilsson, A. High Selectivity for Ethylene from Carbon Dioxide Reduction over Copper Nanocube Electrocatalysts. *Angew. Chem. Int. Ed.* **54,** 5179–5182 (2015).

183. Hori, Y., Murata, A., Takahashi, R. & Suzuki, S. Electrochemical Reduction of Carbon Monoxide to Hydrocarbons at Various Metal Electrodes in Aqueous Solution. *Chem. Lett.* **16,** 1665–1668 (1987).

184. White, J. L., Baruch, M. F., Pander, J. E., Hu, Y., Fortmeyer, I. C., Park, J. E., Zhang, T., Liao, K., Gu, J., Yan, Y., Shaw, T. W., Abelev, E. & Bocarsly, A. B. Light-Driven Heterogeneous Reduction of Carbon Dioxide: Photocatalysts and Photoelectrodes. *Chem. Rev.* **115,** 12888–12935 (2015).

185. Gunathunge, C. M., Li, X., Li, J., Hicks, R. P., Ovalle, V. J. & Waegele, M. M. Spectroscopic Observation of Reversible Surface Reconstruction of Copper Electrodes Under CO_2 Reduction. *J. Phys. Chem. C* **121,** 12337–12344 (2017).

186. Conway, B. E. Kinetics of Electrolytic Hydrogen and Deuterium Evolution. *Proc. R. Soc. London, Ser. A* **256,** 128–144 (1960).

187. Hori, Y., Koga, O., Yamazaki, H. & Matsuo, T. Infrared Spectroscopy of Adsorbed CO and Intermediate Species in Electrochemical Reduction of CO_2 to Hydrocarbons on a Cu Electrode. *Electrochim. Acta* **40,** 2617–2622 (1995).

188. Koga, O., Teruya, S., Matsuda, K., Minami, M., Hoshi, N. & Hori, Y. Infrared Spectroscopic and Voltammetric Study of Adsorbed CO on Stepped Surfaces of Copper Monocrystalline Electrodes. *Electrochim. Acta* **50,** 2475–2485 (2005).

189. Dunwell, M., Wang, J., Yan, Y. & Xu, B. Surface Enhanced Spectroscopic Investigations of Adsorption of Cations on Electrochemical Interfaces. *Phys. Chem. Chem. Phys.* **19,** 971–975 (2017).

190. Gunathunge, C. M., Ovalle, V. J., Li, Y., Janik, M. J. & Waegele, M. M. Existence of an Electrochemically Inert CO Population on Cu Electrodes in Alkaline pH. *ACS Catal.* **8,** 7507–7516 (2018).

191. Ueba, H. Chemical Effects on Vibrational Properties of Adsorbed Molecules on Metal Surfaces: Coverage Dependence. *Surf. Sci.* **188,** 421–455 (1987).

192. Bublitz, G. U. & Boxer, S. G. Stark Spectroscopy: Applications in Chemistry, Biology, and Materials Science. *Annu. Rev. Phys. Chem.* **48,** 213–242 (1997).

193. Sorenson, S. A., Patrow, J. G. & Dawlaty, J. M. Solvation Reaction Field at the Interface Measured by Vibrational Sum Frequency Generation Spectroscopy. *J. Am. Chem. Soc.* **139,** 2369–2378 (2017).

194. Ge, A., Videla, P. E., Lee, G. L., Rudshteyn, B., Song, J., Kubiak, C. P., Batista, V. S. & Lian, T. Interfacial Structure and Electric Field Probed by in Situ Electrochemical Vibrational Stark Effect Spectroscopy and Computational Modeling. *J. Phys. Chem. C* **121,** 18674–18682 (2017).

195. Clark, M. L., Ge, A., Videla, P. E., Rudshteyn, B., Miller, C. J., Song, J., Batista, V. S., Lian, T. & Kubiak, C. P. CO_2 Reduction Catalysts on Gold Electrode Surfaces Influenced by Large Electric Fields. *J. Am. Chem. Soc.* **140,** 17643–17655 (2018).

196. Lambert, D. K. Vibrational Stark Effect of CO on Ni(100), and CO in the Aqueous Double Layer: Experiment, Theory, and Models. *J. Chem. Phys.* **89,** 3847–3860 (1988).

197. Vetter, K. J. *Electrochemical Kinetics, Theoretical Aspects; Academic Press; New York, NY* (1967).

198. Anderson, M. R. & Huang, J. The Influence of Cation Size upon the Infrared Spectrum of Carbon Monoxide Adsorbed on Platinum Electrodes. *J. Electroanal. Chem.* **318,** 335–347 (1991).

199. Jiang, X. & Weaver, M. J. The Role of Interfacial Potential in Adsorbate Bonding: Electrode Potential-Dependent Infrared Spectra for Saturated CO Adlayers on Pt(110) and Related Electrochemical Surfaces in Varying Solvent Environments. *Surf. Sci.* **275,** 237–252 (1992).

200. Andersson, S. & Pendry, J. B. Structure of CO Adsorbed on Cu(100) and Ni(100). *Phys. Rev. Lett.* **43,** 363–366 (July 1979).

201. Łukomska, A. & Sobkowski, J. Potential of Zero Charge of Monocrystalline Copper Electrodes in Perchlorate Solutions. *J. Electroanal. Chem.* **567,** 95–102 (2004).

202. Gileadi, E., Argade, S. D. & Bockris, J. O. The Potential of Zero Charge of Platinum and Its pH Dependence. *J. Phys. Chem.* **70,** 2044–2046 (1966).

203. Che, F., Gray, J. T., Ha, S., Kruse, N., Scott, S. L. & McEwen, J.-S. Elucidating the Roles of Electric Fields in Catalysis: A Perspective. *ACS Catal.* **8,** 5153–5174 (2018).

204. Vollmer, S., Witte, G. & Wöll, C. Determination of Site Specific Adsorption Energies of CO on Copper. *Catal. Lett.* **77,** 97–101 (2001).

205. Verdaguer-Casadevall, A., Li, C. W., Johansson, T. P., Scott, S. B., McKeown, J. T., Kumar, M., Stephens, I. E. L., Kanan, M. W. & Chorkendorff, I. Probing the Active Surface Sites for CO Reduction on Oxide-Derived Copper Electrocatalysts. *J. Am. Chem. Soc.* **137,** 9808–9811 (2015).

206. Kizhakevariam, N., Jiang, X. & Weaver, M. J. Infrared spectroscopy of model electrochemical interfaces in ultrahigh vacuum: The archetypical case of carbon monoxide/water coadsorption on Pt(111). *J. Chem. Phys.* **100,** 6750–6764 (1994).

207. Ogasawara, H., Yoshinobu, J. & Kawai, M. Direct observation of the molecular interaction between chemisorbed CO and water overlayer on Pt(111). *Surf. Sci.* **386,** 73–77 (1997).

208. Nagao, M., Watanabe, K. & Matsumoto, Y. Ultrafast Vibrational Energy Transfer in the Layers of D_2O and CO on Pt(111) Studied with Time-Resolved Sum-Frequency-Generation Spectroscopy. *J. Phys. Chem. C* **113,** 11712–11719 (2009).

209. Yan, Y.-G., Peng, B., Yang, Y.-Y., Cai, W.-B., Bund, A. & Stimming, U. Interfacial Water at a CO-Predosed Platinum Electrode: A Surface Enhanced Infrared Study with Strong Hydrogen Evolution Reaction Control. *J. Phys. Chem. C* **115,** 5584–5592 (2011).

210. Cheng, T., Xiao, H. & Goddard, W. A. Nature of the Active Sites for CO Reduction on Copper Nanoparticles; Suggestions for Optimizing Performance. *J. Am. Chem. Soc.* **139,** 11642–11645 (2017).

211. Pérez-Gallent, E., Figueiredo, M. C., Calle-Vallejo, F. & Koper, M. T. M. Spectroscopic Observation of a Hydrogenated CO Dimer Intermediate During CO Reduction on Cu(100) Electrodes. *Angew. Chem. Int. Ed.* **56,** 3621–3624 (2017).

212. Wonders, A. H., Housmans, T. H. M., Rosca, V & Koper, M. T. M. On-Line Mass Spectrometry System for Measurements at Single-Crystal Electrodes in Hanging Meniscus Configuration. *J. Appl. Electrochem.* **36,** 1215–1221 (2006).

213. Jambunathan, K. & Hillier, A. C. Measuring Electrocatalytic Activity on a Local Scale with Scanning Differential Electrochemical Mass Spectrometry. *J. Electrochem. Soc.* **150,** E312–E320 (2003).

214. Grote, J.-P., Zeradjanin, A. R., Cherevko, S. & Mayrhofer, K. J. J. Coupling of a Scanning Flow Cell With Online Electrochemical Mass Spectrometry for Screening of Reaction Selectivity. *Rev. Sci. Instrum.* **85,** 104101 (2014).

215. Schouten, K., Kwon, Y., van der Ham, C., Qin, Z. & Koper, M. A New Mechanism for the Selectivity to C_1 and C_2 Species in the Electrochemical Reduction of Carbon Dioxide on Copper Electrodes. *Chem. Sci.* **2,** 1902–1909 (2011).

216. Waszczuk, P., Zelenay, P. & Sobkowski, J. Surface Interaction of Benzoic Acid with a Copper Electrode. *Electrochim. Acta* **40,** 1717–1721 (1995).

217. Wallace, W. E. in (National Institute of Standards and Technology, Gaithersburg MD, 20899, 2019).

218. Kim, C., Jeon, H. S., Eom, T., Jee, M. S., Kim, H., Friend, C. M., Min, B. K. & Hwang, Y. J. Achieving Selective and Efficient Electrocatalytic Activity for CO_2 Reduction Using Immobilized Silver Nanoparticles. *J. Am. Chem. Soc.* **137,** 13844–13850 (2015).

219. Kim, D., Kley, C. S., Li, Y. & Yang, P. Copper Nanoparticle Ensembles for Selective Electroreduction of CO_2 to C2–C3 Products. *Proc. Natl. Acad. Sci. U.S.A.* **114,** 10560–10565 (2017).

220. Kauffman, D. R., Alfonso, D. R., Tafen, D. N., Wang, C., Zhou, Y., Yu, Y., Lekse, J. W., Deng, X., Espinoza, V., Trindell, J., Ranasingha, O. K., Roy, A., Lee, J.-S. & Xin, H. L. Selective Electrocatalytic Reduction of CO_2 into CO at Small, Thiol-Capped Au/Cu Nanoparticles. *J. Phys. Chem. C* **122,** 27991–28000 (2018).

221. Kas, R., Kortlever, R., Yilmaz, H., Koper, M. T. M. & Mul, G. Manipulating the Hydrocarbon Selectivity of Copper Nanoparticles in CO_2 Electroreduction by Process Conditions. *ChemElectroChem* **2,** 354–358 (2015).

222. Ma, M., Trzeniewski, B. J., Xie, J. & Smith, W. A. Selective and Efficient Reduction of Carbon Dioxide to Carbon Monoxide on Oxide-Derived Nanostructured Silver Electrocatalysts. *Angew. Chem. Inter. Ed.* **55,** 9748–9752 (2016).

223. Dutta, A., Rahaman, M., Luedi, N. C., Mohos, M. & Broekmann, P. Morphology Matters: Tuning the Product Distribution of CO_2 Electroreduction on Oxide-Derived Cu Foam Catalysts. *ACS Catal.* **6,** 3804–3814 (2016).

224. Lv, J.-J., Jouny, M., Luc, W., Zhu, W., Zhu, J.-J. & Jiao, F. A Highly Porous Copper Electrocatalyst for Carbon Dioxide Reduction. *Adv. Mater.* **30,** 1803111 (2018).

225. Wang, L., Nitopi, S., Wong, A. B., Snider, J. L., Nielander, A. C., Morales-Guio, C. G., Orazov, M., Higgins, D. C., Hahn, C. & Jaramillo, T. F. Electrochemically Converting Carbon Monoxide to Liquid Fuels by Directing Selectivity with Electrode Surface Area. *Nat. Catal.* **2,** 702–708 (2019).

226. Chen, C. S., Handoko, A. D., Wan, J. H., Ma, L., Ren, D. & Yeo, B. S. Stable and Selective Electrochemical Reduction of Carbon Dioxide to Ethylene on Copper Mesocrystals. *Catal. Sci. Technol.* **5,** 161–168 (2015).

227. Kwon, Y., Lum, Y., Clark, E. L., Ager, J. W. & Bell, A. T. CO_2 Electroreduction with Enhanced Ethylene and Ethanol Selectivity by Nanostructuring Polycrystalline Copper. *ChemElectroChem* **3,** 1012–1019 (2016).

228. Gao, D., Scholten, F. & Cuenya, B. R. Improved CO_2 Electroreduction Performance on Plasma-Activated Cu Catalysts via Electrolyte Design: Halide Effect. *ACS Catal.* **7,** 5112–5120 (2017).

229. Reller, C., Krause, R., Volkova, E., Schmid, B., Neubauer, S., Rucki, A., Schuster, M. & Schmid, G. Selective Electroreduction of CO_2 Toward Ethylene on Nano Dendritic Copper Catalysts at High Current Density. *Adv. Energy Mater.* **7,** 1602114 (2017).

230. Gao, D., Sinev, I., Scholten, F., Arn-Ais, R. M., Divins, N. J., Kvashnina, K., Timoshenko, J. & Roldan Cuenya, B. Selective CO_2 Electroreduction to Ethylene and

Multicarbon Alcohols via Electrolyte-Driven Nanostructuring. *Angew. Chem. Inter. Ed.* **58,** 17047–17053 (2019).

231. Hoang, T. T. H., Ma, S., Gold, J. I., Kenis, P. J. A. & Gewirth, A. A. Nanoporous Copper Films by Additive-Controlled Electrodeposition: CO_2 Reduction Catalysis. *ACS Catal.* **7,** 3313–3321 (2017).

232. Chen, X., Henckel, D., Nwabara, U., Li, Y., Frenkel, A. I., Fister, T. T., Kenis, P. J. A. & Gewirth, A. A. Controlling Speciation during CO_2 Reduction on Cu-Alloy Electrodes. *ACS Catal.* **10,** 672–682 (2020).

233. De Luna, P., Quintero-Bermudez, R., Dinh, C.-T., Ross, M. B., Bushuyev, O. S., Todorovic, P., Regier, T., Kelley, S. O., Yang, P. & Sargent, E. H. Catalyst Electro-Redeposition Controls Morphology and Oxidation State for Selective Carbon Dioxide Reduction. *Nat. Catal.* **1,** 103–110 (2018).

234. Yoon, Y., Hall, A. S. & Surendranath, Y. Tuning of Silver Catalyst Mesostructure Promotes Selective Carbon Dioxide Conversion into Fuels. *Angew. Chem. Int. Ed.* **55,** 15282–15286 (2016).

235. Nguyen-Phan, T.-D., Wang, C., Marin, C. M., Zhou, Y., Stavitski, E., Popczun, E. J., Yu, Y., Xu, W., Howard, B. H., Stuckman, M. Y., Waluyo, I., Ohodnicki, P. R. & Kauffman, D. R. Understanding Three-dimensionally Interconnected Porous Oxide-Derived Copper Electrocatalyst for Selective Carbon Dioxide Reduction. *J. Mater. Chem. A* **7,** 27576–27584 (2019).

236. Malkani, A. S., Dunwell, M. & Xu, B. Operando Spectroscopic Investigations of Copper and Oxide-Derived Copper Catalysts for Electrochemical CO Reduction. *ACS Catal.* **9,** 474–478 (2019).

237. Mistry, H., Varela, A. S., Kühl, S., Strasser, P. & Cuenya, B. R. Nanostructured Electrocatalysts with Tunable Activity and Selectivity. *Nat. Rev. Mater.* **1,** 16009 (2016).

238. Eilert, A., Cavalca, F., Roberts, F. S., Osterwalder, J., Liu, C., Favaro, M., Crumlin, E. J., Ogasawara, H., Friebel, D., Pettersson, L. G. M. & Nilsson, A. Subsurface Oxygen in Oxide-Derived Copper Electrocatalysts for Carbon Dioxide Reduction. *J. Phys. Chem. Lett.* **8,** 285–290 (2017).

239. Raciti, D., Mao, M., Park, J. H. & Wang, C. Local pH Effect in the CO_2 Reduction Reaction on High-Surface-Area Copper Electrocatalysts. *J. Electrochem. Soc.* **165,** F799–F804 (2018).

240. Mistry, H., Varela, A. S., Bonifacio, C. S., Zegkinoglou, I., Sinev, I., Choi, Y.-W., Kisslinger, K., Stach, E. A., Yang, J. C., Strasser, P. & Cuenya, B. R. Highly Selective Plasma-Activated Copper Catalysts for Carbon Dioxide Reduction to Ethylene. *Nat. Commun.* **7,** 12123 (June 2016).

241. Ren, D., Deng, Y., Handoko, A. D., Chen, C. S., Malkhandi, S. & Yeo, B. S. Selective Electrochemical Reduction of Carbon Dioxide to Ethylene and Ethanol on Copper(I) Oxide Catalysts. *ACS Catal.* **5,** 2814–2821 (2015).

242. Lum, Y. & Ager, J. W. Stability of Residual Oxides in Oxide-Derived Copper Catalysts for Electrochemical CO_2 Reduction Investigated with ^{18}O Labeling. *Angew. Chem. Int. Ed.* **57,** 551–554 (2018).

243. Mandal, L., Yang, K. R., Motapothula, M. R., Ren, D., Lobaccaro, P., Patra, A., Sherburne, M., Batista, V. S., Yeo, B. S., Ager, J. W., Martin, J. & Venkatesan, T. Investigating the Role of Copper Oxide in Electrochemical CO_2 Reduction in Real Time. *ACS Appl. Mater. Interfaces* **10,** 8574–8584 (2018).

244. Gewirth, A. A. & Niece, B. K. Electrochemical Applications of in Situ Scanning Probe Microscopy. *Chem. Rev.* **97,** 1129–1162 (1997).

245. Kim, Y.-G., Baricuatro, J. H., Javier, A., Gregoire, J. M. & Soriaga, M. P. The Evolution of the Polycrystalline Copper Surface, First to Cu(111) and Then to Cu(100), at a Fixed CO_2RR Potential: A Study by Operando EC-STM. *Langmuir* **30,** 15053–15056 (2014).

246. Firet, N. J., Blommaert, M. A., Burdyny, T., Venugopal, A., Bohra, D., Longo, A. & Smith, W. A. Operando EXAFS Study Reveals Presence of Oxygen in Oxide-Derived Silver Catalysts for Electrochemical CO_2 Reduction. *J. Mater. Chem. A* **7,** 2597–2607 (6 2019).

247. Hollins, P. & Pritchard, J. Infrared Studies of Chemisorbed Layers on Single Crystals. *Prog. Surf. Sci.* **19,** 275–349 (1985).

248. Zou, S., Gomez, R. & Weaver, M. J. Infrared Spectroscopy of Carbon Monoxide at the Ordered Palladium (110)-Aqueous Interface: Evidence for Adsorbate-Induced Surface Reconstruction. *Surf. Sci.* **399,** 270–283 (1998).

249. Pischel, J. & Pucci, A. Low-Temperature Adsorption of Carbon Monoxide on Gold Surfaces: IR Spectroscopy Uncovers Different Adsorption States on Pristine and Rough Au(111). *J. Phys. Chem. C* **119,** 18340–18351 (2015).

250. Eren, B., Liu, Z., Stacchiola, D., Somorjai, G. A. & Salmeron, M. Structural Changes of Cu(110) and Cu(110)-(2 $\times$ 1)-O Surfaces under Carbon Monoxide in the Torr Pressure Range Studied with Scanning Tunneling Microscopy and Infrared Reflection Absorption Spectroscopy. *J. Phys. Chem. C* **120,** 8227–8231 (2016).

251. Ross, M. B., Dinh, C. T., Li, Y., Kim, D., De Luna, P., Sargent, E. H. & Yang, P. Tunable Cu Enrichment Enables Designer Syngas Electrosynthesis from CO_2. *J. Am. Chem. Soc.* **139,** 9359–9363 (2017).

252. Patel, D. A., Hannagan, R. T., Kress, P. L., Schilling, A. C., Cinar, V. & Sykes, E. C. H. Atomic-Scale Surface Structure and CO Tolerance of NiCu Single-Atom Alloys. *J. Phys. Chem. C* **123,** 28142–28147 (2019).

253. Matsushima, H., Taranovskyy, A., Haak, C., Grnder, Y. & Magnussen, O. M. Reconstruction of Cu(100) Electrode Surfaces during Hydrogen Evolution. *J. Am. Chem. Soc.* **131,** 10362–10363 (2009).

254. Yan, B., Krishnamurthy, D., Hendon, C. H., Deshpande, S., Surendranath, Y. & Viswanathan, V. Surface Restructuring of Nickel Sulfide Generates Optimally Coordinated Active Sites for Oxygen Reduction Catalysis. *Joule* **1,** 600–612 (2017).

255. Medina-Ramos, J., Zhang, W., Yoon, K., Bai, P., Chemburkar, A., Tang, W., Atifi, A., Lee, S. S., Fister, T. T., Ingram, B. J., Rosenthal, J., Neurock, M., van Duin, A. C. T. & Fenter, P. Cathodic Corrosion at the Bismuth-Ionic Liquid Electrolyte Interface under Conditions for CO_2 Reduction. *Chem. Mater.* **30,** 2362–2373 (2018).

256. Woodruff, D., Hayden, B., Prince, K. & Bradshaw, A. Dipole Coupling and Chemical Shifts in IRAS of CO Adsorbed on Cu(110). *Surf. Sci.* **123,** 397–412 (1982).

257. Mason, S. E., Grinberg, I. & Rappe, A. M. Adsorbate-Adsorbate Interactions and Chemisorption at Different Coverages Studied by Accurate ab initio Calculations: CO on Transition Metal Surfaces. *J. Phys. Chem. B* **110,** 3816–3822 (2006).

258. Browne, V., Fox, S. & Hollins, P. Infrared Spectroscopy as an In Situ Probe of Morphology. *Catal. Today* **9,** 1–14 (1991).

259. Sheppard, N. & Nguyen, T. T. in *Advances in Infrared and Raman Spectroscopy: v. 5* 67–148 (Heyden, 1978).

260. Mason, S. E., Grinberg, I. & Rappe, A. M. First-Principles Extrapolation Method for Accurate CO Adsorption Energies on Metal Surfaces. *Phys. Rev. B* **69,** 161401 (2004).

261. Schouten, K., Pérez Gallent, E. & Koper, M. Structure Sensitivity of the Electrochemical Reduction of Carbon Monoxide on Copper Single Crystals. *ACS Catal.* **3,** 1292–1295 (2013).

262. Wang, H.-F., Yan, Y.-G., Huo, S.-J., Cai, W.-B., Xu, Q.-J. & Osawa, M. Seeded Growth Fabrication of Cu-on-Si Electrodes for In Situ ATR-SEIRAS Applications. *Electrochim. Acta* **52,** 5950–5957 (2007).

263. Heyes, J., Dunwell, M. & Xu, B. CO_2 Reduction on Cu at Low Overpotentials with Surface-Enhanced in Situ Spectroscopy. *J. Phys. Chem. C* **120,** 17334–17341 (2016).

264. Zhu, S., Li, T., Cai, W.-B. & Shao, M. CO_2 Electrochemical Reduction as Probed Through Infrared Spectroscopy. *ACS Energy Lett.* **4,** 682–689 (2019).

265. Iijima, G., Inomata, T., Yamaguchi, H., Ito, M. & Masuda, H. Role of a Hydroxide Layer on Cu Electrodes in Electrochemical CO_2 Reduction. *ACS Catal.* **9,** 6305–6319 (2019).

266. Schouten, K. J. P., Pérez Gallent, E. & Koper, M. T. M. The Influence of pH on the Reduction of CO and CO_2 to Hydrocarbons on Copper Electrodes. *J. Electroanal. Chem.* **716,** 53–57 (2014).

267. Roberts, F. S., Kuhl, K. P. & Nilsson, A. Electroreduction of Carbon Monoxide over a Copper Nanocube Catalyst: Surface Structure and pH Dependence on Selectivity. *ChemCatChem* **8,** 1119–1124 (2016).

268. Wang, L., Nitopi, S. A., Bertheussen, E., Orazov, M., Morales-Guio, C. G., Liu, X., Higgins, D. C., Chan, K., Nørskov, J. K., Hahn, C., *et al.* Electrochemical Carbon Monoxide Reduction on Polycrystalline Copper: Effects of Potential, Pressure, and pH on Selectivity Toward Multicarbon and Oxygenated Products. *ACS Catal.* **8,** 7445–7454 (2018).

269. Zhang, F. & Co, A. C. Direct Evidence of Local pH Change and the Role of Alkali Cation during CO_2 Electroreduction in Aqueous Media. *Angew. Chem. Inter. Ed.* **58,** 2–10 (2019).

270. Yang, K., Kas, R. & Smith, W. A. In Situ Infrared Spectroscopy Reveals Persistent Alkalinity near Electrode Surfaces during CO_2 Electroreduction. *J. Am. Chem. Soc.* **141,** 15891–15900 (2019).

271. Mistry, H., Reske, R., Strasser, P. & Cuenya, B. R. Size-Dependent Reactivity of Gold-Copper Bimetallic Nanoparticles During CO_2 Electroreduction. *Catal. Today* **288,** 30–36 (2017).

272. Kim, C., Dionigi, F., Beermann, V., Wang, X., Möller, T. & Strasser, P. Alloy Nanocatalysts for the Electrochemical Oxygen Reduction (ORR) and the Direct Electrochemical Carbon Dioxide Reduction Reaction (CO_2RR). *Adv. Mater.* **31,** 1805617 (2019).

273. Wuttig, A., Yaguchi, M., Motobayashi, K., Osawa, M. & Surendranath, Y. Inhibited Proton Transfer Enhances Au-Catalyzed CO_2-to-Fuels Selectivity. *Proc. Natl. Acad. Sci. U.S.A.* **113,** E4585–E4593 (2016).

274. Dunwell, M., Lu, Q., Heyes, J. M., Rosen, J., Chen, J. G., Yan, Y., Jiao, F. & Xu, B. The Central Role of Bicarbonate in the Electrochemical Reduction of Carbon Dioxide on Gold. *J. Am. Chem. Soc.* **139,** 3774–3783 (2017).

275. Hammer, B., Morikawa, Y & Nørskov, J. K. CO Chemisorption at Metal Surfaces and Overlayers. *Phys. Rev. Lett.* **76,** 2141–2144 (1996).

276. Chorkendorff, I. & Niemantsverdriet, J. W. in *Concepts of Modern Catalysis and Kinetics, 2nd, Revised and Enlarged Edition* 217–269 (Wiley-VCH, 2007).

277. Mason, S. E., Grinberg, I. & Rappe, A. M. Orbital-Specific Analysis of CO Chemisorption on Transition-Metal Surfaces. *J. Phys. Chem. C* **112,** 1963–1966 (2008).

278. Bagus, P. & Pacchioni, G. Electric Field Effects on the Surface-Adsorbate Interaction: Cluster Model Studies. *Electrochim. Acta* **36,** 1669–1675 (1991).

279. Head-Gordon, M. & Tully, J. C. Electric Field Effects on Chemisorption and Vibrational Relaxation of CO on Cu(100). *Chem. Phys.* **175,** 37–51 (1993).

280. Hori, Y., Koga, O., Watanabe, Y. & Matsuo, T. FTIR Measurements of Charge Displacement Adsorption of CO on Poly- and Single Crystal (100) of Cu Electrodes. *Electrochim. Acta* **44,** 1389–1395 (1998).

281. Borguet, E. & Dai, H.-L. Site-Specific Properties and Dynamical Dipole Coupling of CO Molecules Adsorbed on a Vicinal Cu(100) Surface. *J. Chem. Phys.* **101,** 9080–9095 (1994).

282. Chang, S.-C. & Weaver, M. J. Coverage-Dependent Dipole Coupling for Carbon Monoxide Adsorbed at Ordered Platinum(111)-Aqueous Interfaces: Structural and Electrochemical Implications. *J. Chem. Phys.* **92,** 4582–4594 (1990).

283. Jović, V. & Jović, B. EIS and Differential Capacitance Measurements onto Single Crystal Faces in Different Solutions: Part II: Cu(111) and Cu(100) in 0.1 M NaOH. *J. Electroanal. Chem.* **541,** 13–21 (2003).

284. Schouten, K. J. P., Gallent, E. P. & Koper, M. T. The Electrochemical Characterization of Copper Single-Crystal Electrodes in Alkaline Media. *J. Electroana. Chem.* **699,** 6–9 (2013).

285. Le Duff, C. S., Lawrence, M. J. & Rodriguez, P. Role of the Adsorbed Oxygen Species in the Selective Electrochemical Reduction of CO_2 to Alcohols and Carbonyls on Copper Electrodes. *Angew. Chem. Int. Ed.* **56,** 12919–12924 (2017).

286. Bagger, A., Arán-Ais, R. M., Halldin Stenlid, J., Campos dos Santos, E., Arnarson, L., Degn Jensen, K., Escudero-Escribano, M., Cuenya, B. R. & Rossmeisl, J. Ab

Initio Cyclic Voltammetry on Cu (111), Cu (100) and Cu (110) in Acidic, Neutral and Alkaline Solutions. *ChemPhysChem* **20,** 3096–3105 (2019).

287. Hori, Y., Wakebe, H., Tsukamoto, T. & Koga, O. Adsorption of CO Accompanied with Simultaneous Charge Transfer on Copper Single Crystal Electrodes Related with Electrochemical Reduction of CO_2 to Hydrocarbons. *Surf. Sci.* **335,** 258–263 (1995).

288. Yaguchi, M., Uchida, T., Motobayashi, K. & Osawa, M. Speciation of Adsorbed Phosphate at Gold Electrodes: A Combined Surface-Enhanced Infrared Absorption Spectroscopy and DFT Study. *J. Phys. Chem. Lett.* **7,** 3097–3102 (2016).

289. Tsuji, M., Yamaguchi, D., Matsunaga, M. & Alam, M. J. Epitaxial Growth of Au@Cu Core- Shell Nanocrystals Prepared Using the PVP-Assisted Polyol Reduction Method. *Cryst. Growth Des.* **10,** 5129–5135 (2010).

290. Ellis, J., Toennies, J. P. & Witte, G. Helium Atom Scattering Study of the Frustrated Translation Mode of CO Adsorbed on the Cu(001) Surface. *J. Chem. Phys.* **102,** 5059–5070 (1995).

291. Malkani, A. S., Li, J., Anibal, J., Lu, Q. & Xu, B. Impact of Forced Convection on Spectroscopic Observations of the Electrochemical CO Reduction Reaction. *ACS Catal.* **10,** 941–946 (2020).

292. Dinh, C.-T., Burdyny, T., Kibria, M. G., Seifitokaldani, A., Gabardo, C. M., García de Arquer, F. P., Kiani, A., Edwards, J. P., De Luna, P., Bushuyev, O. S., Zou, C., Quintero-Bermudez, R., Pang, Y., Sinton, D. & Sargent, E. H. CO_2 Electroreduction to Ethylene via Hydroxide-Mediated Copper Catalysis at an Abrupt Interface. *Science* **360,** 783–787 (2018).

293. Reske, R., Duca, M., Oezaslan, M., Schouten, K. J. P., Koper, M. T. M. & Strasser, P. Controlling Catalytic Selectivities during CO_2 Electroreduction on Thin Cu Metal Overlayers. *J. Phys. Chem. Lett.* **4,** 2410–2413 (2013).

294. Varela, A. S., Schlaup, C., Jovanov, Z. P., Malacrida, P., Horch, S., Stephens, I. E. L. & Chorkendorff, I. CO_2 Electroreduction on Well-Defined Bimetallic Surfaces: Cu Overlayers on Pt(111) and Pt(211). *J. Phys. Chem. C* **117,** 20500–20508 (2013).

295. Schlaup, C., Horch, S. & Chorkendorff, I. On the Stability of Copper Overlayers on Au(111) and Au(100) Electrodes under Low Potential Conditions and in the Presence on CO and CO_2. *Surf. Sci.* **631,** 155–164 (2015).

296. Friebel, D., Mbuga, F., Rajasekaran, S., Miller, D. J., Ogasawara, H., Alonso-Mori, R., Sokaras, D., Nordlund, D., Weng, T.-C. & Nilsson, A. Structure, Redox Chemistry, and Interfacial Alloy Formation in Monolayer and Multilayer Cu/Au(111) Model Catalysts for CO_2 Electroreduction. *J. Phys. Chem. C* **118,** 7954–7961 (2014).

297. Wang, W., Shi, H., Wang, L., Li, Z., Shi, H., Wu, K. & Shao, X. Comparison Study of Structural Properties and CO Adsorption on the Cu/Au(111) and Au/Cu(111) Thin Films. *J. Phys. Chem. C* **122,** 19551–19559 (2018).

298. Shen, J.-R. The Structure of Photosystem II and the Mechanism of Water Oxidation in Photosynthesis. *Annu. Rev. Plant Biol.* **66,** 23–48 (2015).

299. Vinyard, D. J. & Brudvig, G. W. Progress Toward a Molecular Mechanism of Water Oxidation in Photosystem II. *Annu. Rev. Phys. Chem.* **68,** 101–116 (2017).

300. Shaffer, D. W., Xie, Y. & Concepcion, J. J. OO Bond Formation In Ruthenium-Catalyzed Water Oxidation: Single-Site Nucleophilic Attack vs. OO Radical Coupling. *Chem. Soc. Rev.* **46,** 6170–6193 (2017).

301. Suen, N.-T., Hung, S.-F., Quan, Q., Zhang, N., Xu, Y.-J. & Chen, H. M. Electrocatalysis for the Oxygen Evolution Reaction: Recent Development and Future Perspectives. *Chem. Soc. Rev.* **46,** 337–365 (2017).

302. Zhang, M. & Frei, H. Water Oxidation Mechanisms of Metal Oxide Catalysts by Vibrational Spectroscopy of Transient Intermediates. *Annu. Rev. Phys. Chem.* **68,** 209–231 (2017).

303. Yu, Z.-Y., Duan, Y., Gao, M.-R., Lang, C.-C., Zheng, Y.-R. & Yu, S.-H. A One-Dimensional Porous Carbon-Supported Ni/Mo_2C Dual Catalyst for Efficient Water Splitting. *Chem. Sci.* **8,** 968–973 (2017).

304. Grimaud, A., Diaz-Morales, O., Han, B., Hong, W. T., Lee, Y.-L., Giordano, L., Stoerzinger, K. A., Koper, M. T. M. & Shao-Horn, Y. Activating Lattice Oxygen Redox Reactions in Metal Oxides to Catalyse Oxygen Evolution. *Nat. Chem.* **9,** 457–465 (2017).

305. Negahdar, L., Zeng, F., Palkovits, S., Broicher, C. & Palkovits, R. Mechanistic Aspects of the Electrocatalytic Oxygen Evolution Reaction over NiCo Oxides. *ChemElectroChem* **6,** 5588–5595 (2019).

306. Zandi, O. & Hamann, T. W. Determination of Photoelectrochemical Water Oxidation Intermediates on Haematite Electrode Surfaces Using Operando Infrared Spectroscopy. *Nat. Chem.* **8,** 778–783 (2016).

307. Zhang, M., De Respinis, M. & Frei, H. Time-Resolved Observations of Water Oxidation Intermediates on A Cobalt Oxide Nanoparticle Catalyst. *Nat. Chem.* **6,** 362–367 (2014).

308. Rosenthal, J. & Nocera, D. G. Role of Proton-Coupled Electron Transfer in O–O Bond Activation. *Acc. Chem. Res.* **40,** 543–553 (2007).

309. Ullman, A. M., Brodsky, C. N., Li, N., Zheng, S.-L. & Nocera, D. G. Probing Edge Site Reactivity of Oxidic Cobalt Water Oxidation Catalysts. *J. Am. Chem. Soc.* **138,** 4229–4236 (2016).

310. Romain, S., Vigara, L. & Llobet, A. OxygenOxygen Bond Formation Pathways Promoted by Ruthenium Complexes. *Acc. Chem. Res.* **42,** 1944–1953 (2009).

311. Garca-Melchor, M., Vilella, L., Lpez, N. & Vojvodic, A. Computationally Probing the Performance of Hybrid, Heterogeneous, and Homogeneous Iridium-Based Catalysts for Water Oxidation. *ChemCatChem* **8,** 1792–1798 (2016).

312. Chen, X., Aschaffenburg, D. J. & Cuk, T. Selecting Between Two Transition States by Which Water Oxidation Intermediates Decay on An Oxide Surface. *Nat. Catal.* **2,** 820–827 (2019).

313. Craig, M. J., Coulter, G., Dolan, E., Soriano-López, J., Mates-Torres, E., Schmitt, W. & García-Melchor, M. Universal Scaling Relations for The Rational Design of Molecular Water Oxidation Catalysts with Near-Zero Overpotential. *Nat. Commun.* **10,** 4993 (2019).

314. Matheu, R., Ertem, M. Z., Gimbert-Suriach, C., Sala, X. & Llobet, A. Seven Coordinated Molecular RutheniumWater Oxidation Catalysts: A Coordination Chemistry Journey. *Chem. Rev.* **119,** 3453–3471 (2019).

315. Romain, S., Bozoglian, F., Sala, X. & Llobet, A. OxygenOxygen Bond Formation by the Ru-Hbpp Water Oxidation Catalyst Occurs Solely via an Intramolecular Reaction Pathway. *J. Am. Chem. Soc.* **131,** 2768–2769 (2009).

316. Le Formal, F., Pastor, E., Tilley, S. D., Mesa, C. A., Pendlebury, S. R., Grtzel, M. & Durrant, J. R. Rate Law Analysis of Water Oxidation on a Hematite Surface. *J. Am. Chem. Soc.* **137,** 6629–6637 (2015).

317. Zhao, Y., Yang, K. R., Wang, Z., Yan, X., Cao, S., Ye, Y., Dong, Q., Zhang, X., Thorne, J. E., Jin, L., Materna, K. L., Trimpalis, A., Bai, H., Fakra, S. C., Zhong, X., Wang, P., Pan, X., Guo, J., Flytzani-Stephanopoulos, M., Brudvig, G. W., Batista, V. S. & Wang, D. Stable Iridium Dinuclear Heterogeneous Catalysts Supported on Metal-Oxide Substrate for Solar Water Oxidation. *Proc. Natl. Acad. Sci. U.S.A.* **115,** 2902–2907 (2018).

318. Zhao, Y., Yan, X., Yang, K. R., Cao, S., Dong, Q., Thorne, J. E., Materna, K. L., Zhu, S., Pan, X., Flytzani-Stephanopoulos, M., Brudvig, G. W., Batista, V. S. & Wang, D. End-On Bound Iridium Dinuclear Heterogeneous Catalysts on WO3 for Solar Water Oxidation. *ACS Cent. Sci.* **4,** 1166–1172 (2018).

319. Wuttig, A., Yoon, Y., Ryu, J. & Surendranath, Y. Bicarbonate Is Not a General Acid in Au-Catalyzed CO2 Electroreduction. *J. Am. Chem. Soc.* **139,** 17109–17113 (2017).

320. Surendranath, Y., Kanan, M. W. & Nocera, D. G. Mechanistic Studies of the Oxygen Evolution Reaction by a Cobalt-Phosphate Catalyst at Neutral pH. *J. Am. Chem. Soc.* **132,** 16501–16509 (2010).

321. Suo, L., Borodin, O., Gao, T., Olguin, M., Ho, J., Fan, X., Luo, C., Wang, C. & Xu, K. "Water-In-Salt" Electrolyte Enables High-Voltage Aqueous Lithium-Ion Chemistries. *Science* **350,** 938–943 (2015).

322. Dong, Q., Yao, X., Zhao, Y., Qi, M., Zhang, X., Sun, H., He, Y. & Wang, D. Cathodically Stable Li-O_2 Battery Operations Using Water-in-Salt Electrolyte. *Chem* **4,** 1345–1358 (2018).

323. Dong, Q., Zhang, X., He, D., Lang, C. & Wang, D. Role of H_2O in CO_2 Electrochemical Reduction As Studied in a Water-in-Salt System. *ACS Cent. Sci.* **5,** 1461–1467 (2019).

324. Bergmann, A., Jones, T. E., Martinez Moreno, E., Teschner, D., Chernev, P., Gliech, M., Reier, T., Dau, H. & Strasser, P. Unified Structural Motifs of The Catalytically Active State of Co(oxyhydr)oxides During the Electrochemical Oxygen Evolution Reaction. *Nat. Catal.* **1,** 711–719 (2018).

325. Pasquini, C., Zaharieva, I., Gonzlez-Flores, D., Chernev, P., Mohammadi, M. R., Guidoni, L., Smith, R. D. L. & Dau, H. H/D Isotope Effects Reveal Factors Controlling Catalytic Activity in Co-Based Oxides for Water Oxidation. *J. Am. Chem. Soc.* **141,** 2938–2948 (2019).

326. Kanan, M. W. & Nocera, D. G. In Situ Formation of an Oxygen-Evolving Catalyst in Neutral Water Containing Phosphate and Co^{2+}. *Science* **321,** 1072–1075 (2008).

327. Kanan, M. W., Yano, J., Surendranath, Y., Dinc, M., Yachandra, V. K. & Nocera, D. G. Structure and Valency of a CobaltPhosphate Water Oxidation Catalyst Determined by in Situ X-ray Spectroscopy. *J. Am. Chem. Soc.* **132,** 13692–13701 (2010).

328. Li, X. & Siegbahn, P. E. M. Water Oxidation Mechanism for Synthetic CoOxides with Small Nuclearity. *J. Am. Chem. Soc.* **135,** 13804–13813 (2013).

329. Wang, L.-P. & Van Voorhis, T. Direct-Coupling O_2 Bond Forming a Pathway in Cobalt Oxide Water Oxidation Catalysts. *J. Phys. Chem. Lett.* **2,** 2200–2204 (2011).

330. Diaz-Morales, O., Ferrus-Suspedra, D. & Koper, M. T. M. The importance of nickel oxyhydroxide deprotonation on its activity towards electrochemical water oxidation. *Chem. Sci.* **7,** 2639–2645 (2016).

331. McAlpin, J. G., Stich, T. A., Casey, W. H. & Britt, R. D. Comparison of Cobalt and Manganese in the Chemistry of Water Oxidation. *Coord. Chem. Rev.* **256.** Solar Fuels- by invitation only, 2445–2452 (2012).

332. Mattioli, G., Giannozzi, P., Amore Bonapasta, A. & Guidoni, L. Reaction Pathways for Oxygen Evolution Promoted by Cobalt Catalyst. *J. Am. Chem. Soc.* **135,** 15353–15363 (2013).

333. Risch, M., Ringleb, F., Kohlhoff, M., Bogdanoff, P., Chernev, P., Zaharieva, I. & Dau, H. Water Oxidation by Amorphous Cobalt-Based Oxides: In Situ Tracking of Redox Transitions and Mode of Catalysis. *Energy Environ. Sci.* **8,** 661–674 (2015).

334. Nakamura, R. & Nakato, Y. Primary Intermediates of Oxygen Photoevolution Reaction on TiO2 (Rutile) Particles, Revealed by in Situ FTIR Absorption and Photoluminescence Measurements. *J. Am. Chem. Soc.* **126,** 1290–1298 (2004).

335. Pavlovic, Z., Ranjan, C., van Gastel, M. & Schlgl, R. The Active Site for The Water Oxidising Anodic Iridium Oxide Probed through In Situ Raman Spectroscopy. *Chem. Commun.* **53,** 12414–12417 (2017).

336. Sivasankar, N., Weare, W. W. & Frei, H. Direct Observation of a Hydroperoxide Surface Intermediate upon Visible Light-Driven Water Oxidation at an Ir Oxide Nanocluster Catalyst by Rapid-Scan FT-IR Spectroscopy. *J. Am. Chem. Soc.* **133,** 12976–12979 (2011).

337. Zhang, Y., Zhang, H., Liu, A., Chen, C., Song, W. & Zhao, J. Rate-Limiting OO Bond Formation Pathways for Water Oxidation on Hematite Photoanode. *J. Am. Chem. Soc.* **140,** 3264–3269 (2018).

338. Liu, H. & Frei, H. Observation of OO Bond Forming Step of Molecular Co4O4 Cubane Catalyst for Water Oxidation by Rapid-Scan FT-IR Spectroscopy. *ACS Catal.* **10,** 2138–2147 (2020).

339. Chen, X., Choing, S. N., Aschaffenburg, D. J., Pemmaraju, C. D., Prendergast, D. & Cuk, T. The Formation Time of Ti-O· and Ti-O·-Ti Radicals at the n-$SrTiO_3$/Aqueous

Interface during Photocatalytic Water Oxidation. *J. Am. Chem. Soc.* **139,** 1830–1841 (2017).

340. Herlihy, D. M., Waegele, M. M., Chen, X., Pemmaraju, C. D., Prendergast, D. & Cuk, T. Detecting the Oxyl Radical of Photocatalytic Water Oxidation at an n-$SrTiO_3$/Aqueous Interface through Its Subsurface Vibration. *Nat. Chem.* **8,** 549–555 (2016).

341. Yeo, B. S. & Bell, A. T. Enhanced Activity of Gold-Supported Cobalt Oxide for the Electrochemical Evolution of Oxygen. *J. Am. Chem. Soc.* **133,** 5587–5593 (2011).

342. Rao, R. R., Kolb, M. J., Giordano, L., Pedersen, A. F., Katayama, Y., Hwang, J., Mehta, A., You, H., Lunger, J. R., Zhou, H., Halck, N. B., Vegge, T., Chorkendorff, I., Stephens, I. E. L. & Shao-Horn, Y. Operando Identification of Site-Dependent Water Oxidation Activity on Ruthenium Dioxide Single-Crystal Surfaces. *Nat. Catal.* **3,** 516–525 (2020).

343. Osawa, M. in *Near-Field Optics and Surface Plasmon Polaritons* (ed Kawata, S.) 163–187 (Springer Berlin Heidelberg, Berlin, Heidelberg, 2001).

344. Du, P., Kokhan, O., Chapman, K. W., Chupas, P. J. & Tiede, D. M. Elucidating the Domain Structure of the Cobalt Oxide Water Splitting Catalyst by X-ray Pair Distribution Function Analysis. *J. Am. Chem. Soc.* **134,** 11096–11099 (2012).

345. Suzuki, M., Ishiguro, T., Kozuka, M. & Nakamoto, K. Resonance Raman spectra, excitation profiles, and infrared spectra of [N,N'-ethylenebis(salicylideniminato)]cobalt(II) in the solid state. *Inorg. Chem.* **20,** 1993–1996 (1981).

346. Jones, R. D., Summerville, D. A. & Basolo, F. Synthetic oxygen carriers related to biological systems. *Chem. Rev.* **79,** 139–179 (1979).

347. Tejedor-Tejedor, M. I. & Anderson, M. A. The protonation of phosphate on the surface of goethite as studied by CIR-FTIR and electrophoretic mobility. *Langmuir* **6,** 602–611 (1990).

348. Tang, I. N. & Munkelwitz, H. R. Water Activities, Densities, and Refractive Indices of Aqueous Sulfates and Sodium Nitrate Droplets of Atmospheric Importance. *J. Geophys. Res. Atmos.* **99,** 18801–18808 (1994).

349. Gerken, J. B., McAlpin, J. G., Chen, J. Y. C., Rigsby, M. L., Casey, W. H., Britt, R. D. & Stahl, S. S. Electrochemical Water Oxidation with Cobalt-Based Electrocatalysts from pH 0-14: The Thermodynamic Basis for Catalyst Structure, Stability, and Activity. *J. Am. Chem. Soc.* **133,** 14431–14442 (2011).

350. Ronald Fawcett, W. & Ryan, P. J. Is Perchlorate Ion Contact Adsorbed from Aqueous Solutions at Polarizable Electrodes? *J. ElectroAnal. Chem.* **649,** 48–52 (2010).

351. Ding, C., Zhou, X., Shi, J., Yan, P., Wang, Z., Liu, G. & Li, C. Abnormal Effects of Cations (Li^+, Na^+, and K^+) on Photoelectrochemical and Electrocatalytic Water Splitting. *J. Phys. Chem. B* **119,** 3560–3566 (2015).

352. Garcia, A. C., Touzalin, T., Nieuwland, C., Perini, N. & Koper, M. T. M. Enhancement of Oxygen Evolution Activity of Nickel Oxyhydroxide by Electrolyte Alkali Cations. *Angew. Chem. Int. Ed.* **58,** 12999–13003 (2019).

353. Zaffran, J., Stevens, M. B., Trang, C. D. M., Nagli, M., Shehadeh, M., Boettcher, S. W. & Caspary Toroker, M. Influence of Electrolyte Cations on Ni(Fe)OOH Catalyzed Oxygen Evolution Reaction. *Chem. Mater.* **29,** 4761–4767 (2017).

354. Remsing, R. C., McKendry, I. G., Strongin, D. R., Klein, M. L. & Zdilla, M. J. Frustrated Solvation Structures Can Enhance Electron Transfer Rates. *J. Phys. Chem. Lett.* **6,** 4804–4808 (2015).

355. Surendranath, Y., Dincă, M. & Nocera, D. G. Electrolyte-Dependent Electrosynthesis and Activity of Cobalt-Based Water Oxidation Catalysts. *J. Am. Chem. Soc.* **131,** 2615–2620 (2009).

356. Trotochaud, L., Young, S. L., Ranney, J. K. & Boettcher, S. W. Nickel–Iron Oxyhydroxide Oxygen-Evolution Electrocatalysts: The Role of Intentional and Incidental Iron Incorporation. *J. Am. Chem. Soc.* **136,** 6744–6753 (2014).

357. Zhang, Y., Zhang, H., Ji, H., Ma, W., Chen, C. & Zhao, J. Pivotal Role and Regulation of Proton Transfer in Water Oxidation on Hematite Photoanodes. *J. Am. Chem. Soc.* **138,** 2705–2711 (2016).

358. Goldsmith, Z. K., Lam, Y. C., Soudackov, A. V. & Hammes-Schiffer, S. Proton Discharge on a Gold Electrode from Triethylammonium in Acetonitrile: Theoretical Modeling of Potential-Dependent Kinetic Isotope Effects. *J. Am. Chem. Soc.* **141,** 1084–1090 (2019).

359. Qi, J., Chen, M., Zhang, W. & Cao, R. Hierarchical-Dimensional Material: A Co(OH)2 Superstructure with Hybrid Dimensions for Enhanced Water Oxidation. *ChemCatChem* **11,** 5969–5975 (2019).

360. Gorin, C. F., Beh, E. S., Bui, Q. M., Dick, G. R. & Kanan, M. W. Interfacial Electric Field Effects on a Carbene Reaction Catalyzed by Rh Porphyrins. *J. Am. Chem. Soc.* **135,** 11257–11265 (2013).

361. Karlberg, G. S., Rossmeisl, J. & Nørskov, J. K. Estimations of Electric Field Effects on the Oxygen Reduction Reaction Based on the Density Functional Theory. *Phys. Chem. Chem. Phys.* **9,** 5158–5161 (2007).

362. Ledezma-Yanez, I., Wallace, W. D. Z., Sebastián-Pascual, P., Climent, V., Feliu, J. M. & Koper, M. T. M. Interfacial Water Reorganization as a pH-Dependent De-

scriptor of the Hydrogen Evolution Rate on Platinum Electrodes. *Nat. Energy* **2,** 17031 (2017).

363. Schultz, Z. D., Shaw, S. K. & Gewirth, A. A. Potential Dependent Organization of Water at the Electrified MetalLiquid Interface. *J. Am. Chem. Soc.* **127,** 15916–15922 (2005).

364. Toney, M. F., Howard, J. N., Richer, J., Borges, G. L., Gordon, J. G., Melroy, O. R., Wiesler, D. G., Yee, D. & Sorensen, L. B. Voltage-Dependent Ordering of Water Molecules at an Electrode–Electrolyte Interface. *Nature* **368,** 444–446 (1994).

365. McAlpin, J. G., Surendranath, Y., Dincă, M., Stich, T. A., Stoian, S. A., Casey, W. H., Nocera, D. G. & Britt, R. D. EPR Evidence for Co(IV) Species Produced During Water Oxidation at Neutral pH. *J. Am. Chem. Soc.* **132,** 6882–6883 (2010).

366. Bajdich, M., García-Mota, M., Vojvodic, A., Nørskov, J. K. & Bell, A. T. Theoretical Investigation of the Activity of Cobalt Oxides for the Electrochemical Oxidation of Water. *J. Am. Chem. Soc.* **135,** 13521–13530 (2013).

367. Plaisance, C. P. & van Santen, R. A. Structure Sensitivity of the Oxygen Evolution Reaction Catalyzed by Cobalt(II,III) Oxide. *J. Am. Chem. Soc.* **137,** 14660–14672 (2015).

368. Pham, H. H., Cheng, M.-J., Frei, H. & Wang, L.-W. Surface Proton Hopping and Fast-Kinetics Pathway of Water Oxidation on Co_3O_4 (001) Surface. *ACS Catal.* **6,** 5610–5617 (2016).

369. Li, W., Sheehan, S. W., He, D., He, Y., Yao, X., Grimm, R. L., Brudvig, G. W. & Wang, D. Hematite-Based Solar Water Splitting in Acidic Solutions: Functionalization by Mono- and Multilayers of Iridium Oxygen-Evolution Catalysts. *Angew. Chem. Int. Ed.* **54,** 11428–11432 (2015).

370. Frisch, M. J., Trucks, G. W., Schlegel, H. B., Scuseria, G. E., Robb, M. A., Cheeseman, J. R., Scalmani, G., Barone, V., Petersson, G. A., Nakatsuji, H., Li, X., Caricato, M., Marenich, A. V., Bloino, J., Janesko, B. G., Gomperts, R., Mennucci, B., Hratchian, H. P., Ortiz, J. V., Izmaylov, A. F., Sonnenberg, J. L., Williams-Young, D., Ding, F., Lipparini, F., Egidi, F., Goings, J., Peng, B., Petrone, A., Henderson, T., Ranasinghe, D., Zakrzewski, V. G., Gao, J., Rega, N., Zheng, G., Liang, W., Hada, M., Ehara, M., Toyota, K., Fukuda, R., Hasegawa, J., Ishida, M., Nakajima, T., Honda, Y., Kitao, O., Nakai, H., Vreven, T., Throssell, K., Montgomery Jr., J. A., Peralta, J. E., Ogliaro, F., Bearpark, M. J., Heyd, J. J., Brothers, E. N., Kudin, K. N., Staroverov, V. N., Keith, T. A., Kobayashi, R., Normand, J., Raghavachari, K., Rendell, A. P., Burant, J. C., Iyengar, S. S., Tomasi, J., Cossi, M., Millam, J. M., Klene, M., Adamo, C., Cammi, R., Ochterski, J. W., Martin, R. L., Morokuma, K., Farkas, O., Foresman, J. B. & Fox, D. J. *Gaussian16 Revision C.01* Gaussian Inc. Wallingford CT. 2016.

371. Becke, A. D. Density-Functional Thermochemistry. III. The Role of Exact Exchange. *J. Chem. Phys.* **98,** 5648–5652 (1993).

372. Stephens, P. J., Devlin, F. J., Chabalowski, C. F. & Frisch, M. J. Ab Initio Calculation of Vibrational Absorption and Circular Dichroism Spectra Using Density Functional Force Fields. *J. Phys. Chem.* **98,** 11623–11627 (1994).

373. Weigend, F. & Ahlrichs, R. Balanced Basis Sets of Split Valence, Triple Zeta Valence and Quadruple Zeta Valence Quality for H to Rn: Design and Assessment of Accuracy. *Phys. Chem. Chem. Phys.* **7,** 3297–3305 (2005).

374. Marenich, A. V., Cramer, C. J. & Truhlar, D. G. Universal Solvation Model Based on Solute Electron Density and on a Continuum Model of the Solvent Defined by

the Bulk Dielectric Constant and Atomic Surface Tensions. *J. Phys. Chem. B* **113,** 6378–6396 (2009).

375. Grimme, S., Ehrlich, S. & Goerigk, L. Effect of the damping function in dispersion corrected density functional theory. *J. Comput. Chem.* **32,** 1456–1465 (2011).

376. Nørskov, J. K., Rossmeisl, J., Logadottir, A., Lindqvist, L., Kitchin, J. R., Bligaard, T. & Jónsson, H. Origin of the Overpotential for Oxygen Reduction at a Fuel-Cell Cathode. *J. Phys. Chem. B* **108,** 17886–17892 (2004).

377. Kresse, G. & Hafner, J. Ab Initio Molecular Dynamics for Liquid Metals. *Phys. Rev. B* **47,** 558–561 (1993).

378. Kresse, G. & Hafner, J. Ab Initio Molecular-Dynamics Simulation of the Liquid-Metal–Amorphous-Semiconductor transition in germanium. *Phys. Rev. B* **49,** 14251–14269 (1994).

379. Kresse, G. & Furthmüller, J. Efficiency of Ab-Initio Total Energy Calculations for Metals and Semiconductors Using a Plane-Wave Basis Set. *Comput. Mater. Sci.* **6,** 15–50 (1996).

380. Kresse, G. & Furthmüller, J. Efficient Iterative Schemes for Ab Initio Total-Energy Calculations Using A Plane-Wave Basis Set. *Phys. Rev. B* **54,** 11169–11186 (1996).

381. Perdew, J. P., Burke, K. & Ernzerhof, M. Generalized Gradient Approximation Made Simple. *Phys. Rev. Lett.* **77,** 3865–3868 (1996).

382. Blöchl, P. E. Projector Augmented-Wave Method. *Phys. Rev. B* **50,** 17953–17979 (1994).

383. Kresse, G. & Joubert, D. From Ultrasoft Pseudopotentials to the Projector Augmented-Wave Method. *Phys. Rev. B* **59,** 1758–1775 (1999).

384. Dudarev, S. L., Botton, G. A., Savrasov, S. Y., Humphreys, C. J. & Sutton, A. P. Electron-Energy-Loss Spectra and the Structural Stability of Nickel Oxide: An LSDA+U Study. *Phys. Rev. B* **57,** 1505–1509 (1998).

385. Jain, A., Hautier, G., Ong, S. P., Moore, C. J., Fischer, C. C., Persson, K. A. & Ceder, G. Formation Enthalpies by Mixing GGA and GGA + U Calculations. *Phys. Rev. B* **84,** 045115 (2011).

386. Monkhorst, H. J. & Pack, J. D. Special Points for Brillouin-Zone Integrations. *Phys. Rev. B* **13,** 5188–5192 (1976).

387. Delaplane, R., Ibers, J., Ferraro, J. & Rush, J. Diffraction and Spectroscopic Studies of the Cobaltic Acid System $HCoC_2$-$DCoO_2$. English (US). *J. Chem. Phys.* **50,** 1920–1927 (1969).

388. Ullman, A. M., Liu, Y., Huynh, M., Bediako, D. K., Wang, H., Anderson, B. L., Powers, D. C., Breen, J. J., Abruña, H. D. & Nocera, D. G. Water Oxidation Catalysis by Co(II) Impurities in $Co(III)_4O_4$ Cubanes. *J. Am. Chem. Soc.* **136,** 17681–17688 (2014).

389. Kwapien, K., Piccinin, S. & Fabris, S. Energetics of Water Oxidation Catalyzed by Cobalt Oxide Nanoparticles: Assessing the Accuracy of DFT and DFT+U Approaches against Coupled Cluster Methods. *J. Phys. Chem. Lett.* **4,** 4223–4230 (2013).

390. Reynolds, J. G., Mauss, B. M. & Daniel, R. C. The Relative Viscosity of $NaNO_3$ and $NaNO_2$ Aqueous Solutions. *J. Mol. Liq.* **264,** 110–114 (2018).

391. Bard, A. J., Faulkner, L. R., *et al. Electrochemical Methods: Fundamentals and Applications* **482,** 580–632 (Wiley New York, 2001).

392. Morhart, T. A., Unni, B., Lardner, M. J. & Burgess, I. J. Electrochemical ATR-SEIRAS Using Low-Cost, Micromachined Si Wafers. *Anal. Chem.* **89,** 11818–11824 (2017).

393. Xia, Z., Woods, A., Quirk, A., Burgess, I. J. & Lau, B. L. T. Interactions between Polystyrene Nanoparticles and Supported Lipid Bilayers: Impact of Charge and Hydrophobicity Modification by Specific Anions. *Environ. Sci. Nano* **6,** 1829–1837 (2019).

394. Miki, A., Ye, S. & Osawa, M. Surface-Enhanced IR Absorption on Platinum Nanoparticles: An Application to Real-Time Monitoring of Electrocatalytic Reactions. *Chem. Commun.,* 1500–1501 (2002).

395. Pronkin, S. & Wandlowski, T. Time-Resolved In Situ ATR-SEIRAS Study of Adsorption and 2D Phase Formation of Uracil on Gold Electrodes. *J. ElectroAnal. Chem.* **550-551,** 131–147 (2003).

396. Samjeské, G. & Osawa, M. Current Oscillations during Formic Acid Oxidation on a Pt Electrode: Insight into the Mechanism by Time-Resolved IR Spectroscopy. *Angew. Chem. Int. Ed.* **44,** 5694–5698 (2005).

397. Osawa, M., Yoshii, K., Hibino, Y.-i., Nakano, T. & Noda, I. Two-dimensional Infrared Correlation Analysis of Electrochemical Reactions. *J. ElectroAnal. Chem.* **426,** 11–16 (1997).

398. Watanabe, M., Zhu, Y. & Uchida, H. Oxidation of CO on a Pt-Fe Alloy Electrode Studied by Surface Enhanced Infrared Reflection-Absorption Spectroscopy. *J. Phys. Chem. B* **104,** 1762–1768 (2000).

399. Yajima, T., Uchida, H. & Watanabe, M. In-Situ ATR-FTIR Spectroscopic Study of Electro-oxidation of Methanol and Adsorbed CO at Pt-Ru Alloy. *J. Phys. Chem. B* **108,** 2654–2659 (2004).

400. Zhu, S., Wang, Q., Qin, X., Gu, M., Tao, R., Lee, B. P., Zhang, L., Yao, Y., Li, T. & Shao, M. Tuning Structural and Compositional Effects in Pd-Au Nanowires for Highly Selective and Active CO_2 Electrochemical Reduction Reaction. *Adv. Energy Mater.* **8,** 1802238 (2018).

401. Yuan, X., Zhang, L., Li, L., Dong, H., Chen, S., Zhu, W., Hu, C., Deng, W., Zhao, Z.-J. & Gong, J. Ultrathin Pd-Au Shells with Controllable Alloying Degree on Pd Nanocubes toward Carbon Dioxide Reduction. *J. Am. Chem. Soc.* **141,** 4791–4794 (2019).